

South Dakota State University  
**Open PRAIRIE: Open Public Research Access Institutional  
Repository and Information Exchange**

---

Theses and Dissertations


---

2017

# Land Surface Phenologies and Seasonalities Using Cool Earthlight in Temperate and Tropical Croplands

Woubet Gashaw Alemu  
*South Dakota State University*

Follow this and additional works at: <http://openprairie.sdstate.edu/etd>

 Part of the [Environmental Sciences Commons](#), [Geographic Information Sciences Commons](#), and the [Remote Sensing Commons](#)

---

## Recommended Citation

Alemu, Woubet Gashaw, "Land Surface Phenologies and Seasonalities Using Cool Earthlight in Temperate and Tropical Croplands" (2017). *Theses and Dissertations*. 1153.  
<http://openprairie.sdstate.edu/etd/1153>

This Dissertation - Open Access is brought to you for free and open access by Open PRAIRIE: Open Public Research Access Institutional Repository and Information Exchange. It has been accepted for inclusion in Theses and Dissertations by an authorized administrator of Open PRAIRIE: Open Public Research Access Institutional Repository and Information Exchange. For more information, please contact [michael.biondo@sdstate.edu](mailto:michael.biondo@sdstate.edu).

LAND SURFACE PHENOLOGIES AND SEASONALITIES USING COOL  
EARTHLIGHT IN TEMPERATE AND TROPICAL CROPLANDS

BY

WOUBET GASHAW ALEMU

A dissertation submitted in partial fulfillment of the requirements for the

Doctor of Philosophy

Major in Geospatial Science and Engineering

Specialization in Remote Sensing Geography

South Dakota State University

2017



This dissertation is dedicated to my lovely wife, Tirualem Mulat Birhanu, & my two little angels, Yeabsira Woubet Gashaw and Eliana Woubet Gashaw.

## ACKNOWLEDGEMENTS

First and for most, I would like to thank the Almighty God for walking me through all this journey!

I would like to express my deep appreciation and gratitude to my advisor, Dr. Geoffrey Henebry, for the patient guidance and mentorship he provided to me, all the way from when I was first considering applying to the PhD program in the Geospatial Science and Engineering, through to completion of this degree. Dr. Henebry's intellectual heft is matched only by his genuinely good nature and down-to-earth humility, and I am truly fortunate to have had the opportunity to work with him.

I would also like to thank Ato Abere Mihretie, Director of Health, Development and Anti-Malaria Association (HDAMA), Ethiopia, for helping our people through his organization and creating the opportunity for me to volunteer in HDAMA that eventually bring the opportunity to meet with my current PhD advisor, Dr. Henebry, in a collaboration project meetings in Ethiopia, led by Dr. Michael Wimberly (Professor, SDSU) with Dr. Henebry (Professor, SDSU), Dr. Gabriel Senay (USGS/EROS; Adjunct Professor, SDSU) and others partnered with HDAMA. In a similar vein, I'd like to thank Dr. Senay for believing in me and recommending me to my current advisor that I could be a potential PhD student, based on our previous meeting at an international conference in Ethiopia.

I would also like to thank my PhD advisory committee members, Drs. Michael Wimberly, Gabriel Senay, Xiaoyang Zhang, John Kimball (University of Montana), and Graduate Faculty Representatives James Burns and Brian Rex for the friendly guidance, thought-provoking suggestions, and the general collegiality that each of them offered to me over the years.

I would like to thank NASA for awarding me a fellowship through their Earth and Space Sciences Fellowship program (NNX13AN58H) to conduct my PhD research. I also thank the Numerical Terradynamic Simulation Group (NTSG) at the University of Montana for providing me the main datasets for my PhD research.

Finally, I'd be remiss if I didn't acknowledge the innumerable sacrifices made by my wife, Tiruaem Mulat Birhanu, in shouldering far more than her fair share of the parenting and household burdens while I pursued this final degree.

## CONTENTS

ABBREVIATIONS .....	ix
LIST OF FIGURES .....	xiii
LIST OF TABLES .....	xx
ABSTRACT.....	xxii
CHAPTER 1 : Introduction .....	1
1.1 Statement of the Problem.....	2
1.2 Research Questions.....	8
1.3 Data and Methods .....	9
1.3.1 Data Used.....	9
1.3.2 Study Areas.....	11
1.3.3 Methods.....	12
1.4 Significance of the Research.....	16
1.5 Organizational Structure of the Dissertation.....	17
1.6 References.....	18
CHAPTER 2 : Land Surface Phenologies and Seasonalities Using Cool Earthlight in Mid-Latitude Croplands.....	30
2.0 Abstract.....	31
2.1 Introduction.....	31
2.2 Methodology .....	34
2.2.1 Remote Sensing Data.....	34
2.2.2 Study Areas.....	35
2.2.3 Data Processing.....	36
2.3 Results.....	39
2.3.1 Growing Degree-Days .....	39
2.3.2 Vegetation Optical Depth.....	43
2.4 Discussion.....	46
2.4.1 VOD and Crop Type.....	46
2.4.2 VOD and Land Cover .....	47
2.4.3 VOD, GDD, and the 2010 Russian Heat Wave .....	48
2.4.4 VOD Compared to NDVI and Meteorological Station Temperature Data .....	49
2.5 Conclusions and Recommendations .....	51

2.6	Acknowledgements.....	52
2.7	References.....	53
CHAPTER 3 : Characterizing Cropland Phenology in Major Grain Production Areas of Russia, Ukraine, and Kazakhstan by the Synergistic Use of Passive Microwave and Visible to Near Infrared Data.....		
		58
3.0	Abstract.....	59
3.1	Introduction.....	60
3.2	Data and Methodology.....	64
3.2.1	Data.....	64
3.2.1.2	In Situ Data.....	66
3.2.2	Study Region.....	67
3.2.3	Methods.....	72
3.3	Results.....	77
3.3.1	Land Surface Seasonalities of Growing Degree-Days.....	77
3.3.2	Land Surface Phenologies of Vegetation Indices.....	86
3.4	Discussion.....	93
3.4.1	Shifting Patterns of Cropping: Real or Illusory?.....	93
3.4.2	Growing Degree-Day Residuals Versus Vegetation Indices.....	94
3.4.3	Heat Wave Impacts on LSPs.....	97
3.5	Conclusions.....	101
3.6	Acknowledgements.....	104
3.7	Author Contributions.....	105
3.8	Conflicts of Interest.....	105
3.9	References.....	105
3.10	Appendix A.....	120
CHAPTER 4 : Comparing Passive Microwave with Visible-to-Near-Infrared Phenometrics in Croplands of Northern Eurasia.....		
		122
4.0	Abstract.....	123
4.1	Introduction.....	124
4.2	Data and Methodology.....	128
4.2.1	Remote Sensing Data.....	128
4.2.2	Study Region.....	129

4.2.3	Characterizing Land Surface Phenology in VODs and NDVI.....	135
4.3	Results.....	138
4.3.1	Time Series Land Surface Phenologies of NDVI and VODs .....	138
4.3.2	Thermal Time to Peak and Peak Height NDVI and VOD Phenometrics .....	142
4.4	Discussions .....	148
4.4.1	VOD and NDVI Peak Heights: Correlations and Biases .....	148
4.4.2	Heatwave Responses of VODs and NDVI.....	153
4.5	Conclusions and Recommendations .....	155
4.6	Acknowledgements.....	157
4.7	Author Contributions .....	158
4.8	Conflicts of Interest.....	158
4.9	References.....	158
4.10	Appendix A.....	167
CHAPTER 5 : Land Surface Phenology and Seasonality Using Cool Earthlight in Croplands of Eastern Africa .....		168
5.0	Abstract.....	169
5.1	Introduction.....	170
5.2	Study Region, Data, and Methodology .....	173
5.2.1	Study Region.....	173
5.2.2	Remote Sensing Data.....	178
5.2.3	Methods.....	180
5.3	Results.....	185
5.3.1	Land Surface Seasonalities of Precipitable Water Vapor .....	185
5.3.2	Land Surface Seasonality and Phenology of AMSR Land Parameters & TRMM Rainfall	185
5.3.3	Land Surface Seasonality of Soil Moisture.....	188
5.3.4	Land Surface Seasonality of Actual Evapotranspiration .....	189
5.3.5	Seasonal Peak and Moisture Time to Peak (MTP) for Land Surface Phenologies and Seasonalities.....	191
5.4	Discussion.....	193
5.4.1	Climate Modes .....	193
5.4.2	Crop Production Responses to Biophysical Factors .....	198



5.5	Conclusion and Recommendations.....	204
5.6	Acknowledgments.....	207
5.7	References.....	207
CHAPTER 6 : Research Summary and Recommendations.....		219
6.1	Summary of the Research Results .....	220
6.2	Recommendations and Future Directions .....	225
6.3	References.....	226
Supplementary Figures .....		227

## ABBREVIATIONS

AGDD	Accumulated Growing Degree-Days
AMSR2	Advanced Microwave Scanning Radiometer 2
AMSR-E Satellite	Advanced Microwave Scanning Radiometer on Earth Observing Satellite
ANCOVA	Analysis of Covariance
ANSR BoA	Amhara National Regional State Bureau of Agriculture
ASC	Ascending
AUC	Area Under the Curve
BRDF	Bidirectional Reflectance Distribution Function
CETaDd	Cumulative Actual Evapotranspiration-Decade
CGS	Core Growing Season
CMG	Climate Modeling Grid
CNVM	Crop-Natural Vegetation Mosaic
CRP	Crop
CSA	Ethiopian Central Statistical Agency
CUP	Carbon Uptake Period
CVD	Cumulative Precipitable Atmospheric Water Vapor-Days
CVDd	Cumulative Precipitable Atmospheric Water Vapor-Decade
CxQ	Convex Quadratic
DMI	Dipole Mode Index
DOY	Day of Year
DOY	Day of Year
DSC	Descending
ENSO	El Niño Southern Oscillation
EOS	End-of-Season
EROS	Earth Resources Observation and Science
ET	Ethiopia
ETa	Actual Evapotranspiration
EVI	Enhanced Vegetation Index
FAO	Food and Agriculture Organization

FEWS NET	Famine Early Warning System Network
fw	Fractional Open Water Over the Ground
FY3B	Chinese FengYun 3B
GCOM-W1	Global Change Observations Mission 1st–Water
GDD	Growing Degree-Days
GHz	Gigahertz
GIEWS	Global Information and Early Warning System
GPP	Gross Primary Production
GRS	Grass
GSI	Growing Season Index
HadISST	Hadley Centre Sea Ice and Sea Surface Temperature
HDAMA	Health Development and Anti Malaria Association
IGBP	International Geosphere Biosphere Programme
IOD	Indian Ocean Dipole mode
IR	Infrared
JAMSTEC	Japan Agency for Marine-Earth Science and Technology
JAXA	Japan Aerospace Exploration Agency
KZ	Kazakhstan
LC	Land Cover
LSP	Land Surface Phenology
LSS	Land Surface Seasonality
LST	Land Surface Temperature
LULC	Land Use Land Cover
MCD	Modis Combined
MFO	Mixed Forest
MOD	Modis Terra Products Prefix
MODIS	MODerate-resolution Imaging Spectroradiometer
MTP	Moisture Time to Peak
MWRI	Microwave Radiation Imager
MYD	Modis Aqua Products Prefix
NASA	National Aeronautical Space Administration

NBAR	Nadir BRDF-Adjusted Reflectance
NDVI	Normalized Difference Vegetation Index
NEP	Annual Net Ecosystem Productivity
NESSF	NASA Earth and Space Science Fellowship
NOAA	National Oceanic and Atmospheric Administration
NTSG	Numerical Terradynamic Simulation Group
OISST	Optimum Interpolation Sea Surface Temperature
PAR	photosynthetically Active Radiation
PH	Peak Height
PH <sub>GDD</sub>	Peak Height Growing Degree-Day
PH <sub>NDVI</sub>	Peak Height Normalized Difference Vegetation Index
PH <sub>VOD</sub>	Peak Height Vegetation Optical Depth
PAR	Photosynthetic Active Radiation
rf	Rainfall
RMSE/D	Root Mean Square Error/Deviation
RU	Russia
SEE	Standard Error of the Estimate
SMAP	Soil Moisture Active Passive
SOS	Start-Of-Season
SS	South Sudan
SSEB	Simple Surface Energy Balance Model
ta	Air Temperature
tc	Vegetation Transparency
TIR	Thermal Infrared
TMPA	TRMM Multi-Satellite Precipitation Analysis
TRMM	Tropical Rainfall Measuring Mission
TTP	Thermal Time to Peak
TTP <sub>GDD</sub>	Thermal Time to Peak Growing Degree-Day
TTP <sub>NDVI</sub>	Thermal Time to Peak Normalized Difference Vegetation Index
TTP <sub>VOD</sub>	Thermal Time to Peak Vegetation Optical Depth
TZ	Tanzania

UA	Ukraine
UBU	Urban and Built-Up
USAID	United States Agency for International Development
USDA FAS Service	United States Department of Agriculture Foreign Agricultural
USDA NASS	United States Department of Agriculture National Agricultural Statistics Service
USDA	United States Department of Agriculture
USGS	United State Geological Survey
V	Precipitable Atmospheric Water Vapor
VI	Vegetation Index
VNIR	Visible to Near Infrared
VOD	Vegetation Optical Depth
VOD <sub>dd</sub>	Vegetation Optical Depth Diel Difference
vsm/mv	Volumetric Soil Moisture
WMO	World Meteorological Organization

## LIST OF FIGURES

- Figure 1-1.** Cropland stability map for the study regions superimposed with the specific AMSR-E pixels (blue squares) selected for this study: 13 in North Dakota, USA and the Canadian Prairie for the first objective; 49 in northern Eurasia for the second and third objectives; and 100 in east Africa for the fourth objective. .... 12
- Figure 2-1.** Study area location map (upper left) and land cover map (USA and Canada – bottom, Russia – upper right) superimposed with AMSR-E pixels of the specific study sites: 1=Grafton, 2=Munich, 3=Turtle Lake, 4=Maxbass, 5=Winnipeg, 6=Prince Albert, 7=Regina, 8=Lethbridge, 9=Edmonton, 10=Saratov 1, 11=Saratov 2, 12=Saratov 3, and 13=Volgograd. Land cover data is from MODIS product MCD12C1 at 0.05° spatial resolution with the maximum of the dominant IGBP land cover class during 2003-2010. Red indicates grasslands; green is croplands, and blue is mixed forest. Yellow indicates a mixture of grasslands and croplands; cyan is a mixture of croplands and mixed forest; and magenta is a mixture of grasslands and mixed forest. .... 36
- Figure 2-2.** AMSR-E retrieved GDD averaged 2003-2010 (black solid line) as a function of AMSR-E retrieved AGDD averaged 2003-2010 superimposed with similar timespan of meteorological station data (red dash-dotted line) from two study sites. Both AMSR-E time series show a good agreement with the station data; however, the late year divergences may arise from missing AMSR-E retrievals due to frozen surface conditions. .... 40
- Figure 2-3.** (a) Average AMSR-E GDD (2003-2010) as a function of average AMSR-E AGDD for all study sites. Canadian sites Edmonton and Prince Albert show lower GDD and AGDD due to their northernmost locations. The GDD in the Russian croplands was higher than that in the USA or Canada. (b) Thermal time to peak GDD calculated from parameter coefficients plotted as a function of latitude (hollow diamonds=USA, gray circles=Canada, light gray triangles=Russia). It shows a general decrease in  $TTP_{GDD}$  as latitude increases. The uppermost triangle is Saratov 1, which is located relatively far from the Volga River and shows higher  $TTP_{GDD}$ , while the three other Russian sites are located along the river..... 42
- Figure 2-4.** Fitted (dotted lines) average GDD as a function of AGDD superimposed with two standard error GDD error bars (gray crosses) for three croplands. The coefficients of determination for Saratov 1, Grafton, and Edmonton are 0.96, 0.98, and 0.97, respectively. Interannual variability in GDD tended to be greater in the transitional seasons of spring and fall than in summer. Note the higher interannual uncertainty at the Russian site. .... 43
- Figure 2-5.** Interannual average (2003-2010) of vegetation optical depth (VOD) as a function of AGDD at the highest AMSR-E frequency. Croplands in Russia attained their peak VOD much earlier than that of the USA and Canada, but with a lower peak and smaller dynamic range..... 44
- Figure 2-6.** Convex quadratic land surface phenology models for VOD in USA (a) and Russia (b). Green is observed VOD at 18.7 GHz and orange is observed VOD at 10.65 GHz. Black dashed and dotted lines indicate the “core growing season” used to fit each LSP

model. The magenta line shows the fitted CxQ model of VOD at 18.7 GHz and the blue line shows the fitted CxQ model of VOD at 10.65 GHz. .... 46

**Figure 2-7.** The deleterious effect of the 2010 Russian summer heat wave on VOD is evident in the Saratov 1, 2 and 3 time series where (a) GDD and AGDD were higher in 2010, while (b) VODs were low compared to the two standard errors of the other years. In 2010 at Regina and Lethbridge, Canada, neither (c) the thermal regimes nor (d) the VOD exhibited distinct deviations from the other years. The general patterns are representative of the other study sites (data not shown). The presented Canadian sites display temperature drop in mid-September while the Regina site had lower VOD throughout the year due to other factor than heat wave. .... 49

**Figure 2-8.** Time series plots of the VOD (cyan circles) & the NDVI (black circles) (2003–2010) from a single AMSR-E pixel, Saratov 1, in Russia. Temperature data (temp.ms) from a nearby meteorological station (red line) is superimposed. The station and VOD data were smoothed with an 8-day retrospective moving average. These data were aligned to the Aqua MODIS MYD09A1 reflectance compositing periods for comparison. All annual data (January 1<sup>st</sup>-December 31<sup>st</sup>) were considered. Notice that the seasonal bimodality of VOD is more pronounced than in the NDVI. The bimodality arises from the planting of winter grains in the fall, and growth and harvest in the subsequent early summer. .... 50

**Figure 3-1.** Land cover stability in Ukraine, southern Russia, and northern Kazakhstan as revealed by IGBP global land cover classification scheme MODIS 0.05° land cover products (resampled to AMSR-E spatial resolution: 0.25°) from 2003–2010: (a) crop–natural vegetation mosaic (IGBP class 14); (b) cropland (IGBP class 12); and (c) grassland (IGBP class 10). Land cover percentage from 2003–2010 displayed as red = maximum percentage, green = mean percentage, and blue = range of percentages. For legend, refer to Table 3-2. .... 69

**Figure 3-2.** Study region cropland stability map superimposed with the 49 specific AMSR-E pixels selected for this study. The AMSR-E pixels are numbered by latitude starting from the most southern site. Name for each site is their closest large settlement (cf. Table 3-3). Red squares are in Ukraine, cyan squares in Russia, and blue squares in Kazakhstan. .... 71

**Figure 3-3.** Scatter plots and linear regression fits of station GDD with satellite GDD—AMSR-E GDD (black circles) and MODIS GDD (blue diamonds)—at Simferopol, Ukraine (site 4) for 2003. The linear regression fit for the two datasets were high with  $r^2$  of 0.93 for the AMSR-E GDD and  $r^2$  of 0.89 for the MODIS GDD. .... 80

**Figure 3-4.** (left) Time series plot of AMSR-E (black) and station (red) daily GDD as a function of station AGDD for 2003 at Kirovohrad, Ukraine (site 15); and (right) linear regression fit of AMSR-E GDD with station GDD for the same dataset yielding strong correspondence with  $r^2 = 0.95$ . Note also the bias (intercept) and the underestimation (slope < 1) of the AMSR-E GDD relative to the station GDD. .... 81

**Figure 3-5.** Average (2003–2010) MODIS (plus signs) and AMSR-E (circles) GDD and their fitted (solid (MODIS LST) and dashed (AMSR-E ta) lines) average GDD as a function of DOY (left) and AGDD (right) for two cropland sites at the latitudinal extremes of the study region: Cheboksary, Russia (site 48, 55.7°N; (a,b)); and Cherkessk, Russia (site 1, 44.4°N; (c,d)). N.B.: MODIS GDDs are multiplied by 8, while AMSR-E GDDs are eight-day sums. .... 83

- Figure 3-6.** Thermal climates as a function of latitude revealed by: (a) average daily GDD; and (b) Thermal Time to Peak ( $TTP_{GDD}$ ). Latitudes were the geographic centers of AMSR-E pixels. All 49 study sites are displayed in both figures. In (b), hollow circles = Russia, orange diamonds = Kazakhstan, and cyan crosses on blue background = Ukraine. Both panels show a general decrease in (a) GDD or (b) TTP as latitude increases from 44° to 56°N. The uppermost two hollow circles are the northernmost study sites (site 49, Kazan', Russia and site 48, Cheboksary, Russia), while the lowermost two hollow circles are the southernmost study sites (site 1, Cherkessk, Russia and 2, Stavropol, Russia). ... 84
- Figure 3-7.** Line plots of annual observed GDD (blue), annual predicted GDD based on multi-year average model (orange) and observed GDD residuals (green) at Orenburg (RU) for: a cooler year (2003) (left); a close-to-average year (2009) (center); and a hotter year (2010) (right). N.B: GDDs are 8-day sums..... 85
- Figure 3-8.** Average MODIS NDVI and EVI as a function of AMSR-E AGDD for Petropavlovsk 3, Kazakhstan (site 42) for 2003–2010. Note that the NDVI displays a larger dynamic range than the EVI. .... 87
- Figure 3-9. (a–d)** In 2003, lower latitude sites (Cherkessk, Russia: 44.4°N (a) and Simferopol, Ukraine: 45.6°N (c) display bimodal growing seasons, while the higher latitude sites show unimodal, shorter growing seasons (Kazan', Russia: 56.1°N (d)). The middle latitude sites display a longer unimodal growing season (Odesa, Ukraine: 47.3°N (b)). . 88
- Figure 3-10.** NDVI and EVI interannual variability in one of the southernmost study sites (Simferopol, Ukraine at 45.6°N) from 2003–2010. Whether due to changes in cultivation practice or crop failures, the VI curves change from bimodal (2003–2004) to unimodal (2005–2009) and back to bimodal (2010)..... 90
- Figure 3-11. Changes in seasonal patterns by sites during 2003–2010: no change (blue circles), one change (white stars with pink borders), or two changes (red squares). Northern study sites displayed no change in seasonal pattern, while southern study sites experienced multiple changes. .... 91
- Figure 3-12. (a–f)** Comparison of AMSR-E AGDD<sub>95%</sub> at 95% of the initial peak VIs with the MODIS AGDD<sub>95%</sub> at 95% of the initial peak VIs in 2003. The panels span a latitudinal gradient: lowest latitude (Cherkessk, Russia (a,d)), middle latitude (Sumy, Ukraine (b,e)), and highest latitude (Kazan', Russia (c,f)) for 95% of the initial peak NDVI (a–c) and EVI (d–f). There is strong linear relationship between AGDDs from AMSR-E and MODIS at 95% of initial peak VIs for these sites in 2003 with  $r^2$  ranging from 0.88 to >0.99. This strong positive relationship was consistent in space and time with  $r^2$  ranging from 0.60 to >0.99 across all study sites and years..... 92
- Figure 3-13.** Average GDD residuals and NDVI with error bars displaying maxima and minima for sites at similar latitude. (a) Sites 35–37 and 39–41 in Kazakhstan (NDVI—blue triangles and GDD residuals—black diamonds) and sites 34 and 42 in Kazakhstan (NDVI—green crosses and GDD residuals—gray circles); and (b,c) sites 1 and 2 in Russia (NDVI—blue diamonds and GDD residuals—black circles) for selected bimodal cropland pattern years and unimodal years, respectively. .... 96
- Figure 3-14.** Comparison of VIs and GDD at similar places during heat wave years (Kuybuskev 2 (a), Russia in 2010 and Mykolayive (b), Ukraine in 2007) and average years



- (Kuybushev 2 (c), Russia in 2005 and Mykolayive (d), Ukraine in 2009). N.B: GDDs are eight-day sums. .... 99
- Figure 3-15.** Sites affected by: the 2010 heat wave (blue circles), the 2007 heat wave (red squares), both the 2010 and 2007 heat waves (white stars with pink borders), and sites affected by neither the 2010 nor the 2007 heat wave (cyan triangles)..... 101
- Figure 4-1.** Land cover stability in Ukraine (UA), southern Russia (RU), and northern Kazakhstan (KZ) as revealed by IGBP global land cover classification scheme MODIS 0.05° land cover products (resampled to AMSR-E spatial resolution: 0.25°) from 2003-2010. (a) crop-natural vegetation mosaic (IGBP class 14); (b) cropland (IGBP class 12); (c) grassland (IGBP class 10). Land cover percentage from 2003-2010 displayed as R=max%, G=mean%, B=range of %. Yellow=stable core area; Magenta=unstable peripheral areas; Black=no occurrence of the given LC. For legend refer to Table 4-1 (Alemu & Henebry, 2016). .... 131
- Figure 4-2.** Cropland stability map overlaid by the 49 specific cropland and one MFO AMSR-E pixels (site 50 - most northern site) study sites. The AMSR-E pixels are numbered from lower to higher latitude. Sites are named by their closest town (Table 4-1). Modified from (Alemu & Henebry, 2016). .... 133
- Figure 4-3.** VOD time series for the three microwave frequencies: green pluses=18.7; purple circles=10.7; orange triangles=6.9 GHz; and blue diamonds=NDVI. Selected series arranged from south to north of our study region: (a) Cherkessk, RU, 44.4°; (b) Kirovohrad, UA, 48.7°; (c) Petropavlovsk 3, KZ, 54.4°; (d) Kazan, RU, 56.1°; and (e) Mari El, RU, 56.4° (MFO site included for comparison). Note that the y-axis scaling for the MFO site (0.2-1.9) is different from the cropland sites (0.2-1.6). .... 140
- Figure 4-4.** VODs in three microwave frequencies (green squares = 18.7, purple circles = 10.7, & orange triangles = 6.9 GHzs) and NDVI (blue diamonds) interannual variability of a southern study site (Simferopol, UA, 45.6° N) for 2003-2010. The 6.9 GHz vegetation transmissivity was missing from the source dataset in 2004. Seasonal patterns change from bimodal (2003-2004) to unimodal (2005-2009) and back to bimodal (2010). There is also seasonal variability within the bimodal and unimodal growing seasons. .... 141
- Figure 4-5.** Average NDVI (2003–2010) as a function of AGDD for cropland sites that encompass the whole latitudinal range: (a) 48, RU; (b) 28, KZ; (c) 11, UA, and (d) 1, RU. The coefficients of determination ( $R^2$ ) for these sites ranged from 0.88 to 0.97. .... 143
- Figure 4-6.** Scatterplot for TTP NDVI as a function of latitude fitted with a quadratic model. There is a significant positive relationship ( $R^2 = 0.5$ ) that as latitude increases TTP NDVI increases in the lower latitudes to certain limit and then declines in the northernmost study sites (44° – 56° N latitude)..... 144
- Figure 4-7.** Scatterplot for PH NDVI and NDVI at half-TTP phenometrics (a) as a function of latitude, and (b) as a function of latitude (b). Both are fitted with linear trend line yielding strong correspondence for the former ( $R^2 = 0.81$ ), but no clear correspondence for the latter ( $R^2 = 0.07$ ). .... 146
- Figure 4-8.** Annual phenometrics of NDVI at half-TTP as a function of PH NDVI (a) for all study sites and (b) for some selected study sites for 2003 – 2010. Sites are numbered according to their latitudinal position from south (1) to north (50) as in table 4-2 (not shown for 8a). .... 146

- Figure 4-9.** Scatter plot of the maximum value approach determined PH VODs and NDVI as a function of their corresponding TTP. Note the magnitude of the VODs and NDVI PHs; VODs PH lagged their counterpart NDVI PH; and also the lag among the VODs PH relative to their microwave frequency. .... 148
- Figure 4-10.** Scatterplots and linear regression fits of the CxQ model derived NDVI PH and maximum value determined VOD PH at three microwave frequencies (6.9 GHz [orange triangles], 10.7 GHz [purple circles], & 18.7GHz [green plus]) for 2003-2010. The PH linear fit for two datasets were high with  $r^2$  of 0.77, 0.84, and 0.78 for the 6.9, 10.7, and 18.7 GHz frequencies, respectively. .... 151
- Figure 4-11.** Scatter plot of (a) the maximum-value determined PH VODs and CxQ model derived PH NDVI phenological metrics as a function of their corresponding TTP, (b) PH VOD lags relative to their corresponding peak greenness as a function of the respective TTP VODs. Note that the PH VODs for all sites except three sites for the 6.9 GHz and one site for the 10.7 and 18.7 GHz PH VODs were lagged from their corresponding PH NDVI (PH VOD lags are above the zero line, b)..... 152
- Figure 4-12.** Scatter plot and linear fit of the CxQ model derived and maximum-value determined NDVI PH from the same MODIS dataset for 2003-2010. The linear fit for PH phenometrics from the two approaches of the same dataset was high with  $r^2$  0.88. .... 153
- Figure 4-13.** VOD and NDVI plots for sample sites (a) Mykolayiv, UA, and (b) Voronezh, RU, affected by the 2007 and 2010 Ukrainian and Russian heatwaves, respectively. In both plots, purple circle represents  $VOD_{10.7GHz}$  and blue diamond represent NDVI plots average (2003 – 2010) excluding the respective heatwave years with relative maximum and minimum error bars. The red circle and orange diamond plots represent heatwave year VODs and NDVIs respectively for both sites. Note the PH in both the average and heatwave affected years. Note also the shapes and magnitudes of the time series in the heatwave years relative to the average of the other years..... 154
- Figure 4-14.** Scatterplot of NDVI at half-TTP as a function of NDVI PH derived from a CxQ model for the 2010 heatwave affecting Russia and Kazakhstan. Note the position of the 2010 phenometrics presented by red diamonds relative to the other years in their respective sites. Note also the 2010 marker for the upper-right corner which is for the MFO site in Russia (Mari El)..... 155
- Figure 5-1.** Cropland class stability map in East Africa for 2003–2012. Yellow shows stable core cropland areas; white displays unstable core areas; magenta displays unstable peripheral areas; and black shows where croplands do not occur in the study period. Superimposed are 100 AMSR pixels (red dots) selected on dominant cropland areas. Pixels are numbered from S to N and then from W to E (all numbers are not labeled due to space limitations). .... 174
- Figure 5-2.** Percent tree cover, bare ground, and waterbody from the Landsat ETM+ 30m resolution Global Land Cover product. Data from (USGS, 2016). .... 177
- Figure 5-3.** Scatterplot of 30-day retrospective moving average of mean AMSR-E atmospheric water vapor (V) as a function of average growing degree-days (GDD) for Zegie, Ethiopia (maroon circles), and Saratov, Russia (blue diamonds) for 2003 to 2010. Blue arrows indicate initial points in January, while magenta arrows indicate end points of the annual

- cycle in December. Red arrows show intra-annual cycles of V for Zegie, ET and cyan arrows for Saratov, RU. Note the relative dynamical range of the variables..... 182
- Figure 5-4.** V time series graphs for ET (a, site #60), TZ (b, #6), and SS (c, #85) for 2003 – 2015. Note differences in scaling of axes. .... 185
- Figure 5-5.** Line graphs and bars of multiyear average (2003-2015) of AMSR V, GDD, vsm, fw and VOD (10.65GHZ) with TRMM rainfall (Rf) as a function of cumulative vapor days (CVD) for an AMSR pixel at sites in Ethiopia (a, #73), South Sudan (b, #78) and Tanzania (c, #14). Note axes scaling differs. .... 187
- Figure 5-6.** Average GDD, vsm, and (VODdd) VOD diel difference (#93, Ethiopia) time series graphs for 2003 - 2015. Purple indicates VODdd, while legend for others is similar to figure 5-5..... 188
- Figure 5-7.** Average (2003 – 2015) vsm superimposed with its interannual CV (%) and standard error bars for site #35 (a, Ethiopia), #5 (b, South Sudan), & #91 (c, Tanzania). Note axes scaling differs..... 188
- Figure 5-8.** Time series of MODIS rainfall, SSEB ETa, and AMSR GDD and VOD for (a) #87, Ethiopia and (b) #14, Tanzania for 2003–2015. Note relationships among variables. ... 189
- Figure 5-9.** Convex quadratic model fit of average ETa (unimodal [a,  $r^2=0.97$ ] and bimodal [c,  $r^2=0.93&0.96$ ]) and V (unimodal [b,  $r^2=0.79$ ] and bimodal [d,  $r^2=0.63&0.38$ ]) growing season for 2003-2015. Blue bars are rainfall (rf) graphs for the same period. (a&b) are for site #48, Ethiopia, while (c&d) are for site #14, Tanzania. Note the relative dynamics of ETa and V in relation to rf; and also axis value differences for the given variables by site. .... 190
- Figure 5-10.** Moisture Time to Peak (MTP) or Moisture Time to Trough (MTT) for cropland land surface variables in Ethiopia for 2003 to 2015 ( $r^2 > 0.8$ ). The variables listed in the diagonal of the figure from top-left to bottom-right include moisture time to peak or trough for MTP for growing degree-days (MTP GDD), precipitable water vapor (V), volumetric soil moisture (vsm), fractional open water (fw), rainfall (rf), actual evapotranspiration (ETa), vegetation optical depth diel difference (VODdd), MTT for growing degree-day (MTT GDD), and vegetation optical depth (VOD). Note that peak rf lags peak V, peak soil moisture, and peak VOD; but VODdd lags peak rf. Upper panel shows the Pearson correlation coefficients. All correlations were significant with  $p<0.01$ . To identify variables combination for any given plot or r-value, make horizontal and vertical lines towards the diagonal line of the square matrix containing the variables... 192
- Figure 5-11.** Thirty years (1986-2015) standardized anomaly five months retrospective smoothed time series plots of NIÑO3 (blue) and DMI (black) for 2002–2016. Pink horizontal lines represent  $\pm$  standard deviation. .... 195
- Figure 5-12.** Time series cumulative vsm (a), fw (b), and VOD (c) in central Ethiopia. The neutral ENSO/IOD years are represented by the black line, while the maxima and minima of this combination are represented by gray. The rest shows other possible combinations of ENSO/IOD. .... 197
- Figure 5-13.** AUC of VODdd (green area under purple curve) at AMSR pixel cropland site in Ethiopia (Site 82). The cut points were determined based on the seasonality of volumetric soil moisture..... 199

- Figure 5-14.** Relationships between area under VOD<sub>dd</sub> curve and crop production (a) and yield (b) statistical data at the woreda level in the Amhara Region in northwestern Ethiopia for 2014. Both fits are significant at  $p < 0.01$ ..... 201
- Figure 5-15.** Time series graphs of cultivated area (a), crop production (b), and VOD<sub>dd</sub> AUC (c) in five zones (SW=South Wollo, EG=East Gojjam, NW=North Wollo, SG=South Gondar, NS=North Shewa, WS=West Shewa, and Ar=Arsi. Note the rate of change difference of the crop production data particularly relative to the VOD<sub>dd</sub> AUC satellite derived data. .... 203
- Figure 5-16.** Time series graphs of national annual crop production data in Ethiopia and Tanzania for 1993-2015. Source: (FAO, 2013). Note the exponential growth rate of crop production data in Ethiopian relative to the lower linear growth rate in Tanzania. .... 204

## LIST OF TABLES

<b>Table 1-1.</b> Interpretative legend for figure 1-1 that displayed IGBP MODIS 0.05° land cover variation from 2003-2012 in the study region. The table shows how the color in the LC map (figure 1-1) arises from the false color composite of red, green, and blue color planes that display, respectively, the maximum percentage of LC class, the average percentage of LC class, and the range of percentages of LC class over the study period.....	12
<b>Table 2-1.</b> Study site name, location, average fitted peak height of growing degree-days ( $PH_{GDD}$ ), average thermal time to peak GDD ( $TTP_{GDD}$ ), day of year at peak GDD ( $DOY@PH_{GDD}$ ), and average coefficient of determination for convex quadratic ( $CxQ$ ) model fits during the period 2003-2010. ....	41
<b>Table 2-2.</b> Study site name, coefficient of determination, peak height of VOD, thermal time to peak VOD, and day of year at VOD peak for AMSR-E frequencies 10.65 GHz and 18.7 GHz, respectively, and the difference in growing degree-days between $TTP_{VOD}$ at the two frequencies.....	45
<b>Table 3-1.</b> Percentage of days with meteorological station data missing during the growing season.....	67
<b>Table 3-2.</b> Interpretative legend for figure 3-1 that display IGBP MODIS 0.05° land cover variation from 2003-2010 in the study region. The table shows how the color in the LC map (figure 3-1) arises from the false color composite of red, green, and blue color planes that display, respectively, the maximum percentage of LC class, the average percentage of LC class, and the range of percentages of LC class over the study period. Source: (Henebry et al., 2013). ....	68
<b>Table 3-3.</b> Description of 49 study sites named by their closest town and country, numbered from lower latitude (1) to higher latitude (49), their geographic coordinates, and average cropland (CRP) cover percent and range (2003–2010). Note sites with 100% average CRP cover throughout the study period (bold), and larger CRP cover percent range (underlined).....	72
<b>Table 3-4.</b> Average (2003–2010) MODIS land cover with the 10 km buffer zone for meteorological stations and corresponding AMSR-E pixel study sites. Bold indicates the dominant land cover (all sites are in crop dominated areas).....	79
<b>Table 3-5.</b> Root mean square error (RMSE), linear regression model (intercept, slope and $r^2$ ), and analysis of covariance (ANCOVA) between station and satellite GDDs from AMSR-E and MODIS sensors. AMS=AMSR-E; MOD=MODIS.....	79
<b>Table 3-6.</b> Peak GDDs and VIs and corresponding AGDDs during heat wave years and average years at two representative sites.....	100
<b>Table 4-1.</b> Interpretive legend for Figures 4-1 that display IGBP MODIS 0.05° land cover variation from 2003-2010 in the study region. ....	132
<b>Table 4-2.</b> Study sites (named by their closest town) and their country, numbered from lower latitude (1) to higher latitude (50), their geographic locations, and average cropland (CRP) cover % and range from 2003-2010. Note that sites with 100 % average CRP cover throughout the study period are indicated in bold, and extrema in CRP cover % range are indicated by underlines for high and bold italics for low.....	134

<b>Table 4-3.</b> Regression parameters for the linear relationships between peak greenness (PH NDVI) and PH VOD.....	149
<b>Table 5-1.</b> Interpretive legend for Figures 5-1 that display IGBP MODIS 0.05° land cover variation from 2003-2012 in the study region. Modified from (Henebry et al., 2013)...	175
<b>Table 5-2.</b> MTP lag in weeks between each variable averaged in space and time (2003-2015) for Ethiopian sites. Note that these lags can vary in space and time for particular sites. ....	193
<b>Table 5-2.</b> Classification of years when El Niño or La Niña and/or positive or negative Indian Ocean dipole occurred. ....	196

## ABSTRACT

LAND SURFACE PHENOLOGIES AND SEASONALITIES USING COOL  
EARTHLIGHT IN TEMPERATE AND TROPICAL CROPLANDS

WOUBET GASHAW ALEMU

2017

In today's world of increasing food insecurity due to more frequent and extreme events (droughts, floods), a comprehensive understanding of global cropland dynamics is critically needed. Land surface parameters derived from the passive microwave Advanced Microwave Scanning Radiometer on EOS (AMSR-E) and AMSR2 data enable monitoring of cropland dynamics and they can complement visible to near infrared (VNIR) and thermal infrared (TIR) data. Passive microwave data are less sensitive to atmospheric effects, cloud contamination, and solar illumination constraints resulting in finer temporal resolution suitable to track the temporal progression of cropland cover development compared to the VNIR data that has coarser temporal resolution due to compositing to lessen the atmospheric effects. Both VNIR and TIR data have moderate to fine spatial resolution compared to passive microwaves, due to the faint microwave flux from the planetary surface. I used AMSR, MODIS, TRMM, and simplified surface energy balance (SSEB) data to study cropland dynamics from 2003-2015 in North Dakota, USA, the Canadian Prairie Provinces, Northern Eurasia, and East Africa: a contrast between crop exporting regions and a food insecure region. Croplands in the temperate region are better studied compared to that of the tropics. The objective of this research was to characterize cropland dynamics in the tropics based on the knowledge gained about the microwave products in the temperate croplands. This study also aimed at assessing the utility of passive microwave data for cropland dynamics study, especially for tropical cropland regions that are often cloud-obscured during the growing season and have sparse *in situ* data networks. Using MODIS land cover data, I identified 162 AMSR grid cells (25km\*25km=625km<sup>2</sup>) dominated by croplands within the study regions. To fit

the passive microwave time series data to environmental forcings, I used the convex quadratic (CxQ) model fit that has been successfully applied with the VNIR and TIR data to herbaceous vegetation in temperate and boreal ecoregions. Land surface dynamics in the thermally-limited temperate croplands were characterized as a function of temperature; whereas, a function of moisture to model land surface dynamics in the tropical croplands. In the temperate croplands, growing degree-day (GDD), NDVI, and vegetation optical depth (VOD) were modeled as a convex quadratic function of accumulated GDD (AGDD) derived from AMSR air temperature data, yielding high coefficients of determination ( $0.88 \leq r^2 \leq 0.98$ ). Deviations of GDD from the long term average CxQ model by site corresponded to peak VI producing negative residuals (arising from higher latent heat flux) and low VI at beginning and end of growing season producing positive residuals (arising from higher sensible heat flux). In Northern Eurasia, sites at lower latitude ( $44^\circ - 48^\circ$  N) that grow winter grains showed either a longer unimodal growing season or a bimodal growing season; whereas, sites at higher latitude ( $48^\circ - 56^\circ$  N) where spring grains are cultivated showed shorter, unimodal growing seasons. Peak VOD showed strong linear correspondence with peak greenness (NDVI) with  $r^2 > 0.8$ , but with a one-week lag. The AMSR data were able to capture the effects of the 2010 and 2007 heat waves that devastated grain production in southwestern Russia and Northern Kazakhstan, and Ukraine, respectively, better than the MODIS data. In East African croplands, the AMSR, TRMM, and SSEB datasets modeled as a convex quadratic function of cumulative water-vapor-days displayed distinct cropland dynamics in space and time, including unimodal and bimodal growing seasons. Interannual moisture variability is at its highest at the beginning of the growing season affecting planting times of crops. Moisture time to peak from AMSR and TRMM land surface parameters displayed strong correspondence ( $r^2 > 0.80$ ) and logical lags among variables. Characterizing cropland dynamics based on the synergistic use of complementary remote sensing data should help to advance and improve agricultural monitoring in tropical croplands that are often associated with food insecurity.



## **CHAPTER 1 : Introduction**

## 1.1 Statement of the Problem

In the face of increasing concerns about the food-water-energy nexus, a better understanding of global cropland dynamics is urgently needed. About 10% of the earth's terrestrial surface (1.5 billion ha) is covered by crops, both irrigated and rainfed (Thenkabail et al., 2009). Wheat is one of important crops to assure global food security (Fischer et al., 2014). It's among few global crops such as rice, maize and soybean in terms of harvested area extent, production and yield (Fischer et al., 2014). The USA is a major wheat producing country in the world, followed by China, the European Union, and India. Wheat ranked third among US field crops both in terms of planted acreage and farm receipts and about half of the yield is exported (USDA-ERS, 2013). In 2011, wheat in the USA constituted an area of about 18 million ha (FAO, 2013). About 80% of the wheat grown on the Canadian Prairies is exported (Qian et al., 2009).

Northern Eurasia is the other potential region of the world with important croplands producing food crops to combat global food insecurity. About 80% of the Volga River Basin is cultivated (Golosov & Belyaev, 2007), of which 21 million ha were covered by wheat in 2011 (FAO, 2013). Although grain production in Russia (RU), Ukraine (UA), and Kazakhstan (KZ) declined significantly following the collapse of the Soviet Union, it has begun to recover due to favorable market conditions (Lindeman, 2014; Lioubimtseva & Henebry, 2012; Sobolev, 2015; Whitney, 2014). If the recent increases in crop production continue, this region may become a key source to address food security crises in the coming decades, despite ongoing challenges arising from land use change, regional conflicts, and climatic variability, extremes, and change.

In contrast to the surplus crop producing and exporting temperate regions, crop production in East Africa is merely subsistence. Croplands in this region cover 45 million ha. Ethiopia (ET) and Tanzania (TZ) are the two major crop producing countries in the region, accounting 14 million ha and 13 million ha of croplands, respectively. South Sudan remains a bit of a mystery as it is still too new to appear in the FAO agricultural databases. The economy in East Africa is heavily dependent on traditional rain-fed agriculture, which is vulnerable to extreme weather events such as drought and floods (Becker-Reshef et al., 2010; Brown et al., 2010). Moreover, the region has mismatched population growth and economic development with population growth outpacing economic development. Rainfall trend in the region has been decreasing and is highly variable in space and time (Lyon & DeWitt, 2012). Thus, the region has been one of the most food insecure parts of the world. During the past century, shortage of rainfall in Ethiopia led to recurrent drought, which resulted in substantial shortfalls in agricultural production and recurrent famine (Rientjes et al., 2013).

To address issues of food insecurity, we need a comprehensive understanding of cropland dynamics for major commodities and regionally important foodstuffs. Land surface phenology and seasonality play important roles in monitoring cropland dynamics. Phenology and seasonality are complementary aspects of ecosystem functioning: phenology deals with timing of biotic phenomena; whereas, seasonality concerns temporal patterns of abiotic variables. Land surface phenology (LSP) deals with the timing of vegetated land surface dynamics as observed by satellite remote sensors, particularly at spatial resolutions and extents relevant to meteorological processes in the

atmospheric boundary layer (de Beurs & Henebry, 2004, 2010). Due to the coarse spatial resolution of remote sensors relative to the biotic elements (e.g., leaves, individual plants, or crop canopies), LSP deals with the dynamics of mixtures of signals from the land surface as opposed to traditional species-centric plant phenology (de Beurs & Henebry, 2008b; Reed et al., 1994). In a similar manner, land surface seasonality (LSS) describes the timing of abiotic phenomena occurring across the land surface as observed by remote sensing. Examples of LSS include albedo, temperature, soil moisture, soil freeze/thaw, ponding and flooding, snow cover, and other recurrent and variable aspects of land surface dynamics.

Comparative studies of cropland LSPs enable the discrimination between crop types (Gumma et al., 2011; Thenkabail et al., 2007; Xiao et al., 2006; Xiao et al., 2005), provide observations which can be assimilated into process-based crop models increasing model prediction accuracy (Doraiswamy et al., 2004; Fang et al., 2011), enable impact assessment and early warning for drought (Rojas et al., 2011), and can aid forecasting of crop yields (Bolton & Friedl, 2013b; Moriondo et al., 2007). Phenological studies integrate climate-biosphere relationships because the timing of vegetation lifecycle events is influenced by temperature and precipitation (de Beurs & Henebry, 2008a; Los et al., 2001; Morisette et al., 2009; Pitt & Heady, 1978).

The mid-latitudes are thermally limited with respect to net primary production; temperature is the primary constraint for crop production (Moriondo et al., 2007; Zhang et al., 2004). Air temperature is a key forcing for crop growth and development (Asseng

et al., 2011; Gordon & Bootsma, 1993; Ritchie & NeSmith, 1991; Wang et al., 2011).

The concept of heat units or thermal time was introduced by Réaumur in 1730 (McMaster & Wilhelm, 1997). A common metric of thermal time is the growing degree-day (GDD), which weights the passage of calendar time by the temperature deemed useful for plant growth (de Beurs & Henebry, 2004; Goodin & Henebry, 1997; Gordon & Bootsma, 1993). Use of GDD and accumulated GDD (AGDD) can improve phenological analyses (Boschetti et al., 2009; McMaster & Wilhelm, 1997; Viña et al., 2004a), and crop yield models (Raun et al., 2001; Sarma et al., 2008; Teal et al., 2006). On the other hand, tropical croplands can be moisture limited. Croplands in Africa are strongly dependent on rainfall and soil moisture for crop growth and development. A study in West Africa found that the length of sowing period depended mainly on rainfall and soil moisture (Brown & de Beurs, 2008).

In most countries, observations from the network of weather stations is sparse in space and incomplete in time. Remote sensing offers multiple approaches to estimate temperature and moisture in a spatially comprehensive way at the cost of spatial precision and temporal resolution. The theoretical basis of using remotely sensed information to monitor crop growth and development was based on United States Department of Agriculture (USDA) research in the 1960s through the 1970s that characterized the optical properties of crop type and crop fields (Becker-Reshef et al., 2010). Satellite-based studies of LSP and LSS first began with the launch of the first remote sensing satellite, namely Earth Resource Technology Satellite (ERTS-1; later named Landsat 1) launched on July 23, 1972 and operating in the VNIR spectrum (Henebry & de Beurs,

2013). Various research projects were conducted on agricultural monitoring and yield estimation through the analysis of crop phenology, benefiting from the fine spatial resolution of Landsat data (< 60m) but with the cost of the coarse temporal resolution (every 16 days) relative to crop vegetation dynamics (Henebry & de Beurs, 2013). The much finer temporal but coarser spatial resolution VNIR imagery from the National Oceanic and Atmospheric Administration (NOAA) Advanced Very High Resolution Radiometer (AVHRR) and then the National Aeronautics and Space Administration (NASA) Moderate Resolution Imaging Spectroradiometer (MODIS) compared to the Landsat series have been widely used for land surface phenology and land surface seasonality studies in later years.

The USDA Foreign Agricultural Service now routinely uses remote sensing to monitor conditions in key crop production areas across the globe to generate market intelligence, particularly in regions where information is scarce or unreliable (USDA-FAS, 2015b). Vegetation indices from the VNIR spectrum are developed usually using the red, which is strongly absorbed by green vegetation, and NIR, strongly reflected by green vegetation, bands (Henebry & de Beurs, 2013). Therefore, the spring-summer increase, for example, in NDVI is governed by increased absorption of the red wavelength by chlorophyll, and increased reflectance of the NIR due to the complex interaction with the internal leaf structure and between the leaves, canopy structure, and the background soil. Remotely sensed vegetation indices such as the Normalized Vegetation Index (NDVI; Tucker, 1979) have been widely utilized for agricultural mapping and monitoring (Benedetti & Rossini, 1993; Funk & Budde, 2009; Maselli et

al., 1992; Mkhabela et al., 2011; Rasmussen, 1992). However, such indices have limitation, such as the loss of sensitivity over dense canopies or soil background contamination in areas of sparse vegetation.

Land surface phenology studies have long been limited to the conventional VNIR imagery, predominantly from AVHRR and MODIS sensors, given the free accessibility of the data and standard formats and products. However, imagery from the VNIR spectrum is affected by cloud cover, atmospheric aerosols, and solar illumination constraints. LSP and LSS measurements from satellite passive microwave radiometers are less sensitive to such adverse effects and can complement the VNIR measurements. Microwave radiometers measure microwave emission, expressed in terms of brightness temperature for vertical and horizontal polarizations. Microwave radiometers have been operating on various satellites since 1978, the Scanning Multichannel Microwave Radiometer (SMMR) being the first sensor, followed by the Special Sensor Microwave Imager (SSM/I), and then the Advanced Microwave Scanning Radiometer on Earth Observing Systems (AMSR-E), Microwave Sounding Unit (MSU), Advanced Microwave Sounding Unit (AMSU), Soil Moisture and Ocean Salinity (SMOS), Advanced Microwave Scanning Radiometer 2 (AMSR 2; Wagner et al., 2007).

Therefore, the whole story of this research is about:

- Assessing the utility of passive microwave data for land surface phenology and land surface seasonality studies, which have been dominantly conducted using the VNIR and TIR data;

- Acquiring a better understanding about the performance of the passive microwave data in well-characterized temperate croplands using VNIR and TIR data that can help us to interpret the results in the less well-characterized tropical croplands;
- Assessing the utility of passive microwave data in the tropical croplands, where VNIR data are impaired by dense cloud cover and atmospheric aerosols, and *in situ* data are sparse and of variable quality;
- Comparing cropland dynamics in the thermally limited temperate croplands against the moisture limited tropical croplands; and
- Comparing cropland dynamics in the major food crop producing and exporting regions of the world against that of a highly food insecure part of the world.

## 1.2 Research Questions

To address the above mentioned broad aims of this study, we have designed the following four specific research questions.

Research Question 1:

*Can we use convex quadratic (CxQ) models of land surface phenology, which have been successfully used with VNIR and TIR data on herbaceous vegetation in the temperate and boreal regions, with AMSR-E passive microwave data products—air temperature and VOD—to study land surface phenology & seasonality in temperate croplands?*

Research Question 2:



*Can the synergistic use of the VNIR MODIS NDVI and the passive microwave AMSR-E-retrieved air temperature data enable characterization of cropland dynamics in the mid-latitudes?*

Research Question 3:

*Can AMSR-E passive microwave derived VOD peak height (PH) phenometrics track cropland seasonal dynamics be complementary to the VNIR MODIS NDVI peak vegetation greenness?*

Research Question 4:

*Is it possible to characterize cropland dynamics in tropical eastern Africa using the blended AMSR-E/AMSR2 passive microwave dataset?*

## **1.3 Data and Methods**

### **1.3.1 Data Used**

#### ***1.3.1.1 Remote Sensing Data***

We used products from the satellite passive Advanced Microwave Scanning Radiometer on EOS (AMSR-E; Jones et al., 2010) and AMSR2 (Du et al., 2014). These datasets include surface air temperatures ( $t_a$ ; ~2 m height; valid range: 240-340 K), fractional coverage of open water over land ( $fw$ ; valid range: 0-1), vegetation canopy transmittance ( $t_c$ ) at three microwave frequencies (6.925 GHz, 10.65 GHz and 18.7 GHz), surface soil moisture ( $mv$ ;  $\leq 2$  cm soil depth; valid range: 0-1  $\text{cm}^3/\text{cm}^3$ ), and integrated water vapor content ( $V$ ; valid range: 0-80mm) of the total column (Du et al.,

2014; Jones & Kimball, 2011). We have also used data from the optical sensor Moderate Resolution Imaging Spectroradiometer (MODIS; DAAC-LP, 2014). These products include land surface temperature (LST) from both Terra (MOD11C2) and Aqua (MYD11C2) satellites and Nadir BRDF-Adjusted Reflectance, which combines observations from Terra and Aqua MCD43C4 satellites (DAAC-LP, 2014). The third dataset used in this study is rainfall from the Tropical Rainfall Measuring Mission (TRMM 3B42 (V7)) dataset. We have also used 1km resolution dekadal (10-day) actual evapotranspiration (ETa) data from the simple surface energy balance model (SSEB, Senay et al., 2007; Senay et al., 2013).

To identify our specific cropland study areas, we used three datasets: the International Geosphere Biosphere Programme (IGBP) land cover scheme in the MODIS land cover product (MCD12C1; DAAC-LP, 2014), the USDA Foreign Agriculture Service (FAS) crop layers by oblast (for Russia: [\(USDA-FAS, 2011b\)](#), for Kazakhstan: [\(USDA-FAS, 2011a\)](#), for Ukraine: [\(USDA-FAS, 2011c\)](#)), and Google Earth images. Detailed descriptions of these datasets is given in the respective articles, which are dissertation chapters here.

### ***1.3.1.2 In Situ Data***

Meteorological station data from National Oceanic and Atmospheric Administration (NOAA) historical climate data (FEWS-NET, 2014) was also used in this study to compare it with the satellite retrievals.

### 1.3.2 Study Areas

Our study areas encompass the spring wheat producing areas of the USA and the Canadian Prairie, the major grain producing areas of northern Eurasia, and the most food insecure East Africa (figure 1.1). In order to select specific study sites (size of AMSR-E pixels each: 25km\*25km) with a high and stable percentage of cropland, we conducted a temporal stability analysis for cropland cover class over the study period by first calculating the maximum, minimum, and mean land cover percentage over the study period and then displaying the maximum, mean, and range in the red, green, and blue color planes, respectively (Henebry et al., 2013). Yellow (high maximum and high mean and low range) identifies land cover that is stable over the study period (figure 1-1, table 1-1). Expanses of yellow in figure 1-1 indicate where croplands continues to be the dominant land cover during the study period.

We selected the study sites within the stable core areas of cropland, but we also used the USDA Crop Explorer maps to identify wheat producing areas in the relatively bigger temperate croplands. In contrast, in the fragmented and smaller croplands of tropical East Africa, we have used the MODIS land cover product (MCD12C1) as a general guidance, while we mainly used higher resolution imagery available in Google Earth to select the specific study sites.

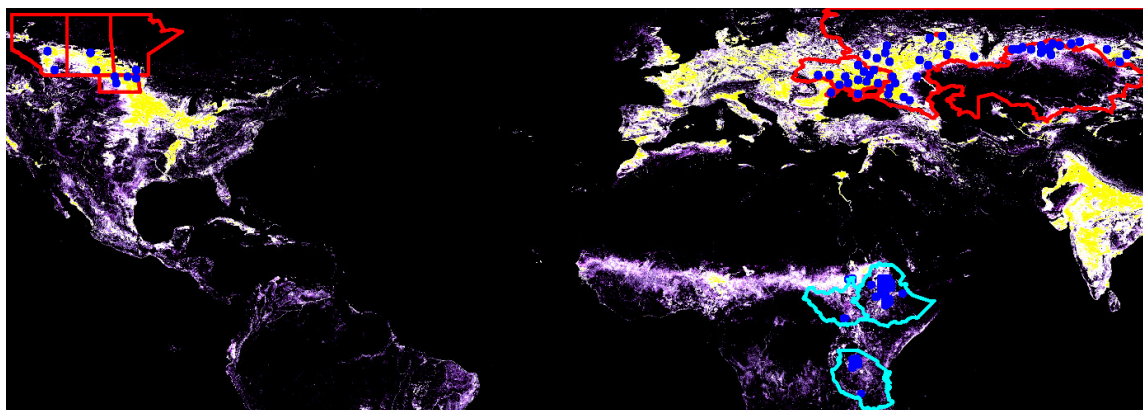


**Figure 1-1.** Cropland stability map for the study regions superimposed with the specific AMSR-E pixels (blue squares) selected for this study: 13 in North Dakota, USA and the Canadian Prairie for the first objective; 49 in northern Eurasia for the second and third objectives; and 100 in east Africa for the fourth objective.

**Table 1-1.** Interpretative legend for figure 1-1 that displayed IGBP MODIS 0.05° land cover variation from 2003-2012 in the study region. The table shows how the color in the LC map (figure 1-1) arises from the false color composite of red, green, and blue color planes that display, respectively, the maximum percentage of LC class, the average percentage of LC class, and the range of percentages of LC class over the study period.

Color in LC Map	Red = Max % LC	Green = Mean% LC	Blue = Range % LC	Interpretation
Black	None	None	None	Land cover (LC) class absent
Blues	Low	Low	High	Unstable but ephemeral periphery; rare and erratic
Magentas	High	Low	High	Unstable but persistent periphery; sometimes high, but usually low
Whites	High	High	High	Unstable core; sometimes low, but usually high
Yellows	High	High	Low	Stable core of LC; always high so low range

Source: (Henebry et al., 2013)

### 1.3.3 Methods

For research questions one to three that were conducted in the temperate croplands, we used eight years—2003 through 2010 of AMSR-E and/or MODIS data. To

avoid the frozen season and to maintain a consistent analysis period across all study pixels, we restricted our focus to data from DOY 89-305, which ranges between 30 March to 1 November for non-leap years and between 29 March to 31 October for leap years.

GDDs were calculated with a base temperature of 273.15 K (=0 °C) as follows:

$$\text{GDD} = \max\left[\frac{t_{ASC} + t_{DSC}}{2} - 273.15, 0\right] \quad [1]$$

where  $t_{ASC}$  and  $t_{DSC}$  are the air temperature retrievals at the ascending and descending passes. Accumulated GDD (or AGDD) was calculated from GDD.

$$\text{AGDD}_t = \text{AGDD}_{t-1} + \text{GDD}_t \quad [2]$$

where  $\text{GDD}_t$  is daily temperature increment of growing degree-days at time  $t$ .

To characterize the seasonal progression of thermal time, we fitted the GDDs as a convex quadratic (CxQ) function of AGDD. The CxQ model has been successfully applied in temperate herbaceous vegetation and boreal ecosystems (de Beurs & Henebry, 2010; Raun et al., 2001; Yang et al., 1997).

$$\text{GDD}_t = \alpha + \beta \text{AGDD}_t - \gamma \text{AGDD}_t^2 \quad [3]$$

The intercept  $\alpha$  is the start of observation period GDD value, the linear parameter  $\beta$  affects the slope, and the quadratic parameter  $\gamma$  controls the curvature. Since our model is convex quadratic in shape, the sign of  $\beta$  is positive while the sign of  $\gamma$  is negative.

Two phenometrics were derived from the fitted parameter coefficients of the CxQ model. The peak height (PH) (equation 4) describes the maximum GDD from the fitted model, and the thermal time to peak (TTP) (equation 5) describes the amount of AGDD needed to reach the peak GDD:

$$PH_{GDD} = \alpha - (\beta^2/4\gamma) \quad [4]$$

$$TTP_{GDD} = -\beta/2\gamma \quad [5]$$

where  $\alpha$ ,  $\beta$ ,  $\gamma$  are the fitted parameter coefficients.

NDVI and EVI were calculated from the MODIS NBAR reflectance data using the formula developed by Tucker (1979) and Huete et. al (2002). We fitted NDVI as a function of AGDD with convex quadratic (CxQ) model (equation 3). The PH and TTP phenometrics for the NDVI CxQ fit were derived in a similar procedure as in equation 4 and 5 above respectively. Vegetation Optical Depth (VOD) was derived as a negative logarithm of vegetation transmittance [ $VOD = -\log_e(tc) = -\ln(tc)$ ]. The transparency (or transmissivity) of the canopy is inversely related to canopy thickness or Vegetation Optical Depth (VOD; Owe et al., 2001). The VOD parameter is a frequency dependent measure of canopy attenuation of microwave emissions due to vegetation biomass structure and water content (Jones et al., 2012). Lower VOD (higher transmissivity) indicates lower attenuation of soil-emitted microwave radiation by overlying vegetation canopy and vice versa. VOD equal to 0 corresponds to a transmissivity of 1 indicating bare soil, and for dense vegetation the transmissivity gets close to 0 (Liu et al., 2011; Owe et al., 2001).

For research question four that was conducted in East Africa, we have used thirteen years (2003-2015) of passive microwave AMSR-E and TRMM and ETa from SSEB model product. The tropical system is moisture limited. Thus, we analyzed the biophysical and climatic variables time series data as a function of atmospheric precipitable water vapor, rather than using AGDD as in the temperate croplands. Cumulative water vapor days (CVD) are the summation of AMSR V throughout the whole year. That is, the passage of days is weighted by the quantity of V occurring that day (equation 6).

$$CVD_t = CVD_{t-1} + V_t \quad [6]$$

where  $V_t$  is daily atmospheric precipitable water vapor at time  $t$ .

We have accumulated annual ETa and V data (designated as CETaDd [Cumulative ETa Decad] and CVDDd [Cumulative V Decad]) to characterize all our study variables as a function of CETaDd and CVDDd (equation 7). Water vapor days (CVD) are the summation of AMSR V throughout the whole year. That is, the passage of days is weighted by the quantity of V occurring that day (equation 8).

$$CETaDd_t = CETaDd_{t-1} + ETa_t \quad [7]$$

$$CVDDd_t = CVDDd_{t-1} + V_t \quad [8]$$

where ETa is 10-day actual evapotranspiration;  $V_t$  is 10-day atmospheric precipitable water vapor at time  $t$ .

To characterize the seasonal progression of moisture, we fitted the ETa from SSEB model product and V from AMSR as a convex quadratic (CxQ) function of

CETaDd and CVDD respectively (equation 9&10; de Beurs & Henebry, 2004, 2010; Henebry & de Beurs, 2013):

$$ETa_t = \alpha + \beta CETaDd_t - \gamma CETaDd_t^2 \quad [9]$$

$$V_t = \alpha + \beta CVDD_t - \gamma CVDD_t^2 \quad [10]$$

where the intercept  $\alpha$  is the start of observation period GDD value (which may not be zero due to the compositing), the linear parameter  $\beta$  affects the slope, and the quadratic parameter  $\gamma$  controls the curvature. Specific datasets and more detailed description of the methods is given under each chapter that hold each research question.

#### **1.4 Significance of the Research**

This study demonstrated the use of satellite passive microwave dataset for cropland land surface phenology and seasonality. Microwave radiometers can sense terrestrial emissions (earthlight) at night and through clouds that leads to finer temporal resolution relative to VNIR imagery, which must be composited to minimize cloud contamination and atmospheric effects. Microwave radiometers can sense emissions from both leaf and woody components of aboveground vegetation. The main disadvantage of passive microwave radiometry is its coarse spatial resolution (25 km in this study) due to low energy terrestrial microwave emissions (Jones et al., 2012; Liu et al., 2011), while VNIR datasets have fine to moderate spatial resolution. This study demonstrated the synergistic use of VNIR and passive microwave remote sensing datasets. Since the



temperate croplands are temperature limited, we have modeled LSP and LSS as a function of AGDD.

The tropical croplands such as east Africa, *in situ* data are sparse and even the existing ones have poor quality. VNIR datasets usually obscured by clouds and atmospheric aerosols. Microwave datasets can be good alternatives to overcome such problems. Given the small-sized and fragmented farmlands in the tropics, using the coarse spatial resolution microwave datasets may have a limitation. But the synergistic use of the VNIR and microwaves can minimize such drawbacks. Tropical croplands are moisture limited. Thus, this study characterizes LSP and LSS of the tropical croplands as a function of atmospheric precipitable water vapor. This research makes all these efforts and arrive at encouraging results. Therefore, this study makes a valuable addition to the existing knowledge and skills of the research community concerning the use of microwave data products and more particularly the synergistic use of both the microwave and VNIR data products to monitor cropland dynamics for food security.

## **1.5 Organizational Structure of the Dissertation**

This research dissertation has six chapters, including this introductory first chapter. Chapter Two explores the use of microwave data for LSP and LSS studies on the spring wheat croplands of North America and the spring and winter wheat producing areas of the Volga river basin of Russia. It uses the CxQ modeling process for GDD and VOD. Chapter Three is about the synergistic use of passive microwave and VNIR and TIR satellite data to characterize cropland dynamics in the major grain producing areas of

northern Eurasia. It presents VNIR VIs as a function of AGDD from passive microwave air temperature. The chapter also describes the impact of major heatwaves of the region on croplands. The research presented in Chapter Four is conducted in the same study area as Chapter Three, but the emphasis is on different land surface parameters and methodology. This chapter compares peak height phenometrics of the VNIR NDVI and the passive microwave VOD of croplands. Chapter Five focuses on tropical east African croplands, using both passive microwave datasets and modeled evapotranspiration data to characterize tropical cropland dynamics. This chapter links LSP and LSS to crop production and yield statistics in the study region. It also presented the effect of ENSO and IOD on the LSP and LSS of the region croplands. Finally, Chapter Six presents the main research summaries and recommendations.

## 1.6 References

- Asseng, S., Foster, I., & Turner, N. C. (2011). The impact of temperature variability on wheat yields. *Global Change Biology*, 17(2), 997-1012. doi: <http://dx.doi.org/10.1111/j.1365-2486.2010.02262.x>
- Becker-Reshef, I., Justice, C., Sullivan, M., Vermote, E., Tucker, C., Anyamba, A., Small, J., Pak, E., Masuoka, E., Schmaltz, J., Hansen, M., Pittman, K., Birkett, C., Williams, D., Reynolds, C., & Doorn, B. (2010). Monitoring Global Croplands with Coarse Resolution Earth Observations: The Global Agriculture Monitoring (GLAM) Project. *Remote Sensing*, 2(6), 1589. doi: <http://www.mdpi.com/2072-4292/2/6/1589>

- Benedetti, R., & Rossini, P. (1993). On the Use of NDVI Profiles as a Tool for Agricultural Statistics - the Case-Study of Wheat Yield Estimate and Forecast in Emilia-Romagna. *Remote Sensing of Environment*, 45(3), 311-326. doi: [http://dx.doi.org/10.1016/0034-4257\(93\)90113-C](http://dx.doi.org/10.1016/0034-4257(93)90113-C)
- Bolton, D. K., & Friedl, M. A. (2013). Forecasting crop yield using remotely sensed vegetation indices and crop phenology metrics. *Agricultural and Forest Meteorology*, 173(0), 74-84. doi: <http://dx.doi.org/10.1016/j.agrformet.2013.01.007>
- Boschetti, M., Stroppiana, D., Brivio, P. A., & Bocchi, S. (2009). Multi-year monitoring of rice crop phenology through time series analysis of MODIS images. *International Journal of Remote Sensing*, 30(18), 4643-4662. doi: <http://dx.doi.org/10.1080/01431160802632249>
- Brown, M. E., de Beurs, K., & Vrieling, A. (2010). The response of African land surface phenology to large scale climate oscillations. *Remote Sensing of Environment*, 114(10), 2286-2296. doi: <http://dx.doi.org/10.1016/j.rse.2010.05.005>
- Brown, M. E., & de Beurs, K. M. (2008). Evaluation of multi-sensor semi-arid crop season parameters based on NDVI and rainfall. *Remote Sensing of Environment*, 112(5), 2261-2271. doi: <http://dx.doi.org/10.1016/j.rse.2007.10.008>
- DAAC-LP. (2014). MODIS Products Table doi: [https://lpdaac.usgs.gov/dataset\\_discovery/modis/modis\\_products\\_table](https://lpdaac.usgs.gov/dataset_discovery/modis/modis_products_table).
- de Beurs, K. M., & Henebry, G. M. (2004). Land surface phenology, climatic variation, and institutional change: Analyzing agricultural land cover change in Kazakhstan.

*Remote Sensing of Environment*, 89(4), 497-509. doi:

<http://dx.doi.org/10.1016/j.rse.2003.11.006>

de Beurs, K. M., & Henebry, G. M. (2008a). Northern Annular Mode Effects on the Land Surface Phenologies of Northern Eurasia. *Journal of Climate*, 21(17), 4257-4279.

doi: <http://dx.doi.org/10.1175/2008jcli2074.1>

de Beurs, K. M., & Henebry, G. M. (2008b). War, drought, and phenology: changes in the land surface phenology of Afghanistan since 1982. *Journal of Land Use Science*, 3(2-3), 95-111.

de Beurs, K. M., & Henebry, G. M. (2010). Spatio-Temporal Statistical Methods for Modelling Land Surface Phenology. In I. L. Hudson & M. R. Keatley (Eds.), *Phenological Research: Methods for Environmental and Climate Change Analysis* (2nd edition ed., [http://dx.doi.org/10.1007/978-90-481-3335-2\\_9pp](http://dx.doi.org/10.1007/978-90-481-3335-2_9pp). 177-208): Springer Netherlands.

Doraiswamy, P. C., Hatfield, J. L., Jackson, T. J., Akhmedov, B., Prueger, J., & Stern, A. (2004). Crop condition and yield simulations using Landsat and MODIS. *Remote Sensing of Environment*, 92(4), 548-559. doi:

<http://dx.doi.org/10.1016/j.rse.2004.05.017>

Du, J., Kimball, J. S., Shi, J., Jones, L. A., Wu, S., Sun, R., & Yang, H. (2014). Inter-Calibration of Satellite Passive Microwave Land Observations from AMSR-E and AMSR2 Using Overlapping FY3B-MWRI Sensor Measurements. *Remote Sensing*, 6(9), 8594-8616. doi: <http://dx.doi.org/10.3390/rs6098594>

- Fang, H., Liang, S., & Hoogenboom, G. (2011). Integration of MODIS LAI and vegetation index products with the CSM–CERES–Maize model for corn yield estimation. *International Journal of Remote Sensing*, 32(4), 1039-1065. doi: <http://dx.doi.org/10.1080/01431160903505310>
- FEWS-NET. (2014). USGS FEWS NET Data Portal. Retrieved February 15, 2014, from <http://earlywarning.usgs.gov/fews>
- Funk, C., & Budde, M. E. (2009). Phenologically-tuned MODIS NDVI-based production anomaly estimates for Zimbabwe. *Remote Sensing of Environment*, 113(1), 115-125. doi: <http://dx.doi.org/10.1016/j.rse.2008.08.015>
- Golosov, V., & Belyaev, V. (2007). *The Volga River Basin report*. Lomonosov Moscow State University, Faculty of Geography Retrieved from [http://www.irtces.org/isi/isi\\_document/2010/ISI\\_Case\\_Study\\_Volga.pdf](http://www.irtces.org/isi/isi_document/2010/ISI_Case_Study_Volga.pdf)
- Goodin, D. G., & Henebry, G. M. (1997). A technique for monitoring ecological disturbance in tallgrass prairie using seasonal NDVI trajectories and a discriminant function mixture model. *Remote Sensing of Environment*, 61(2), 270-278. doi: [http://dx.doi.org/10.1016/S0034-4257\(97\)00043-6](http://dx.doi.org/10.1016/S0034-4257(97)00043-6)
- Gordon, R., & Bootsma, A. (1993). Analyses of growing degree-days for agriculture in Atlantic Canada. *Climate Research*, 3, 169-176.
- Gumma, M. K., Nelson, A., Thenkabail, P. S., & Singh, A. N. (2011). Mapping rice areas of South Asia using MODIS multitemporal data. *Journal of Applied Remote Sensing*, 5(1), 053547-053547-053526. doi: <http://dx.doi.org/10.1117/1.3619838>

- Henebry, G., & de Beurs, K. (2013). Remote Sensing of Land Surface Phenology: A Prospectus. In M. D. Schwartz (Ed.), *Phenology: An Integrative Environmental Science* ([http://dx.doi.org/10.1007/978-94-007-6925-0\\_21](http://dx.doi.org/10.1007/978-94-007-6925-0_21)pp. 385-411): Springer Netherlands.
- Henebry, G. M., de Beurs, K. M., Wright, C. K., Ranjeet, J., & Lioubimtseva, E. (2013). Dryland East Asia in Hemispheric Context. In J. Chen, et al. (Eds.), *Dryland East Asia: Land Dynamics amid Social and Climate Change* (<http://dx.doi.org/10.1515/9783110287912.23>pp. 23-43). Berlin/Boston: Higher Education Press and Walter de Gruyter GmbH.
- Huete, A., Didan, K., Miura, T., Rodriguez, E. P., Gao, X., & Ferreira, L. G. (2002). Overview of the radiometric and biophysical performance of the MODIS vegetation indices. *Remote Sensing of Environment*, 83(1-2), 195-213. doi: [http://dx.doi.org/10.1016/S0034-4257\(02\)00096-2](http://dx.doi.org/10.1016/S0034-4257(02)00096-2)
- Jones, L. A., Ferguson, C. R., Kimball, J. S., Zhang, K., Chan, S. T. K., McDonald, K. C., Njoku, E. G., & Wood, E. F. (2010). Satellite Microwave Remote Sensing of Daily Land Surface Air Temperature Minima and Maxima From AMSR-E. *IEEE Journal of Selected Topics in Applied Earth Observations and Remote Sensing*, 3(1), 111-123. doi: <http://dx.doi.org/10.1109/Jstars.2010.2041530>
- Jones, L. A., & Kimball, J. S. (2011). Daily Global Land Surface Parameters Derived from AMSR-E. Boulder Colorado USA: National Snow and Ice Data Center. *Digital media* (<http://nsidc.org/data/nsidc-0451.html>).

- Jones, M. O., Kimball, J. S., Jones, L. A., & McDonald, K. C. (2012). Satellite passive microwave detection of North America start of season. *Remote Sensing of Environment*, 123, 324-333. doi: <http://dx.doi.org/10.1016/j.rse.2012.03.025>
- Lindeman, M. (2014). Ukraine: Crop Production Forecasts for 2014/15. Retrieved 10-29-2015, from <http://www.fas.usda.gov/data/ukraine-crop-production-forecasts-201415>
- Lioubimtseva, E., & Henebry, G. M. (2012). Grain production trends in Russia, Ukraine and Kazakhstan: New opportunities in an increasingly unstable world? *Frontiers of Earth Science*, 6(2), 157-166. doi: <http://dx.doi.org/10.1007/s11707-012-0318-y>
- Liu, Y. Y., van Dijk, A. I. J. M., McCabe, M. F., Evans, J. P., & de Jeu, R. A. M. (2011). Global long-term passive microwave satellite-based retrievals of vegetation optical depth. *Geophysical Research Letters*, 38(18), L18402. doi: <http://dx.doi.org/10.1029/2011GL048684>
- Los, S. O., Collatz, G. J., Bounoua, L., Sellers, P. J., & Tucker, C. J. (2001). Global interannual variations in sea surface temperature and land surface vegetation, air temperature, and precipitation. *Journal of Climate*, 14(7), 1535-1549. doi: [http://dx.doi.org/10.1175/1520-0442\(2001\)014<1535:Giviss>2.0.Co;2](http://dx.doi.org/10.1175/1520-0442(2001)014<1535:Giviss>2.0.Co;2)
- Lyon, B., & DeWitt, D. G. (2012). A recent and abrupt decline in the East African long rains. *Geophysical Research Letters*, 39(2), L02702. doi: 10.1029/2011GL050337
- Maselli, F., Conese, C., Petkov, L., & Gilabert, M. A. (1992). Use of NOAA-AVHRR NDVI Data for Environmental Monitoring and Crop Forecasting in the Sahel -

- Preliminary-Results. *International Journal of Remote Sensing*, 13(14), 2743-2749. doi: <http://dx.doi.org/10.1080/01431169208904076>
- McMaster, G. S., & Wilhelm, W. W. (1997). Growing degree-days: one equation, two interpretations. *Agricultural and Forest Meteorology*, 87(4), 291-300. doi: [http://dx.doi.org/10.1016/S0168-1923\(97\)00027-0](http://dx.doi.org/10.1016/S0168-1923(97)00027-0)
- Mkhabela, M. S., Bullock, P., Raj, S., Wang, S., & Yang, Y. (2011). Crop yield forecasting on the Canadian Prairies using MODIS NDVI data. *Agricultural and Forest Meteorology*, 151(3), 385-393. doi: <http://dx.doi.org/10.1016/j.agrformet.2010.11.012>
- Moriondo, M., Maselli, F., & Bindi, M. (2007). A simple model of regional wheat yield based on NDVI data. *European Journal of Agronomy*, 26(3), 266-274. doi: <http://dx.doi.org/10.1016/j.eja.2006.10.007>
- Morisette, J. T., Richardson, A. D., Knapp, A. K., Fisher, J. I., Graham, E. A., Abatzoglou, J., Wilson, B. E., Breshears, D. D., Henebry, G. M., Hanes, J. M., & Liang, L. (2009). Tracking the rhythm of the seasons in the face of global change: phenological research in the 21st century. *Frontiers in Ecology and the Environment*, 7(5), 253-260. doi: <http://dx.doi.org/10.1890/070217>
- Pitt, M. D., & Heady, H. F. (1978). Responses of Annual Vegetation to Temperature and Rainfall Patterns in Northern California. *Ecology*, 59(2), 336. doi: <http://dx.doi.org/10.2307/1936378>
- Qian, B., De Jong, R., Warren, R., Chipanshi, A., & Hill, H. (2009). Statistical spring wheat yield forecasting for the Canadian prairie provinces. *Agricultural and*



*Forest Meteorology*, 149(6–7), 1022-1031. doi:

<http://dx.doi.org/10.1016/j.agrformet.2008.12.006>

Rasmussen, M. S. (1992). Assessment of Millet Yields and Production in Northern Burkina-Faso Using Integrated NDVI from the AVHRR. *International Journal of Remote Sensing*, 13(18), 3431-3442. doi:

*Remote Sensing*, 13(18), 3431-3442. doi:

<http://dx.doi.org/10.1080/01431169208904132>

Raun, W. R., Solie, J. B., Johnson, G. V., Stone, M. L., Lukina, E. V., Thomason, W. E., & Schepers, J. S. (2001). In-season prediction of potential grain yield in winter

wheat using canopy reflectance. *Agronomy Journal*, 93(1), 131-138. doi:

<http://dx.doi.org/10.2134/agronj2001.931131x>

Reed, B. C., Brown, J. F., Vanderzee, D., Loveland, T. R., Merchant, J. W., & Ohlen, D. O. (1994). Measuring Phenological Variability from Satellite Imagery. *Journal of Vegetation Science*, 5(5), 703-714. doi: Doi 10.2307/3235884

*Journal of Vegetation Science*, 5(5), 703-714. doi: Doi 10.2307/3235884

Rientjes, T., Haile, A. T., & Fenta, A. A. (2013). Diurnal rainfall variability over the

Upper Blue Nile Basin: A remote sensing based approach. *International Journal of Applied Earth Observation and Geoinformation*, 21, 311-325. doi:

<http://dx.doi.org/10.1016/j.jag.2012.07.009>

Ritchie, J. T., & NeSmith, D. S. (1991). Temperature and crop development. In R. J.

Hanks & J. T. Ritchie (Eds.), *Modeling Plant and Soil Systems* (Vol. Agronomy

Monograph 31, pp. 5-29): American Society of Agronomy, Crop Science Society

of America, Soil Science Society of America.

- Rojas, O., Vrieling, A., & Rembold, F. (2011). Assessing drought probability for agricultural areas in Africa with coarse resolution remote sensing imagery. *Remote Sensing of Environment*, 115(2), 343-352. doi: <http://dx.doi.org/10.1016/j.rse.2010.09.006>
- Sarma, A., Kumar, T. V. L., & Koteswararao, K. (2008). Development of an agroclimatic model for the estimation of rice yield. *Journal of Indian Geophysical Union*, 12(2), 89-96. doi: <http://igu.in/12-2/4sarma.pdf>
- Senay, B. G., Budde, M., Verdin, P. J., & Melesse, M. A. (2007). A Coupled Remote Sensing and Simplified Surface Energy Balance Approach to Estimate Actual Evapotranspiration from Irrigated Fields. *Sensors*, 7(6). doi: 10.3390/s7060979
- Senay, G. B., Bohms, S., Singh, R. K., Gowda, P. H., Velpuri, N. M., Alemu, H., & Verdin, J. P. (2013). Operational Evapotranspiration Mapping Using Remote Sensing and Weather Datasets: A New Parameterization for the SSEB Approach. *JAWRA Journal of the American Water Resources Association*, 49(3), 577-591. doi: 10.1111/jawr.12057
- Sobolev, D. (2015). Grain and Feed Update: Ukraine (doi: [http://gain.fas.usda.gov/Recent%20GAIN%20Publications/Grain%20and%20Feed%20Update\\_Kiev\\_Ukraine\\_10-5-2015.pdf](http://gain.fas.usda.gov/Recent%20GAIN%20Publications/Grain%20and%20Feed%20Update_Kiev_Ukraine_10-5-2015.pdf) pp. 15). USA: USDA Foreign Agricultural Service.
- Teal, R. K., Tubana, B., Girma, K., Freeman, K. W., Arnall, D. B., Walsh, O., & Raun, W. R. (2006). In-season prediction of corn grain yield potential using normalized

difference vegetation index. *Agronomy Journal*, 98(6), 1488-1494. doi:

<http://dx.doi.org/10.2134/agronj2006.0103>

Thenkabail, P., GangadharaRao, P., Biggs, T., Krishna, M., & Turrall, H. (2007). Spectral matching techniques to determine historical land-use/land-cover (LULC) and irrigated areas using time-series 0.1-degree AVHRR Pathfinder datasets.

*Photogrammetric Engineering and Remote Sensing*, 73(10), 1029-1040. doi:

[http://info.asprs.org/publications/pers/2007journal/september/2007\\_sep\\_1029-1040.pdf](http://info.asprs.org/publications/pers/2007journal/september/2007_sep_1029-1040.pdf)

Thenkabail, P., Lyon, J. G., Turrall, H., & Biradar, C. (2009). *Remote sensing of global croplands for food security*. USA: CRC Press.

Tony, F., Derek, B., & Greg, E. (2014). *Crop yields and global food security: Will yield increase continue to feed the world?* (doi:

[http://aciarc.gov.au/files/mn158\\_web\\_5\\_0.pdf](http://aciarc.gov.au/files/mn158_web_5_0.pdf)). Canberra, Australia: Australian Centre for International Agricultural Research (ACIAR)

Tucker, C. J. (1979). Red and photographic infrared linear combinations for monitoring vegetation. *Remote Sensing of Environment*, 8(2), 127-150. doi:

[http://dx.doi.org/10.1016/0034-4257\(79\)90013-0](http://dx.doi.org/10.1016/0034-4257(79)90013-0)

USDA-ERS. (2013). Wheat. Retrieved March 16, 2013, from

<http://www.ers.usda.gov/topics/crops/wheat.aspx>

USDA-FAS. (2011a). Kazakhstan - Crop Production Maps. Retrieved 15 February, 2014,

from [http://www.pecad.fas.usda.gov/rssiws/al/kz\\_cropprod.htm](http://www.pecad.fas.usda.gov/rssiws/al/kz_cropprod.htm)

- USDA-FAS. (2011b). Russia - Crop Production Maps. Retrieved 15 February, 2014, from [http://www.pecad.fas.usda.gov/rssiws/al/rs\\_cropprod.htm](http://www.pecad.fas.usda.gov/rssiws/al/rs_cropprod.htm)
- USDA-FAS. (2011c). Ukraine - Crop Production Maps. Retrieved 15 February, 2014, from [http://www.pecad.fas.usda.gov/rssiws/al/up\\_cropprod.htm](http://www.pecad.fas.usda.gov/rssiws/al/up_cropprod.htm)
- USDA-FAS. (2015). *U.S. Department of Agriculture Foreign Agricultural Service Strategic Plan FY 2015-2018*.
- Viña, A., Gitelson, A. A., Rundquist, D. C., Keydan, G., Leavitt, B., & Schepers, J. (2004). Monitoring Maize (*Zea mays* L.) Phenology with Remote Sensing. *Agronomy Journal*, [http://dx.doi.org/10.2134/agronj2004.1139\(4\)](http://dx.doi.org/10.2134/agronj2004.1139(4)), 1139-1147. doi: <http://dx.doi.org/10.2134/agronj2004.1139>
- Wagner, W., Blöschl, G., Pampaloni, P., Calvet, J.-C., Bizzarri, B., Wigneron, J.-P., & Kerr, Y. (2007). Operational readiness of microwave remote sensing of soil moisture for hydrologic applications. *Hydrology Research*, 38(1), 1. doi: <http://hr.iwaponline.com/content/38/1/1.abstract>
- Wang, X., Piao, S., Ciais, P., Li, J., Friedlingstein, P., Koven, C., & Chen, A. (2011, Jan 25). *Spring temperature change and its implication in the change of vegetation growth in North America from 1982 to 2006*. Paper presented at the Proceedings of the National Academy of Sciences U S A.
- Whitney, M. (2014). World Wheat Production Forecast Raised on EU to Ukraine Retrieved 10-2-2015, 2015, from <http://www.bloomberg.com/news/articles/2014-09-25/world-wheat-production-forecast-raised-on-eu-to-ukraine>

- Xiao, X. M., Boles, S., Frohling, S., Li, C. S., Babu, J. Y., Salas, W., & Moore, B. (2006). Mapping paddy rice agriculture in South and Southeast Asia using multi-temporal MODIS images. *Remote Sensing of Environment*, *100*(1), 95-113. doi: <http://dx.doi.org/10.1016/j.rse.2005.10.004>
- Xiao, X. M., Boles, S., Liu, J. Y., Zhuang, D. F., Frohling, S., Li, C. S., Salas, W., & Moore, B. (2005). Mapping paddy rice agriculture in southern China using multi-temporal MODIS images. *Remote Sensing of Environment*, *95*(4), 480-492. doi: <http://dx.doi.org/10.1016/j.rse.2004.12.009>
- Yang, W., Yang, L., & Merchant, J. W. (1997). An assessment of AVHRR/NDVI-ecoclimatological relations in Nebraska, U.S.A. *International Journal of Remote Sensing*, *18*(10), 2161-2180. doi: <http://dx.doi.org/10.1080/014311697217819>
- Zhang, X. Y., Friedl, M. A., Schaaf, C. B., & Strahler, A. H. (2004). Climate controls on vegetation phenological patterns in northern mid- and high latitudes inferred from MODIS data. *Global Change Biology*, *10*(7), 1133-1145. doi: <http://dx.doi.org/10.1111/j.1529-8817.2003.00784.x>

## CHAPTER 2 : Land Surface Phenologies and Seasonalities Using Cool Earthlight in Mid-Latitude Croplands

### Paper #1

Alemu, W. G., & Henebry, G. M. (2013). Land surface phenologies and seasonalities using cool earthlight in mid-latitude croplands. *Environmental Research Letters*, 8(4). doi: <http://dx.doi.org/10.1088/1748-9326/8/4/045002>

Journal Impact Factor: 4.134

**Research Question:** Can we use convex quadratic (CxQ) models of land surface phenology, which have been successfully used with VNIR and TIR data on herbaceous vegetation in the temperate and boreal regions, with AMSR-E passive microwave data products—air temperature and VOD—to study land surface phenology & seasonality in temperate croplands?

**Research Answer:** Yes, in part.

- Microwave retrieved air temperature GDDs and core growing season VODs were well fitted using the CxQ models that have been successfully applied to optical data in many biomes.
- However, the shape of the entire growing season VOD is not well represented by a quadratic function.

## 2.0 Abstract

Phenology deals with timing of biotic phenomena and seasonality concerns temporal patterns of abiotic variables. Studies of land surface phenology (LSP) and land surface seasonality (LSS) have long been limited to visible to near infrared (VNIR) wavelengths, despite degradation by atmospheric effects and solar illumination constraints. Enhanced land surface parameters derived from passive microwave data enable improved temporal monitoring of agricultural land surface dynamics compared to the vegetation index data available from VNIR data. LSPs and LSSs in grain growing regions of the Volga River Basin of Russia and the spring wheat belts of the USA and Canada were characterized using AMSR-E enhanced land surface parameters for the period from April through October for 2003 through 2010. Growing degree-days (GDDs) were calculated from AMSR-E air temperature retrievals using both ascending and descending passes with a base of 0° C and then accumulated (AGDD) with an annual restart each March 30. Tracking the AMSR-E parameters as a function of AGDD revealed the expected seasonal pattern of thermal limitation in mid-latitude croplands. Vegetation optical depth (VOD), a microwave analog of a vegetation index, was modeled as a function of AGDD with the resulting fitted convex quadratic models yielding both high coefficients of determination ( $r^2 > 0.90$ ) and phenometrics that could characterize cropland differences between the Russian and North American sites. The AMSR-E data were also able to capture the effects of the 2010 heat wave that devastated grain production in European Russia. These results showed the potential of AMSR-E in monitoring and modeling cropland dynamics.

## 2.1 Introduction

Phenology and seasonality are complementary aspects of ecosystem functioning: phenology deals with timing of biotic phenomena; whereas, seasonality concerns

temporal patterns of abiotic variables. Land surface phenology (LSP) describes the timing of vegetated land surface dynamics as observed by remote sensing at spatial resolutions and extents relevant to meteorological processes in the atmospheric boundary layer (de Beurs & Henebry, 2004, 2010). In a similar manner, we use the term land surface seasonality (LSS) to describe the timing of abiotic phenomena occurring across the land surface as observed by remote sensing. Examples of LSS include albedo, temperature, soil moisture, soil freeze/thaw, ponding and flooding, snow cover, and other recurrent and variable aspects of land surface dynamics.

Studies of LSP have long been limited to the visible to near infrared (VNIR) regions, despite degradation by atmospheric effects and solar illumination constraints (Jones et al., 2012). For example, the Normalized Difference Vegetation Index (NDVI; Tucker, 1979) is the most commonly used satellite-based vegetation index for studying LSP. It is limited to monitoring the top of the vegetation canopy and the signal is prone to degradation due both to atmospheric effects and to loss of sensitivity over vegetation with high leaf area index (Gitelson, 2004; Liu et al., 2011, 2013).

Phenological studies exploiting time series from flux tower have shown the power of the approach, particularly in forested ecosystems (Garrity et al., 2011; Noormets, 2009; Richardson et al., 2010). Progress has been made recently in linking flux tower data to land surface phenology (Gonsamo et al., 2012; Kovalsky et al., 2012). Both evergreen and deciduous forested ecosystems show consistency in inter-annual and spatial patterns of sensitivity in annual net ecosystem productivity (NEP) as a function of



the carbon uptake period (CUP) characterized by flux tower data (Wu et al., 2012). However, the CUP was not a good indicator of NEP in non-forested ecosystems, *e.g.*, croplands, grasslands, wetlands (Wu et al., 2012).

Remote sensing of emitted microwaves, or cool earthlight, provides alternative means for global studies of land surface phenology and seasonality (Jones et al., 2011; Jones et al., 2012). Microwave radiometers can sense emissions of earthlight at night and through clouds, which leads to increased temporal resolution relative to VNIR imagery, which must be composited to minimize cloud contamination. They can sense both leaf and woody components of aboveground vegetation. Vegetation optical depth (VOD) is a measure of aboveground vegetation canopy thickness using passive microwave remote sensing (Owe et al., 2001). VOD is less prone to saturation in dense canopies than the NDVI (Liu et al., 2013). The main disadvantage of passive microwave radiometry is its coarse spatial resolution (25 km in this study) due to low energy emissions (Jones et al., 2012; Liu et al., 2011, 2013).

The question we explore here is whether it is possible to apply an LSP model used widely with VNIR data to the Advanced Microwave Scanning Radiometer on Earth Observing System (AMSR-E) products. Geophysical data products derived from passive microwave time series were used to study LSP and LSS in three high-latitude cropland areas: the Volga River Basin in the southeast European Russia, and the spring wheat belts in North Dakota, USA, and in the Prairie Provinces of Canada. We demonstrate that the convex quadratic LSP model well describes the seasonality of air temperature at each site

and that the VOD is also well described by the convex quadratic model form. However, the models fit in North America differ substantially from those in Russia.

## **2.2 Methodology**

### **2.2.1 Remote Sensing Data**

The Advanced Microwave Scanning Radiometer (AMSR-E) was launched onboard the NASA-EOS Aqua satellite in May 2002. Data from AMSR-E were acquired at both daytime (~1330) and nighttime (~0130) overpasses from mid-June 2002 until its failure in early October 2011. The Numerical Terradynamic Simulation Group (NTSG) at the University of Montana has produced an enhanced land surface parameter suite from AMSR-E data for 2003 through 2010. The data product includes twice-daily air temperatures ( $ta$ ; ~2 m height), fractional coverage of open water over land ( $fw$ ), vegetation canopy transmittance ( $tc$ ) at three microwave frequencies, surface soil moisture ( $mv$ ;  $\leq 2$  cm soil depth), and integrated water vapor content of the intervening atmosphere ( $v$ ) for the total column (Jones & Kimball, 2011).

Soil moisture measurement was the primary land surface objective of AMSR-E. Accurate soil moisture retrieval is constrained by vegetation opacity as it reduces the observed microwave sensitivity to soil moisture. The transparency (or transmissivity) of the canopy is inversely related to canopy thickness or Vegetation Optical Depth (VOD; Owe et al., 2001). The VOD parameter is a frequency dependent measure of canopy attenuation of microwave emissions due to vegetation biomass structure and water content (Jones et al., 2012). Lower VOD (higher transmissivity) indicates lower

attenuation of soil-emitted microwave radiation by overlying vegetation canopy and vice versa. VOD equal to 0 corresponds to a transmissivity of 1 indicating bare soil, and for dense vegetation the transmissivity gets close to 0 (Liu et al., 2011; Owe et al., 2001). A long-term (1988-2008) global vegetation biomass change study on major world biomes found correspondence between VOD and production of major crops (Liu et al., 2013).

We evaluated eight years (2003-2010) of the air temperature ( $t_a$ ) and canopy transmittance data in three microwave frequencies: 6.925 GHz (tc06), 10.65 GHz (tc10), and 18.7 GHz (tc18). Over North America, there were many gaps in the VOD retrievals at 6.925 GHz, likely due to radio frequency interference (RFI; Li et al., 2004; Njoku et al., 2005). We omitted these data from further analysis and restricted our focus to the two higher frequency VOD retrievals at 10.65 GHz and 18.7 GHz.

### **2.2.2 Study Areas**

To select AMSR-E pixels for analysis, we used the International Geosphere Biosphere Programme (IGBP) global land cover classification scheme in the MODIS land cover product at spatial resolution of  $0.05^\circ$  (MCD12C1). At this coarser resolution each land cover class is available as a percentage cover. In Russia, we selected three AMSR-E pixels near Saratov and one near Volgograd, along the Volga River. For the USA, four pixels were selected in the major spring wheat producing state of North Dakota. In the USA, we also use finer resolution USDA NASS county-level crop maps ([http://www.nass.usda.gov/Charts\\_and\\_Maps/Crops\\_County/index.asp](http://www.nass.usda.gov/Charts_and_Maps/Crops_County/index.asp)) to identify spring wheat areas. Five AMSR-E pixels from Canada were selected in the Prairie Provinces of Manitoba, Saskatchewan, and Alberta (Figure 2-1).

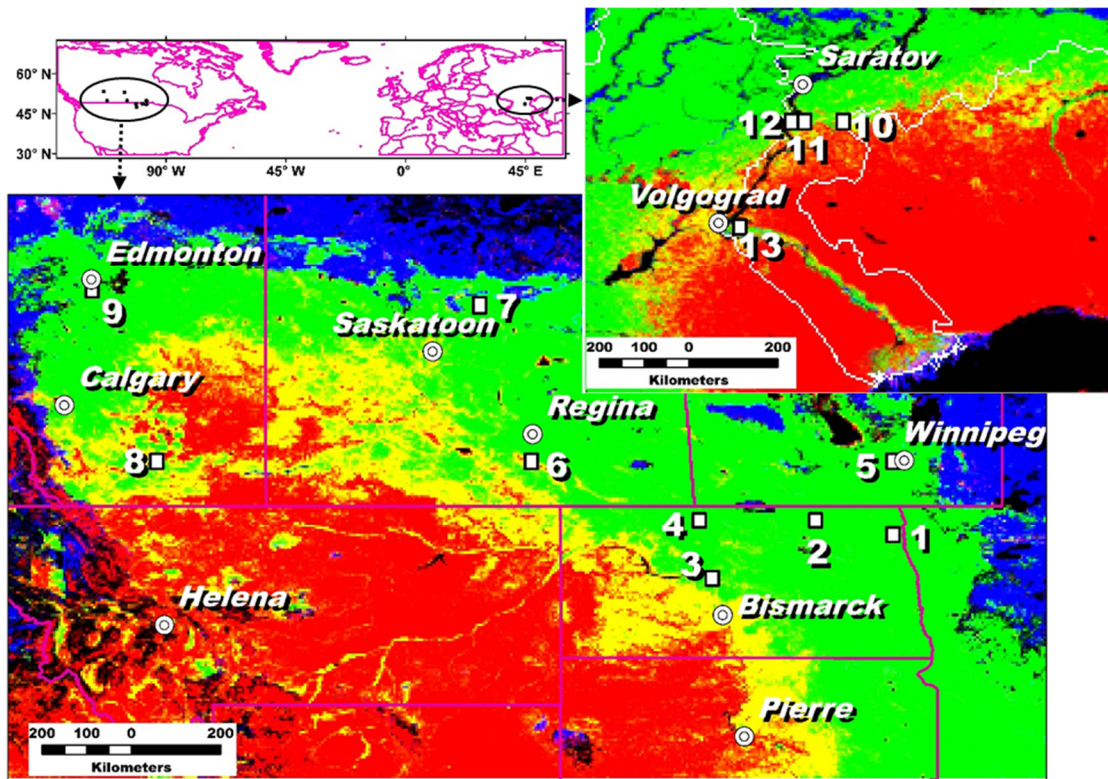


**Figure 2-1.** Study area location map (upper left) and land cover map (USA and Canada – bottom, Russia – upper right) superimposed with AMSR-E pixels of the specific study sites: 1=Grafton, 2=Munich, 3=Turtle Lake, 4=Maxbass, 5=Winnipeg, 6=Prince Albert, 7=Regina, 8=Lethbridge, 9=Edmonton, 10=Saratov 1, 11=Saratov 2, 12=Saratov 3, and 13=Volgograd. Land cover data is from MODIS product MCD12C1 at 0.05° spatial resolution with the maximum of the dominant IGBP land cover class during 2003-2010. Red indicates grasslands; green is croplands, and blue is mixed forest. Yellow indicates a mixture of grasslands and croplands; cyan is a mixture of croplands and mixed forest; and magenta is a mixture of grasslands and mixed forest.

### 2.2.3 Data Processing

The AMSR-E parameters were analyzed from 30 March to 1 November (29 March to 31 October for leap years) to avoid the frozen season. We applied a 10-day retrospective moving average filter to each parameter time series to minimize data gaps due to orbit and swath width. Meteorological station temperature and rainfall data from

NOAA National Climatic Data Center was used for comparative assessment.

Additionally, NDVI derived from MODIS MYD09A1 was obtained from the Oak Ridge National Laboratory Distributed Active Archive Center ([http://daac.ornl.gov/cgi-bin/MODIS/GR\\_col5\\_1/mod\\_viz.html](http://daac.ornl.gov/cgi-bin/MODIS/GR_col5_1/mod_viz.html)) for one AMSR-E pixel in one of the Russian croplands for comparison with the microwave data.

The thermal regime of growing season can be characterized in terms of accumulated growing degree-days (AGDD; de Beurs & Henebry, 2004, 2010; de Beurs et al., 2009). Growing degree-days were calculated from AMSR-E air temperature data ( $ta$ ) using a base temperature of 273.15 K (0 °C) as follows:

$$GDD = \max\left[\frac{ta_{\text{day}} + ta_{\text{night}}}{2} - 273.15, 0\right] \quad [1]$$

where  $ta_{\text{day}}$  and  $ta_{\text{night}}$  are the air temperatures retrieved during the ascending pass (day) and descending pass (night). The AGDD were derived from simple summation of the GDD:

$$AGDD_t = AGDD_{t-1} + GDD_t \quad [2]$$

where  $GDD_t$  is the daily increment of growing degree-days at day  $t$ , and  $AGDD_{t-1}$  is the growing degree-days accumulated from the beginning of the study period (here April 1<sup>st</sup>) until day  $t$ .

GDD as a function of AGDD was fitted with a quadratic model:

$$GDD = \alpha + \beta AGDD_t + \gamma AGDD_t^2 \quad [3]$$

These three parameters have straightforward interpretations: (1) the intercept  $\alpha$  indicates the background GDD value at the beginning of the observation period; (2) the linear parameter  $\beta$  affects the slope; and (3) the quadratic parameter  $\gamma$  controls the curvature. When the fitted model (eq. 3) is convex in shape, i.e., the sign of the  $\beta$  is positive and the sign of the  $\gamma$  is negative, the curve first rises and then falls as thermal time advances.

LSP studies have shown that vegetation index time series, such as the NDVI of herbaceous vegetation in temperate and boreal ecosystems can be readily modeled by a quadratic function of AGDD (de Beurs & Henebry, 2004, 2010; Henebry & de Beurs, 2013). Here we test if VOD can be modeled in a similar fashion:

$$\text{VOD}_t = \alpha + \beta \text{AGDD}_t + \gamma \text{AGDD}_t^2 \quad [4]$$

The parameter coefficients of the fitted convex quadratic land surface phenology (CxQ LSP) model yield two phenometrics: (1) the peak height (PH), which is the maximum value in the fitted model or the vertex of the parabola (eq. 5); and (2) the thermal time to peak (TTP), which is the amount of accumulated growing degree-days required to reach the peak height (eq. 6):

$$\text{PH} = \alpha - (\beta^2/4\gamma) \quad [5]$$

$$\text{TTP} = -\beta/2\gamma \quad [6]$$

Note that these phenometrics are derived from the parametric model fitted to the data rather than from the data directly.

The VOD time series were modeled in two phases. Convex quadratic models can parsimoniously link GDD as a function of AGDD (Figure 2-2). Thus, in the first phase the  $TTP_{GDD}$  was used as a starting point to model VOD, but the duration of the growing period differed between study areas. In the North American sites, peak VODs nearly co-occurred with peak GDDs. Accordingly, we considered the core growing season (CGS) as the period from  $0.5 * TTP_{GDD}$  through  $1.5 * TTP_{GDD}$ , and we fitted the CxQ LSP model using the VOD and AGDD time series from this period. In the Russian sites crops attain their peak VOD very much earlier than peak GDD. Accordingly, we considered core growing season in these croplands to extend from April 1<sup>st</sup> to date of  $TTP_{GDD}$ , and we fitted the CxQ LSP model using the VOD and AGDD time series from this period. The  $PH_{VOD}$  and  $TTP_{VOD}$  for all sites were derived using equations 5 and 6, respectively (Table 2-1). Since we want to model VOD based on its own behavior, the  $TTP_{VOD}$  derived from the first phase was used to refine the fit of the VOD models. In the second phase, we considered the CGS as the period from  $0.5 * TTP_{VOD}$  through  $1.25 * TTP_{VOD}$ , and we fitted the CxQ LSP model using the VOD and AGDD time series from this period. The  $PH_{VOD}$  and  $TTP_{VOD}$  metrics reported in Table 2-2 were derived from these second phase models.

## **2.3 Results**

### **2.3.1 Growing Degree-Days**

GDD from AMSR-E and that from weather station data at two study sites compared favorably (Figure 2-2). However, there is some divergence towards the end of the season that likely arises from data gaps due to a lack of AMSR-E retrievals over frozen surfaces.

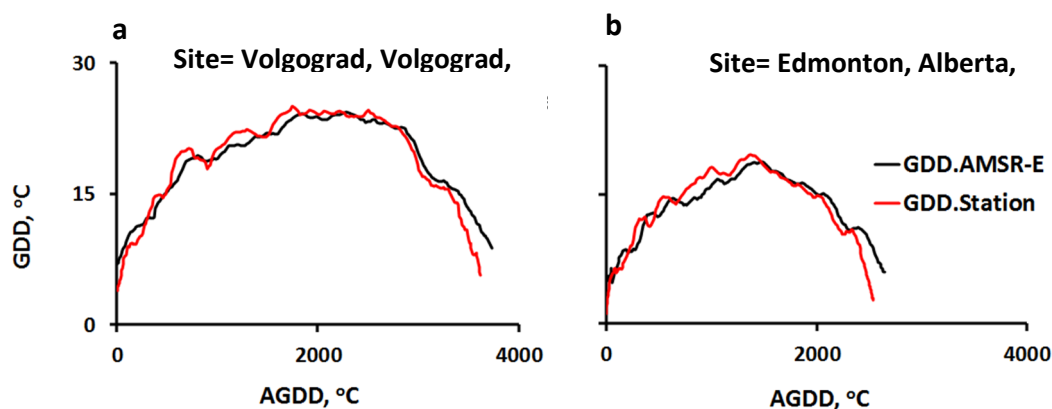


**Figure 2-2.** AMSR-E retrieved GDD averaged 2003-2010 (black solid line) as a function of AMSR-E retrieved AGDD averaged 2003-2010 superimposed with similar timespan of meteorological station data (red dash-dotted line) from two study sites. Both AMSR-E time series show a good agreement with the station data; however, the late year divergences may arise from missing AMSR-E retrievals due to frozen surface conditions.

Behavior of the GDD as a function of AGDD displayed strong seasonality with a convex quadratic shape at each study site (Figure 2-3a & 2-4). Given that mid-latitudes are temperature limited, this quasi-parabolic relationship during the frost-free period is expected, and the coefficients of determination are uniformly high ( $r^2 > 0.90$ ; Table 2-1, Figure 2-4). In the USA and Canada croplands, the modeled peak GDD occurred on 27 July (DOY 208) on average; whereas, it occurred four days earlier, on average, in the Volga River basin of Russia (DOY 204) (Table 2-1).

While there is an expected inverse relationship between the thermal time at peak GDD ( $TTP_{GDD}$ ) and latitude, the pattern is relatively weak suggesting that other factors influence the seasonal progression of thermal time (Figure 2-3b). The GDDs were higher in Russia than in the North American sites (Figures 2-3 & 2-4, Table 2-1). The northernmost study sites in Canada, Edmonton and Prince Albert, experienced much



lower GDDs. Site Saratov 1 had higher GDD compared to the other three Russia croplands (Figure 2-3a, Table 2-1); it is located relatively far from the Volga River, while the other three Russian sites are adjacent to the river. Interannual variation in GDD as a function of AGDD appeared higher during the transitional seasons of spring and fall (Figure 2-4).

**Table 2-1.** Study site name, location, average fitted peak height of growing degree-days ( $PH_{GDD}$ ), average thermal time to peak GDD ( $TTP_{GDD}$ ), day of year at peak GDD ( $DOY@PH_{GDD}$ ), and average coefficient of determination for convex quadratic (CxQ) model fits during the period 2003-2010.

Country	Site	Latitude	Longitude	$PH_{GDD}$ (°C)	$TTP_{GDD}$ (°C)	$DOY@PH_{GDD}$	$r^2$
USA	Turtle Lake	47.54	-101.00	21.5	1772	209	0.96
USA	Grafton	48.41	-97.35	21.1	1707	206	0.98
USA	Maxbass	48.71	-101.26	21.7	1847	211	0.97
USA	Munich	48.71	-98.92	20.4	1616	211	0.98
Canada	Lethbridge	49.90	-112.19	21.1	1803	207	0.92
Canada	Regina	49.90	-104.64	22.6	1836	210	0.96
Canada	Winnipeg	49.90	-97.35	20.4	1608	209	0.97
Canada	Prince Albert	53.04	-105.68	18.2	1416	207	0.98
Canada	Edmonton	53.36	-113.49	17.6	1376	206	0.97
Russia	Volgograd	48.71	44.77	24.0	1943	206	0.97
Russia	Saratov 1	50.82	46.85	26.9	2088	203	0.96
Russia	Saratov 2	50.82	46.07	23.4	1811	204	0.97
Russia	Saratov 3	50.82	45.81	22.9	1781	205	0.97

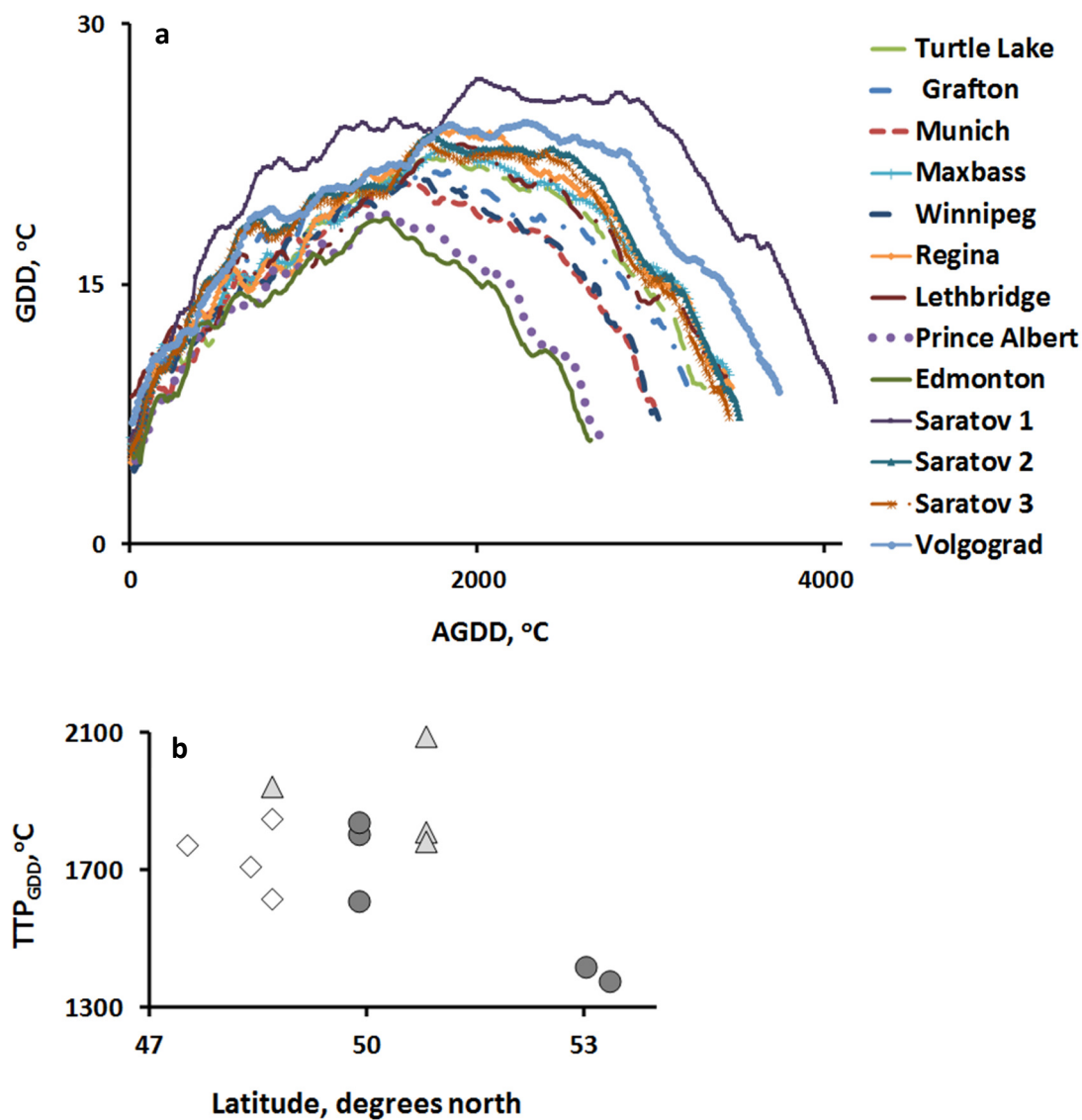


**Figure 2-3.** (a) Average AMSR-E GDD (2003-2010) as a function of average AMSR-E AGDD for all study sites. Canadian sites Edmonton and Prince Albert show lower GDD and AGDD due to their northernmost locations. The GDD in the Russian croplands was higher than that in the USA or Canada. (b) Thermal time to peak GDD calculated from parameter coefficients plotted as a function of latitude (hollow diamonds=USA, gray circles=Canada, light gray triangles=Russia). It shows a general decrease in  $TTP_{GDD}$  as latitude increases. The uppermost triangle is Saratov 1, which is located relatively far

from the Volga River and shows higher  $TTP_{GDD}$ , while the three other Russian sites are located along the river.

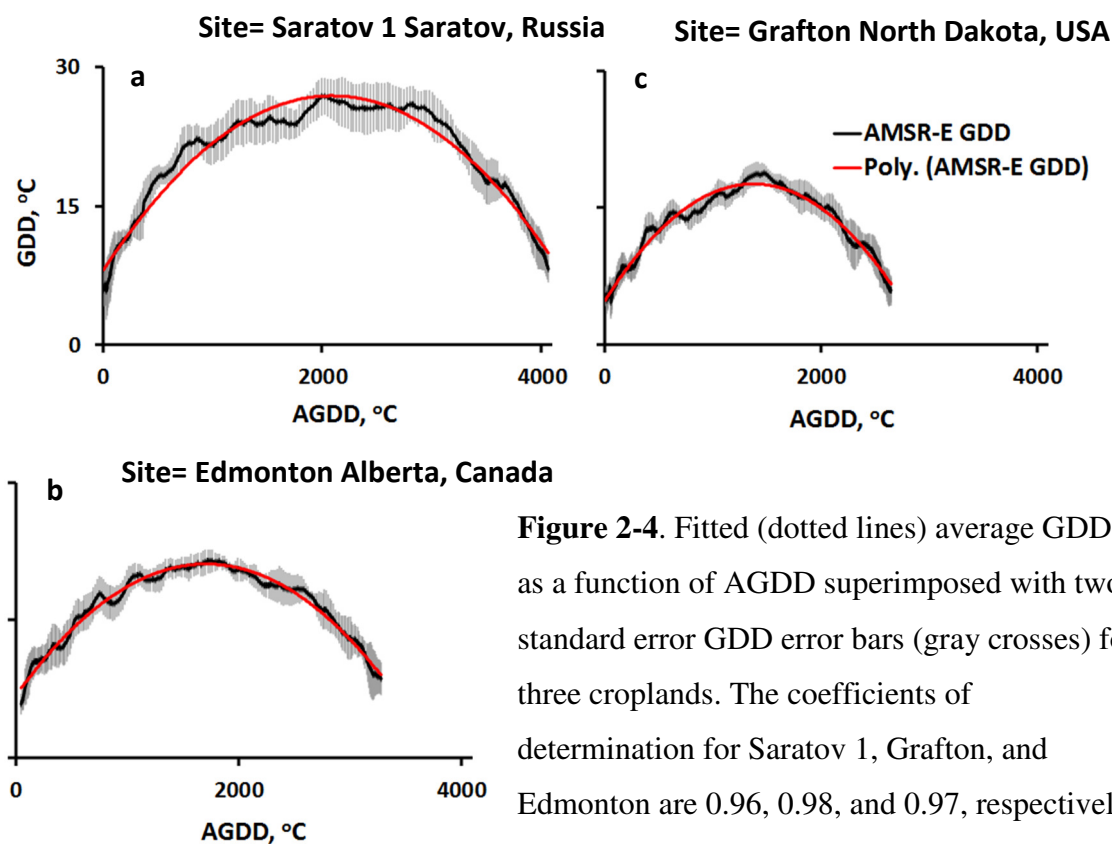


**Figure 2-4.** Fitted (dotted lines) average GDD as a function of AGDD superimposed with two standard error GDD error bars (gray crosses) for three croplands. The coefficients of determination for Saratov 1, Grafton, and Edmonton are 0.96, 0.98, and 0.97, respectively. Interannual variability in GDD tended to be

greater in the transitional seasons of spring and fall than in summer. Note the higher interannual uncertainty at the Russian site.

### 2.3.2 Vegetation Optical Depth

The behaviors of VOD as a function of AGDD exhibit distinct LSPs. During the growing season, VODs ascend to a unimodal peak value and then decline gradually. Peak VOD in the USA and Canada croplands occurred in early August for both frequencies on average. In contrast at the Russian sites the VOD peaks significantly earlier in mid-June (Figure 2-5, Table 2-2). VOD time series showed steep slopes towards their annual peak

and then descended gently. The shapes of these seasonal trajectories may reflect microwaves' sensitivity to the timing of vegetation biomass growth and associated changes in canopy water content and the later season drydown and harvest. The pace of fractional green vegetation cover development is quicker than during its disappearance.  $TTP_{VOD}$  differences between the AMSR-E two frequencies, 10.65 GHz and 18.7 GHz, was notably higher for Winnipeg (316 AGDD °C) (Table 2-2).

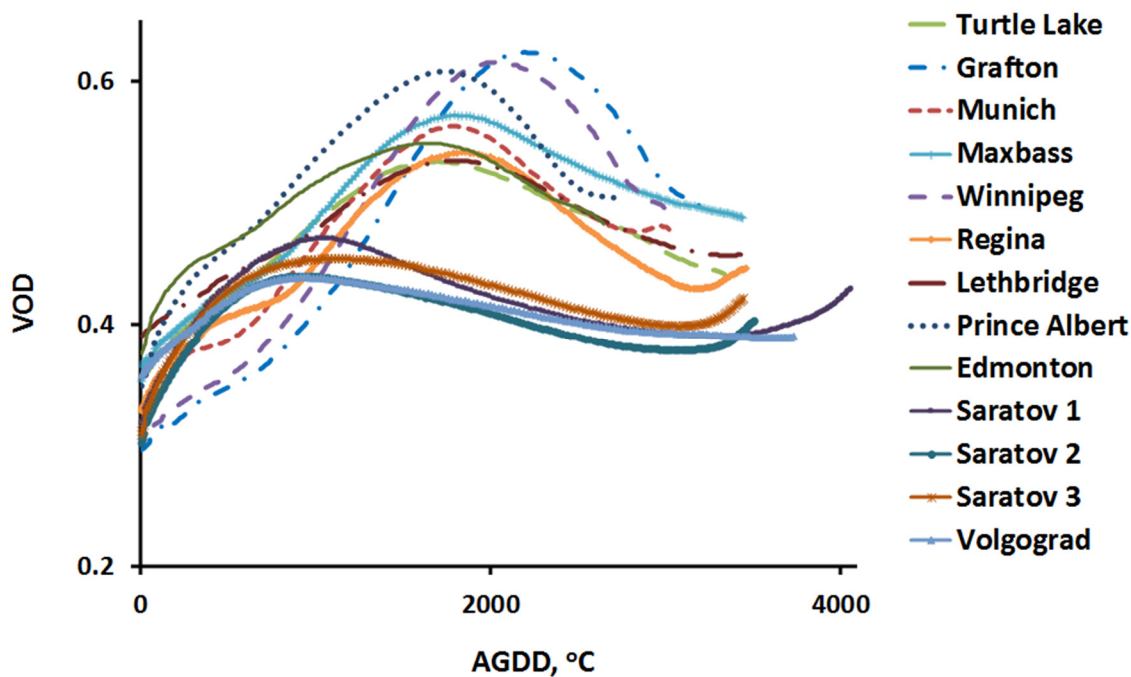


**Figure 2-5.** Interannual average (2003-2010) of vegetation optical depth (VOD) as a function of AGDD at the highest AMSR-E frequency. Croplands in Russia attained their peak VOD much earlier than that of the USA and Canada, but with a lower peak and smaller dynamic range.

**Table 2-2.** Study site name, coefficient of determination, peak height of VOD, thermal time to peak VOD, and day of year at VOD peak for AMSR-E frequencies 10.65 GHz and 18.7 GHz, respectively, and the difference in growing degree-days between  $TTP_{VOD}$  at the two frequencies.

Country	Site	$r^2$	PH	TTP	DOY	$r^2$	PH	TTP	DOY	$\Delta TTP$
		VOD10	VOD10	VOD10 (°C)	@PH VOD10	VOD18	VOD18	VOD18 (°C)	@PH VOD18	VOD18- VOD10 (°C)
USA	Turtle Lake	0.99	0.52	1679	205	0.99	0.53	1721	207	42
USA	Grafton	0.99	0.57	2219	228	0.99	0.62	2153	231	66
USA	Maxbass	0.99	0.56	1816	209	0.99	0.57	1843	209	27
USA	Munich	0.99	0.55	1741	217	0.99	0.56	1793	220	51
Canada	Lethbridge	0.98	0.50	1820	223	0.99	0.53	1808	207	-12
Canada	Regina	0.99	0.51	1853	210	0.99	0.54	1843	210	-10
Canada	Winnipeg	0.98	0.53	1735	215	0.99	0.62	2051	231	316
Canada	Prince Albert	0.97	0.60	1686	221	0.98	0.60	1710	223	24
Canada	Edmonton	0.98	0.52	1619	219	0.99	0.55	1629	220	10
Russia	Volgograd	0.97	0.41	1113	168	0.92	0.44	1004	163	-109
Russia	Saratov 1	0.98	0.44	1096	163	0.99	0.47	1067	161	-29
Russia	Saratov 2	0.97	0.42	1032	168	0.94	0.44	991	166	-40
Russia	Saratov 3	0.98	0.43	1142	174	0.98	0.45	1150	175	8

The fitted convex quadratic LSP models for every site for both frequencies showed high coefficients of determination ( $r^2 > 0.90$ , Figure 2-6, Table 2-2). The Russian sites displayed lower peak VODs that occurred earlier; whereas, the North American sites displayed higher VOD peaks that occurred at higher AGDD (Figure 2-5, 2-6, Table 2-2). At each study site the VOD peak at the higher frequency (18.7 GHz) was higher than the VOD peak at the lower frequency (10.65 GHz), with the exception of the Prince Albert site, where the peaks were equal in magnitude (Table 2-2). This pattern accords with the

fact that the shorter wavelengths are more attenuated by the vegetation canopy and, thus, register higher VOD.

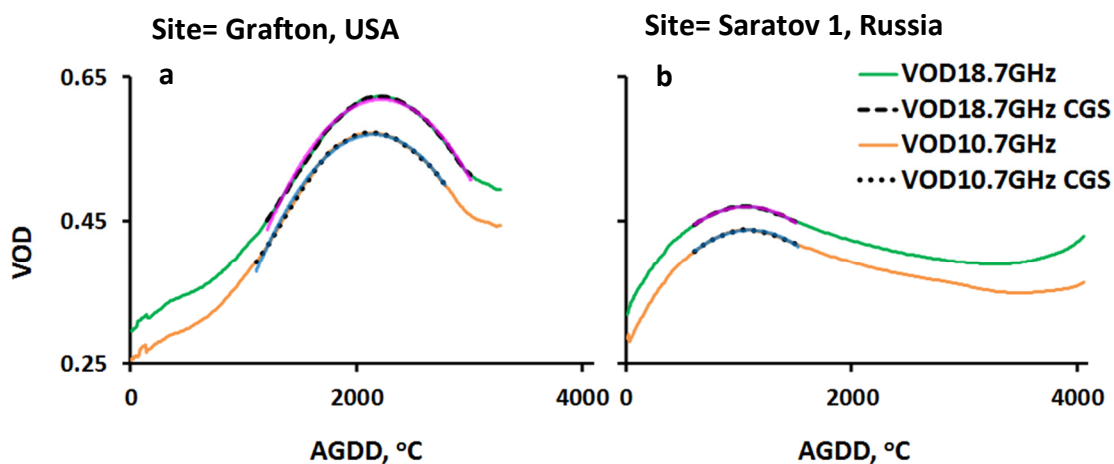


**Figure 2-6.** Convex quadratic land surface phenology models for VOD in USA (a) and Russia (b). Green is observed VOD at 18.7 GHz and orange is observed VOD at 10.65 GHz. Black dashed and dotted lines indicate the “core growing season” used to fit each LSP model. The magenta line shows the fitted CxQ model of VOD at 18.7 GHz and the blue line shows the fitted CxQ model of VOD at 10.65 GHz.

## 2.4 Discussion

### 2.4.1 VOD and Crop Type

Peak VOD in Russia occurs much earlier (mid-Jun) compared to that of the North America (early August) (Figure 2-5, Table 2-2). The North American sites were planted to spring wheat that matures in the first half of August; whereas, the Russian sites were planted to winter grains and some grasses that grow and mature soon after the end of frozen season. Major crops that covered the Volgograd site include winter wheat, while the three Saratov sites were covered by winter wheat and some spring wheat. According to USDA Foreign Agricultural Service (FAS), each of these Russian sites was within the

five major winter wheat producing oblasts that produce more than 60% of the Russian winter wheat crop (USDA-FAS, 2009). The USDA FAS also indicates that these Russian sites had minimal cover in rye (USDA-FAS, 2003). The North America croplands had longer growing season and much higher VOD peaks while the Russia croplands exhibited shorter growing season and lower peak VODs. While the difference in peak VOD timing results from phenological differences in winter versus spring grains, the magnitude of the VOD peak suggests differences in cultivation practices and grain varieties as well.

#### **2.4.2 VOD and Land Cover**

Some cropland sites show distinctive VOD trajectories. For example, the Edmonton site exhibited higher VOD much earlier in the season compared to other Canadian sites. Land cover information, gleaned from MODIS MCD12C1 IGBP 0.05° LC Type 1 percent, indicates that ~16% of the Edmonton study site falls within suburbs of Edmonton. The earlier season VOD may then result from woods, lawns, parks, and cemeteries in the suburban areas. Other sites having an urbanized component include Winnipeg and Volgograd (~12% each). A study conducted in eastern North America using MODIS NDVI found the effects of urbanized areas on land surface phenology to decay exponentially from the urban boundary to 10km into rural land covers (Zhang et al., 2004). Vegetation in urbanized areas can experience longer growing season and lower canopy density compared to those in rural areas, i.e., they have earlier green-up and later dormancy (White et al., 2002; Zhang et al., 2004).

### **2.4.3 VOD, GDD, and the 2010 Russian Heat Wave**

The effects of the 2010 Russian heat wave (Trenberth & Fasullo, 2012) were evident in the AMSR-E time series. At the three Saratov sites, the GDDs were well above the expectation based on the 2003-2009 period, especially at Saratov 1 (Figure 2-7a). The VODs were below expectation for much of the growing season as croplands were negatively impacted by the heat wave (Grumm, 2011). Curiously, the VOD trajectory at Saratov 1 was closer to expectation than the other two sites that experienced more modestly elevated temperatures (Figure 2-7b). At two Canadian sites at comparable latitude, the thermal regime was substantially lower than expectation (Figure 2-7c). The VODs were significantly depressed at one location (Regina) but not the other (Figure 2-7d), despite comparable thermal regimes (Figure 2-7c), suggesting that factors other than the temperature affected the Regina LSP. The third Canadian site at the same latitude, Winnipeg, was not included in the comparison due to the influence of (sub)urban land uses within the AMSR-E pixel.



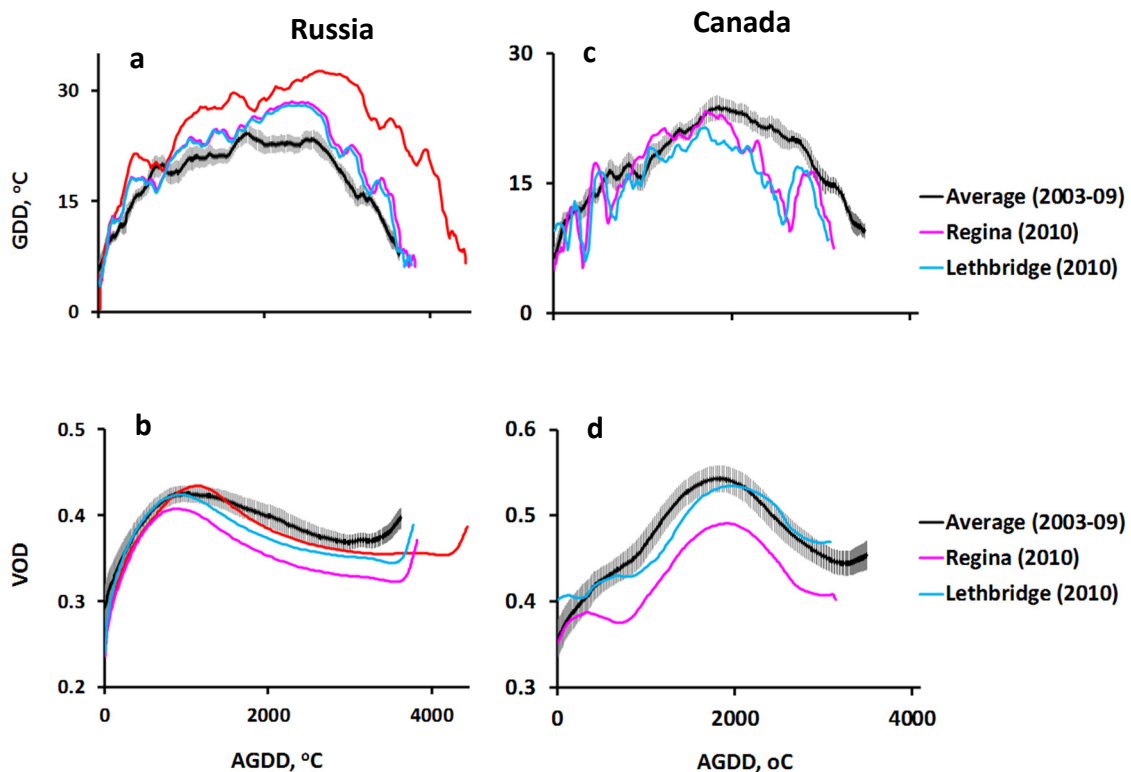


**Figure 2-7.** The deleterious effect of the 2010 Russian summer heat wave on VOD is evident in the Saratov 1, 2 and 3 time series where (a) GDD and AGDD were higher in 2010, while (b) VODs were low compared to the two standard errors of the other years. In 2010 at Regina and Lethbridge, Canada, neither (c) the thermal regimes nor (d) the VOD exhibited distinct deviations from the other years. The general patterns are representative of the other study sites (data not shown). The presented Canadian sites display temperature drop in mid-September while the Regina site had lower VOD throughout the year due to other factor than heat wave.

#### 2.4.4 VOD Compared to NDVI and Meteorological Station Temperature Data

Time series analysis of NDVI from Aqua MODIS (calculated from 8-day reflectance) and VOD from AMSR-E (8-day retrospective moving average) for the Saratov 1 site in Russia showed similar LSPs (Figure 2-8). Both indicators of the vegetated land surface displayed correspondence with temperature data from a nearby

meteorological station. The peak in the VOD time series lagged those in the NDVI. This behavior was expected since the VOD is sensitive to canopy water content; whereas, the NDVI is sensitive to photosynthetically active radiation (PAR) absorption (Viña et al., 2004c). Noise in the NDVI time series likely resulted from atmospheric effects, such as sub-pixel cloud contamination. While the NDVI displayed a higher dynamic range than the VOD, the late season secondary peak in winter grains is captured more consistently by the VOD than the NDVI (Figure 2-8). Note how the dynamics in 2010 differ from the earlier years, particularly the long decline in VOD.

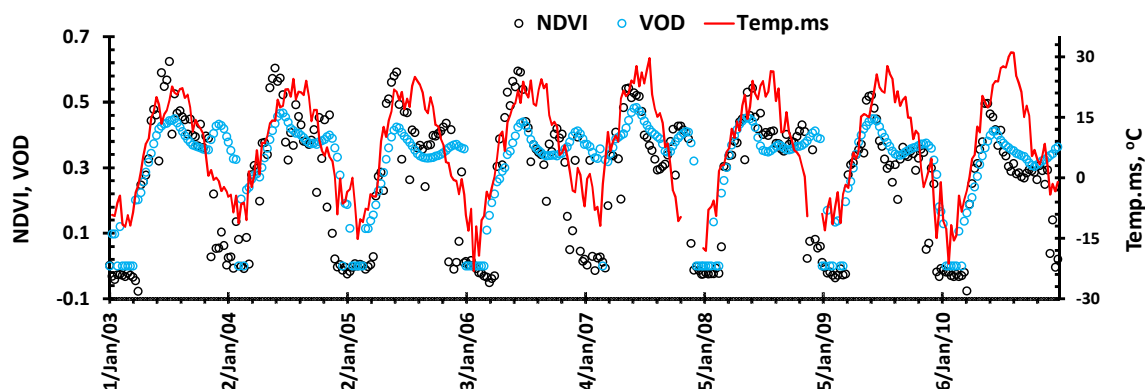


**Figure 2-8.** Time series plots of the VOD (cyan circles) & the NDVI (black circles) (2003–2010) from a single AMSR-E pixel, Saratov 1, in Russia. Temperature data (temp.ms) from a nearby meteorological station (red line) is superimposed. The station and VOD data were smoothed with an 8-day retrospective moving average. These data were aligned to the Aqua MODIS MYD09A1 reflectance compositing periods for comparison. All annual data (January 1<sup>st</sup>-December 31<sup>st</sup>) were considered. Notice that the seasonal bimodality of VOD is more pronounced than in the NDVI. The bimodality arises from the planting of winter grains in the fall, and growth and harvest in the subsequent early summer.

An important limitation of the microwave data is its relatively coarse spatial resolution necessitated by the earth's surface low microwave energy emissions, limiting its ability to detect fine spatial scale changes (Jones et al., 2012; Liu et al., 2011, 2013). At the same time, the higher temporal resolution of the microwave data offers different insights in the land surface dynamics. Particularly useful is the retrieval of air temperature (rather than skin temperature) at much fine spatial resolution than ground-based meteorological station networks over most of the planetary land surface (although these temperature retrievals are limited in temporal resolution). Although the VOD retrievals span a very large area—nominally 625 km<sup>2</sup>—the sensitivity to the water content in the vegetated land surface offers a different perspective that may be more temporally responsive to root-zone soil moisture changes than the absorption of PAR which the NDVI indicates. Additional research is needed to investigate how best to use these complementary perspectives for monitoring and modeling the dynamics of the vegetated land surface.

## **2.5 Conclusions and Recommendations**

Land surface phenologies (LSPs) of VODs and land surface seasonalities (LSSs) of GDDs based on times series of the AMSR-E enhanced land parameters followed seasonal patterns expected from thermally limited croplands. Both the microwave retrieved GDDs and VODs could be well fit using the convex quadratic land surface phenology (CxQ LSP) model that has been successfully applied in many biomes using optical data. The AMSR-E data were also able to detect the impact of the severe heat wave that devastated Russian crops in the summer of 2010. These results show the

potential for passive microwave data in general and the AMSR-E enhanced land parameters in particular to be used for modeling cropland dynamics and, possibly, for forecasting agricultural productivity in data sparse regions of the world.

Despite the loss of the AMSR-E, there is a future for information from passive microwave land surface products. The Advanced Microwave Scanning Radiometer 2 (AMSR-2) onboard the Global Change Observations Mission 1st–Water (GCOM-W1), recently renamed SHIZUKU, was successfully launched by Japan Aerospace Exploration Agency (JAXA) on May 2012 and data products were released to the public in May 2013 (<https://gcom-w1.jaxa.jp/>). AMSR-2 has similar functions with AMSR-E, but with some improvements. The NTSG plans to continue the production of the enhanced land parameters using AMSR-2 datastreams (John S. Kimball, personal communication). Extending this data record is an important step toward harnessing the power of passive microwave remote sensing for monitoring and modeling landscape dynamics beyond freeze-thaw transitions.

## **2.6 Acknowledgements**

This research was supported in part by NASA grants NNX11AB77G and NNX13AN58G. The AMSR-E data were accessed from Numerical Terradynamic Simulation Group (NTSG) website (<http://www.ntsg.umn.edu/project/amsrelp>). The MODIS MYD09A1 data were obtained from the Oak Ridge National Laboratory Distributed Active Archive Center ([http://daac.ornl.gov/cgi-bin/MODIS/GLBVIZ\\_1\\_Glb/modis\\_subset\\_order\\_global\\_col5.pl](http://daac.ornl.gov/cgi-bin/MODIS/GLBVIZ_1_Glb/modis_subset_order_global_col5.pl)). The meteorological

data were acquired from NOAA National Climatic Data Center website

(<http://gis.ncdc.noaa.gov/map/viewer/#app=cdo&cfg=cdo&theme=temp&layers=1>). We

gratefully acknowledge the thoughtful comments from two anonymous reviewers that increased the clarity of the presentation.

## 2.7 References

de Beurs, K. M., & Henebry, G. M. (2004). Land surface phenology, climatic variation, and institutional change: Analyzing agricultural land cover change in Kazakhstan.

*Remote Sensing of Environment*, 89(4), 497-509. doi:

<http://dx.doi.org/10.1016/j.rse.2003.11.006>

de Beurs, K. M., Wright, C. K., & Henebry, G. M. (2009). Dual scale trend analysis for evaluating climatic and anthropogenic effects on the vegetated land surface in

Russia and Kazakhstan. *Environmental Research Letters*, 4(4), 045012. doi:

<http://stacks.iop.org/1748-9326/4/i=4/a=045012>

de Beurs, K. M., & Henebry, G. M. (2010). Spatio-Temporal Statistical Methods for Modelling Land Surface Phenology. In I. L. Hudson & M. R. Keatley (Eds.),

*Phenological Research: Methods for Environmental and Climate Change*

*Analysis* (2nd edition ed., [http://dx.doi.org/10.1007/978-90-481-3335-2\\_9pp](http://dx.doi.org/10.1007/978-90-481-3335-2_9pp). 177-

208): Springer Netherlands.

Garrity, S. R., Bohrer, G., Maurer, K. D., Mueller, K. L., Vogel, C. S., & Curtis, P. S.

(2011). A comparison of multiple phenology data sources for estimating seasonal transitions in deciduous forest carbon exchange. *Agricultural and Forest*

*Meteorology*, 151(12), 1741-1752. doi: <http://ac.els->

cdn.com/S0168192311002437/1-s2.0-S0168192311002437-  
main.pdf?\_tid=4baa5482-a604-11e6-b5f4-

00000aacb361&acdnat=1478644986\_3327d159fc74b2e95160fe7ca5c35c23

Gitelson, A. A. (2004). Wide Dynamic Range Vegetation Index for remote quantification of biophysical characteristics of vegetation. *Journal of Plant Physiology*, *161*(2), 165-173. doi: <http://dx.doi.org/10.1078/0176-1617-01176>

Gonsamo, A., Chen, J. M., Wu, C., & Dragoni, D. (2012). Predicting deciduous forest carbon uptake phenology by upscaling FLUXNET measurements using remote sensing data. *Agricultural and Forest Meteorology*, *165*, 127-135. doi: <http://dx.doi.org/10.1016/j.agrformet.2012.06.006>

Grumm, R. H. (2011). The Central European and Russian Heat Event of July–August 2010 *Bulletin of the American Meteorological Society* (Vol. 92, pp. 1285-1296): American Meteorological Society.

Henebry, G. M., & de Beurs, K. M. (2013). Remote Sensing of Land Surface Phenology: A Prospectus. In M. D. Schwartz (Ed.), *Phenology: An Integrative Environmental Science* ([http://dx.doi.org/10.1007/978-94-007-6925-0\\_21](http://dx.doi.org/10.1007/978-94-007-6925-0_21)pp. 385-411): Springer Netherlands.

Jones, L. A., & Kimball, J. S. (2011). Daily Global Land Surface Parameters Derived from AMSR-E. Boulder Colorado USA: National Snow and Ice Data Center. *Digital media* (<http://nsidc.org/data/nsidc-0451.html>).

Jones, M. O., Jones, L. A., Kimball, J. S., & McDonald, K. C. (2011). Satellite passive microwave remote sensing for monitoring global land surface phenology. *Remote*

*Sensing of Environment*, 115(4), 1102-1114. doi:

<http://dx.doi.org/10.1016/j.rse.2010.12.015>

Jones, M. O., Kimball, J. S., Jones, L. A., & McDonald, K. C. (2012). Satellite passive microwave detection of North America start of season. *Remote Sensing of Environment*, 123, 324-333. doi: <http://dx.doi.org/10.1016/j.rse.2012.03.025>

*Environment*, 123, 324-333. doi: <http://dx.doi.org/10.1016/j.rse.2012.03.025>

Kovalskyy, V., Roy, D. P., Zhang, X. Y., & Ju, J. (2012). The suitability of multi-temporal web-enabled Landsat data NDVI for phenological monitoring – a comparison with flux tower and MODIS NDVI. *Remote Sensing Letters*, 3(4), 325-334. doi: 10.1080/01431161.2011.593581

Li, L., Njoku, E. G., Im, E., Chang, P. S., & Germain, K. S. (2004). A preliminary survey of radio-frequency interference over the US in Aqua AMSR-E data. *IEEE Transactions on Geoscience and Remote Sensing*, 42(2), 380-390. doi:

*Transactions on Geoscience and Remote Sensing*, 42(2), 380-390. doi:

<http://dx.doi.org/10.1109/TGRS.2003.817195>

Liu, Y. Y., van Dijk, A. I. J. M., McCabe, M. F., Evans, J. P., & de Jeu, R. A. M. (2011).

Global long-term passive microwave satellite-based retrievals of vegetation optical depth. *Geophysical Research Letters*, 38(18), L18402. doi:

<http://dx.doi.org/10.1029/2011GL048684>

Liu, Y. Y., van Dijk, A. I. J. M., McCabe, M. F., Evans, J. P., & de Jeu, R. A. M. (2013).

Global vegetation biomass change (1988-2008) and attribution to environmental and human drivers. *Global Ecology and Biogeography*, 22(6), 692-705. doi:

10.1111/geb.12024

- Njoku, E. G., Ashcroft, P., Chan, T. K., & Li, L. (2005). Global survey and statistics of radio-frequency interference in AMSR-E land observations. *IEEE Transactions on Geoscience and Remote Sensing*, 43(5), 938-947. doi: <http://dx.doi.org/10.1109/TGRS.2004.837507>
- Noormets, A. (2009). *Phenology of Ecosystem Processes*: Springer.
- Owe, M., de Jeu, R., & Walker, J. (2001). A methodology for surface soil moisture and vegetation optical depth retrieval using the microwave polarization difference index. *IEEE Transactions on Geoscience and Remote Sensing*, 39(8), 1643-1654. doi: <http://dx.doi.org/10.1109/36.942542>
- Richardson, A. D., Black, T. A., Ciais, P., Delbart, N., Friedl, M. A., Gobron, N., Hollinger, D. Y., Kutsch, W. L., Longdoz, B., & Luysaert, S. (2010). Influence of spring and autumn phenological transitions on forest ecosystem productivity. *Philosophical Transactions of the Royal Society of London B: Biological Sciences*, 365(1555), 3227-3246. doi: <https://www.ncbi.nlm.nih.gov/pmc/articles/PMC2981939/pdf/rstb20100102.pdf>
- Trenberth, K. E., & Fasullo, J. T. (2012). Climate extremes and climate change: The Russian heat wave and other climate extremes of 2010. *Journal of Geophysical Research, Atmospheres*, 117(D17), D17103. doi: <http://dx.doi.org/10.1029/2012jd018020>
- Tucker, C. J. (1979). Red and photographic infrared linear combinations for monitoring vegetation. *Remote Sensing of Environment*, 8(2), 127-150. doi: [http://dx.doi.org/10.1016/0034-4257\(79\)90013-0](http://dx.doi.org/10.1016/0034-4257(79)90013-0)



- USDA-FAS. (2003). Russia: Agricultural Overview. United States Department of Agriculture Foreign Agricultural Service Production Estimate and Crop Assessment Division Retrieved July 15, 2013, from [http://www.fas.usda.gov/pecad/highlights/2004/11/rs\\_18nov04/index.htm](http://www.fas.usda.gov/pecad/highlights/2004/11/rs_18nov04/index.htm)
- Viña, A., Henebry, G. M., & Gitelson, A. A. (2004). Satellite monitoring of vegetation dynamics: Sensitivity enhancement by the wide dynamic range vegetation index. *Geophysical Research Letters*, *31*(4), L04503. doi: <http://dx.doi.org/10.1029/2003GL019034>
- White, M. A., Nemani, R. R., Thornton, P. E., & Running, S. W. (2002). Satellite Evidence of Phenological Differences Between Urbanized and Rural Areas of the Eastern United States Deciduous Broadleaf Forest. *Ecosystems*, *5*(3), 260-273. doi: 10.1007/s10021-001-0070-8
- Wu, C., Gonsamo, A., Chen, J. M., Kurz, W. A., Price, D. T., Lafleur, P. M., Jassal, R. S., Dragoni, D., Bohrer, G., Gough, C. M., Verma, S. B., Suyker, A. E., & Munger, J. W. (2012). Interannual and spatial impacts of phenological transitions, growing season length, and spring and autumn temperatures on carbon sequestration: A North America flux data synthesis. *Global and Planetary Change*, *92–93*, 179-190. doi: <http://dx.doi.org/10.1016/j.gloplacha.2012.05.021>
- Zhang, X. Y., Friedl, M. A., Schaaf, C. B., & Strahler, A. H. (2004). Climate controls on vegetation phenological patterns in northern mid- and high latitudes inferred from MODIS data. *Global Change Biology*, *10*(7), 1133-1145. doi: <http://dx.doi.org/10.1111/j.1529-8817.2003.00784.x>

## **CHAPTER 3 : Characterizing Cropland Phenology in Major Grain Production Areas of Russia, Ukraine, and Kazakhstan by the Synergistic Use of Passive Microwave and Visible to Near Infrared Data**

### Paper #2

Alemu, W. G., & Henebry, G. M. (2016). Characterizing Cropland Phenology in Major Grain Production Areas of Russia, Ukraine, and Kazakhstan by the Synergistic Use of Passive Microwave and Visible to Near Infrared Data. *Remote Sensing*, 8(12). doi: <http://dx.doi.org/10.3390/rs8121016>

Journal Impact Factor: 3.036

**Research Question:** Can the synergistic use of the VNIR MODIS NDVI and the passive microwave AMSR-E-retrieved air temperature data enable characterization of cropland dynamics in the mid-latitudes?

**Research Answer:** Yes.

- AMSR-E air temperature GDD were found to fit the convex quadratic (CxQ) model better than the counterpart MODIS LST GDD.
- Synergistic use of MODIS VIs with AMSR-E air temperature GDD were able to differentiate spring and winter croplands.
- AMSR-E GDD residuals were able to manifest the evaporative cooling effect from vegetation during the vegetation peak greenness period.

### 3.0 Abstract

We demonstrate the synergistic use of surface air temperature retrieved from AMSR-E (Advanced Microwave Scanning Radiometer on Earth observing satellite) and two vegetation indices (VIs) from the shorter wavelengths of MODIS (MODerate resolution Imaging Spectroradiometer) to characterize cropland phenology in the major grain production areas of Northern Eurasia from 2003–2010. We selected 49 AMSR-E pixels across Ukraine, Russia, and Kazakhstan, based on MODIS land cover percentage data. AMSR-E air temperature growing degree-days (GDD) captures the weekly, monthly, and seasonal oscillations, and well correlated with station GDD. A convex quadratic (CxQ) model that linked thermal time measured as growing degree-days to accumulated growing degree-days (AGDD) was fitted to each pixel's time series yielding high coefficients of determination ( $0.88 \leq r^2 \leq 0.98$ ). Deviations of observed GDD from the CxQ model predicted GDD by site corresponded to peak VI for negative residuals (period of higher latent heat flux) and low VI at beginning and end of growing season for positive residuals (periods of higher sensible heat flux). Modeled thermal time to peak, i.e., AGDD at peak GDD, showed a strong inverse linear trend with respect to latitude with  $r^2$  of 0.92 for Russia and Kazakhstan and 0.81 for Ukraine. MODIS VIs tracked similar seasonal responses in time and space and were highly correlated across the growing season with  $r^2 > 0.95$ . Sites at lower latitude ( $\leq 49^\circ\text{N}$ ) that grow winter and spring grains showed either a bimodal growing season or a shorter unimodal winter growing season with substantial inter-annual variability, whereas sites at higher latitude ( $\geq 56^\circ\text{N}$ ) where spring grains are cultivated exhibited shorter, unimodal growing seasons.

Sites between these extremes exhibited longer unimodal growing seasons. At some sites there were shifts between unimodal and bimodal patterns over the study period. Regional heat waves that devastated grain production in 2007 in Ukraine and in 2010 in Russia and Kazakhstan appear clearly anomalous. Microwave based surface air temperature data holds great promise to extend to parts of the planet where the land surface is frequently obscured by clouds, smoke, or aerosols, and where routine meteorological observations are sparse or absent.

### **3.1 Introduction**

About 10% of the earth's terrestrial surface (1.5 billion ha) is covered by crops, both irrigated and rainfed (Thenkabail et al., 2009). In the face of increasing concerns about the food–water–energy nexus, a better understanding of global crop dynamics is urgently needed. Although grain production in Russia (RU), Ukraine (UA), and Kazakhstan (KZ) declined significantly following the collapse of the Soviet Union, it has begun to recover (Lioubimtseva & Henebry, 2012), and wheat production in Ukraine was largely unaffected by Russia's annexation of Crimea, due to favorable weather (Lindeman, 2014; Sobolev, 2015; Whitney, 2014). If the recent increases in crop production continue, this region may become a key source to address food security crises in the coming decades, despite ongoing challenges arising from land use change, regional conflicts, and climatic variability, extremes, and change.

The theoretical basis of using remotely sensed information to monitor crop growth and development was based on United States Department of Agriculture (USDA) research in the 1960s through the 1970s that characterized the optical properties of crop

type and crop fields (Becker-Reshef et al., 2010). The USDA Foreign Agricultural Service now routinely uses remote sensing to monitor conditions in key crop production areas across the globe to generate market intelligence, particularly in regions where information is scarce or unreliable (USDA-FAS, 2015b). The normalized difference vegetation index (NDVI; Tucker, 1979) is the most commonly used and a well-documented vegetation index. Remotely sensed vegetation indices (VIs) such as the NDVI have been widely utilized for agricultural mapping and monitoring (Benedetti & Rossini, 1993; Funk & Budde, 2009; Maselli et al., 1992; Mkhabela et al., 2011; Rasmussen, 1992). The United States Agency for International Development (USAID) funded and United States Geological Survey (USGS) implemented Famine Early Warning System Network (FEWS NET) uses NDVI-based measures of cropland activity as part of its integrated early warning system for food security and drought monitoring (FEWS-NET, 2014). FAO's Global Information and Early Warning System (GIEWS) uses NDVI data to detect vegetation health as a proxy for crop production. Despite the great advantages, the NDVI has some limitations including reduced sensitivity in denser vegetation, reduced detection of green vegetation in sparsely vegetated areas due to soil background, and reliance on just two spectral bands, the red and near infrared (NIR) bands (Czerwinski et al., 2014; Gitelson, 2004; Viña et al., 2004b). The enhanced vegetation index (EVI; [18]) was designed to overcome this loss of sensitivity over dense vegetation, adjust for soil background effects, and reduce atmospheric effects in the red band by including information from the blue portion of the spectrum (Huete et al., 2002). These vegetation indices—NDVI and EVI—are complementary for global vegetation

studies and together improve detection of changes in surface vegetation and extraction of canopy biophysical variables (Huete et al., 2002; Wardlow et al., 2007).

Land surface phenology (LSP) deals with the timing of vegetated land surface dynamics as observed by satellite remote sensors, particularly at spatial resolutions and extents relevant to meteorological processes in the atmospheric boundary layer (de Beurs & Henebry, 2004, 2010). LSP plays an important role in monitoring cropland dynamics. Comparative studies of cropland LSPs enable the discrimination between crop types (Gumma et al., 2011; Thenkabail et al., 2007; Xiao et al., 2006; Xiao et al., 2005), provide observations which can be assimilated into process-based crop models increasing model prediction accuracy (Doraiswamy et al., 2004; Fang et al., 2011), enable impact assessment and early warning for drought (Rojas et al., 2011), and can aid forecasting of crop yields (Bolton & Friedl, 2013a; Moriondo et al., 2007).

Phenological studies integrate climate-biosphere relationships because the timing of vegetation lifecycle events is influenced by temperature and precipitation (de Beurs & Henebry, 2008a; Los et al., 2001; Morissette et al., 2009; Pitt & Heady, 1978). The mid-latitudes are thermally limited with respect to net primary production; temperature is the primary constraint for crop production (Alemu & Henebry, 2013; Moriondo et al., 2007; Zhang et al., 2004). Air temperature is a key forcing for crop growth and development (Asseng et al., 2011; Gordon & Bootsma, 1993; Ritchie & NeSmith, 1991; Wang et al., 2011). The concept of heat units or thermal time was introduced by Réaumur in 1730 (McMaster & Wilhelm, 1997). A common metric of thermal time is the growing degree-day (GDD), which weights the passage of calendar time by the temperature deemed

useful for plant growth (de Beurs & Henebry, 2004; Goodin & Henebry, 1997; Gordon & Bootsma, 1993). Use of GDD and accumulated GDD (AGDD) can improve phenological analyses (Boschetti et al., 2009; McMaster & Wilhelm, 1997; Viña et al., 2004a), and crop yield models (Raun et al., 2001; Sarma et al., 2008; Teal et al., 2006).

In most countries, observations from the network of weather stations are sparse in space and incomplete in time. Remote sensing offers multiple approaches to estimate temperature and moisture in a spatially comprehensive way at the cost of spatial precision and temporal resolution. Land surface temperature (LST) can be retrieved from moderate resolution ( $\leq 1$  km) spatial resolution thermal infrared (TIR) sensors, such as MODIS (MODerate-resolution Imaging Spectroradiometer). Although LST is often very different than surface air temperature measured nominally at 2 m, some studies argue that it may be more relevant for modeling plant growth (Henebry & de Beurs, 2013; Henebry et al., 2013; Still et al., 2014). However, TIR sensors cannot see through clouds to retrieve LST (de Beurs & Henebry, 2004; Hassan et al., 2007; Neteler, 2010). Passive microwave radiometers, which operate at much coarser spatial resolution (25 km) relative to TIR sensors, can penetrate most clouds to retrieve air temperature, although it is more challenging over snow covered surfaces (Jones et al., 2011; Jones et al., 2012; Liu et al., 2013; Neteler, 2010). Although 25 km may be considered very coarse relative to many kinds of land surface features and phenomena, it is still a much finer spatial resolution for air temperature data than exists across most of the global land surface (Jones et al., 2010; Piper & Stewart, 1996).

Here we explore whether the synergistic use of vegetation indices from visible and near infrared (VNIR) reflectance and surface air temperature data retrieved through microwave radiometry can improve the characterization of cropland phenology at the mid-latitudes. The higher spatial but lower temporal resolution VNIR VIs are sensitive to green-up and brown-down dynamics of the growing season, and the coarser spatial but finer temporal resolution surface air temperature data provide the biometeorological tempo to improve modeling the land surface dynamics. In Section 2, we describe the data and modeling methods used. The results of our analyses appear in Section 3, including modeling the land surface seasonality of thermal time, latitudinal patterns in thermal time, and the identification of unimodal and bimodal seasonality. Section 4 discusses the identification of the period of canopy evapotranspiration detected from the thermal time residuals, and the detection of anomalous patterns arising from the impact of heat waves on crops. Section 5 concludes with remarks about the significance of this study and directions for further research.

## **3.2 Data and Methodology**

### **3.2.1 Data**

#### ***3.2.1.1 Remote Sensing Data***

We used products from two sensors: MODIS for the VNIR and TIR data and AMSR-E (Advanced Microwave Scanning Radiometer on EOS) for the microwave data. AMSR-E, onboard the NASA-EOS Aqua satellite since May 2002, is a multi-frequency microwave radiometer (6.925, 10.65, 18.7, 23.8, 36.5, 89.0 GHz) that detects faint microwave emissions from the earth's surface and atmosphere. The Numerical



Terradynamic Simulation Group at the University of Montana has produced various geophysical parameters from AMSR-E twice daily data records (daytime, ~13:30, and nighttime, ~01:30) overpasses, and 25 km spatial resolution from mid-June 2002 to October 2011 (antenna failure). These include surface air temperatures ( $t_a$ ; ~2 m height), fractional coverage of open water over land ( $fw$ ), vegetation canopy transmittance ( $t_c$ ) at three microwave frequencies (6.925 GHz, 10.65 GHz and 18.7 GHz), surface soil moisture ( $mv$ ;  $\leq 2$  cm soil depth), and integrated water vapor content ( $V$ ) of the total column (Jones & Kimball, 2011). Only surface air temperature retrievals were used in this study (Jones et al., 2010). The average surface air temperature calculated from the 01:30/13:30 overpass pair is quite likely to differ from average air temperature calculated from the daily extrema. We do not consider this potential bias to be a problem for our analysis because the accumulated average daily temperature serves to provide the tempo for growth rather than establish temperature threshold that would trigger phenophase transitions. In other words, the discrepancies introduced by the potential bias are negligible with respect to the modeling.

MODIS is aboard the Terra and Aqua satellites launched by NASA in 1999 and 2002, respectively. MODIS has 36 spectral bands from which different groups of data products are processed at different spatial and temporal resolutions tuned for specific applications. For this study, we used MODIS collection 5 level 3 data products in a 0.05 degree (~5.6 km) Climate Modeling Grid (CMG). These products included 8-day composites of land surface temperature (LST) from both satellites (Terra: MOD11C2; Aqua: MYD11C2) and 16-day composites of Nadir BRDF-Adjusted Reflectance

(NBAR), which combines observations from Terra and Aqua (MCD43C4; DAAC-LP, 2014). NBAR provides improved retrievals of surface reflectance through consistent normalization of multiple views of the surface to a nadir view using bidirectional reflectance distributions functions (BRDF) to model surface anisotropies (Friedl et al., 2010; Schaaf et al., 2002).

To identify our specific cropland study areas, we used two datasets: (1) the International Geosphere Biosphere Programme (IGBP) land cover scheme in the MODIS land cover product at a spatial resolution of  $0.05^\circ$  (MCD12C1; DAAC-LP, 2014); and (2) the USDA Foreign Agriculture Service (FAS) crop layers by oblast (for Russia: [\(USDA-FAS, 2011b\)](#), for Kazakhstan: [\(USDA-FAS, 2011a\)](#), for Ukraine: [\(USDA-FAS, 2011c\)](#)). Details on the selection process of the study sites are presented in Section 2.2.

### **3.2.1.2 In Situ Data**

Meteorological station data from National Oceanic and Atmospheric Administration (NOAA) historical climate data (FEWS-NET, 2014) was used to compare with the satellite retrievals. Among the 49 sites on which the study is conducted, we selected six meteorological stations within 25 km distance from the geographic centers of these study sites. From these six stations, a considerable amount of data was missing except for the year 2003 (Table 3-1). Missing data pose a problem for calculating accumulated growing degree-days. While there are more meteorological stations and data available within these countries, we restricted the analysis to what is freely available through WMO data-sharing agreements. In this study, we first selected our study cropland sites using criteria described in Section 2.2, and only then searched for

meteorological stations within a reasonable distance from the selected cropland study sites.

**Table 3-1.** Percentage of days with meteorological station data missing during the growing season.

Year/Site	Simferopol, UA		Odesa, UA		Mykolayiv, UA		Kirovohrad, UA		Kharkiv 2, UA		Saratov 4, RU	
	Tmax	Tmin	Tmax	Tmin	Tmax	Tmin	Tmax	Tmin	Tmax	Tmin	Tmax	Tmin
2003	0	0	4	6	0	0	0	2	3	4	0	0
2004	57	51	70	70	58	52	58	52	58	53	0	0
2005	59	41	61	41	60	43	59	42	59	41	0	0
2006	44	21	49	28	45	22	44	22	44	22	0	0
2007	68	56	68	59	68	59	70	59	68	55	0	0
2008	70	55	71	56	71	56	71	56	70	55	0	0
2009	90	82	91	84	91	84	90	86	90	82	0	0
2010	100	100	100	100	100	100	100	100	100	100	0	0

### 3.2.2 Study Region

Our study region spans the major grain producing areas of Ukraine, southern Russia, and northern Kazakhstan. Based on MODIS Land Cover Type 1 Percentage Product for the IGBP scheme (2003–2010), the dominant classes in the study region are Grassland (IGBP class 10 at 34%), Cropland (IGBP class 12 at 27%), Crop–Natural Vegetation Mosaic (IGBP class 14 at 14%), and Mixed Forest (IGBP class 5 at 11%). The overall land cover classification accuracy for this product is about 75%, but the range in class-specific accuracies is large (Friedl et al., 2010). In order to select specific AMSR-E study pixels with a high and stable percentage of cropland, we conducted a temporal stability analysis for each of the three dominant land cover classes over the 8 years study period by first calculating the maximum, minimum, and mean land cover percentage over the study period and then displaying the maximum, mean, and range in

the red, green, and blue color planes, respectively (Henebry et al., 2013). Yellow (high maximum and high mean and low range) identifies land cover that is stable over the study period (Table 3-2, Figure 3-1). Expanses of yellow in Figure 3-1 indicate where Crop–Natural Vegetation Mosaic (Figure 3-1a), croplands (Figure 3-1b), and grasslands (Figure 3-1c) continue to be the dominant land cover during the study period.

**Table 3-2.** Interpretative legend for figure 3-1 that display IGBP MODIS 0.05° land cover variation from 2003-2010 in the study region. The table shows how the color in the LC map (figure 3-1) arises from the false color composite of red, green, and blue color planes that display, respectively, the maximum percentage of LC class, the average percentage of LC class, and the range of percentages of LC class over the study period.

Color in LC Map	Red = Max % LC	Green = Mean% LC	Blue = Range% LC	Interpretation
Black	None	None	None	Land cover (LC) class absent
Blues	Low	Low	High	Unstable but ephemeral periphery; rare and erratic
Magentas	High	Low	High	Unstable but persistent periphery; sometimes high, but usually low
Whites	High	High	High	Unstable core; sometimes low, but usually high
Yellows	High	High	Low	Stable core of LC; always high so low range

Source: (Henebry et al., 2013).

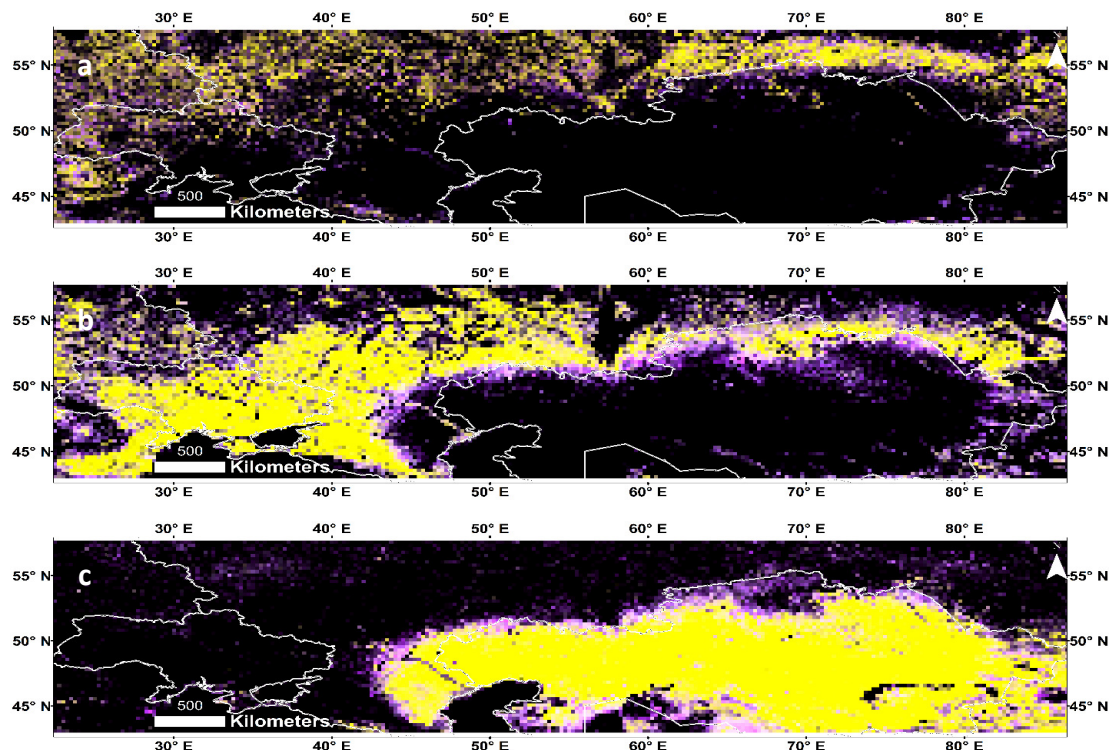


**Figure 3-1.** Land cover stability in Ukraine, southern Russia, and northern Kazakhstan as revealed by IGBP global land cover classification scheme MODIS 0.05° land cover products (resampled to AMSR-E spatial resolution: 0.25°) from 2003–2010: (a) crop–natural vegetation mosaic (IGBP class 14); (b) cropland (IGBP class 12); and (c) grassland (IGBP class 10). Land cover percentage from 2003–2010 displayed as red = maximum percentage, green = mean percentage, and blue = range of percentages. For legend, refer to Table 3-2.

We selected the study sites within the stable core areas of cropland, but we also used the USDA Crop Explorer maps to identify wheat producing areas. We identified 49 AMSR-E pixels (study sites) in the three countries: 14 in Ukraine, 24 in Russia, and 11 in Kazakhstan (Figure 3-2, Table 3-3). Land cover percentage for each AMSR-E pixel study site was determined by aggregating the MCD12C1 Land cover percentage within each AMSR-E pixel. The collection of sites spans nearly 12° of latitude and 56° of longitude.

The most extreme latitudinal sites (Cherkessk and Kazan', both in Russia) have a maximum day length difference of two hours at the summer and winter solstices. The site-to-site multi-year average cropland cover ranges between 46% (Volgograd, Russia) to 100% (a number of sites mostly in Ukraine), while the mean cropland cover for all sites over the study period was 88%. While the sites are dominated by crops, there is some degree of fragmentation or heterogeneity within the 25 km pixels. However, the Soviet era heritage of very large field sizes persists across the region and minimizes that fragmentation. The rest of the land cover proportion is mainly crop–natural vegetation mosaic (CNVM), followed by grassland. Factors that could affect the temporal variation in cropland cover include class indeterminacy due to site adjacency and spectral mixing, drought and recovery, soil freeze-thaw state, disturbance, and land cover change.

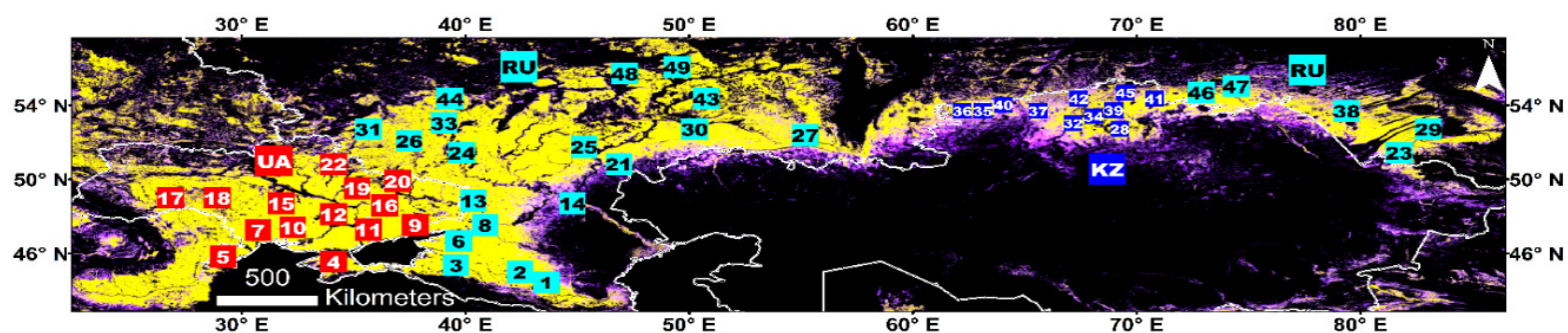


**Figure 3-2.** Study region cropland stability map superimposed with the 49 specific AMSR-E pixels selected for this study. The AMSR-E pixels are numbered by latitude starting from the most southern site. Name for each site is their closest large settlement (cf. Table 3-3). Red squares are in Ukraine, cyan squares in Russia, and blue squares in Kazakhstan.

Sites adjacent to land cover transition zones experience higher temporal variation in cropland cover (sites closer to the unstable peripheral areas with the magenta color in Figure 3-2 (see also Table 3-2). For example, Saratov 1 in Russia (site 21) had the largest grassland encroachment with 69% and 31% mean cropland and grassland cover, respectively, over the eight years and, thus, had the largest cropland cover range (28%). Omsk 1 in Russia (site 46), and Kostanay 2 in Kazakhstan (site 36) are other examples of this phenomenon.

**Table 3-3.** Description of 49 study sites named by their closest town and country, numbered from lower latitude (1) to higher latitude (49), their geographic coordinates, and average cropland (CRP) cover percent and range (2003–2010). Note sites with 100% average CRP cover throughout the study period (bold), and larger CRP cover percent range (underlined).

Site No.	Name	Latitude	Longitude	Cropland (%)	Range (%)	Site No.	Name	Latitude	Longitude	Cropland (%)	Range (%)
1	Cherkessk, RU	44.4	43.5	99	0.6	26	Kursk, RU	52.1	37.5	95	4.1
2	Stavropol, RU	45.0	42.4	<b>100</b>	0.3	27	Orenburg, RU	52.4	55.2	94	4.7
3	Krasnodar, RU	45.6	39.6	98	0.6	28	Kokshetau 1, KZ	52.7	69.2	91	8.5
4	Simferopol', UA	45.6	34.1	<b>100</b>	1.2	29	Barnaul 2, RU	52.7	83.0	99	0.7
5	Tulcea, UA	45.8	29.2	96	0.3	30	Kuybyshev 2, RU	52.7	50.2	91	9.6
6	Rostov-on-Don 2, RU	46.7	39.8	<b>100</b>	0.2	31	Orel, RU	52.7	35.7	64	2.7
7	Odesa, UA	47.3	30.7	<b>100</b>	<b>0.0</b>	32	Kokshetau 2, KZ	53.0	67.4	79	10.6
8	Rostov-on-Do 1, RU	47.5	40.9	88	6.2	33	Lipetsk, RU	53.0	39.1	84	4.4
9	Donets'k, UA	47.5	37.7	<b>100</b>	0.7	34	Kokshetau 3, KZ	53.7	68.2	84	10.0
10	Mykolayiv, UA	47.5	32.3	<b>100</b>	0.1	35	Kostanay 1, KZ	53.7	63.3	78	8.0
11	Zaporihzhya 1, UA	47.8	35.7	<b>100</b>	0.1	36	Kostanay 2, KZ	53.7	62.2	86	<u>18.5</u>
12	Zaporihzhya 2, UA	48.1	34.1	<b>100</b>	<b>0.0</b>	37	Kurgan, KZ	53.7	65.6	74	<u>17.3</u>
13	Luhans'k, RU	48.7	40.4	99	2.1	38	Barnaul_1, RU	53.7	79.4	82	11.3
14	Volgograd, RU	48.7	44.8	<b>46</b>	13.4	39	Kokshetau 4, KZ	54.0	69.0	93	4.7
15	Kirovohrad, UA	48.7	31.8	99	1.0	40	Kostanay 3, KZ	54.0	64.0	79	15.7
16	Kharkiv 2, UA	49.0	36.2	91	6.6	41	Petropavlovsk 2, KZ	54.4	70.8	97	3.6
17	Khmel'nyts'kyz, UA	49.0	26.8	88	11.0	42	Petropavlovsk 3, KZ	54.4	67.4	92	5.4
18	Vinnitsya, UA	49.0	28.9	96	0.5	43	Kuybyshev 1, RU	54.4	50.8	95	8.8
19	Poltava, UA	49.6	35.1	97	1.6	44	Ryazan, RU	54.4	39.3	65	13.7
20	Kharkiv 1, UA	49.9	37.0	72	3.9	45	Petropavlovsk 1, KZ	54.7	69.5	86	4.4
21	Saratov 1, RU	50.8	46.9	69	<u>27.9</u>	46	Omsk 1, RU	54.7	72.9	61	<u>18.7</u>
22	Sumy, UA	50.8	34.1	85	7.1	47	Omsk 2, RU	55.0	74.5	59	14.5
23	Semipalatinsk, RU	51.4	81.7	98	3.3	48	Cheboksary, RU	55.7	47.1	93	6.1
24	Voronezh, RU	51.4	39.8	98	1.7	49	Kazan', RU	56.1	49.5	81	2.3
25	Saratov 4, RU	51.8	45.3	88	3.6						

### 3.2.3 Methods

We used the AMSR-E and MODIS data from all eight years (2003–2010) for all the pixels. To avoid the frozen season and to maintain a consistent analysis period across



all pixels, we restricted our focus to data from DOY 89–305, which ranges 30 March to 1 November for non-leap years and 29 March to 31 October for leap years. For the AMSR-E data, 8-day moving average filter was applied to the daily data to minimize data gaps due to orbit and swath width. Growing degree-day (GDD) is the daily thermal-time increment above a certain threshold (base temperature) for plant growth (de Beurs & Henebry, 2004; McMaster & Wilhelm, 1997; Sarma et al., 2008), and accumulated growing degree-days (AGDD) are the simple summation of heat units throughout the annual observation period (de Beurs & Henebry, 2010; Wang et al., 2001; Yang et al., 1997); that is, “the passage of days is weighted by the quantity of growing degrees occurring that day, with zero (but not negative) degrees being a permissible weight” (Henebry, 2013). McMaster (2005) concluded that the base temperature of 0 °C is a robust and sufficient threshold for wheat phenology, which is the main crop in our study area. GDDs were calculated for both AMSR-E air temperature ( $t_a$ ) data and MODIS land surface temperature (LST) data with a base temperature of 273.15 K (=0 °C) as follows:

$$\text{GDD} = \max\left[\frac{t_{ASC} + t_{DSC}}{2} - 273.15, 0\right] \quad [1]$$

where  $t_{ASC}$  and  $t_{DSC}$  are the air temperature retrievals at the ascending and descending passes.

GDDs were accumulated from DOY 89–305 to generate each year’s AGDD trajectory. The GDDs calculated from MODIS LST 8-day composites were multiplied by eight to rescale them into the proper range for eight daily values, rather than a single value occurring in eight days. The daily AMSR-E GDDs were summed over eight days to

align temporally them with the particular MODIS compositing periods. GDDs from both sensors were compared with available nearby meteorological station (stations within 25 km distance from the geographic centers of the AMSR-E pixel study sites) daily air temperature GDD to check for consistency using linear regression model. The station data were processed using similar methods as the AMSR-E daily air temperature data. We then tested whether the slopes and/or intercepts from the linear regression model fit were significantly different by sensor. For this test, we used analysis of covariance (ANCOVA; Owen & Froman, 1998)—in which sensors (AMSR-E and MODIS) were the independent categorical effect variables, the meteorological station GDD was the covariate, and satellite GDD was the response variable. In this analysis,  $p \leq 0.05$  was considered significant.

Accumulated GDD (or AGDD) was calculated from GDD for both sensors.

$$AGDD_t = AGDD_{t-1} + GDD_t \quad [2]$$

where  $GDD_t$  is daily temperature increment of growing degree-days at time  $t$ .

During summer in the Northern hemisphere, the maximum and minimum air temperatures typically occur late afternoon and predawn, respectively, while data from AMSR-E and MODIS Aqua (N.B.: AMSR-E is onboard Aqua satellite) are recorded twice daily (ascending—daytime, ~13:30, and descending—nighttime, ~01:30 overpasses), and that of Terra is on ~22:30 and ~10:30, respectively. We use MODIS Aqua and Terra average LST for GDD from MODIS. As a consequence, the satellite AGDD may be biased when compared with meteorological measurements, which in turn

may limit the modeling of quantitative vegetation specific AGDD that drive phenophase transitions.

To characterize the seasonal progression of thermal time, we fitted the GDDs as a convex quadratic (CxQ) function of AGDD. The CxQ model have been successfully applied in temperate herbaceous vegetation and boreal ecosystems (de Beurs & Henebry, 2010; Raun et al., 2001; Yang et al., 1997).

$$\text{GDD}_t = \alpha + \beta \times \text{AGDD}_t - \gamma \times \text{AGDD}_t^2 \quad [3]$$

The intercept  $\alpha$  is the start of observation period GDD value (which may not be zero due to the compositing), the linear parameter  $\beta$  affects the slope, and the quadratic parameter  $\gamma$  controls the curvature. Since our model is convex quadratic in shape, the sign of  $\beta$  is positive while the sign of  $\gamma$  is negative.

Two phenometrics were derived from the fitted parameter coefficients of the CxQ model. The peak height (PH) (Equation (4)) describes the maximum GDD from the fitted model, and the thermal time to peak (TTP) (Equation (5)) describes the amount of AGDD needed to reach the peak GDD:

$$\text{PH}_{\text{GDD}} = \alpha - (\beta^2/4 \times \gamma) \quad [4]$$

$$\text{TTP}_{\text{GDD}} = -\beta/2 \times \gamma \quad [5]$$

where  $\alpha$ ,  $\beta$ , and  $\gamma$  are the fitted parameter coefficients.

Our consideration of the growing season from day of year (DOY) 89–305 (roughly the beginning of April through October), allows us to characterize all the study cropland sites within a similar time frame. However, since our study sites have 12°

latitudinal range, there might be sites and years in the lower latitude winter cropland study sites that have above 0 °C temperature before DOY 89 or after DOY 305.

Consequently, an underestimation of AGDD is possible for these sites or when either the early spring or the fall is warmer than normal. This warmer weather may affect the trajectory of NDVI or EVI as a function of AGDD, in particular for croplands with winter crops where the dormancy starts after DOY 305 and ends before DOY 89 of the following year, possibly biasing the  $TTP_{GDD}$ . However, other factors such as different sowing dates, management practices, changes in crops under production, and field conditions around sowing and harvesting, may also affect cropland phenology.

We calculated the deviation of individual years' GDD time series from the CxQ model based on the average of eight years of GDD data. The root mean square deviation (RMSD) was used to calculate the average magnitude of the annual GDD deviation. Although eight years' time span is too a short period to construct a climatology, the expectation based on the shorter time series still provides a useful contrast to highlight seasonal differences in particular years.

NDVI and EVI were calculated from the MODIS NBAR reflectance data using formulas developed by Tucker (1979) and Huete et al. (2002), respectively. We have plotted time series of NDVI and EVI (from the VNIR MODIS) as a function of AGDD (from the passive microwave AMSR-E). In the result section, we have described AGDDs at peak VIs based on growing season VI maximum values. AGDDs at 95% of the first peak VIs (peak height determined using growing season maximum value) were used to analyze temporal and spatial LSP responses to their thermal regime. In each AMSR-E

pixel there are 25 to 36 corresponding MODIS pixels, depending on the latitude of the site. We generated corresponding MODIS and AMSR-E AGDDs for the 95% value of the initial seasonal peaks of NDVI and EVI. Since the peak VIs were selected based on the seasonal maximum value, sometimes these single peak values may occur in error. To avoid such errors, we use the 95% value of these peak VIs. While the NDVI, EVI and AGDD for the MODIS data were generated for each MODIS pixel within an AMSR-E pixel, the same AMSR-E AGDD was used for all the MODIS pixels within the same AMSR-E pixel. We assume that air temperature did not significantly vary within the AMSR-E pixel, an assumption that is reasonable in relatively flat terrain that is distant from large bodies of water. Here we compare the seasonal development of MODIS VIs at the MODIS Climate Modeling Grid (CMG) resolution ( $0.05^\circ$ ) as a function of the AGDD derived from MODIS and from AMSR-E AGDDs.

### **3.3 Results**

#### **3.3.1 Land Surface Seasonalities of Growing Degree-Days**

In this subsection, we present the comparisons of satellite GDDs with meteorological station GDDs for quality assessment. The convex quadratic (CxQ) models of GDD are followed. We then present the AMSR-E thermal time to peak (TTP) (AGDD) in relation to latitude. Finally, AMSR-E GDD time series deviations from the multi-year average GDD model are presented.

##### ***3.3.1.1 Comparisons of GDD Derived from Satellite and Station Data***

Meteorological stations 10 km buffer zone land cover displayed a similar cropland (CRP) dominated average land use for 2003–2010 study period (>90%

cropland; Table 3-4). Saratov 4 is an AMSR-E pixel study site with considerable proportion of crop–natural vegetation mosaic (CNVM; 12%), while Kharkiv\_2 meteorological station buffer has 7% urban and built-up (UBU) area. Comparison between Satellite GDD and station GDD was made using the 2003 GDD as nearly all the selected stations (that are within 25 km distance from the centers of AMSR-E pixel study sites) had full data during this year’s growing period (Table 3-1). Root mean square errors/deviations (RMSE or RMSD) between AMSR-E GDD and station GDD were lower than those between the MODIS GDD and station GDD (14–24 °C versus 16–30 °C; Table 3-5). Satellite GDD from both AMSR-E and MODIS showed strong linear correspondence with meteorological station GDD with  $r^2 > 0.87$  (the covariate station GDD is correlated with response variable Satellite GDD; Figure 3-3 and Table 3-5). Overall,  $r^2$  from the station and AMSR-E GDD fits was higher than those between the station and MODIS GDDs. GDDs from both satellite sensors had relatively higher magnitude compared to station GDDs. Based on analysis of covariance (ANCOVA), slopes from the linear regression fit of the two satellite sensors GDD with station GDD were partially significantly different (three out of six sites). That means that the covariate (station GDD) is not correlated to the independent variables (factor; sensors) for three sites while it is correlated for the rest three sites at  $\alpha = 95\%$  significance level. In addition, the ANCOVA model revealed that intercepts resulted from the linear regression fit between station GDD and satellite GDD are not significantly different by sensor in four sites ( $p > 0.05$ ) while it is significantly different for two sites ( $p \leq 0.05$ ). Further analysis that incorporates many station data is needed to reach at a conclusion that linear

fit of station GDD with AMSR-E GDD is significantly different from that with the MODIS GDD.

**Table 3-4.** Average (2003–2010) MODIS land cover with the 10 km buffer zone for meteorological stations and corresponding AMSR-E pixel study sites. Bold indicates the dominant land cover (all sites are in crop-dominated areas).

Site	LULC (Stations)			LULC (AMSR-E Pixels)		
	CRP	CNVM	UBU	CRP	CNVM	UBU
Simferopol, UA	<b>97.9</b>	0.0	2.1	<b>99.7</b>	0.0	0.0
Odesa, UA	<b>100.0</b>	0.0	0.0	<b>100.0</b>	0.0	0.0
Mykolaiv, UA	<b>98.5</b>	0.0	1.5	<b>99.6</b>	0.0	0.0
Kirovohrad, UA	<b>99.5</b>	0.3	0.0	<b>98.7</b>	0.2	0.0
Kharkiv_2, UA	<b>91.5</b>	0.7	7.4	<b>91.0</b>	0.3	3.4
Saratov_4, RU	<b>97.3</b>	2.7	0.0	<b>88.4</b>	11.4	0.0

**Table 3-5.** Root mean square error (RMSE), linear regression model (intercept, slope and  $r^2$ ), and analysis of covariance (ANCOVA) between station and satellite GDDs from AMSR-E and MODIS sensors. AMS=AMSR-E; MOD=MODIS.

Site	RMSE *		Intercept		Slope		$r^2$		ANCOVA ( $p$ Value)	
	AMS	MOD	AMS	MOD	AMS	MOD	AMS	MOD	Slope	Intercept
Simferopol, UA	<b>13.77</b>	29.89	16.84	17.71	0.95	1.05	<b>0.95</b>	0.88	0.447	<b>&lt;0.05</b>
Odesa, UA	<b>23.95</b>	24.19	31.88	8.29	0.88	1.06	0.87	<b>0.88</b>	0.177	0.080
Mykolaiv, UA	<b>20.56</b>	23.81	25.82	0.74	0.92	1.13	0.92	0.92	<b>&lt;0.05</b>	0.224
Kirovohrad, UA	<b>18.34</b>	22.25	23.58	-1.70	0.92	1.11	<b>0.93</b>	0.89	0.096	0.328
Kharkiv_2, UA	<b>17.41</b>	18.23	28.80	-5.94	0.83	1.09	0.91	0.91	<b>&lt;0.05</b>	0.231
Saratov_4, RU	20.22	<b>16.31</b>	32.52	-1.76	0.84	1.06	<b>0.96</b>	0.92	<b>&lt;0.05</b>	<b>&lt;0.05</b>

\* RMSE of satellite and meteorological station GDDs (not using fitted GDDs)

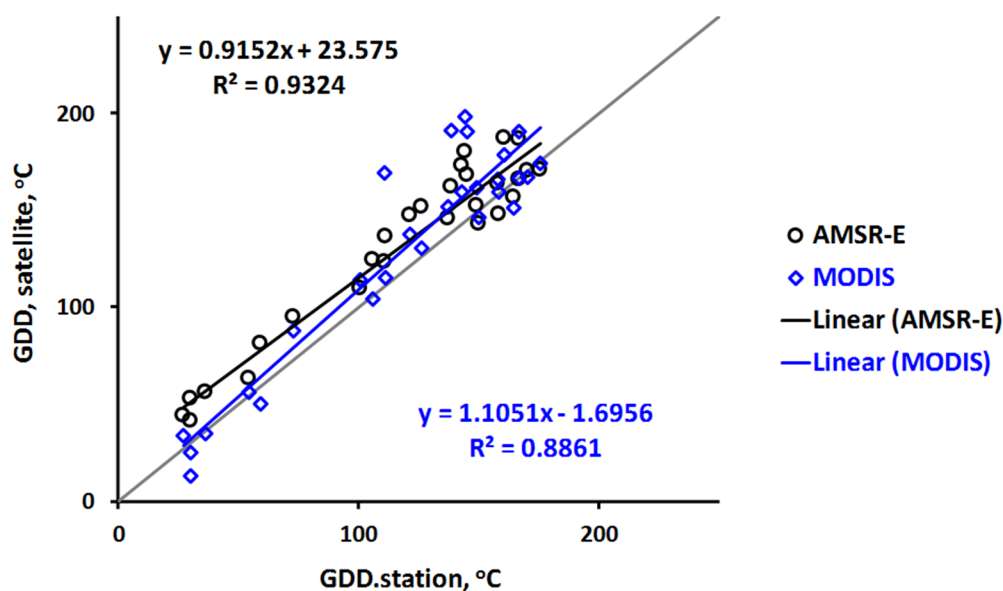


**Figure 3-3.** Scatter plots and linear regression fits of station GDD with satellite GDD—AMSR-E GDD (black circles) and MODIS GDD (blue diamonds)—at Simferopol, Ukraine (site 4) for 2003. The linear regression fit for the two datasets were high with  $r^2$  of 0.93 for the AMSR-E GDD and  $r^2$  of 0.89 for the MODIS GDD.

We further closely examined the correspondence between daily station GDDs and AMSR-E GDDs. AMSR-E GDD not only tracked the seasonal dynamics of the station GDDs, but it also tracked the finer weekly and monthly GDD dynamics (Figure 3-4 left). The root mean squared difference (RMSD) between these daily datasets from the two sources was very low (1.86–3.16 °C). This result is in line with (Jones et al., 2010) that found a bias of 1.0–3.5 K between the 2003 WMO weather station and AMSR-E daily air temperature data on vegetated lands in the Northern Hemisphere. It is also important to note that there are times that the magnitude of GDDs from the two data sources is different, despite the similarities in dynamics, and this divergence occurs earlier and later in the growing season (e.g. Figure 3-4 left). These GDDs display strong linear



correspondence with  $r^2 > 0.82$  (e.g., Figure 3-4 right). However, there is a bias in these correspondence (as shown by the intercept) and underestimation (displayed by the slope) of the AMSR-E GDD relative to that of the station.

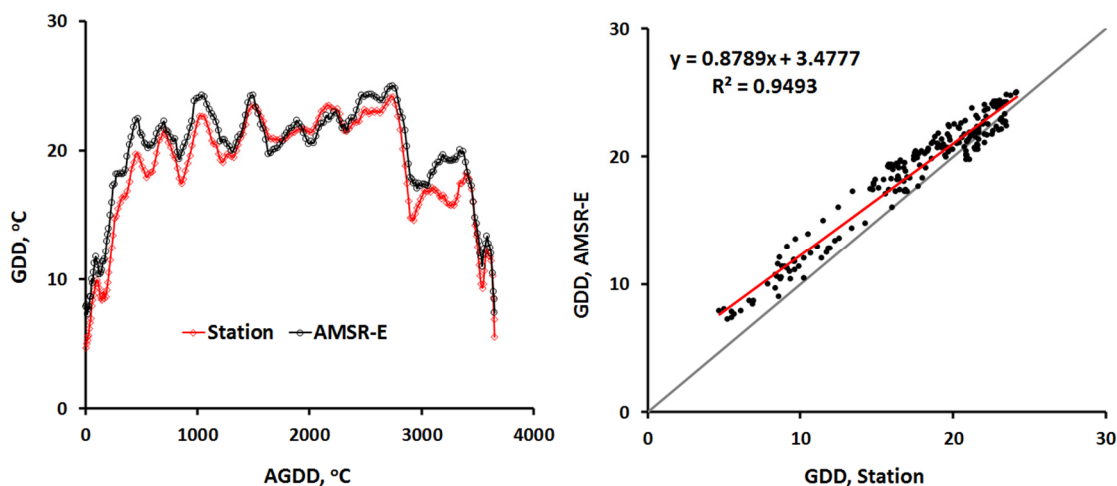


**Figure 3-4.** (left) Time series plot of AMSR-E (black) and station (red) daily GDD as a function of station AGDD for 2003 at Kirovohrad, Ukraine (site 15); and (right) linear regression fit of AMSR-E GDD with station GDD for the same dataset yielding strong correspondence with  $r^2 = 0.95$ . Note also the bias (intercept) and the underestimation (slope  $< 1$ ) of the AMSR-E GDD relative to the station GDD.

### 3.3.1.2 Convex Quadratic Models of GDD

The CxQ model fit well the relationship between GDD and AGDD for both the AMSR-E  $t_a$  and MODIS LST, with coefficients of determination ( $r^2$ ) ranging from 0.88 to 0.98. In contrast to the traditional approach of fitting GDD as a function of day of year (DOY), the CxQ fits for GDD as a function of AGDD displayed clear latitudinal shifts and more finely resolved intra-seasonal dynamics of GDD (Figure 3-5a,c versus Figure 3-5b,d). The more northern sites displayed a shorter summer growing season with narrower base and shorter peak GDD curves (Figure 3-5b), while the more southern sites

displayed a longer growing season with broader base and larger peak GDD curves (Figure 3-5d). The fits for the two datasets (AMSR-E and MODIS) exhibited strong similar seasonalities (Figure 3-5). However, in 76% of our study sites, AMSR-E AGDD is larger than MODIS AGDD even though this difference is not statistically significant. The discrepancy may result from one or more of the following factors: (1) differences between surface air temperature and land surface temperature; (2) spatial scales of the retrievals—a single 25 km pixel versus ~25 pixels of 5.6 km; (3) differences between accumulating daily GDDs over eight days (AMSR-E) versus an eight-day composite (MODIS); and (4) residual atmospheric contamination in the MODIS retrievals.

Generally, higher and middle latitude study sites ( $>49^{\circ}\text{N}$ ) have higher AMSR-E AGDD while those at lower latitudes have higher MODIS AGDD. This discrepancy may arise from the differences in LST versus surface air temperature, particularly during periods of low vegetation cover. All 49 study sites displayed consistently good fits with the CxQ model with coefficients of determination ranging from 0.88 to 0.98 (Table A.1). The CxQ models fitted to the AMSR-E surface air temperature data displayed higher coefficients of determination for almost every site (42 of 49 sites) compared to the MODIS LST data (Table A.1) and, considered as a group, the AMSR-E model fits were significantly ( $p < 0.00001$ ) better than the MODIS model fits. The reasons may include the lower sensitivity of the microwave data to cloud contamination and atmospheric effects, while the MODIS data is composited to filter out degradation from these sources of noise, and the MODIS land surface temperature fluctuates more due to land surface heterogeneity, compared to the AMSR-E air temperature.

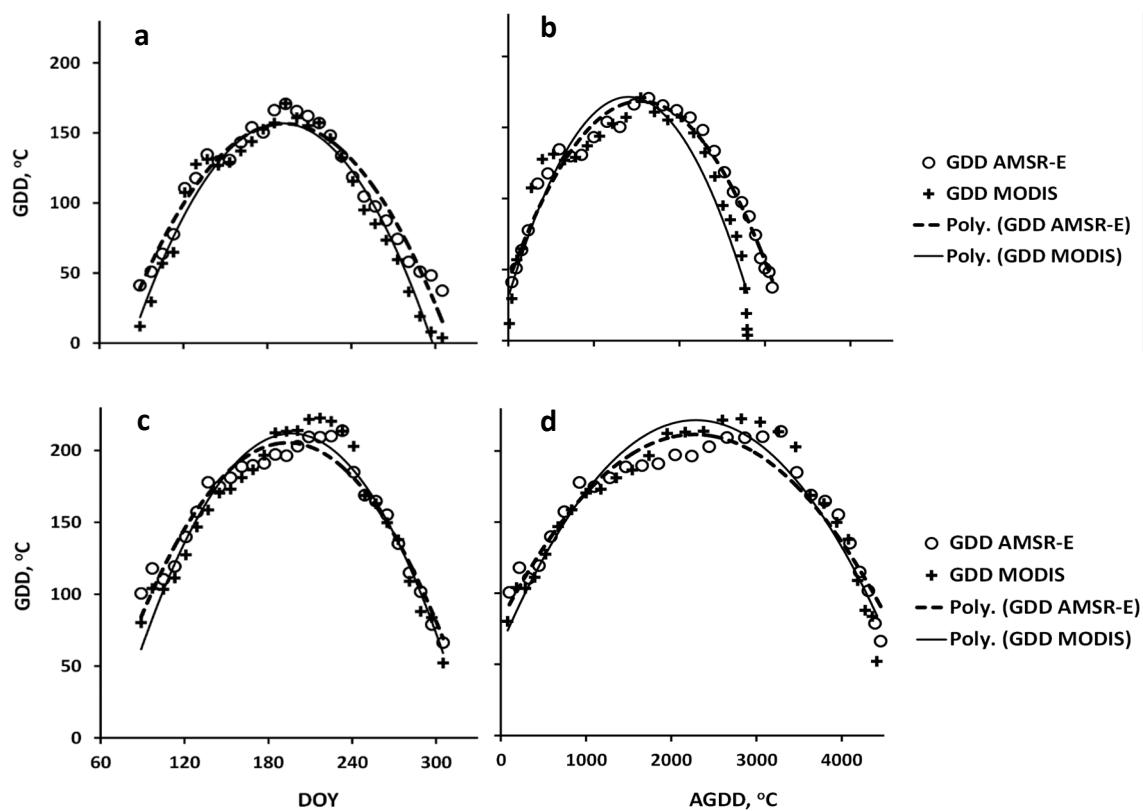


**Figure 3-5.** Average (2003–2010) MODIS (plus signs) and AMSR-E (circles) GDD and their fitted (solid (MODIS LST) and dashed (AMSR-E ta) lines) average GDD as a function of DOY (**left**) and AGDD (**right**) for two cropland sites at the latitudinal extremes of the study region: Cheboksary, Russia (site 48, 55.7°N; **a,b**); and Cherkessk, Russia (site 1, 44.4°N; **c,d**). N.B.: MODIS GDDs are multiplied by 8, while AMSR-E GDDs are eight-day sums.

GDD at the beginning and end of the observational season were well above 0 °C at lower latitude sites (Figure 3-5c,d), but closer to zero at higher latitude sites (Figure 3-5a,b). The end-of-season AGDD was also larger (>4000 °C) at the lower latitude sites (Figure 3-5d) and smaller (~3000 °C) at the higher latitude sites (Figure 3-5b). For the rest of the analyses, we used the GDD and AGDD calculated from the AMSR-E surface air temperature data (unless stated otherwise).

### 3.3.1.3 Latitudinal Distributions of Thermal Regimes

Average daily GDD for 2003 through 2010 exhibited a strong inverse linear relationship with respect to latitude with  $r^2 > 0.90$ , in accordance with the long-established geographic fact that, at comparable elevation, temperature decreases as the absolute value of latitude increases (Figure 3-6a). The Thermal Time to Peak ( $TTP_{GDD}$ ) graphed as a function of latitude revealed strong significant negative linear relationship (Figure 3-6b). The coefficient of determination for the sites in Ukraine was 0.81 and, for the sites in Russia and Kazakhstan combined, it is 0.92. Saratov 1 (RU) tends to be an outlier with higher TTP, likely due to its location farther inland from the Volga River. Across the  $12^\circ$  latitudinal range of the study sites, there is a maximum difference in day length of two hours at the summer solstice.

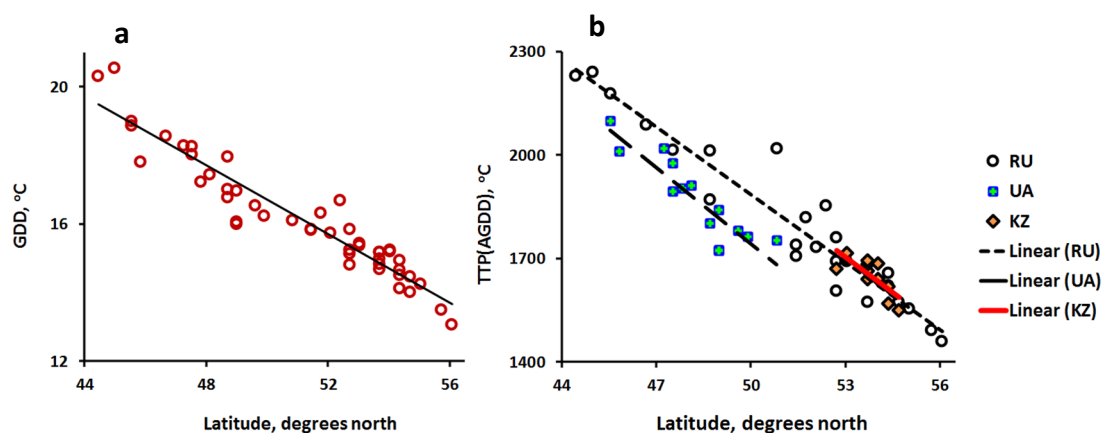


**Figure 3-6.** Thermal climates as a function of latitude revealed by: (a) average daily GDD; and (b) Thermal Time to Peak ( $TTP_{GDD}$ ). Latitudes were the geographic centers of AMSR-E pixels. All 49 study sites are displayed in both figures. In (b), hollow circles = Russia, orange diamonds = Kazakhstan, and cyan crosses on blue background = Ukraine. Both panels show a general decrease in (a) GDD or (b) TTP as latitude increases from  $44^\circ$  to  $56^\circ$ N. The uppermost two hollow circles are the northernmost study sites (site 49,

Kazan', Russia and site 48, Cheboksary, Russia), while the lowermost two hollow circles are the southernmost study sites (site 1, Cherkessk, Russia and 2, Stavropol, Russia).

### 3.3.1.4 Time Series of GDD Residuals

During warmer years, GDDs were well above the GDDs predicted by the multi-year average model, yielding positive GDD residuals and a larger root mean squared difference (RMSD) (Figure 3-7, right; RMSD = 46.3 °C). The 2010 Russian heat wave that devastated grain production in European Russia (Dole et al., 2011), had a clear impact at Orenburg (Figure 3-7). During cooler years, GDDs were below the predicted GDDs yielding negative GDD residuals and a larger RMSD (Figure 3-7, left; RMSD = 22.3 °C). There were also some years that had GDDs that were comparable with the GDDs predicted by the average model, resulting in a smaller RMSD (Figure 3-7, center; RMSD = 19.5 °C).

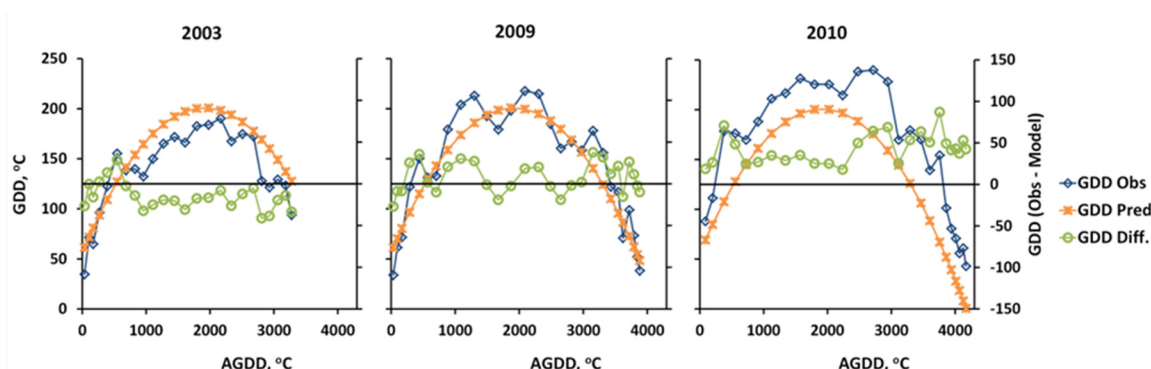


**Figure 3-7.** Line plots of annual observed GDD (blue), annual predicted GDD based on multi-year average model (orange) and observed GDD residuals (green) at Orenburg (RU) for: a cooler year (2003) (**left**); a close-to-average year (2009) (**center**); and a hotter year (2010) (**right**). N.B: GDDs are 8-day sums.

### 3.3.2 Land Surface Phenologies of Vegetation Indices

In this subsection we first present the general LSP characteristics of the NDVI and EVI time series, then describe the cropland dynamics using the VIs in space and time, and we conclude with the responses of peak VIs to thermal time measured by AMSR-E and MODIS sensors.

#### 3.3.2.1 NDVI and EVI

Synergistic use of the MODIS vegetation indices (VIs) NDVI and EVI with AMSR-E AGDD captures well the LSP typical for crops in the mid-to-high latitudes that are planted in spring and harvested in the fall (Figure 3-8). Cropland NDVI and EVI start to rise (green-up onset) as crops start to grow in spring, ascend to their peak seasonal value (maturity), and then decline during senescence and crop drying before harvest. Winter crops are planted in the fall and grow before a period of dormancy over the winter, then emerge in the spring and rapidly develop, before crop drying and harvesting in early summer. Both spring and winter crops could be found with the study region, but winter crops are restricted to the south tier of the region in Ukraine and in southern Russia north of the Black Sea. Since vegetation in the mid-latitudes is temperature-limited, the time series of each VI as a function of AGDD can be well fitted by the CxQ model (Alemu & Henebry, 2013; Henebry & de Beurs, 2013). A general unimodal pattern of LSP was evident across the study region. However, there were variations to this pattern, as detailed below.

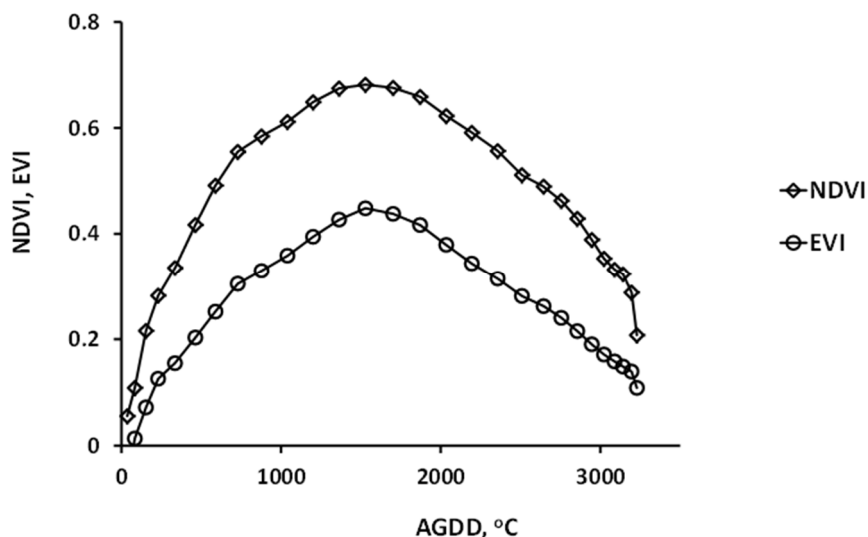


**Figure 3-8.** Average MODIS NDVI and EVI as a function of AMSR-E AGDD for Petropavlovsk 3, Kazakhstan (site 42) for 2003–2010. Note that the NDVI displays a larger dynamic range than the EVI.

### 3.3.2.2 Types of Land Surface Phenologies in Croplands

The MODIS VIs as a function of AMSR-E AGDD revealed that lower latitude cropland sites (in southern Russia and Ukraine) had growing seasons that generally exhibited bimodal VI patterns. These sites are warmer and longer in terms of AGDD: first VI peaks at about AGDD = 1300 °C (Figure 3-9a) and AGDD = 900 °C (Figure 3-9c), and second VI peaks at about AGDD = 2800 °C (Figure 3-9a) and AGDD = 2400 °C (Figure 3-9c). In contrast, higher latitude cropland sites (northern sites in RU) had unimodal, shorter growing seasons in terms of AGDD (peak VIs at about AGDD = 1200 °C); Figure 3-9d). The middle latitude sites behave as unimodal but with a broader base of growing season (peak VI at about AGDD = 2000 °C; Figure 3-9b). Sites exhibiting bimodality in the VI curve are associated with the cultivation of both winter and spring

crops in one year (Figure 3-9a,c). Those sites exhibiting unimodal VI curves were associated with either usually with only a spring crop (Figure 3-9b,d) or, less commonly, with only a winter crop (Figure 3-10, 2005–2009).

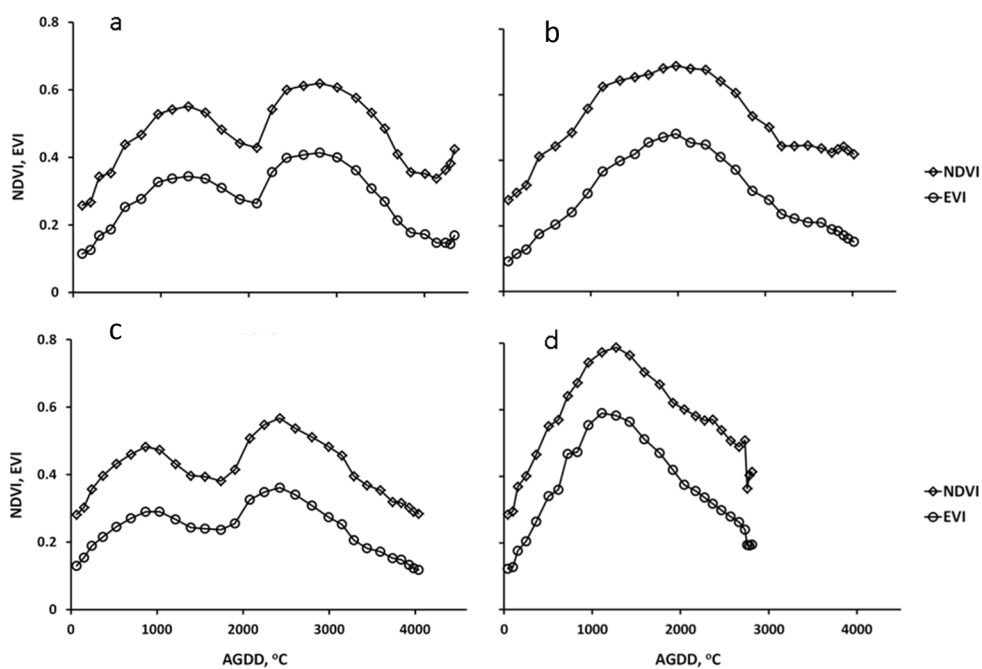


**Figure 3-9.** (a–d) In 2003, lower latitude sites (Cherkessk, Russia: 44.4°N (a) and Simferopol, Ukraine: 45.6°N (c)) display bimodal growing seasons, while the higher latitude sites show unimodal, shorter growing seasons (Kazan', Russia: 56.1°N (d)). The middle latitude sites display a longer unimodal growing season (Odesa, Ukraine: 47.3°N (b)).

Winter grains grown in the region—wheat, rye, and barley—are planted and emerge in the fall before becoming dormant over the winter. Resuming growth in the early spring when the air and soil temperatures warm, they produce a rapid increase in VI earlier in the year. Winter grains' ripening and senescence phase occurs in late spring through early summer, expressed by the rapid VI decrease by mid-summer. A second



increase in VI is due to late spring planting and emergence with the cycle peaking late summer with early fall harvest. For areas that grow winter grains, another smaller VI peak appeared in mid-fall (Figure 3-9a), corresponding to the emergence and growth of the next year's crop before winter dormancy.

### ***3.3.2.3 Interannual Variation in Land Surface Phenologies***

Over the eight years of study, NDVI and EVI displayed similar patterns, but with clear seasonal and interannual variation. In the same location, some years displayed growing season bimodality while others exhibited unimodality. Variation in the timing of peak VI was higher in some locations than others. For example, Simferopol, located in Crimea, had three bimodal years (2003, 2004, and 2010) and five unimodal years (2005–2009) (Figure 3-10). Variation was evident within bimodal growing seasons: in 2003 the second peak was higher (peak NDVI of 0.57 versus 0.48); in 2004 peaks were wider apart in time (difference between first and second peak AGDD of 1900 °C in 2004 versus 1550 °C in 2003); and in 2010 the second peak was much smaller (peak NDVI of 0.51 versus 0.59). Years with a unimodal peak generally had peaks that were larger compared to the bimodal peaks (peak NDVI of >0.63 versus <0.63). In 2007 and 2008 the peaks were earlier; while in 2003, 2009, and 2010 the peak heights were lower. Moreover, since Simferopol is a southern site, the growing season can start before DOY 89, but with interannual variation due to weather. The effect on the VI curves in Figure 3-10 is clear: the early season green-up pattern in 2003–2005 has initial NDVI (EVI) at or below 0.4 (0.2). In contrast, initial VIs in 2006–2010 are well above 0.4 and 0.2 for the NDVI and EVI, respectively.

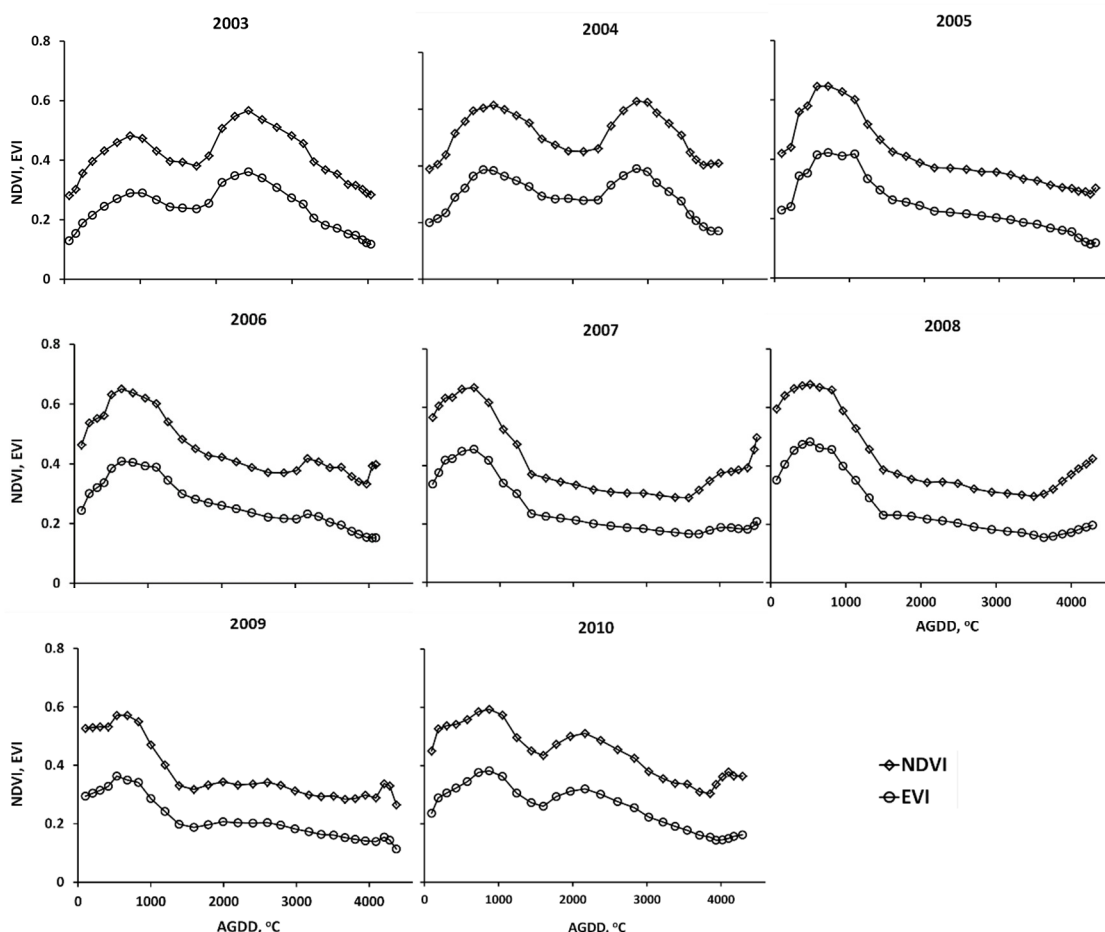


**Figure 3-10.** NDVI and EVI interannual variability in one of the southernmost study sites (Simferopol, Ukraine at 45.6°N) from 2003–2010. Whether due to changes in cultivation practice or crop failures, the VI curves change from bimodal (2003–2004) to unimodal (2005–2009) and back to bimodal (2010).

Some sites exhibited changes in seasonal pattern during the study period. We grouped the phenological patterns into three broad categories: no change, one change, or two changes (Figure 3-11 and Table A.2). Supplementary Figures S1–S49 illustrate the interannual variation of LSPs at each site. Those sites exhibiting only a single seasonal pattern (either unimodal or bimodal) throughout the study period were categorized as no change and totaled 33 sites (these were consistently unimodal seasonal pattern throughout

the study period). The seven sites that changed from unimodal to bimodal or from bimodal to unimodal were classified as one change. Finally, nine sites changes from one seasonal pattern to another and then back again (unimodal→bimodal→unimodal or bimodal→unimodal→bimodal) were classified as two changes. A geographic pattern of change in seasonal pattern is evident in Figure 3-11: only sites at the lower latitudes displayed any changes in seasonal pattern. Details are presented in Table A.2.

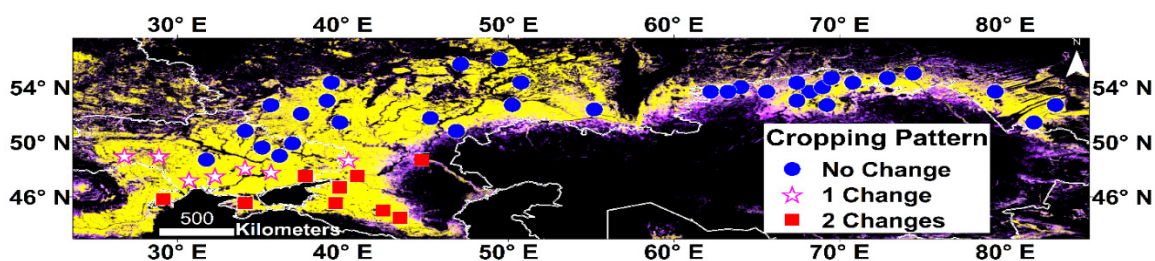
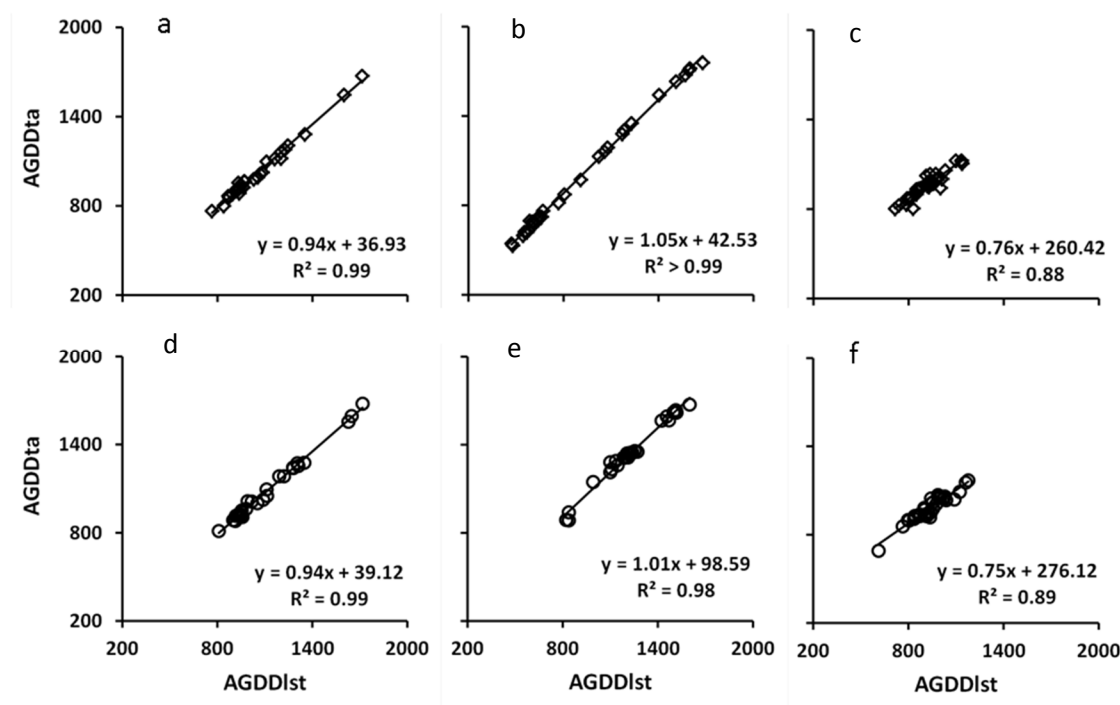


Figure 3-11. Changes in seasonal patterns by sites during 2003–2010: no change (blue circles), one change (white stars with pink borders), or two changes (red squares). Northern study sites displayed no change in seasonal pattern, while southern study sites experienced multiple changes.

Croplands in Ukraine exhibited a wider range of seasonal patterns: some sites changed from unimodal to bimodal (three sites), some from bimodal to unimodal (three sites), and some others from bimodal to unimodal and then back again (three sites; Table A.2). Croplands in southern parts of Russia similarly experienced a cycling of seasonal patterns: bimodal to unimodal (one site), bimodal→unimodal→bimodal (three sites) and unimodal→bimodal→unimodal (three sites). All sites in Kazakhstan retained the unimodal seasonal pattern throughout the study period.

### 3.3.2.4 Sensor-Specific Differences in Thermal Time to Peak VI

MODIS pixels within each AMSR-E pixel exhibit generally similar but distinct spatial and temporal thermal time patterns. MODIS and AMSR-E AGDDs at 95% of the initial peak VI values display a strong positive linear relationship across space and time with coefficients of determination ranging from 0.60 to 0.99 (Figure 3-12). This relationship was generally strong for the lower latitude sites compared to that of the higher latitudes. Although it could be expected that the VIs for each MODIS pixel are more related to the same pixel's LST. However, the strong correlation of the two sensors' AGDDs showed that the much coarser spatial resolution AMSR-E surface air temperature (ta) data did an excellent job of capturing the progress of finer spatial resolution MODIS VIs (Figure 3-12).



**Figure 3-12.** (a–f) Comparison of AMSR-E AGDDta at 95% of the initial peak VIs with the MODIS AGDDlst at 95% of the initial peak VIs in 2003. The panels span a

latitudinal gradient: lowest latitude (Cherkessk, Russia (**a,d**)), middle latitude (Sumy, Ukraine (**b,e**)), and highest latitude (Kazan', Russia (**c,f**)) for 95% of the initial peak NDVI (**a–c**) and EVI (**d–f**). There is strong linear relationship between AGDDs from AMSR-E and MODIS at 95% of initial peak VIs for these sites in 2003 with  $r^2$  ranging from 0.88 to  $>0.99$ . This strong positive relationship was consistent in space and time with  $r^2$  ranging from 0.60 to  $>0.99$  across all study sites and years.

### 3.4 Discussion

#### 3.4.1 Shifting Patterns of Cropping: Real or Illusory?

How do we interpret the apparent variation between double and single seasonal patterns that were evident in southern Ukraine and southern Russia? Note that the southern tier of the study region hosts winter crops and can also support spring crops. In Figure 3-10, fall green-up is evident in 2007 and 2008 due to winter crops. The 2003 European heat wave affected winter croplands in western and southern Ukraine (*De Bono et al., 2004*), while the 2007 Ukrainian heat wave devastated spring grains in 2007 (*Founda & Giannakopoulos, 2009*). These impacts are evident in the VI curves of Figure 3-10. Figures 3-8 to 3-10 give representative examples of land surface phenologies exhibiting unimodality and bimodality with variation in the placement of the single and double modes. Should we interpret a unimodal LSP as a single annual crop? Clearly, the answer is not always. The more northerly sites in Russia and Kazakhstan exhibit a single mode that peaks roughly mid-season (blue circles in Figure 3-11). These sites do have a single annual spring crop. In contrast, there are multiple instances of early season peaks, indicative of a winter crop, with no second peak, especially in the southern tier of the study region. These

patterns—such as seen for 2005–2009 in Figure 3-10—could indicate either changes in cultivation practices or crop failures.

A study of cropping frequency in European Russia found areas in southern Russia, e.g., Stavropol (site 2 in this study) and Saratov (sites 21 and 25) were successfully cropped during fewer years than areas located farther north in the grain belt, e.g., Cheboksary and Kazan (sites 48 and 49) (*de Beurs & Ioffe, 2014*). Lower cropping frequency was a result of longer fallowing periods and hotter, drier summer conditions. However, they also reported widespread shifts from cereals to soybean, sunflower, and rapeseed as well as changes in crop rotation periods, including changes in fallow periods (*de Beurs & Ioffe, 2014; Roland et al., 2015*). Changes have been occurring across this vast agricultural landscape, but the proximate causes of those changes may not be readily accessible to remote sensing (*de Beurs & Henebry, 2004; Henebry, 2009; Ioffe et al., 2014; Ioffe et al., 2012; Kamp et al., 2011; Kuemmerle et al., 2008; Schierhorn et al., 2013*). However, there is a rich set of variations in land surface phenologies across the study region through the study period that the AGDD based on the AMSR-E surface temperature data makes more readily apparent.

### **3.4.2 Growing Degree-Day Residuals Versus Vegetation Indices**

Rainfed croplands at mid-latitude croplands are thermally limited (*Nemani et al., 2003*); thus, vegetation dynamics are strongly linked to the seasonal progression of temperature. Residuals resulting from the comparison of average GDD as a convex quadratic function of AGDD with average GDD time series showed clear patterns associated with average VI time series for 2003–2010 across sites. Negative GDD

residuals occurred at times of higher VIs, presumably due to higher latent heat flux; whereas, positive GDD residuals corresponded to the times earlier and later in the growing season when VIs were low, presumably due to higher sensible heat flux.

For example, Figure 3-13a shows the average NDVI and average GDD residuals along with maximum and minimum values as error bars for six cropland sites and two cropland/natural vegetation mosaic sites both in Kazakhstan at a similar latitude. These sites show clear unimodality with the cropland/natural vegetation mosaic exhibiting distinctly higher VI earlier and later than in the croplands. However, the GDD residual patterns are comparable but have distinctive responses to a given heat accumulation. Figure 3-13b,c display the average NDVI and GDD residuals for the southernmost two sites that experienced bimodal and unimodal cropland pattern alternately: Figure 3-13b,c shows the average for the bimodal (unimodal) years. The bimodal seasonal pattern results in a more complicated relationship between NDVI and the GDD residuals compared to the sites with unimodal seasonal pattern.

These residuals appear to track the shift from sensible heat dominated surface flux to latent heat dominated surface flux due to canopy development back again to sensible heat dominance as the canopy fades later season. Note that these are not direct observations of the surface but, rather, the difference between the model of average GDD as a quadratic function of AGDD and the average AMSR-E GDD observations. The information embedded in the model lack of fit arises from changes in the surface condition, viz., transpiring vegetation, which affects the surface air temperature. That such a pattern can be sensed at the coarse spatial resolution of AMSR-E grid cells is

remarkable and points to the need for additional work to explore how much additional information can be gleaned from these time series. However, to stress again, these informative residuals result from “filtering” the time series using a CxQ model of GDD, which is, in turn, motivated by the widespread pattern observed in mid-latitude landscapes dominated by herbaceous vegetation (e.g., grasslands and croplands) that the surface air temperature is primarily driven by insolation (Jones et al., 2010).

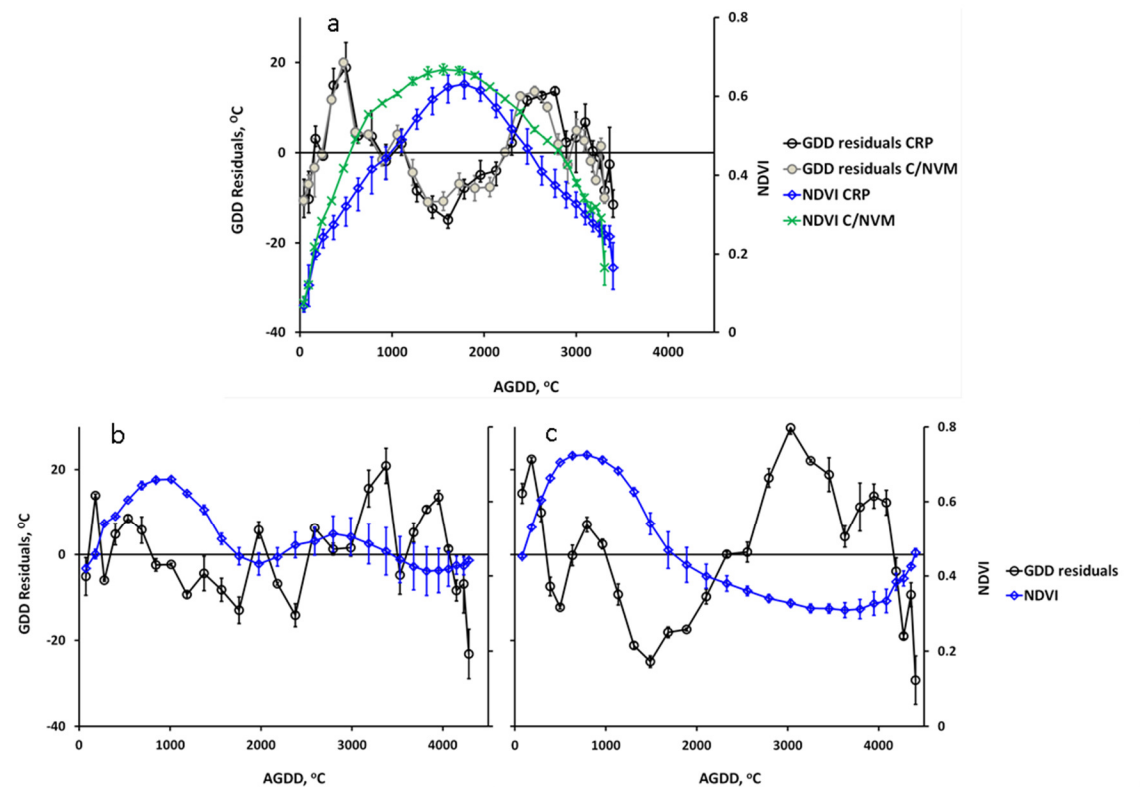


**Figure 3-13.** Average GDD residuals and NDVI with error bars displaying maxima and minima for sites at similar latitude. **(a)** Sites 35–37 and 39–41 in Kazakhstan (NDVI—blue triangles and GDD residuals—black diamonds) and sites 34 and 42 in Kazakhstan (NDVI—green crosses and GDD residuals—gray circles); and **(b,c)** sites 1 and 2 in Russia (NDVI—blue diamonds and GDD residuals—black circles) for selected bimodal cropland pattern years and unimodal years, respectively.



We have shown that the time series of residuals between observed GDDs and the GDDs predicted from the CxQ model can show distinct shifts in air temperature corresponding to the growth and development and eventual senescence of the vegetated canopy. Specifically, above average air temperatures (positive residuals) occur in the weeks prior to increasing vegetation indices, followed by below average temperatures (negative residuals) as the vegetation indices are near peak, and then back to above average temperatures during vegetation senescence. This sequence points to the detection of shifts in the surface energy balance from high values of the Bowen ratio ( $BR = \text{sensible heat flux/latent heat flux}$ ) to low and back again to high. More study is needed to see how far this provocative finding can be pushed. Is it apparent over land covers other than croplands or in other locations? How does it compare to both coarser and finer remote sensing data streams?

### **3.4.3 Heat Wave Impacts on LSPs**

The influence of two regional heat waves—the 2010 heat wave in Russia and Kazakhstan (Dole et al., 2011; Trenberth & Fasullo, 2012; Wright et al., 2014) and the 2007 heat wave in Ukraine (Founda & Giannakopoulos, 2009)—were evident in LSP patterns generated from the MODIS and AMSR-E data. Western Russia experienced an extraordinary heat wave in 2010, in which July was the warmest month since 1980 and numerous locations setting all-time maximum temperature records (Dole et al., 2011). The 2003 European heat wave affected western and southern Ukraine but was only slightly evident in the seasonal GDD pattern and not in its accumulation (De Bono et al.,

2004). Winter grains of croplands in those areas appeared affected, displaying lower VI peaks for winter grains but higher VI peaks for spring grains.

For example, Figure 3-14 presented sample areas that combine GDD and VIs. GDD and VIs for the 2010 and 2007 heat wave years and average years for the same place are presented. During the average years, peak NDVIs and EVIs were above 0.60 and 0.35, respectively, while these peaks were attained at about 1230 °C AGDD for Kuybuskev 2 (Russia) and 960 °C AGDD for Mykolayive (Ukraine) (Table 3-6). Peak GDD for these sites was below 200 °C, which is equivalent to a daily average of ~25 °C over 8 days). In contrast, during the heat wave years, the maximum attained NDVIs and EVIs were below 0.50 and 0.25, respectively, while these maxima were attained earlier at about 960 °C AGDD for Kuybuskev 2 and 660 °C AGDD for Mykolayive. Peak GDD for these sites was at about 250 °C ( $\approx 31$  °C average daily GDD), well above the average years' peak GDD. Crops were devastated by the heat waves before maturity resulting in crop production very much reduced compared to cooler, wetter years (Grumm, 2011).

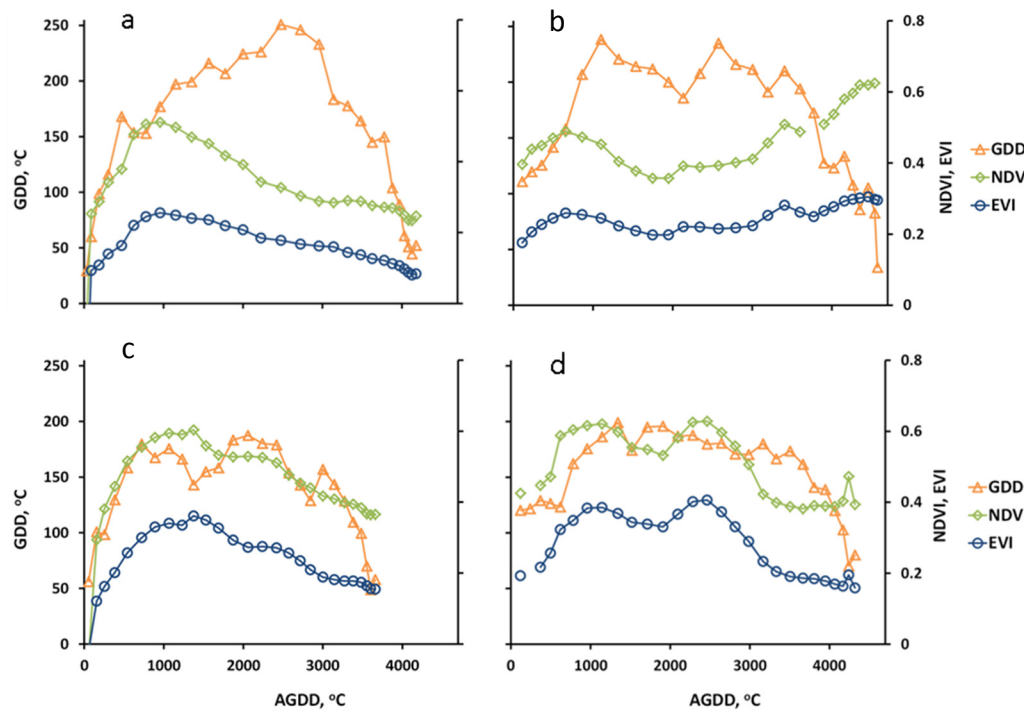


**Figure 3-14.** Comparison of VIs and GDD at similar places during heat wave years (Kuybuskev 2 (a), Russia in 2010 and Mykolayive (b), Ukraine in 2007) and average years (Kuybuskev 2 (c), Russia in 2005 and Mykolayive (d), Ukraine in 2009). N.B: GDDs are eight-day sums.

**Table 3-6.** Peak GDDs and VIs and corresponding AGDDs during heat wave years and average years at two representative sites.

Site	Weather	Metric	1st Peak		2nd Peak	
			Value	AGDD	Value	AGDD
Kuybyshev_2, RU	Average	GDD	180.00	722	190.00	2060
		NDVI	0.59	1230		
		EVI	0.34	1230		
Kuybyshev_2, RU	Heat wave	GDD	250.00	2480		
		NDVI	0.51	960		
		EVI	0.26	960		
Mykolayiv, UA	Average	GDD	196.00	1910		
		NDVI	0.62	960	0.63	2460
		EVI	0.38	960	0.41	2460
Mykolayiv, UA	Heat wave	GDD	240.00	1100	230.00	2580
		NDVI	0.49	660		
		EVI	0.26	660		

We grouped sites by the effects of the 2007 and 2010 major heat waves into four categories: (a) affected only in 2010; (b) affected only in 2007; (c) affected in both years; and (d) affected in neither year (Figure 3-15). The northern portion of the study region (both Russia and Kazakhstan) was strongly affected by the exceptional 2010 heat wave, southern Russia and eastern Ukraine croplands were affected by both heat waves, the southern portion of Ukraine was affected only by the 2007 heat wave, and some parts of western Ukraine, eastern and southern Russia were affected by neither heat wave. The heat wave affected areas exhibited AGDD time series were consistently higher than the other years (data not shown). Crop production was devastated in areas that were affected by these heat waves (Founda & Giannakopoulos, 2009; Trenberth & Fasullo, 2012).

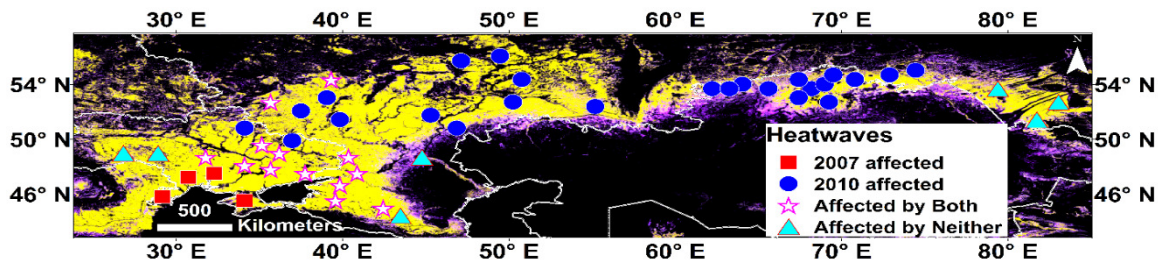


**Figure 3-15.** Sites affected by: the 2010 heat wave (blue circles), the 2007 heat wave (red squares), both the 2010 and 2007 heat waves (white stars with pink borders), and sites affected by neither the 2010 nor the 2007 heat wave (cyan triangles).

### 3.5 Conclusions

Although the spatial resolution of AMSR-E data appears coarse relative to imaging sensors, having a time series of surface air temperature every 25 km translates into a significant increase in spatial coverage over the weather station networks in most countries in the world, including developing nations that do not have dense networks of meteorological stations. Moreover, due to the long wavelengths of the microwaves, cloudiness does not pose the problem it does at the much shorter wavelengths of the thermal infrared. Instead, data gaps arise over frozen surfaces, during very heavy precipitation events, as a result of radio frequency interference over some parts of the planet, and due to orbital paths. Simple retrospective smoothing of the AMRS-E data yielded air temperature time series that compared well with ground observations. In the past AGDD has been calculated from meteorological station data (point coverage), meteorological station reanalysis (moderate to coarse spatial resolution), model reanalysis (very coarse spatial resolution), and thermal remote sensing data (moderate spatial resolution but temporally composited). The balance of coarse spatial resolution with high

temporal resolution, due to the availability of nighttime acquisitions and cloud penetration, makes the AMSR-E data attractive as an additional source of surface air temperature data.

We have demonstrated that the surface air temperature data retrieved from a passive microwave radiometer (AMSR-E) agrees well with the weekly, monthly, and seasonal oscillations of meteorological station air temperature data. AMSR-E GDD also showed lower RMSD from station GDD compared to the corresponding MODIS GDD. Both GDDs from AMSR-E and MODIS showed strong correlation with station air temperature GDD with slight superiority of the AMSR-E GDD, but with significantly different fit in some sites and not in some other. Further study using more station data is needed to conclude whether the agreement between the AMSR-E GDDs and the station GDDs significantly differs from agreement between the MODIS GDDs and the station GDDs.

We have demonstrated the temporal relationship between GDD and AGDD from AMSR-E could be parsimoniously represented using a simple parametric convex quadratic (CxQ) model, which is particularly helpful to portray a climatology. Moreover, this relationship has a clear geographic pattern in mid-latitude croplands: decreasing thermal time to peak GDD ( $TTP_{GDD}$ ) as latitude increases. This concise parametric representation of the expected progression of thermal time may offer some advantages in modeling vegetation growth and development.

We have shown how the AGDD can be combined with vegetation indices from MODIS to illustrate land surface phenology (LSP). What is new here is not that the CxQ

model works for LSP—that has been shown many times before (Alemu & Henebry, 2013; de Beurs & Henebry, 2004, 2008a, 2010; Goodin & Henebry, 1997; Henebry, 2013; Henebry & de Beurs, 2013; Still et al., 2014)—but rather that the surface air temperature data from a passive microwave source can be used to calculate the AGDD, which can, in turn, be used to model VIs from the moderate spatial resolution sensor MODIS.

AMSR-E failed in October 2011. AMSR-2 is onboard the Global Change Observations Mission 1st-Water (GCOM-W1), renamed SHIZUKU. It was launched in May 2012 by the Japan Aerospace Exploration Agency (JAXA). Data products were released to the public in May 2013 (<https://gcom-w1.jaxa.jp/>). AMSR-2 is the improved version of AMSR-E that has similar functionality and data products. The NTSG group has continued the production of the enhanced land parameters using the AMSR-2 data streams ([ftp://ftp.ntsg.umd.edu/pub/data/AMSR\\_Results/AMSR\\_E\\_2/](ftp://ftp.ntsg.umd.edu/pub/data/AMSR_Results/AMSR_E_2/)) as well as filled the data gap using a Chinese microwave radiometer (Du et al., 2015; Du et al., 2014). Thus, the continued relevance of this approach is assured for the next several years, at least.

The failure of the radar in NASA's Soil Moisture Active Passive (SMAP) mission during the summer of 2015 has refocused attention on the L-band passive radiometer data that has a 36 km resolution. While L-band seems too long a wavelength to detect crop dynamics, it should work well for soil moisture monitoring as well as potentially providing insight on land surface dynamics in ecosystems dominated by woody species.

The approach developed here may also find traction with the L-band data, if it can be blended with the AMSR-2 data.

Finally, although this paper has focused on the use of the air temperature data from AMSR-E, there is another variable from the NTSG's dataset that is relevant to vegetation dynamics, the vegetation optical depth (VOD), which is a microwave analog to the NDVI. In a similar manner to the way that the NDVI and other vegetation indices look at the differential absorption of sunlight by green vegetation, the VOD looks at the absorption of earthlight (at specific microwave frequencies) by the water-laden vegetation canopy. It is beyond the scope of this paper to detail how VODs can describe the temporal development of the vegetated land surface, but we will describe our finding for VOD dynamics in the same region in a future paper.

Although there has traditionally been little overlap between the microwave and VNIR communities, the time has come to explore the synergistic use of reflected sunlight and transmitted earthlight for potential applications in agricultural monitoring, natural resource management, ecosystems ecology, and earth system science.

### **3.6 Acknowledgements**

This research was supported in part through the NASA Earth and Space Sciences Fellowship program (NNX13AN58H), and NASA LCLUC (NNX11AB77G) and Science of Terra and Aqua (NNX14AJ32G) programs. The AMSR-E data were accessed from Numerical Terradynamic Simulation Group (NTSG) website ([www.ntsg.umt.edu/project/amsrelp](http://www.ntsg.umt.edu/project/amsrelp)). The MODIS data were obtained from the NASA/USGS Land Processes Distributed Active Archive Center (LP DAAC)



([https://lpdaac.usgs.gov/products/modis\\_products\\_table](https://lpdaac.usgs.gov/products/modis_products_table)). We thank the four anonymous reviewers for their constructive comments that improved the clarity of the presentation.

### 3.7 Author Contributions

W.G.A. and G.M.H conceived and designed the experiments; W.G.A. performed the experiments; W.G.A. and G.M.H. analyzed the data; and W.G.A. and G.M.H. wrote the paper.

### 3.8 Conflicts of Interest

The authors declare no conflicts of interest.

### 3.9 References

- Alemu, W. G., & Henebry, G. M. (2013). Land surface phenologies and seasonalities using cool earthlight in mid-latitude croplands. *Environmental Research Letters*, 8(4). doi: <http://dx.doi.org/10.1088/1748-9326/8/4/045002>
- Asseng, S., Foster, I., & Turner, N. C. (2011). The impact of temperature variability on wheat yields. *Global Change Biology*, 17(2), 997-1012. doi: <http://dx.doi.org/10.1111/j.1365-2486.2010.02262.x>
- Becker-Reshef, I., Justice, C., Sullivan, M., Vermote, E., Tucker, C., Anyamba, A., Small, J., Pak, E., Masuoka, E., Schmaltz, J., Hansen, M., Pittman, K., Birkett, C., Williams, D., Reynolds, C., & Doorn, B. (2010). Monitoring Global Croplands with Coarse Resolution Earth Observations: The Global Agriculture Monitoring

(GLAM) Project. *Remote Sensing*, 2(6), 1589. doi: <http://www.mdpi.com/2072-4292/2/6/1589>

Benedetti, R., & Rossini, P. (1993). On the Use of NDVI Profiles as a Tool for Agricultural Statistics - the Case-Study of Wheat Yield Estimate and Forecast in Emilia-Romagna. *Remote Sensing of Environment*, 45(3), 311-326. doi: [http://dx.doi.org/10.1016/0034-4257\(93\)90113-C](http://dx.doi.org/10.1016/0034-4257(93)90113-C)

Bolton, D. K., & Friedl, M. A. (2013). Forecasting crop yield using remotely sensed vegetation indices and crop phenology metrics. *Agricultural and Forest Meteorology*, 173(0), 74-84. doi: <http://dx.doi.org/10.1016/j.agrformet.2013.01.007>

Boschetti, M., Stroppiana, D., Brivio, P. A., & Bocchi, S. (2009). Multi-year monitoring of rice crop phenology through time series analysis of MODIS images. *International Journal of Remote Sensing*, 30(18), 4643-4662. doi: <http://dx.doi.org/10.1080/01431160802632249>

Czerwinski, C. J., King, D. J., & Mitchell, S. W. (2014). Mapping forest growth and decline in a temperate mixed forest using temporal trend analysis of Landsat imagery, 1987–2010. *Remote Sensing of Environment*, 141(0), 188-200. doi: <http://dx.doi.org/10.1016/j.rse.2013.11.006>

DAAC-LP. (2014). MODIS Products Table doi: [https://lpdaac.usgs.gov/dataset\\_discovery/modis/modis\\_products\\_table](https://lpdaac.usgs.gov/dataset_discovery/modis/modis_products_table). Retrieved 16, April 2014, from Land Processes Distributed Active Archive Center [https://lpdaac.usgs.gov/dataset\\_discovery/modis/modis\\_products\\_table](https://lpdaac.usgs.gov/dataset_discovery/modis/modis_products_table)

- de Beurs, K. M., & Henebry, G. M. (2004). Land surface phenology, climatic variation, and institutional change: Analyzing agricultural land cover change in Kazakhstan. *Remote Sensing of Environment*, 89(4), 497-509. doi:  
<http://dx.doi.org/10.1016/j.rse.2003.11.006>
- de Beurs, K. M., & Henebry, G. M. (2008). Northern Annular Mode Effects on the Land Surface Phenologies of Northern Eurasia. *Journal of Climate*, 21(17), 4257-4279. doi: <http://dx.doi.org/10.1175/2008jcli2074.1>
- de Beurs, K. M., & Henebry, G. M. (2010). Spatio-Temporal Statistical Methods for Modelling Land Surface Phenology. In I. L. Hudson & M. R. Keatley (Eds.), *Phenological Research: Methods for Environmental and Climate Change Analysis* (2nd edition ed., [http://dx.doi.org/10.1007/978-90-481-3335-2\\_9pp](http://dx.doi.org/10.1007/978-90-481-3335-2_9pp). 177-208). Dordrecht: Springer Netherlands.
- de Beurs, K. M., & Ioffe, G. (2014). Use of Landsat and MODIS data to remotely estimate Russia's sown area. *Journal of Land Use Science*, 9(4), 377-401. doi: 10.1080/1747423X.2013.798038
- De Bono, A., Peduzzi, P., Kluser, S., & Giuliani, G. (2004). *Impacts of Summer 2003 Heat Wave in Europe*. Geneva, Switzerland: UNEP/DEWA/GRID-Europe  
Retrieved from <http://archive-ouverte.unige.ch/unige:32255>.
- Dole, R., Hoerling, M., Perlwitz, J., Eischeid, J., Pegion, P., Zhang, T., Quan, X.-W., Xu, T., & Murray, D. (2011). Was there a basis for anticipating the 2010 Russian heat wave? *Geophysical Research Letters*, 38(6), L06702. doi:  
<http://dx.doi.org/10.1029/2010GL046582>

- Doraiswamy, P. C., Hatfield, J. L., Jackson, T. J., Akhmedov, B., Prueger, J., & Stern, A. (2004). Crop condition and yield simulations using Landsat and MODIS. *Remote Sensing of Environment*, 92(4), 548-559. doi: <http://dx.doi.org/10.1016/j.rse.2004.05.017>
- Du, J., Kimball, J. S., & Jones, L. A. (2015). Satellite Microwave Retrieval of Total Precipitable Water Vapor and Surface Air Temperature Over Land From AMSR2. *IEEE Transactions on Geoscience and Remote Sensing*, 53(5), 2520-2531. doi: <http://dx.doi.org/10.1109/TGRS.2014.2361344>
- Du, J., Kimball, J. S., Shi, J., Jones, L. A., Wu, S., Sun, R., & Yang, H. (2014). Inter-Calibration of Satellite Passive Microwave Land Observations from AMSR-E and AMSR2 Using Overlapping FY3B-MWRI Sensor Measurements. *Remote Sensing*, 6(9), 8594-8616. doi: <http://dx.doi.org/10.3390/rs6098594>
- Fang, H., Liang, S., & Hoogenboom, G. (2011). Integration of MODIS LAI and vegetation index products with the CSM–CERES–Maize model for corn yield estimation. *International Journal of Remote Sensing*, 32(4), 1039-1065. doi: <http://dx.doi.org/10.1080/01431160903505310>
- FEWS-NET. (2014). USGS FEWS NET Data Portal. Retrieved February 15, 2014, from <http://earlywarning.usgs.gov/fews>
- Founda, D., & Giannakopoulos, C. (2009). The exceptionally hot summer of 2007 in Athens, Greece — A typical summer in the future climate? *Global and Planetary Change*, 67(3-4), 227-236. doi: <http://dx.doi.org/10.1016/j.gloplacha.2009.03.013>

- Friedl, M. A., Sulla-Menashe, D., Tan, B., Schneider, A., Ramankutty, N., Sibley, A., & Huang, X. M. (2010). MODIS Collection 5 global land cover: Algorithm refinements and characterization of new datasets. *Remote Sensing of Environment*, *114*(1), 168-182. doi: <http://dx.doi.org/10.1016/j.rse.2009.08.016>
- Funk, C., & Budde, M. E. (2009). Phenologically-tuned MODIS NDVI-based production anomaly estimates for Zimbabwe. *Remote Sensing of Environment*, *113*(1), 115-125. doi: <http://dx.doi.org/10.1016/j.rse.2008.08.015>
- Gitelson, A. A. (2004). Wide Dynamic Range Vegetation Index for remote quantification of biophysical characteristics of vegetation. *Journal of Plant Physiology*, *161*(2), 165-173. doi: <http://dx.doi.org/10.1078/0176-1617-01176>
- Goodin, D. G., & Henebry, G. M. (1997). A technique for monitoring ecological disturbance in tallgrass prairie using seasonal NDVI trajectories and a discriminant function mixture model. *Remote Sensing of Environment*, *61*(2), 270-278. doi: [http://dx.doi.org/10.1016/S0034-4257\(97\)00043-6](http://dx.doi.org/10.1016/S0034-4257(97)00043-6)
- Gordon, R., & Bootsma, A. (1993). Analyses of growing degree-days for agriculture in Atlantic Canada. *Climate Research*, *3*, 169-176.
- Grumm, R. H. (2011). The Central European and Russian Heat Event of July–August 2010 *Bulletin of the American Meteorological Society* (Vol. 92, pp. 1285-1296): American Meteorological Society.
- Gumma, M. K., Nelson, A., Thenkabail, P. S., & Singh, A. N. (2011). Mapping rice areas of South Asia using MODIS multitemporal data. *Journal of Applied Remote Sensing*, *5*(1), 053547-053547-053526. doi: <http://dx.doi.org/10.1117/1.3619838>

- Hassan, Q. K., Bourque, C. P. A., & Meng, F. R. (2007). Application of Landsat-7 ETM+ and MODIS products in mapping seasonal accumulation of growing degree days at an enhanced resolution. *Journal of Applied Remote Sensing*, 1(1), 013539-013539. doi: <http://dx.doi.org/10.1117/1.2800284>
- Henebry, G. M. (2009). Global change: Carbon in idle croplands. *Nature*, 457(7233), 1089-1090. doi: <http://dx.doi.org/10.1038/4571089a>
- Henebry, G. M. (2013). Phenologies of North American Grasslands and Grasses. In M. D. Schwartz (Ed.), *Phenology: An Integrative Environmental Science* ([http://dx.doi.org/10.1007/978-94-007-6925-0\\_11](http://dx.doi.org/10.1007/978-94-007-6925-0_11)pp. 197-210). Netherlands: Springer.
- Henebry, G. M., & de Beurs, K. M. (2013). Remote Sensing of Land Surface Phenology: A Prospectus. In M. D. Schwartz (Ed.), *Phenology: An Integrative Environmental Science* ([http://dx.doi.org/10.1007/978-94-007-6925-0\\_21](http://dx.doi.org/10.1007/978-94-007-6925-0_21)pp. 385-411). Dordrecht: Springer Netherlands.
- Henebry, G. M., de Beurs, K. M., Wright, C. K., Ranjeet, J., & Lioubimtseva, E. (2013). Dryland East Asia in Hemispheric Context. In J. Chen, et al. (Eds.), *Dryland East Asia: Land Dynamics amid Social and Climate Change* (<http://dx.doi.org/10.1515/9783110287912.23>pp. 23-43). Berlin/Boston: Higher Education Press and Walter de Gruyter GmbH.
- Huete, A., Didan, K., Miura, T., Rodriguez, E. P., Gao, X., & Ferreira, L. G. (2002). Overview of the radiometric and biophysical performance of the MODIS

- vegetation indices. *Remote Sensing of Environment*, 83(1-2), 195-213. doi:  
[http://dx.doi.org/10.1016/S0034-4257\(02\)00096-2](http://dx.doi.org/10.1016/S0034-4257(02)00096-2)
- Ioffe, G., Nefedova, T., & de Beurs, K. (2014). Agrarian transformation in the Russian breadbasket: contemporary trends as manifest in Stavropol'. *Post-Soviet Affairs*, 30(6), 441-463. doi: 10.1080/1060586X.2013.858509
- Ioffe, G., Nefedova, T., & Kirsten, D. B. (2012). Land Abandonment in Russia. *Eurasian Geography and Economics*, 53(4), 527-549. doi: 10.2747/1539-7216.53.4.527
- Jones, L. A., Ferguson, C. R., Kimball, J. S., Zhang, K., Chan, S. T. K., McDonald, K. C., Njoku, E. G., & Wood, E. F. (2010). Satellite Microwave Remote Sensing of Daily Land Surface Air Temperature Minima and Maxima From AMSR-E. *IEEE Journal of Selected Topics in Applied Earth Observations and Remote Sensing*, 3(1), 111-123. doi: <http://dx.doi.org/10.1109/Jstars.2010.2041530>
- Jones, L. A., & Kimball, J. S. (2011). Daily Global Land Surface Parameters Derived from AMSR-E. Boulder Colorado USA: National Snow and Ice Data Center. *Digital media* (<http://nsidc.org/data/nsidc-0451.html>).
- Jones, M. O., Jones, L. A., Kimball, J. S., & McDonald, K. C. (2011). Satellite passive microwave remote sensing for monitoring global land surface phenology. *Remote Sensing of Environment*, 115(4), 1102-1114. doi:  
<http://dx.doi.org/10.1016/j.rse.2010.12.015>
- Jones, M. O., Kimball, J. S., Jones, L. A., & McDonald, K. C. (2012). Satellite passive microwave detection of North America start of season. *Remote Sensing of Environment*, 123, 324-333. doi: <http://dx.doi.org/10.1016/j.rse.2012.03.025>

- Kamp, J., Urazaliev, R., Donald, P. F., & Hölzel, N. (2011). Post-Soviet agricultural change predicts future declines after recent recovery in Eurasian steppe bird populations. *Biological Conservation*, *144*(11), 2607-2614. doi: <http://dx.doi.org/10.1016/j.biocon.2011.07.010>
- Kuemmerle, T., Hostert, P., Radeloff, V. C., van der Linden, S., Perzanowski, K., & Kruhlov, I. (2008). Cross-border Comparison of Post-socialist Farmland Abandonment in the Carpathians. *Ecosystems*, *11*(4), 614-628. doi: [10.1007/s10021-008-9146-z](https://doi.org/10.1007/s10021-008-9146-z)
- Lindeman, M. (2014). Ukraine: Crop Production Forecasts for 2014/15. Retrieved 10-29-2015, 2015, from <http://www.fas.usda.gov/data/ukraine-crop-production-forecasts-201415>
- Lioubimtseva, E., & Henebry, G. M. (2012). Grain production trends in Russia, Ukraine and Kazakhstan: New opportunities in an increasingly unstable world? *Frontiers of Earth Science*, *6*(2), 157-166. doi: <http://dx.doi.org/10.1007/s11707-012-0318-y>
- Liu, Y. Y., van Dijk, A. I. J. M., McCabe, M. F., Evans, J. P., & de Jeu, R. A. M. (2013). Global vegetation biomass change (1988-2008) and attribution to environmental and human drivers. *Global Ecology and Biogeography*, *22*(6), 692-705. doi: <http://dx.doi.org/10.1111/geb.12024>
- Los, S. O., Collatz, G. J., Bounoua, L., Sellers, P. J., & Tucker, C. J. (2001). Global interannual variations in sea surface temperature and land surface vegetation, air



- temperature, and precipitation. *Journal of Climate*, 14(7), 1535-1549. doi:  
[http://dx.doi.org/10.1175/1520-0442\(2001\)014<1535:Giviss>2.0.Co;2](http://dx.doi.org/10.1175/1520-0442(2001)014<1535:Giviss>2.0.Co;2)
- Maselli, F., Conese, C., Petkov, L., & Gilabert, M. A. (1992). Use of NOAA-AVHRR NDVI Data for Environmental Monitoring and Crop Forecasting in the Sahel - Preliminary-Results. *International Journal of Remote Sensing*, 13(14), 2743-2749. doi: <http://dx.doi.org/10.1080/01431169208904076>
- McMaster, G. S. (2005). Phytomers, phyllochrons, phenology and temperate cereal development. *Journal of Agricultural Science*, 143(2-3), 137-150. doi:  
<http://dx.doi.org/10.1017/S0021859605005083>
- McMaster, G. S., & Wilhelm, W. W. (1997). Growing degree-days: one equation, two interpretations. *Agricultural and Forest Meteorology*, 87(4), 291-300. doi:  
[http://dx.doi.org/10.1016/S0168-1923\(97\)00027-0](http://dx.doi.org/10.1016/S0168-1923(97)00027-0)
- Mkhabela, M. S., Bullock, P., Raj, S., Wang, S., & Yang, Y. (2011). Crop yield forecasting on the Canadian Prairies using MODIS NDVI data. *Agricultural and Forest Meteorology*, 151(3), 385-393. doi:  
<http://dx.doi.org/10.1016/j.agrformet.2010.11.012>
- Moriondo, M., Maselli, F., & Bindi, M. (2007). A simple model of regional wheat yield based on NDVI data. *European Journal of Agronomy*, 26(3), 266-274. doi:  
<http://dx.doi.org/10.1016/j.eja.2006.10.007>
- Morisette, J. T., Richardson, A. D., Knapp, A. K., Fisher, J. I., Graham, E. A., Abatzoglou, J., Wilson, B. E., Breshears, D. D., Henebry, G. M., Hanes, J. M., & Liang, L. (2009). Tracking the rhythm of the seasons in the face of global change:

- phenological research in the 21st century. *Frontiers in Ecology and the Environment*, 7(5), 253-260. doi: <http://dx.doi.org/10.1890/070217>
- Nemani, R. R., Keeling, C. D., Hashimoto, H., Jolly, W. M., Piper, S. C., Tucker, C. J., Myneni, R. B., & Running, S. W. (2003). Climate-Driven Increases in Global Terrestrial Net Primary Production from 1982 to 1999. *Science*, 300(5625), 1560-1563. doi: <http://science.sciencemag.org/content/300/5625/1560.abstract>
- Neteler, M. (2010). Estimating Daily Land Surface Temperatures in Mountainous Environments by Reconstructed MODIS LST Data. *Remote Sensing*, 2(1), 333-351. doi: <http://dx.doi.org/10.3390/Rs1020333>
- Owen, S. V., & Froman, R. D. (1998). Focus on qualitative methods uses and abuses of the analysis of covariance. *Research in nursing and health*, 21(6), 557-562.
- Piper, S. C., & Stewart, E. F. (1996). A gridded global data set of daily temperature and precipitation for terrestrial biospheric modeling. *Global Biogeochemical Cycles*, 10(4), 757-782. doi: <http://dx.doi.org/10.1029/96GB01894>
- Pitt, M. D., & Heady, H. F. (1978). Responses of Annual Vegetation to Temperature and Rainfall Patterns in Northern California. *Ecology*, 59(2), 336. doi: <http://dx.doi.org/10.2307/1936378>
- Rasmussen, M. S. (1992). Assessment of Millet Yields and Production in Northern Burkina-Faso Using Integrated NDVI from the AVHRR. *International Journal of Remote Sensing*, 13(18), 3431-3442. doi: <http://dx.doi.org/10.1080/01431169208904132>

- Raun, W. R., Solie, J. B., Johnson, G. V., Stone, M. L., Lukina, E. V., Thomason, W. E., & Schepers, J. S. (2001). In-season prediction of potential grain yield in winter wheat using canopy reflectance. *Agronomy Journal*, *93*(1), 131-138. doi: <http://dx.doi.org/10.2134/agronj2001.931131x>
- Ritchie, J. T., & NeSmith, D. S. (1991). Temperature and crop development. In R. J. Hanks & J. T. Ritchie (Eds.), *Modeling Plant and Soil Systems* (Vol. Agronomy Monograph 31, pp. 5-29): American Society of Agronomy, Crop Science Society of America, Soil Science Society of America.
- Rojas, O., Vrieling, A., & Rembold, F. (2011). Assessing drought probability for agricultural areas in Africa with coarse resolution remote sensing imagery. *Remote Sensing of Environment*, *115*(2), 343-352. doi: <http://dx.doi.org/10.1016/j.rse.2010.09.006>
- Roland, K., Alexander, V. P., Daniel, M., Tobias, K., Volker, C. R., Andrey, D., Alexey, T., & Manfred, F. (2015). Long-term agricultural land-cover change and potential for cropland expansion in the former Virgin Lands area of Kazakhstan. *Environmental Research Letters*, *10*(5), 054012. doi: <http://stacks.iop.org/1748-9326/10/i=5/a=054012>
- Sarma, A., Kumar, T. V. L., & Koteswararao, K. (2008). Development of an agroclimatic model for the estimation of rice yield. *Journal of Indian Geophysical Union*, *12*(2), 89-96. doi: <http://igu.in/12-2/4sarma.pdf>
- Schaaf, C. B., Gao, F., Strahler, A. H., Lucht, W., Li, X. W., Tsang, T., Strugnell, N. C., Zhang, X. Y., Jin, Y. F., Muller, J. P., Lewis, P., Barnsley, M., Hobson, P.,

- Disney, M., Roberts, G., Dunderdale, M., Doll, C., d'Entremont, R. P., Hu, B. X., Liang, S. L., Privette, J. L., & Roy, D. (2002). First operational BRDF, albedo Nadir reflectance products from MODIS. *Remote Sensing of Environment*, 83(1-2), 135-148. doi: [http://dx.doi.org/10.1016/S0034-4257\(02\)00091-3](http://dx.doi.org/10.1016/S0034-4257(02)00091-3)
- Schierhorn, F., Müller, D., Beringer, T., Prishchepov, A. V., Kuemmerle, T., & Balmann, A. (2013). Post-Soviet cropland abandonment and carbon sequestration in European Russia, Ukraine, and Belarus. *Global Biogeochemical Cycles*, 27(4), 1175-1185. doi: 10.1002/2013GB004654
- Sobolev, D. (2015). Grain and Feed Update: Ukraine (doi: [http://gain.fas.usda.gov/Recent%20GAIN%20Publications/Grain%20and%20Feed%20Update\\_Kiev\\_Ukraine\\_10-5-2015.pdf](http://gain.fas.usda.gov/Recent%20GAIN%20Publications/Grain%20and%20Feed%20Update_Kiev_Ukraine_10-5-2015.pdf) pp. 15). USA: USDA Foreign Agricultural Service.
- Still, C. J., Pau, S., & Edwards, E. J. (2014). Land surface skin temperature captures thermal environments of C3 and C4 grasses. *Global Ecology and Biogeography*, 23(3), 286-296. doi: 10.1111/geb.12121
- Teal, R. K., Tubana, B., Girma, K., Freeman, K. W., Arnall, D. B., Walsh, O., & Raun, W. R. (2006). In-season prediction of corn grain yield potential using Normalized Difference Vegetation Index. *Agronomy Journal*, 98(6), 1488-1494. doi: <http://dx.doi.org/10.2134/agronj2006.0103>
- Thenkabail, P., GangadharaRao, P., Biggs, T., Krishna, M., & Turrall, H. (2007). Spectral matching techniques to determine historical land-use/land-cover (LULC) and irrigated areas using time-series 0.1-degree AVHRR Pathfinder datasets.

- Photogrammetric Engineering and Remote Sensing*, 73(10), 1029-1040. doi:  
[http://info.asprs.org/publications/pers/2007journal/september/2007\\_sep\\_1029-1040.pdf](http://info.asprs.org/publications/pers/2007journal/september/2007_sep_1029-1040.pdf)
- Thenkabail, P., Lyon, J. G., Turrall, H., & Biradar, C. (2009). *Remote sensing of global croplands for food security*. USA: CRC Press.
- Trenberth, K. E., & Fasullo, J. T. (2012). Climate extremes and climate change: The Russian heat wave and other climate extremes of 2010. *Journal of Geophysical Research, Atmospheres*, 117(D17), D171103. doi:  
<http://dx.doi.org/10.1029/2012jd018020>
- Tucker, C. J. (1979). Red and photographic Infrared linear combinations for monitoring vegetation. *Remote Sensing of Environment*, 8(2), 127-150. doi:  
[http://dx.doi.org/10.1016/0034-4257\(79\)90013-0](http://dx.doi.org/10.1016/0034-4257(79)90013-0)
- USDA-FAS. (2011a). Kazakhstan - Crop Production Maps. Retrieved February 15, 2014, from [http://www.pecad.fas.usda.gov/rssiws/al/kz\\_cropprod.htm](http://www.pecad.fas.usda.gov/rssiws/al/kz_cropprod.htm)
- USDA-FAS. (2011b). Russia - Crop Production Maps. Retrieved February 15, 2014, from [http://www.pecad.fas.usda.gov/rssiws/al/rs\\_cropprod.htm](http://www.pecad.fas.usda.gov/rssiws/al/rs_cropprod.htm)
- USDA-FAS. (2011c). Ukraine - Crop Production Maps. Retrieved February 15, 2014, from [http://www.pecad.fas.usda.gov/rssiws/al/up\\_cropprod.htm](http://www.pecad.fas.usda.gov/rssiws/al/up_cropprod.htm)
- USDA-FAS. (2015). *U.S. Department of Agriculture Foreign Agricultural Service Strategic Plan FY 2015-2018*.
- Viña, A., Gitelson, A. A., Rundquist, D. C., Keydan, G., Leavitt, B., & Schepers, J. (2004a). Monitoring Maize (*Zea mays* L.) Phenology with Remote Sensing.

*Agronomy Journal*, [http://dx.doi.org/10.2134/agronj2004.1139\(4\)](http://dx.doi.org/10.2134/agronj2004.1139(4)), 1139-1147.

doi: <http://dx.doi.org/10.2134/agronj2004.1139>

Viña, A., Henebry, G. M., & Gitelson, A. A. (2004b). Satellite monitoring of vegetation dynamics: Sensitivity enhancement by the wide dynamic range vegetation index.

*Geophysical research letters*, 31(4).

Wang, J., Price, K. P., & Rich, P. M. (2001). Spatial patterns of NDVI in response to precipitation and temperature in the central Great Plains. *International Journal of Remote Sensing*, 22(18), 3827-3844. doi:

<http://dx.doi.org/10.1080/01431160010007033>

<http://dx.doi.org/10.1080/01431160010007033>

Wang, X., Piao, S., Ciais, P., Li, J., Friedlingstein, P., Koven, C., & Chen, A. (2011, Jan 25). *Spring temperature change and its implication in the change of vegetation growth in North America from 1982 to 2006*. Paper presented at the Proceedings of the National Academy of Sciences U S A.

Wardlow, B., Egbert, S., & Kastens, J. (2007). Analysis of time-series MODIS 250 m vegetation index data for crop classification in the U.S. Central Great Plains.

*Remote Sensing of Environment*, 108(3), 290-310. doi:

<http://dx.doi.org/10.1016/j.rse.2006.11.021>

Whitney, M. (2014). World Wheat Production Forecast Raised on EU to Ukraine.

Retrieved 10 February, 2015, from

<http://www.bloomberg.com/news/articles/2014-09-25/world-wheat-production-forecast-raised-on-eu-to-ukraine>

- Wright, C. K., de Beurs, K. M., & Henebry, G. M. (2014). Land surface anomalies preceding the 2010 Russian heat wave and a link to the North Atlantic oscillation. *Environmental Research Letters*, 9(12), 124015. doi: <http://dx.doi.org/10.1088/1748-9326/9/12/124015>
- Xiao, X. M., Boles, S., Frohling, S., Li, C. S., Babu, J. Y., Salas, W., & Moore, B. (2006). Mapping paddy rice agriculture in South and Southeast Asia using multi-temporal MODIS images. *Remote Sensing of Environment*, 100(1), 95-113. doi: <http://dx.doi.org/10.1016/j.rse.2005.10.004>
- Xiao, X. M., Boles, S., Liu, J. Y., Zhuang, D. F., Frohling, S., Li, C. S., Salas, W., & Moore, B. (2005). Mapping paddy rice agriculture in southern China using multi-temporal MODIS images. *Remote Sensing of Environment*, 95(4), 480-492. doi: <http://dx.doi.org/10.1016/j.rse.2004.12.009>
- Yang, W., Yang, L., & Merchant, J. W. (1997). An assessment of AVHRR/NDVI-ecoclimatological relations in Nebraska, U.S.A. *International Journal of Remote Sensing*, 18(10), 2161-2180. doi: <http://dx.doi.org/10.1080/014311697217819>
- Zhang, X. Y., Friedl, M. A., Schaaf, C. B., & Strahler, A. H. (2004). Climate controls on vegetation phenological patterns in northern mid- and high latitudes inferred from MODIS data. *Global Change Biology*, 10(7), 1133-1145. doi: <http://dx.doi.org/10.1111/j.1529-8817.2003.00784.x>

### 3.10 Appendix A

**Table A.1.** Comparison of coefficients of determination ( $r^2$ ) for GDD CxQ model fit from the AMSR-E air temperature data and the MODIS land surface temperature data. In almost all study sites, coefficients of determination for the AMSR-E GDD is greater than that for the MODIS GDD, except on seven sites (underlined) at lower latitudes.

Site No.	Name	Latitude	Longitude	$r^2$ (AMSR-E)	$r^2$ (MODIS)	Site No.	Name	Latitude	Longitude	$r^2$ (AMSR-E)	$r^2$ (MODIS)
1	Cherkessk, RU	44.4	43.5	0.92	<u>0.94</u>	26	Kursk, RU	52.1	37.5	0.96	0.88
2	Stavropol, RU	45.0	42.4	0.95	<u>0.95</u>	27	Orenburg, RU	52.4	55.2	0.95	0.90
3	Krasnodar, RU	45.6	39.6	0.89	<u>0.91</u>	28	Kokshetau 1, KZ	52.7	69.2	0.96	0.88
4	Simferopol', UA	45.6	34.1	0.96	0.95	29	Barnaul 2, RU	52.7	83.0	0.97	0.89
5	Tulcea, UA	45.8	29.2	0.94	<u>0.95</u>	30	Kuybyshev 2, RU	52.7	50.2	0.96	0.90
6	Rostov-on-Don 2, RU	46.7	39.8	0.88	<u>0.89</u>	31	Orel, RU	52.7	35.7	0.97	0.89
7	Odesa, UA	47.3	30.7	0.94	0.93	32	Kokshetau 2, KZ	53.0	67.4	0.96	0.87
8	Rostov-on-Do 1, RU	47.5	40.9	0.94	0.92	33	Lipetsk, RU	53.0	39.1	0.97	0.89
9	Donets'k, UA	47.5	37.7	0.93	0.90	34	Kokshetau 3, KZ	53.7	68.2	0.96	0.89
10	Mykolayiv, UA	47.5	32.3	0.92	<u>0.92</u>	35	Kostanay 1, KZ	53.7	63.3	0.97	0.90
11	Zaporihzhya 1, UA	47.8	35.7	0.91	0.89	36	Kostanay 2, KZ	53.7	62.2	0.97	0.89
12	Zaporihzhya 2, UA	48.1	34.1	0.90	0.88	37	Kurgan, KZ	53.7	65.6	0.96	0.89
13	Luhans'k, RU	48.7	40.4	0.95	0.92	38	Barnaul_1, RU	53.7	79.4	0.96	0.87
14	Volgograd, RU	48.7	44.8	0.97	0.94	39	Kokshetau 4, KZ	54.0	69.0	0.96	0.90
15	Kirovohrad, UA	48.7	31.8	0.94	0.90	40	Kostanay 3, KZ	54.0	64.0	0.96	0.89
16	Kharkiv 2, UA	49.0	36.2	0.92	0.87	41	Petropavlovsk 2, KZ	54.4	70.8	0.96	0.90
17	Khmel'nyts'kyz, UA	49.0	26.8	0.97	0.92	42	Petropavlovsk 3, KZ	54.4	67.4	0.97	0.90
18	Vinnitsya, UA	49.0	28.9	0.96	0.92	43	Kuybyshev 1, RU	54.4	50.8	0.96	0.89
19	Poltava, UA	49.6	35.1	0.92	0.86	44	Ryazan, RU	54.4	39.3	0.97	0.89
20	Kharkiv 1, UA	49.9	37.0	0.95	0.90	45	Petropavlovsk 1, KZ	54.7	69.5	0.97	0.90
21	Saratov 1, RU	50.8	46.9	0.96	0.92	46	Omsk 1, RU	54.7	72.9	0.96	0.90
22	Sumy, UA	50.8	34.1	0.96	0.90	47	Omsk 2, RU	55.0	74.5	0.96	0.91
23	Semipalatinsk, RU	51.4	81.7	0.96	0.90	48	Cheboksary, RU	55.7	47.1	0.95	<u>0.96</u>
24	Voronezh, RU	51.4	39.8	0.95	0.88	49	Kazan', RU	56.1	49.5	0.96	0.89
25	Saratov 4, RU	51.8	45.3	0.96	0.90						



**Table A.2.** Cropland sites that showed no change and those with changes in cropping pattern in the considered study period. Sites that showed changes include those with one change (unimodal to bimodal or bimodal to unimodal) and those with two changes (unimodal-bimodal-unimodal or bimodal-unimodal-bimodal). The year(s) when these changes occur and the number of years with continuous similar cropping pattern were also identified.

No Change				Change			
Site No.	Name, Country	Site No.	Name, Country	Site No.	Name, Country	Year Change	No. of years
	<b>Unimodal</b>		<b>Unimodal</b>		<b>Unimodal → Bimodal</b>		<b>uni/bi</b>
15	Kirovohrad, UA	34	Kokshetau 3, KZ	7	Odesa, UA	2008	5/3
16	Kharkiv 2, UA	35	Kostanay 1, KZ	10	Mykolayiv, UA	2009	6/2
19	Poltava, UA	36	Kostanay 2, KZ	12	Zaporiyhzhya_2, UA	2010	7/1
20	Kharkiv 1, UA	37	Kurgan, KZ		<b>Bimodal → Unimodal</b>		<b>bi/uni</b>
21	Saratov 1, RU	38	Barnaul_1, RU	11	Zaporiyhzhya_1, UA	2004	1/7
22	Sumy, UA	39	Kokshetau 4, KZ	13	Luhans'k, RU	2003	1/7
23	Semipalatinsk, RU	40	Kostanay 3, KZ	17	Khmelnyskyz, UA	2009	6/2
24	Voronezh, RU	41	Petropavlovsk 2, KZ	18	Vinnytsya, UA	2009	6/2
25	Saratov 4, RU	42	Petropavlovsk 3, KZ		<b>Unimodal → Bimodal → Unimodal</b>		<b>uni/bi/uni</b>
26	Kursk, RU	43	Kuybyshev 1, RU	6	Rostov-on-Don 2, RU	2007; 2008	4/1/3
27	Orenburg, RU	44	Ryazan, RU	8	Rostov-on-Do 1, RU	2007; 2008	4/1/3
28	Kokshetau 1, KZ	45	Petropavlovsk 1, KZ	14	Volgograd, RU	2009; 2010	6/1/1
29	Barnaul 2, RU	46	Omsk 1, RU		<b>Bimodal → Unimodal → Bimodal</b>		<b>bi/uni/bi</b>
30	Kuybyshev 2, RU	47	Omsk 2, RU	1	Cherkessk, RU	2005; 2009	2/4/2
31	Orel, RU	48	Cheboksary, RU	2	Stavropol, RU	2005; 2009	2/4/2
32	Kokshetau 2, KZ	49	Kazan', RU	3	Krasnodar, RU	2007; 2008	4/1/3
33	Lipetsk, RU			4	Simferopol, UA	2005; 2010	2/5/1
				5	Tulcea, UA	2006; 2010	3/4/1
				9	Donetsk, UA	2006; 2008	3/2/3

## CHAPTER 4 : Comparing Passive Microwave with Visible-to-Near-Infrared Phenometrics in Croplands of Northern Eurasia

### Paper #3

Alemu, W.G.; Henebry, G.M. Comparing Passive Microwave with Visible-to-Near-Infrared Phenometrics in Croplands of Northern Eurasia. (under review at *Remote Sensing*, submitted December 2016)

**Research Question:** Can AMSR-E passive microwave derived VOD peak height (PH) phenometrics track cropland seasonal dynamics be complementary to the VNIR MODIS NDVI peak vegetation greenness?

**Research Answer:** Yes,

- Time series of LSP of VODs were able to capture the seasonality of croplands (both bimodal & unimodal patterns) similar to the NDVI.
- Passive microwave PH VOD favorably corresponded with that of the VNIR PH NDVI over the study domain, but peaks occurred 1-2 weeks later. Canopy water content (aboveground biomass) peaks later than canopy greenness.
- However, more research is needed on how best to use that complementarity.

#### 4.0 Abstract

Planting and harvesting times drive cropland phenology. There are only few datasets that derive explicit phenological metrics, and these datasets use the visible to near infrared (VNIR) spectrum. Many different methods have been used to derive the phenometrics Start of Season (SOS) and End of Season (EOS), leading to different results. This discrepancy is partly due to spatial and temporal compositing of the VNIR satellite data to minimize data gaps resulting from cloud cover, atmospheric aerosols, and solar illumination constraints. Phenometrics derived from the Convex Quadratic model include Peak Height (PH) and Thermal Time to Peak (TTP), which are more consistent than SOS and EOS because they are minimally affected by snow and frost and other non-vegetation related issues. Here, we have determined PH using the vegetation optical depth in three microwave frequencies (6.9, 10.7 and 18.7 GHz) and accumulated growing degree-days derived from AMSR-E (Advanced Microwave Scanning Radiometer on EOS) data at a spatial resolution of (25 km). We focus on 50 AMSR-E cropland pixels in the major grain production areas of Northern Eurasia (Ukraine, southwestern Russia, and northern Kazakhstan) for 2003 – 2010. We compare the land surface phenologies of AMSR-E VOD and MODIS NDVI data. VOD time series tracked cropland seasonal dynamics similar to that recorded by the NDVI. The coefficients of determination for the NDVI data CxQ model fit were high for all sites ( $0.78 < r^2 < 0.99$ ). The 10.7 GHz VOD ( $VOD_{10.7GHz}$ ) achieved the best linear regression fit ( $r^2=0.84$ ) with lowest standard error (SEE=0.128); it is therefore recommended for microwave VOD studies of cropland land surface phenology. Based on an ANCOVA analysis, the slopes from the linear regression

fit are not significantly different by microwave frequency; whereas, the intercepts were significantly different, given the different magnitudes of the VODs. PHs for NDVI and VOD were highly correlated. Despite their significant strong correspondence, there was a general lag of AMSR-E PH VOD<sub>10.7GHz</sub> by about two weeks compared to that of MODIS peak greenness. To check the usefulness of the maximum value-based PH phenometrics determination approach, we correlated the CxQ derived and maximum value determined PH NDVI and found that they were highly correlated with  $r^2$  of 0.87, but with a one-week bias. Deducting the two methods one-week bias, PH VOD<sub>10.7GHz</sub> lags PH NDVI by one week. Therefore, we conclude that maximum-value based PH VOD can be a complementary phenometric for the CxQ model derived PH NDVI, especially in cloud and aerosol obscured regions of the world.

#### **4.1 Introduction**

Planting and harvesting times drive the phenologies of crops. A complex network of factors influences when farmers plant particular crops and when they harvest them, including: recent and forecast weather; commodity prices, situation of local markets, and foreign crop conditions; crop insurance and governmental policies and subsidies; agronomic practices; and the cold hardiness, drought tolerance, or differential maturities of planted crop varieties. Most of these factors cannot be observed through remote sensing technologies. The remote sensing of land surface phenology (LSP) can reliably reveal the seasonality of the vegetation in croplands in an ordinal sequence of broad phases: greenup onset (start-of-season, SOS), maturity onset, senescence onset, and dormancy onset (end-of-season, EOS). The dates or days of the year of the SOS and EOS

are commonly used as phenological metrics (or phenometrics) to study the land surface phenology of croplands in relation to climatic and hydrological variability and, to some extent, the variation in land management (Jones et al., 2012).

Cropland phenology is not equivalent to crop phenology. The phenologies of crops describe particular observable life history events in the specific species of crop. Implicit in crop phenology is a human observing the crop at sufficiently close distance to distinguish the plant parts relevant to the phenological phases (or phenophases). In contrast, cropland phenologies describe the land surface phenologies of croplands captured through remote sensing. These may include a mixture of multiple crop types with non-crop elements such as roads, vegetated ditches, hedgerows, woodlots, and rural buildings. Crop phenologies can be quite detailed; cropland phenologies offer relatively few phenophases. Cropland phenologies are useful for models of land surface, weather, and climate. Crop phenologies are useful for models of crop growth and yield and field-scale hydrological and biogeochemical processes.

Few remote sensing data products are used to derive explicit phenometrics, and each of these datasets uses the VNIR (visible-to-near-infrared) spectrum (Henebry & de Beurs, 2013). Moreover, each of the phenologically explicit LSP products uses different methods to derive phenological metrics, resulting in different metrics for SOS and EOS (Henebry & de Beurs, 2013). This discrepancy is also partly due to the challenge of equating satellite derived LSP metrics to *in situ* observations of plant phenology, and the spatial and temporal compositing of the VNIR satellite data to minimize data gaps that

result from cloud cover, atmospheric aerosols, and orbital and solar illumination constraints (Schwartz & Hanes, 2010; Wang et al., 2005).

Microwave remote sensing is based on the dielectric property of materials, which is largely governed by the material's water content. Thus, microwave measurements are sensitive to vegetation and soil water content and to changes in plant biomass and soil moisture. The frequencies of microwaves emitted by the land surface are much lower than VNIR light. These longer wavelengths are less attenuated by the atmosphere, and the earth's surface constantly emits microwaves. Satellite active and passive microwave data have been successfully applied in many LSP studies such as vegetation phenology assessment (Frolking et al., 2006; Jones et al., 2011; Min & Lin, 2006; Shi et al., 2008), vegetation drought response (Frolking et al., 2005; Frolking et al., 2011), and growing season variability (Kimball et al., 2004; Kimball et al., 2006). Limitations of microwave LSP monitoring include very coarse spatial resolution (25 km in this study) due to the faint microwave signal emissions of land surface materials (Jones et al., 2012; Liu et al., 2011), sensitivity to radio frequency interference (RFI; Li et al., 2004; Njoku et al., 2005), signal degradation or loss due to snow cover and frozen ground (Frolking et al., 2006; Jones et al., 2011).

Vegetation optical depth (VOD) is a measure of aboveground vegetation canopy thickness (Owe et al., 2001) that is less sensitive to dense biomass saturation, less sensitive to atmospheric contamination and solar illumination constraints, and it can have high temporal resolution (Jones et al., 2011; Jones et al., 2012; Liu et al., 2013). VOD is

directly proportional to the vegetation dielectric constant and canopy water content. VOD responds to vegetation seasonal dynamics similar to those recorded by the VNIR MODIS vegetation indices (VIs: NDVI, EVI, LAI) and an independent bioclimatic growing season index (GSI; Jolly et al., 2005; Jones et al., 2011; Jones et al., 2012). VOD has been shown to track seasonal changes in croplands in spring wheat producing regions of North America and winter wheat producing areas of Volga River Basin in Russia, and heatwaves that devastated crop production in Northern Eurasia (Dole et al., 2011; Trenberth & Fasullo, 2012) similar to that of NDVI and EVI (Alemu & Henebry, 2013, 2016). VOD SOS corresponds well to MODIS NDVI and EVI green-up dates, and SOS estimates from flux tower gross primary production (GPP) and ecosystem respiration, but with temporal offsets (Jones et al., 2012).

Phenometrics derived from the Convex Quadratic model include Peak Height (PH) and Thermal Time to Peak (TTP), which are more consistent than SOS and EOS because they are minimally affected by snow and frost and other non-vegetation related issues (de Beurs & Henebry, 2008a, 2010). PH estimated through accumulated growing degree-days (AGDD) or accumulated relative humidity has been found to have significant positive correlation with agricultural production statistics for rainfed agriculture (Brown et al., 2012). In the application of the Convex Quadratic (CxQ) model, a piece of a parabola is fit to the response variable as a function of thermal time. The advantage of the CxQ model is the PH and TTP can be calculated directly from the fitted parameter coefficients. The disadvantage is that some LSP shapes are not well approximated by a parabolic curve. We observed in earlier work (Alemu & Henebry,

2013) that only the very center of the growing season VOD time series was well fitted by the CxQ model. In this study, we hypothesize that VOD phenometrics characterize cropland dynamics in a manner complementary to MODIS NDVI phenometrics, but with temporal lag. The aims of this study are to (1) compare the VOD TTP and PH phenometrics from passive microwave data using the growing season maximum value approach with NDVI TTP and PH phenometrics from MODIS data using the CxQ model; (2) quantify temporal offsets between the two sets of phenometrics; (3) interpret the origin of these offsets; and, importantly, (4) demonstrate the validity of the VOD approach so that these microwave phenometrics can be used in cloud-obscured areas.

## **4.2 Data and Methodology**

### **4.2.1 Remote Sensing Data**

We used two very different remote sensing datasets: emitted terrestrial microwave radiation and reflected solar shortwave radiation. The microwave dataset was based Advanced Microwave Scanning Radiometer (AMSR-E) enhanced land parameters developed by the Numerical Terradynamic Simulation Group at the University of Montana (Jones & Kimball, 2011). These parameters include near surface air temperature ( $t_a$ ; ~2 m height) and vegetation canopy transmittance ( $t_c$ ) at three microwave frequencies (6.925 GHz, 10.65 GHz, and 18.7 GHz). Onboard the NASA-EOS Aqua satellite, AMSR-E recorded data twice daily (daytime, ~1330, and nighttime, ~0130) from mid-June 2002 to October 2011, when the antenna failed. The second dataset included optical reflectance data from the Moderate-resolution Imaging Spectroradiometer (MODIS). We used MODIS collection 5 level 3 data product in a 0.05 degree (~5.6 km) Climate



Modeling Grid (CMG), specifically the Nadir Bidirectional Reflectance Distribution Function (BRDF)-Adjusted Reflectance (NBAR) data that combines observations from Terra and Aqua (MCD43C4; DAAC-LP, 2014). NBAR provides 16-day retrievals (updated every 8 days) of surface reflectance is normalized to a nadir view using BRDF models of surface anisotropy (Friedl et al., 2010; Schaaf et al., 2002).

Croplands for this study were identified based on the International Geosphere Biosphere Programme (IGBP) global land cover classification scheme in the MODIS land cover CMG product (MCD12C1; DAAC-LP, 2014), and the USDA Foreign agriculture service (FAS) crop layers by oblast (for Russia: [USDA-FAS, 2011b](#)), for Kazakhstan: [USDA-FAS, 2011a](#)), for Ukraine: [USDA-FAS, 2011c](#)).

#### **4.2.2 Study Region**

The major grain producing areas of Ukraine (UA), southern Russia (RU), and northern Kazakhstan (KZ) were our focal areas. The dominant land cover classes across the entire study region in terms of the MODIS IGBP Land Cover Type 1 Percentage Product were grassland (GRS, 34%, IGBP class 10), cropland (CRP, 27%, IGBP class 12), crop-natural vegetation mosaic (CNVM, 14%, IGBP class 14), and mixed forest (MFO, 11%, IGBP class 5). This land cover product has an overall classification accuracy of about 75%, but the range of class-specific accuracies can be large (Friedl et al., 2010). Pixel-based land cover temporal stability analysis was made by first calculating the maximum, minimum, and mean land cover percentage over the study period (2003 – 2010) and then displaying the maximum, mean, and range of the percentages in the red, green, and blue color planes, respectively (Henebry et al., 2013).

The resulting yellow in figure 4-1 display where the particular land cover continued to be the dominant during the study period (Table 4-1).

Forty-nine (49) AMSR-E pixels (study sites) were selected across the three countries (14 in UA, 24 in RU & 11 in KZ) (figure 4-2 & table 4-2). For comparison, we identified one AMSR-E pixel dominated by mixed forest cover (IGBP class 5) in the Mari El republic of Russia. We didn't incorporate this MFO site in our analyses unless otherwise indicated in figure captions or text descriptions. The study region in which the specific sites were identified has nearly 12° latitudinal (44° N – 56° N) and 56° (27° E – 83° E) longitudinal extension. The most extreme latitudinal sites have a maximum of daylength difference of 2 hours that occurs on the solstices. Over the 8 years, average cropland cover for all sites was 88%, while the mixed forest site was 93% mixed forest. Many sites in UA and some in RU had 100% average maximum cropland cover over the study time period. While Volgograd in RU had the minimum average cropland cover (46%). Saratov 1 in RU (site 21) had the largest grassland encroachment with 69% and 31% mean cropland and grassland cover respectively over the eight years, and thus had the largest cropland cover variation (range=28%). Omsk 1 in RU (site 46), and Kostanay 2 in KZ (site 36) are also other examples.

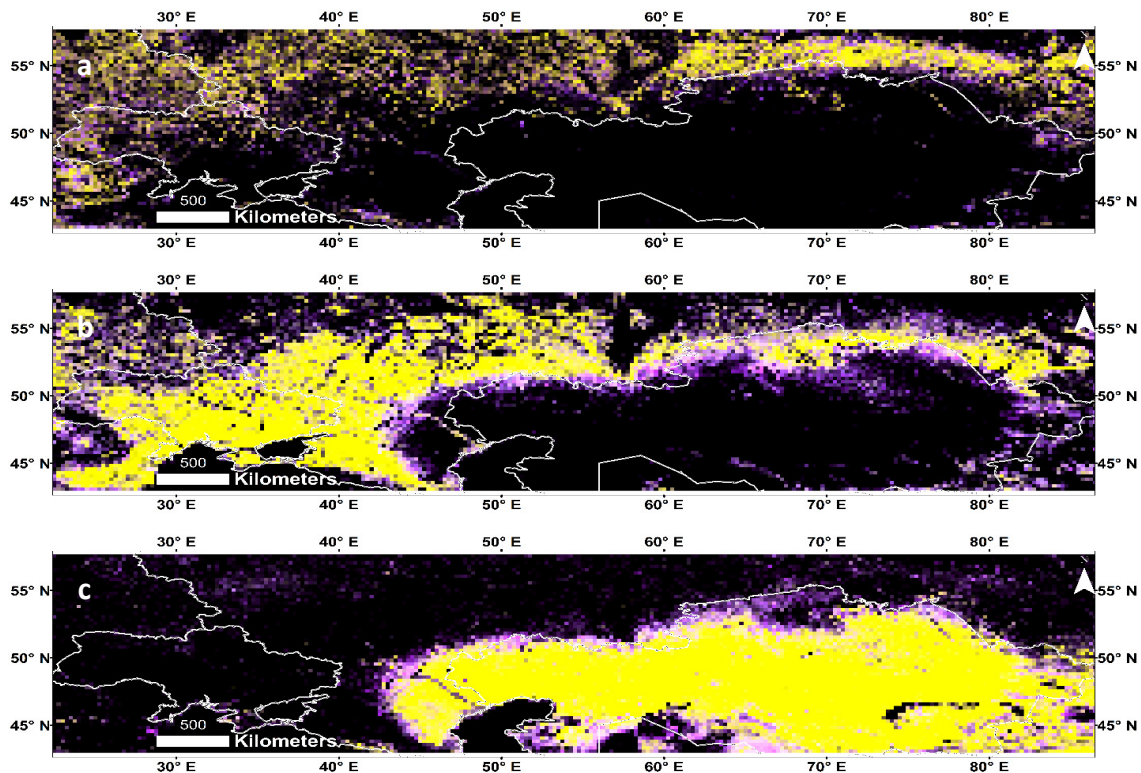


**Figure 4-1.** Land cover stability in Ukraine (UA), southern Russia (RU), and northern Kazakhstan (KZ) as revealed by IGBP global land cover classification scheme MODIS 0.05° land cover products (resampled to AMSR-E spatial resolution: 0.25°) from 2003-2010. (a) crop-natural vegetation mosaic (IGBP class 14); (b) cropland (IGBP class 12); (c) grassland (IGBP class 10). Land cover percentage from 2003-2010 displayed as R=max%, G=mean%, B=range of %. Yellow=stable core area; Magenta=unstable peripheral areas; Black=no occurrence of the given LC. For legend refer to Table 4-1 (Alemu & Henebry, 2016).

**Table 4-1.** Interpretive legend for Figures 4-1 that display IGBP MODIS 0.05° land cover variation from 2003-2010 in the study region.

Color in LC Map	Red = Max% LC	Green = Mean% LC	Blue = Range% LC	Interpretation
Black	None	None	None	Land cover (LC) class absent
Blues	Low	Low	High	Unstable but ephemeral periphery; rare and erratic
Magentas	High	Low	High	Unstable but persistent periphery; sometimes high, but usually low
Whites	High	High	High	Unstable core; sometimes low, but usually high
Yellows	High	High	Low	Stable core of LC; always high so low range

Source: (Henebry et al., 2013)

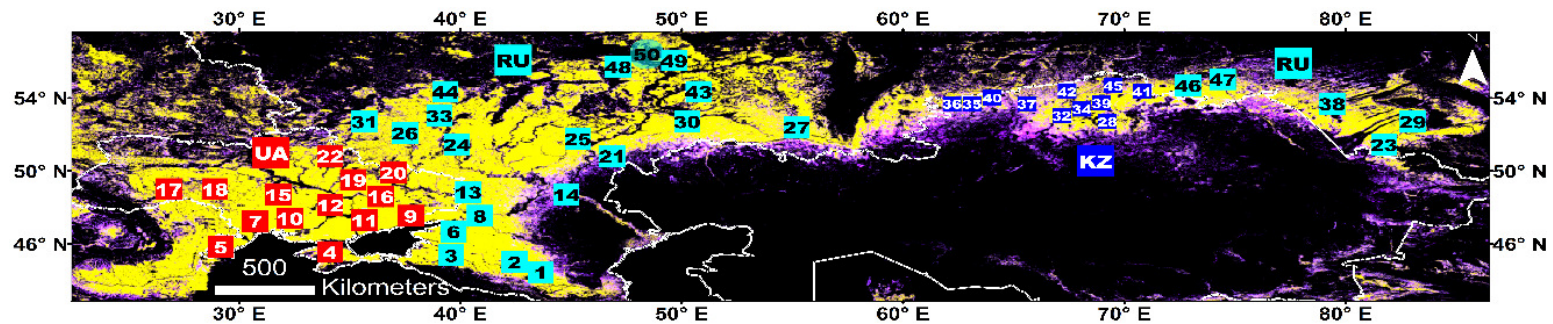


**Figure 4-2.** Cropland stability map overlaid by the 49 specific cropland and one MFO AMSR-E pixels (site 50 - most northern site) study sites. The AMSR-E pixels are numbered from lower to higher latitude. Sites are named by their closest town (Table 4-1). Modified from (Alemu & Henebry, 2016).

**Table 4-2.** Study sites (named by their closest town) and their country, numbered from lower latitude (1) to higher latitude (50), their geographic locations, and average cropland (CRP) cover % and range from 2003-2010. Note that sites with 100 % average CRP cover throughout the study period are indicated in bold, and extrema in CRP cover % range are indicated by underlines for high and bold italics for low.

Site No.	Name	Latitude	Longitude	CRP (%)	Range (%)	Site No.	Name	Latitude	Longitude	CRP (%)	Range (%)
1	Cherkessk, RU	44.4	43.5	99	0.6	26	Kursk, RU	52.1	37.5	95	4.1
2	Stavropol, RU	45.0	42.4	<b>100</b>	0.3	27	Orenburg, RU	52.4	55.2	94	4.7
3	Krasnodar, RU	45.6	39.6	98	0.6	28	Kokshetau 1, KZ	52.7	69.2	91	8.5
4	Simferopol', UA	45.6	34.1	<b>100</b>	1.2	29	Barnaul 2, RU	52.7	83.0	99	0.7
5	Tulcea, UA	45.8	29.2	96	0.3	30	Kuybyshev 2, RU	52.7	50.2	91	9.6
6	Rostov-on-Don 2, RU	46.7	39.8	<b>100</b>	0.2	31	Orel, RU	52.7	35.7	64	2.7
7	Odesa, UA	47.3	30.7	<b>100</b>	<b>0.0</b>	32	Kokshetau 2, KZ	53.0	67.4	79	10.6
8	Rostov-on-Do 1, RU	47.5	40.9	88	6.2	33	Lipetsk, RU	53.0	39.1	84	4.4
9	Donets'k, UA	47.5	37.7	<b>100</b>	0.7	34	Kokshetau 3, KZ	53.7	68.2	84	10.0
10	Mykolayiv, UA	47.5	32.3	<b>100</b>	0.1	35	Kostanay 1, KZ	53.7	63.3	78	8.0
11	Zaporihzhya 1, UA	47.8	35.7	<b>100</b>	0.1	36	Kostanay 2, KZ	53.7	62.2	86	<u>18.5</u>
12	Zaporihzhya 2, UA	48.1	34.1	<b>100</b>	<b>0.0</b>	37	Kurgan, KZ	53.7	65.6	74	<u>17.3</u>
13	Luhans'k, RU	48.7	40.4	99	2.1	38	Barnaul_1, RU	53.7	79.4	82	11.3
14	Volgograd, RU	48.7	44.8	<b>46</b>	13.4	39	Kokshetau 4, KZ	54.0	69.0	93	4.7
15	Kirovohrad, UA	48.7	31.8	99	1.0	40	Kostanay 3, KZ	54.0	64.0	79	15.7
16	Kharkiv 2, UA	49.0	36.2	91	6.6	41	Petropavlovsk 2, KZ	54.4	70.8	97	3.6
17	Khmel'nyts'kyz, UA	49.0	26.8	88	11.0	42	Petropavlovsk 3, KZ	54.4	67.4	92	5.4
18	Vinnitsya, UA	49.0	28.9	96	0.5	43	Kuybyshev 1, RU	54.4	50.8	95	8.8
19	Poltava, UA	49.6	35.1	97	1.6	44	Ryazan, RU	54.4	39.3	65	13.7
20	Kharkiv 1, UA	49.9	37.0	72	3.9	45	Petropavlovsk 1, KZ	54.7	69.5	86	4.4
21	Saratov 1, RU	50.8	46.9	69	<u>27.9</u>	46	Omsk 1, RU	54.7	72.9	61	<u>18.7</u>
22	Sumy, UA	50.8	34.1	85	7.1	47	Omsk 2, RU	55.0	74.5	59	14.5
23	Semipalatinsk, RU	51.4	81.7	98	3.3	48	Cheboksary, RU	55.7	47.1	93	6.1
24	Voronezh, RU	51.4	39.8	98	1.7	49	Kazan', RU	56.1	49.5	81	2.3
25	Saratov 4, RU	51.8	45.3	88	3.6	50	Mari El*	56.4	48.4	93	4.9

\* Mixed forest (MFO) cover. Source: Modified from (Alemu & Henebry, 2016)

#### 4.2.3 Characterizing Land Surface Phenology in VODs and NDVI

We used the AMSR-E and MODIS data from all eight years (2003–2010) for all the pixels. The AMSR-E data record has winter data gaps as it was pre-filtered for snow covered or frozen land surfaces (Kim et al., 2011). To avoid the frozen season and to maintain a consistent analysis period across all pixels, we restricted our focus to data from DOY 89–305, which ranges 30 March to 1 November for non-leap years and 29 March to 31 October for leap years. An 8-day forward moving average filter was applied to the AMSR-E data to align it with the MODIS compositing dates and to minimize data gaps due to orbit and swath width. Growing degree-day (GDD) is the daily thermal time increment above a certain threshold (or base temperature) for plant growth (de Beurs & Henebry, 2004; McMaster & Wilhelm, 1997; Sarma et al., 2008), and accumulated growing degree-days (AGDD) are the summation of daily thermal time increments throughout the whole growing period (de Beurs & Henebry, 2010; Wang et al., 2001; Yang et al., 1997). In other words, the passage of days is weighted by the quantity of growing degrees occurring that day, with zero (but not negative) degrees being a permissible weight (Henebry, 2013). McMaster (2005) concluded that the base temperature of 0 °C is a robust and sufficient threshold for wheat phenology, which is the main crop in our study region. GDD was calculated from the AMSR-E air temperature ( $t_a$ ) data with a base temperature of 273.15 K (= 0 °C) as follows:

$$\text{GDD} = \max\left[\frac{t_{ASC} + t_{DES}}{2} - 273.15, 0\right] \quad [1]$$

where  $t_{ASC}$  and  $t_{DES}$  are ascending and descending pass temperatures, which roughly corresponds to the day and night time temperatures respectively. We applied 8-day

forward moving summation to the GDDs and picked up those values corresponded with the MODIS reflectance data (MCD43C4) acquisition dates to mimic the whole growing season GDD (DOY 89-305 in this case) and to align it with the MODIS data respectively. Thus each annual growing period has 28 GDD values. These GDD values were accumulated to yield AGDD.

$$AGDD_t = AGDD_{t-1} + GDD_t \quad [2]$$

where  $GDD_t$  is daily temperature increment of growing degree days at time  $t$ .

Daily GDD from AMSR-E tracked seasonal, weekly and monthly dynamics of corresponding weather station GDD (Alemu & Henebry, 2016). The root mean square deviation (RMSD) between these daily datasets from the two sources was very low, 1.86 – 3.16 °C (Alemu & Henebry, 2016). Linear regression of AMSR-E GDD with weather station GDD on these cropland sites yielded  $r^2 > 0.82$  (Alemu & Henebry, 2016). This result is in line with Jones et al. (2010) who found a bias of 1.0 – 3.5 K between WMO weather station and AMSR-E daily air temperature data on vegetated lands across the Northern Hemisphere.

NDVI was calculated from the MODIS NBAR reflectance data using the standard formula by Tucker (1979). We fitted the MODIS NDVI as a function AMSR-E AGDD using the CxQ model.

$$NDVI_t = \alpha + \beta AGDD_t - \gamma AGDD_t^2 \quad [3]$$



The intercept  $\alpha$  is the background NDVI at the start of observation period, the linear parameter  $\beta$  affects the slope, and the quadratic parameter  $\gamma$  controls the curvature. Since the model is convex quadratic, the sign of  $\beta$  is positive and  $\gamma$  is negative.

Two phenometrics were derived from the fitted parameter coefficients of the CxQ model. These are Peak Height NDVI (PH; equation 4) and Thermal Time to Peak NDVI ( $TTP_{NDVI}$ ; equation 5):

$$PH = \alpha - (\beta^2/4\gamma) \quad [4]$$

$$TTP_{NDVI} = -\beta/2\gamma \quad [5]$$

where  $\alpha$ ,  $\beta$ ,  $\gamma$  are the fitted parameter coefficients.

Vegetation Optical Depth (VOD) was derived as a negative natural logarithm of vegetation transmittance [ $VOD = -\log_e(tc) = -\ln(tc)$ ]. In a previous study (Alemu & Henebry, 2013), we fitted the core growing season VODs from the three microwave frequencies (6.9 GHz, 10.7 GHz, and 18.7 GHz) using the CxQ model in a two-step process. The fits were good and from these fits we derived two phenological metrics, namely the PH and TTP VODs. However, here we consider a larger fraction of the growing season, and thus another approach was needed. The VOD shapes for the entire growing season are not well fit using CxQ models. VOD is sensitive to aboveground biomass structure, including crop residues, and to the vegetation water content found in entire aboveground biomass, while NDVI is sensitive primarily to vegetation greenness. Thus, VOD has a different seasonal progression shape that is not suitably captured by a

quadratic curve compared to that of NDVI. Therefore, we used the maximum VOD value approach to determine cropland vegetation PH and TTP. That is, the observed maximum VOD value was taken as PH VOD, while the corresponding AGDD was taken as TTP. Similar approach was also used for the NDVI for a direct comparison with the CxQ model fit derived PH and TTP NDVI. The PH NDVI and PH VOD values were regressed to see the relationship between cropland vegetation peak greenness and peak biomass and water content. We then used analysis of covariance (ANCOVA) to test whether the slopes and/or intercepts from of the linear regression model fit were significantly different by microwave frequency: the microwave frequencies (6.9, 10.7, 18.7 GHz) were the independent categorical effect variables, the peak greenness was covariate, and PH VOD was the response variable. The first statistical assumption for ANCOVA is that the covariate (peak greenness in our case) is uncorrelated with other independent variables (microwave frequencies), and the second assumption is that the covariate (peak greenness) is correlated with the dependent variable (PH VOD; Owen & Froman, 1998). In all cases,  $p \leq 0.05$  was considered significant.

## **4.3 Results**

### **4.3.1 Time Series Land Surface Phenologies of NDVI and VODs**

All three VOD time series were able to capture the seasonality of croplands (both bimodal patterns and unimodal patterns), similar to MODIS NDVI (figure 4-3). The bimodality arises from the planting of winter grains in the fall, and growth and harvest in the subsequent early summer. After snow melts, croplands are primarily barren or contain crop residuals (non-photosynthetic biomass) prior to tilling and planting. Greenup occurs

at seed germination (initiation of visible above-ground photosynthetic vegetation growth) that occurs prior to significant biomass occurrence. This pattern is evident in figure 4-3 & 4-4 where the rise in VOD occurs later than NDVI. Cropland LSP peak VODs (that measure vegetation water content and biomass) consistently lagged in time and space from the peak NDVI (that measure vegetation greenness) (figure 4-3 & 4-4).

Furthermore, the VODs showed slower senescence likely a consequence of residual biomass (crop residue) following harvest (McNairn et al., 2001; McNairn et al., 2002; figure 4-3 & 4-4). The higher microwave frequency has larger VOD signatures since the shorter wavelengths are more attenuated by vegetation canopy (figure 4-3 & 4-4).

LSPs at the lower latitudes exhibit longer and/or bimodal patterns due to cultivation of winter grains (figure 4-4a&b). On the other hand, LSPs at the higher latitudes exhibit shorter unimodal growing season due to cultivation of spring grains (figure 4-4c&d). At each study site the VOD and NDVI exhibit similar seasonal patterns, amid interannual variation. For example, in Petropavlovsk 3, KZ (figure 4-4c), in 2003 there was high and earlier peak LSPs in fewer AGDD, while in 2010 there was lower & flatter peak in more AGDD due to the 2010 heatwave in Russia (Dole et al., 2011; Trenberth & Fasullo, 2012). Note the 2007 VOD in Kirovohrad, UA (figure 4-4b) is almost flattened compared to other years due to the devastation of crops by the 2007 heatwave in Ukraine (Founda & Giannakopoulos, 2009). The heatwave effect is more evident on the VODs compared to their counterpart NDVI (figure 4-4b), due to the sensitivity of VODs to vegetation water content. As Mari El in Russia is a mixed forest (MFO) site, it displayed a distinct LSP in magnitude and shape compared to the rest of the 49 cropland sites (figure 4-4e).

Both VOD and NDVI were larger in magnitude (note the y-scale) and flatter in shape. The VODs in particular showed a much delayed senescence compared to the NDVI. Figure 4-4 shows time series of VODs and NDVIs in a southern study site (Simferopol, UA) that experienced alternate unimodal and bimodal patterns over the 8 years of the study. All the three microwave frequencies VOD were able to capture these LSP patterns similar to their counterpart NDVI, despite some differences in magnitude and shape.

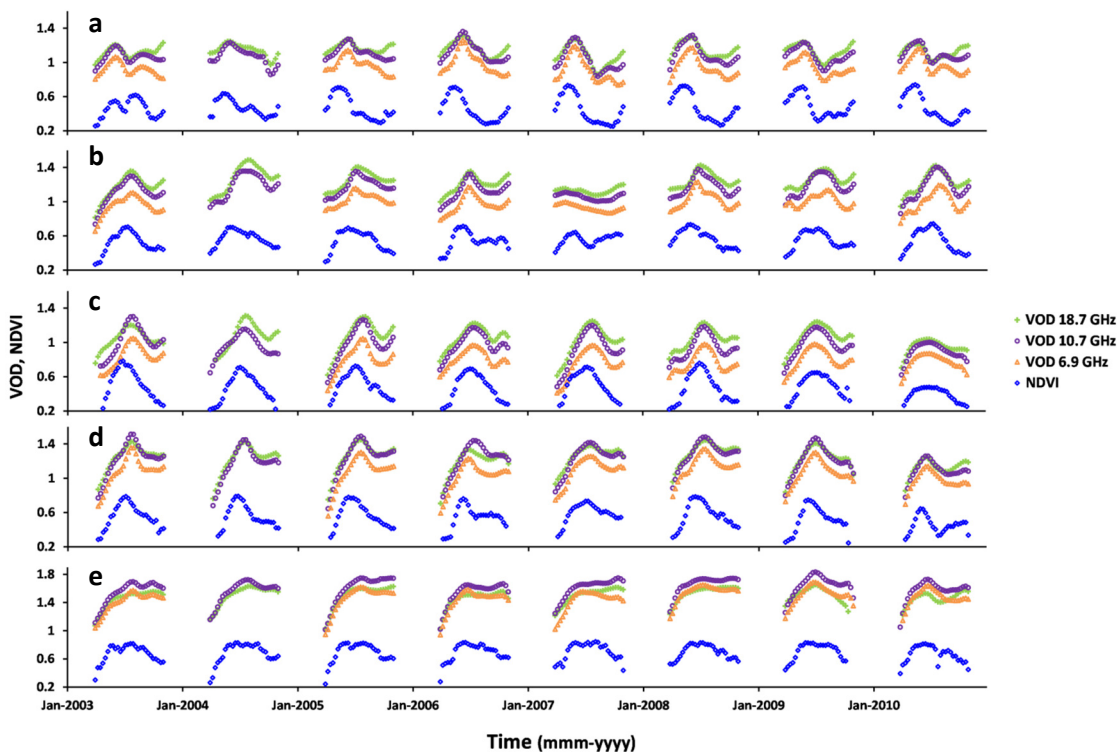


**Figure 4-3.** VOD time series for the three microwave frequencies: green pluses=18.7; purple circles=10.7; orange triangles=6.9 GHz; and blue diamonds=NDVI. Selected series arranged from south to north of our study region: (a) Cherkessk, RU, 44.4°; (b) Kirovohrad, UA, 48.7°; (c) Petropavlovsk 3, KZ, 54.4°; (d) Kazan, RU, 56.1°; and (e) Mari El, RU, 56.4° (MFO site included for comparison). Note that the y-axis scaling for the MFO site (0.2-1.9) is different from the cropland sites (0.2-1.6).

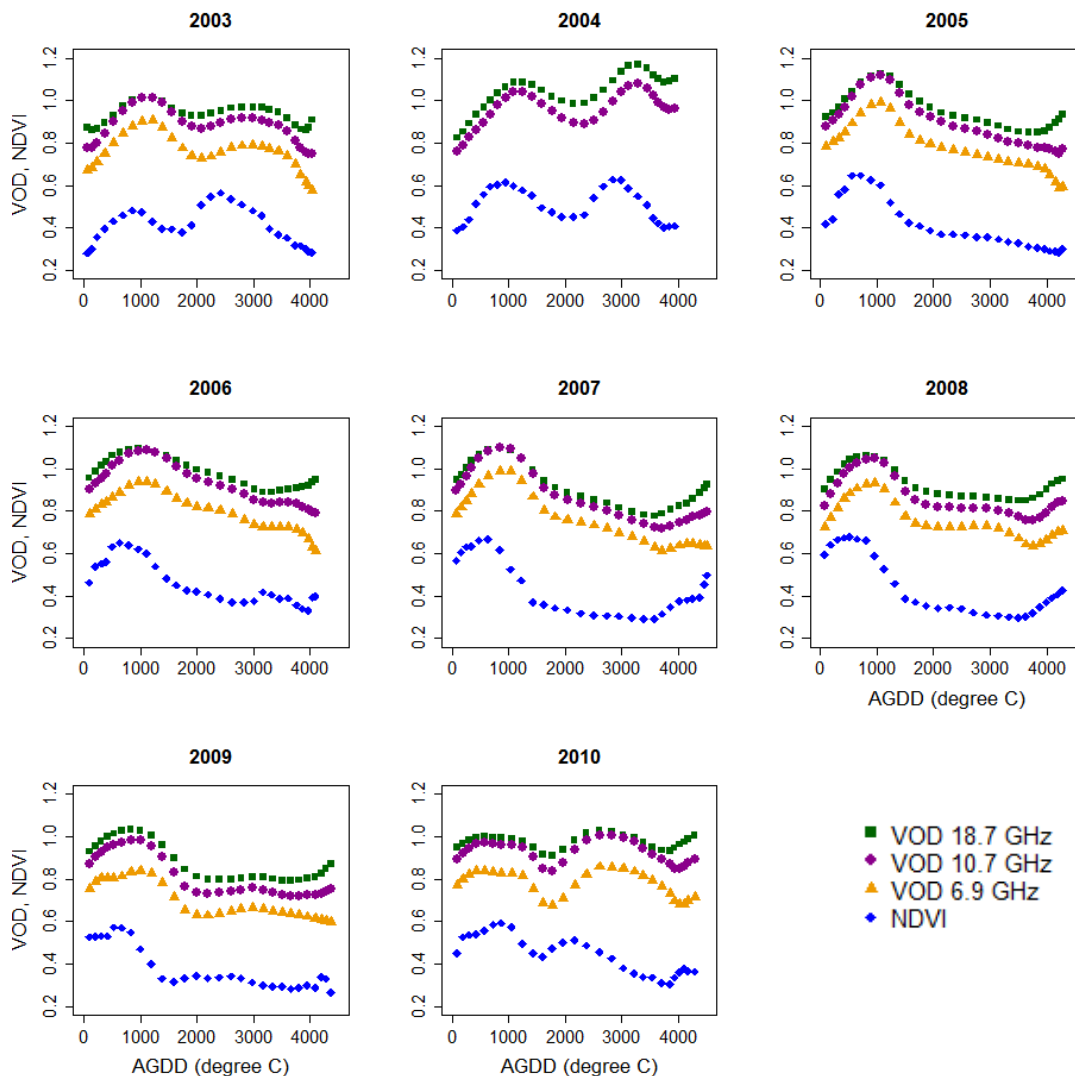


**Figure 4-4.** VODs in three microwave frequencies (green squares = 18.7, purple circles = 10.7, & orange triangles = 6.9 GHzs) and NDVI (blue diamonds) interannual variability of a southern study site (Simferopol, UA, 45.6° N) for 2003-2010. The 6.9 GHz vegetation transmissivity was missing from the source dataset in 2004. Seasonal patterns change from bimodal (2003-2004) to unimodal (2005-2009) and back to bimodal (2010). There is also seasonal variability within the bimodal and unimodal growing seasons.

### 4.3.2 Thermal Time to Peak and Peak Height NDVI and VOD Phenometrics

In this section, we present TTP and PH NDVI derived from the CxQ model, followed by VODs and NDVI determined from the growing season maximum value approach.

#### 4.3.2.1 The CxQ Model Derived NDVI Phenometrics

The NDVI CxQ model fit for all sites perform great in time and space with  $0.78 < r^2 < 0.99$ . Sample fitted plots across latitudes appear in figure 4-5. Sites in the lower latitudes that can support double growing season attain their first peaks at the earliest ( $< 1000$  AGDD, e.g. figure 4-5d, Cherkessk, RU,  $44^\circ$ ); moving farther north, the seasonal pattern changes from bimodal to unimodal, and the TTP NDVI pushed up further to the growing season (between  $1000 - 2000$  AGDD, e.g. figure 4-5c, Zaporizhzhya 1, UA,  $48^\circ$  & 4-5b, Kokshetau 1, KZ,  $53^\circ$ ). Moving towards the northern study sites, the TTP starts to decrease to  $1000$  AGDD due to the thermal limitation and shorter growing season (e.g., figure 4-5a, Cheboksary, RU,  $56^\circ$ ). Figure 4-6 presented the general relationship of  $TTP_{NDVI}$  as a function of latitude for all sites. Note also the NDVI CxQ fit intercept in the different latitudes in figure 4-5 that the growing season in the lower latitudes (e.g. figure 4-5d) starts a bit earlier than the time we considered in this study (DOY 89 = March 30 (March 29 for leap years)).

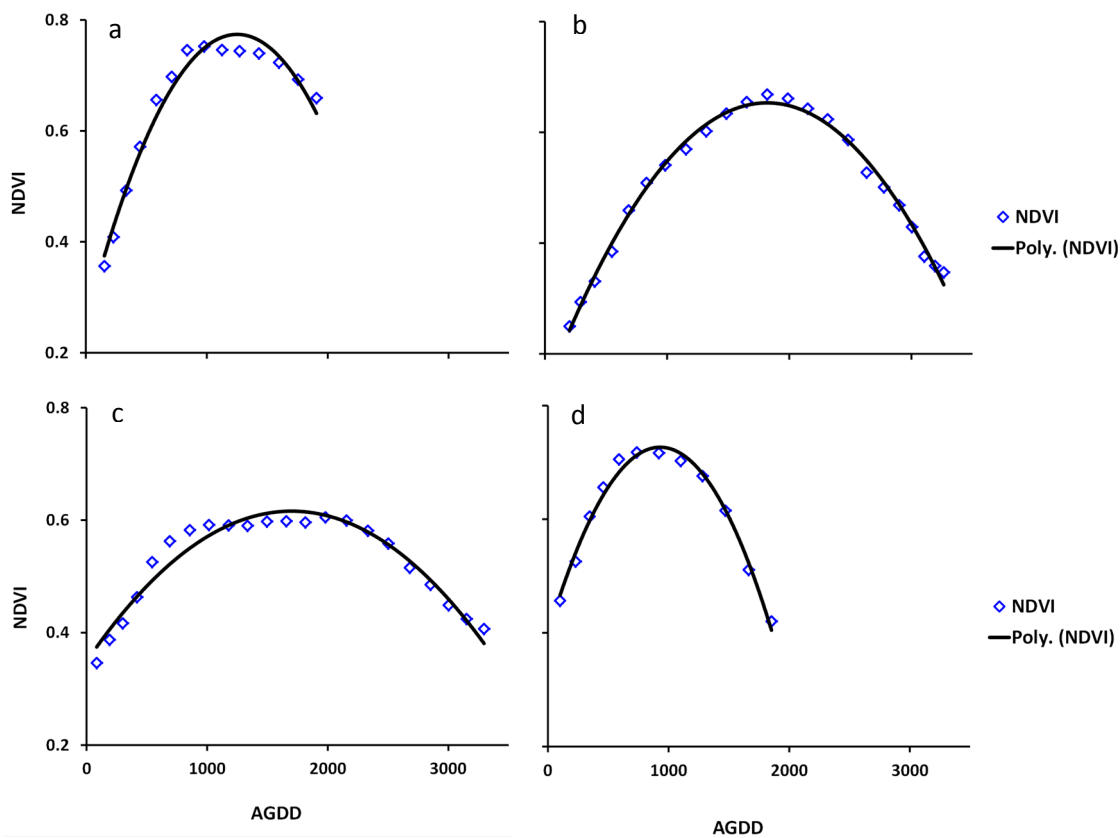


**Figure 4-5.** Average NDVI (2003–2010) as a function of AGDD for cropland sites that encompass the whole latitudinal range: (a) 48, RU; (b) 28, KZ; (c) 11, UA, and (d) 1, RU. The coefficients of determination ( $R^2$ ) for these sites ranged from 0.88 to 0.97.

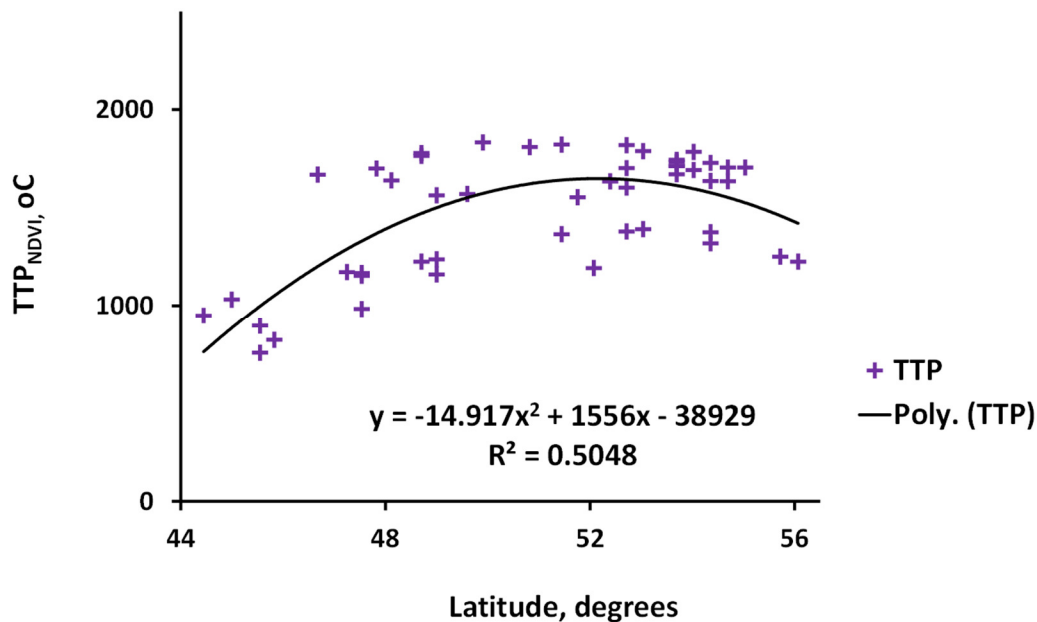


**Figure 4-6.** Scatterplot for TTP NDVI as a function of latitude fitted with a quadratic model. There is a significant positive relationship ( $R^2 = 0.5$ ) that as latitude increases TTP NDVI increases in the lower latitudes to certain limit and then declines in the northernmost study sites ( $44^\circ - 56^\circ$  N latitude).

Average (2003–2010) NDVI PH phenology metric in our study croplands ranges between 0.58 – 0.84 (figure not shown here). NDVI at half-TTP as a function of PH NDVI display a distinct trend indicating that NDVI in these sites is driven by local climates (figure 4-8a). Generally, lower latitude study sites have gentler NDVI gradient time series with longer growing season compared to the steeper NDVI gradient of the shorter summer growing season higher latitudes. Thus, the difference between PH NDVI and NDVI at half-TTP increases as latitude increases yielding a strong linear fit with  $R^2$  0.81 (figure 4-7a). However, PH NDVI as a function of latitude did not show a clear trend (figure 4-7b). The NDVI at half-TTP as a function of PH NDVI for some selected sites showed a positive correspondence (figure 4-8b). The two phenometrics for the



mixed forest in the most northern study site Mari El, Russia (site 50 appears as the outlying green circles in upper right corner) displayed strong correspondence with  $r^2 = 0.94$ . In contrast the correspondence between these phenometrics for croplands exhibited more interannual variability due to the fact that crops are annual vegetation and due to possible crop and land rotation annually or every few years. Moreover, croplands are more vulnerable to climatic variability compared to the perennial mixed forests. The southern study sites showed smaller NDVI at half-TTP and PH NDVI phenometrics in 2003 due to minimal effect of the European heatwave on croplands in our study area (De Bono et al., 2004). As the winter grains were affected in this year, many croplands were sown spring grains and therefore many southern study croplands in 2003 supported double cropping. The affected winter croplands (first peak) exhibit smaller NDVI at half-TTP and PH NDVI (figure 4-8b sites 1, 2, 4, and 13). However, the smaller values for the two phenometrics were recorded in 2010 for the northern study sites due to the effect of the 2010 Russian and Kazakhstan heatwave (Dole et al., 2011; Trenberth & Fasullo, 2012; figure 8b, sites 13, 24, and 36). As forests are perennial and resilient to climatic variability, the two phenometrics in Mari El, Russia were not that affected by the 2010 Russian heatwave and displayed closer values consistent trend throughout the study period. The 2010 half-TTP NDVI as a function of PH NDVI value for this MF site was just about at an average position of the other 7 years of values (figure 4-8b).

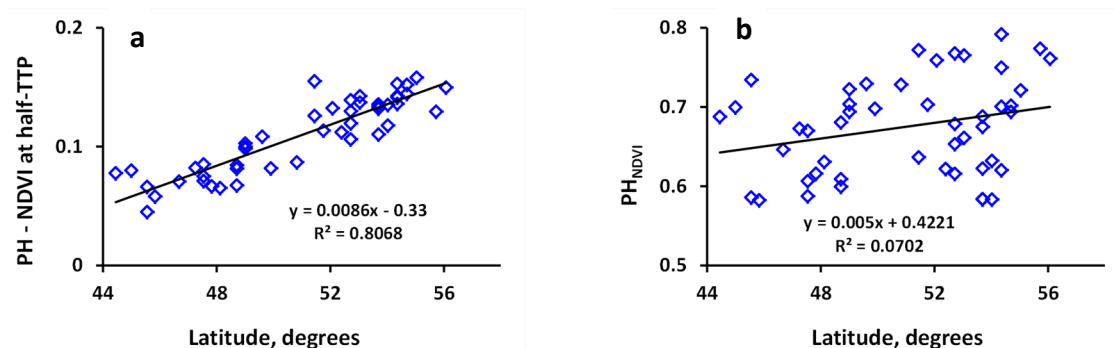


**Figure 4-7.** Scatterplot for PH NDVI and NDVI at half-TTP phenometrics (a) as a function of latitude, and (b) as a function of latitude (b). Both are fitted with linear trend line yielding strong correspondence for the former ( $R^2 = 0.81$ ), but no clear correspondence for the latter ( $R^2 = 0.07$ ).

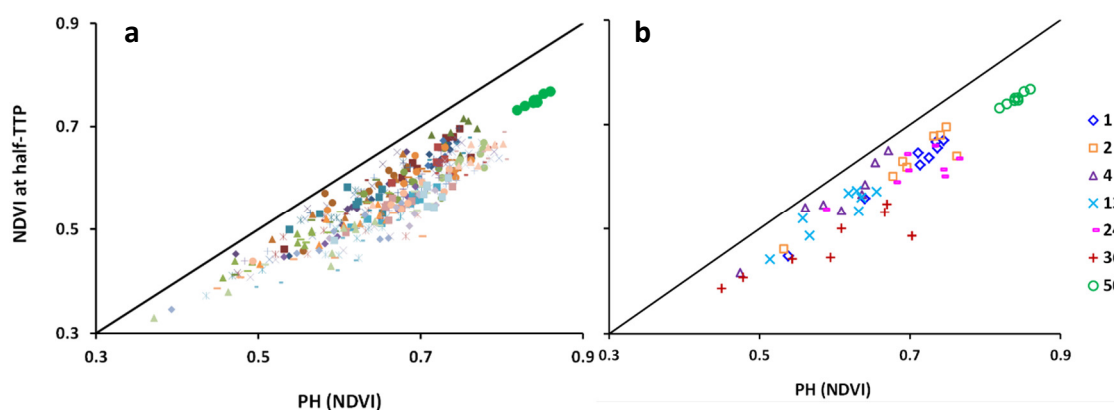


**Figure 4-8.** Annual phenometrics of NDVI at half-TTP as a function of PH NDVI (a) for all study sites and (b) for some selected study sites for 2003 – 2010. Sites are numbered according to their latitudinal position from south (1) to north (50) as in table 4-2 (not shown for 8a).

#### 4.3.2.2 The Maximum Value Approach VOD Phenometrics

For the VOD LSP, PH VOD as a function of the corresponding TTP VOD for all sites is presented in figure 4-9. In our study croplands, VOD PHs range between 0.85 – 1.74, while the NDVI PH (also calculated using the maximum value approach) ranged

between 0.60 – 0.83. VOD by microwave frequency was proportional to the magnitude of VOD PH metric, i.e., the ordering of the VOD PH from high to low was 18.7 GHz > 10.7 GHz > 6.9 GHz. The higher the frequency (the shorter the wavelength), the higher the attenuation by cropland vegetation, and thus the larger the VOD magnitude. One would expect that longer wavelength VOD may be more sensitive to higher biomass level while shorter wavelength VOD may attain its peak early in time due to saturation issue. However, the VOD microwave frequencies for the AMSR-E data are less sensitive to saturation. The VOD PH, which is responsive to vegetation water content and biomass, lags the NDVI PH, which is responsive to vegetation greenness or absorption of photosynthetically active radiation. Generally, the shorter the microwave wavelength, the later in terms of AGDD the VOD PH would be, i.e., the 18.7 GHz VOD PH lags the 10.7 GHz VOD PH which, in turn, lags the 6.9 GHz (shorter wavelength) PH VOD. The lag between the 10.7 and 18.7 GHz VOD PHs was narrower than the 6.9 GHz VOD PH from the other two. We have presented a quantified lag graph (figure 4-11b) among the maximum value determined PH VODs and the CxQ model derived PH NDVI in section 4.4.1.

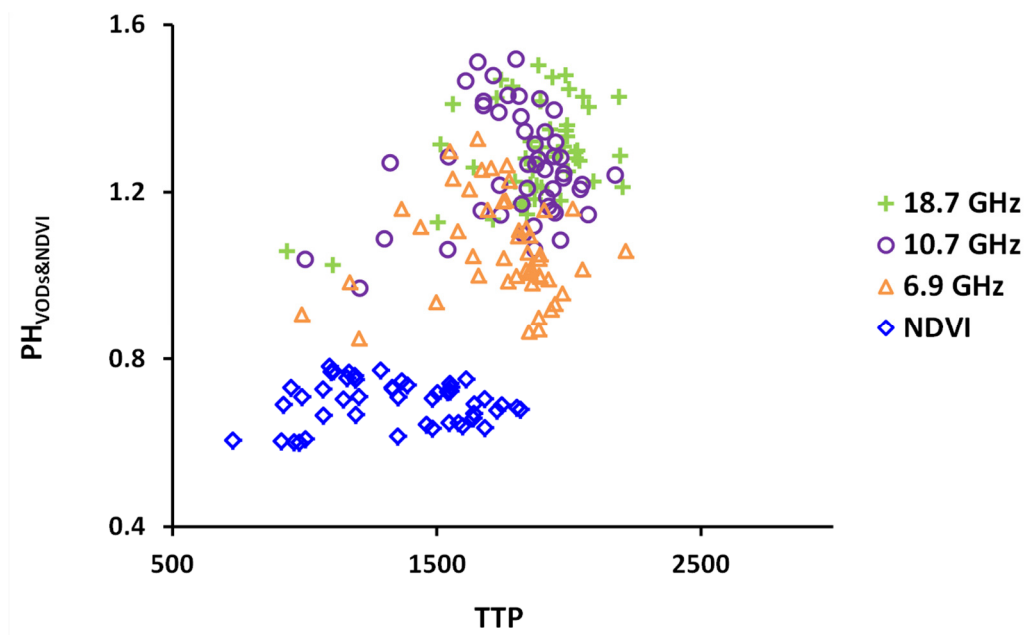


**Figure 4-9.** Scatter plot of the maximum value approach determined PH VODs and NDVI as a function of their corresponding TTP. Note the magnitude of the VODs and NDVI PHs; VODs PH lagged their counterpart NDVI PH; and also the lag among the VODs PH relative to their microwave frequency.

## 4.4 Discussions

### 4.4.1 VOD and NDVI Peak Heights: Correlations and Biases

Peak heights are less sensitive to snow and other non-vegetation related issues compared to the start-of-season (SOS; de Beurs & Henebry, 2008a, 2010). PH NDVI has significant positive correlation to agricultural production (Brown et al., 2012). The microwave based VOD PH derived using the maximum value approach favorably corresponded with the VNIR based NDVI PH derived using the CxQ model over the study domain. The 10.7 GHz VOD PH achieved the highest correspondence with the NDVI PH with a high coefficient of determination ( $r^2 = 0.84$ ) and the lowest standard error (SEE = 0.127; Table 4-3, figure 4-10). PH for the eight years' average VOD and

NDVI for all the study cropland sites except Saratov 1, which had a significant proportion of grassland (31%), were considered in this correspondence analysis.

**Table 4-3.** Regression parameters for the linear relationships between peak greenness (PH NDVI) and PH VOD.

Frequency	n	Intercept	Slope	R <sup>2</sup>	SEE*
6.9 GHz	48	-0.10648	1.73519	0.770	0.14005
10.7 GHz	48	-0.09882	2.00788	0.844	0.12754
18.7 GHz	48	0.17280	1.66521	0.7814	0.12984

\* indicates standard error of the estimate

The two assumptions for analysis of covariance (ANCOVA) were achieved in our analysis: first, the covariate (peak greenness) was not correlated to the independent variables (factor=microwave frequency) at  $\alpha = 0.05$  significance level; and, second, the covariate NDVI PH was correlated with response variable VOD PH as described in the previous paragraph and in Table 4-3 and figure 4-10. The ANCOVA model revealed that slopes resulted from the linear regression fit between NDVI PH and VOD PH were not significantly different while intercepts were significantly different between pairs of microwave frequencies at 95% significance level ( $\alpha = 0.05$ ;  $p < 0.001$ ). The interpretation is peak greenness (NDVI PH) had a significant and positive effect on VOD PH and the effect is similar for all three microwave frequencies (the effect of NDVI PH on VOD PH did not depend on microwave frequency).

Even though NDVI PH and VOD PH have significant positive correspondence, the latter lagged the former (figure 4-11b). This behavior was expected since microwaves are differentially sensitive to aboveground biomass and canopy water content; in contrast, the VNIR is differentially sensitive to photosynthetically active radiation (PAR) absorption (Viña et al., 2004c). The peak VOD lags the peak greenness by several weeks following delayed increases in vegetation water content and development of aboveground biomass. Average VOD lag for all study years and sites was about two to three weeks, but it varied in time and space, and by microwave frequency (figure 4-11b). We have also presented the PH VOD and NDVI as a function of their respective TTP metric in figure 4-11a for ease of interpretation of the lags in figure 4-11b. The temporal and spatial average PH VOD lag increases as microwave frequency increases. The 6.9, 10.7, and 18.7 GHz VOD PH average lags are 2.1, 2.3 and 2.8 weeks relative to the peak greenness (figure 4-11b and appendix 4-1). PH NDVI lags PH VOD 6.9 GHz on 3 sites only. There were only few sites that showed NDVI PH temporal average lag to that of the PH VOD – three sites for the 6.9, one site for the 10.7 and one site for the 18.7 GHz VOD PH over the study period (all lags less than a week). The 6.9, 10.7, and 18.7 GHz VOD PH temporal average lag ranges between (-) 0.8 – 5.1, (-) 0.1 – 6.7, and (-) 0.9 – 7.2 weeks by site, respectively. These are VOD PH to NDVI PH temporal average lag ranges among the 50 study sites for the three microwave frequencies. The minus signs in parenthesis (-) indicates the PH VOD lead time to the PH NDVI. To check the usefulness of the maximum value-based PH phenometrics determination approach, we correlated NDVI PH determined using this approach with that of the CxQ model. The PH NDVI

from the two methods showed a strong linear relationship with an  $r^2$  of 0.88 (figure 4-12). However, the CxQ model derived peak greenness lags the maximum-value determined peak greenness. On average, the CxQ model derived PH NDVI lags the maximum-value determined PH NDVI by one-half week. Therefore, there was a general underestimation of the PH VOD lags by about one week. On an ecoregional scale, studying AMSR-E SOS and MODIS green-up dates in North America, Jones et al. (2012) found a correspondence between VOD SOS and greenup dates with  $r^2=0.45$  for VOD and NDVI, and  $r^2=0.48$  for VOD and LAI. In cropland dominated ecoregions (63% cropland) in North America, VOD SOS lagged by 5.7 to 12.9 weeks (mean=8.6) compared to the NDVI greenup date (Brown & de Beurs, 2008).

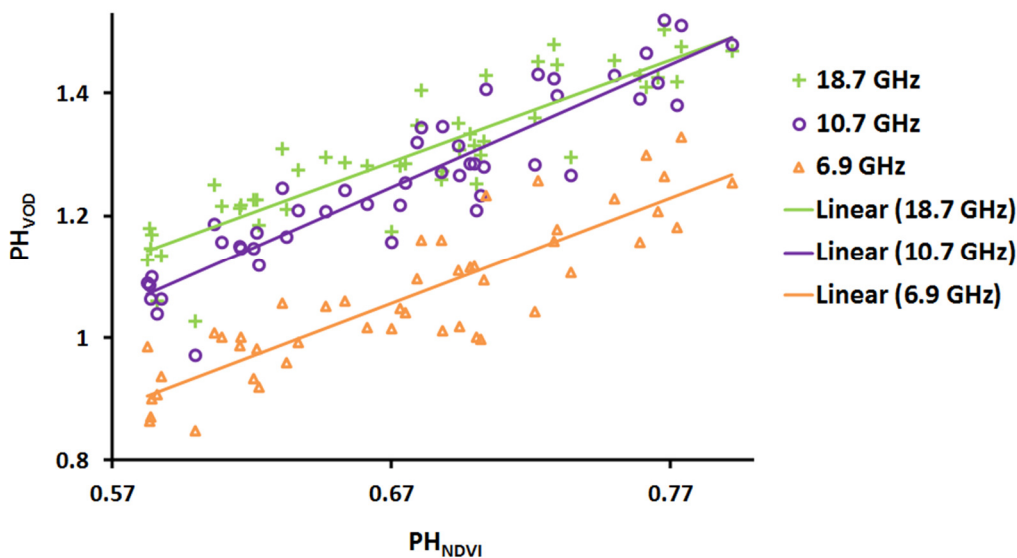


**Figure 4-10.** Scatterplots and linear regression fits of the CxQ model derived NDVI PH and maximum value determined VOD PH at three microwave frequencies (6.9 GHz [orange triangles], 10.7 GHz [purple circles], & 18.7GHz [green plus]) for 2003-2010.

The PH linear fit for two datasets were high with  $r^2$  of 0.77, 0.84, and 0.78 for the 6.9, 10.7, and 18.7 GHz frequencies, respectively.

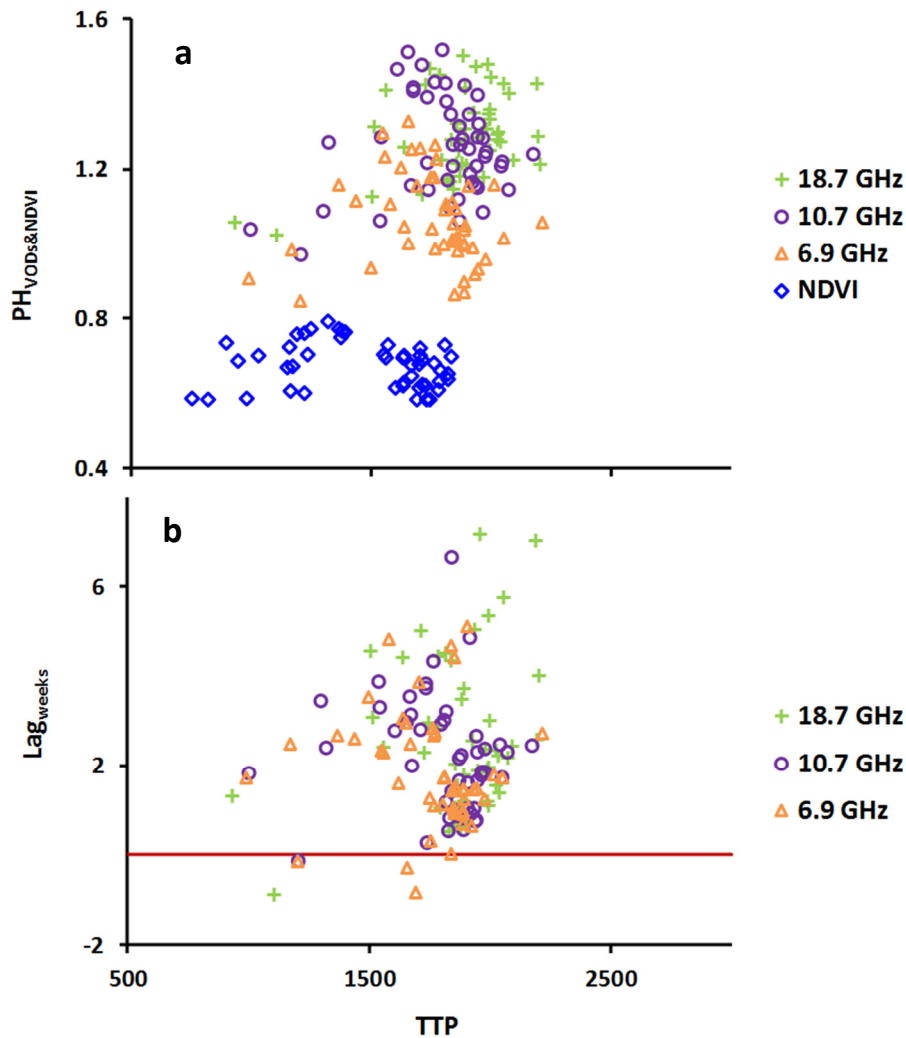


**Figure 4-11.** Scatter plot of (a) the maximum-value determined PH VODs and CxQ model derived PH NDVI phenological metrics as a function of their corresponding TTP, (b) PH VOD lags relative to their corresponding peak greenness as a function of the respective TTP VODs. Note that the PH VODs for all sites except three sites for the 6.9 GHz and one site for the 10.7 and 18.7 GHz PH VODs were lagged from their corresponding PH NDVI (PH VOD lags are above the zero line, b).



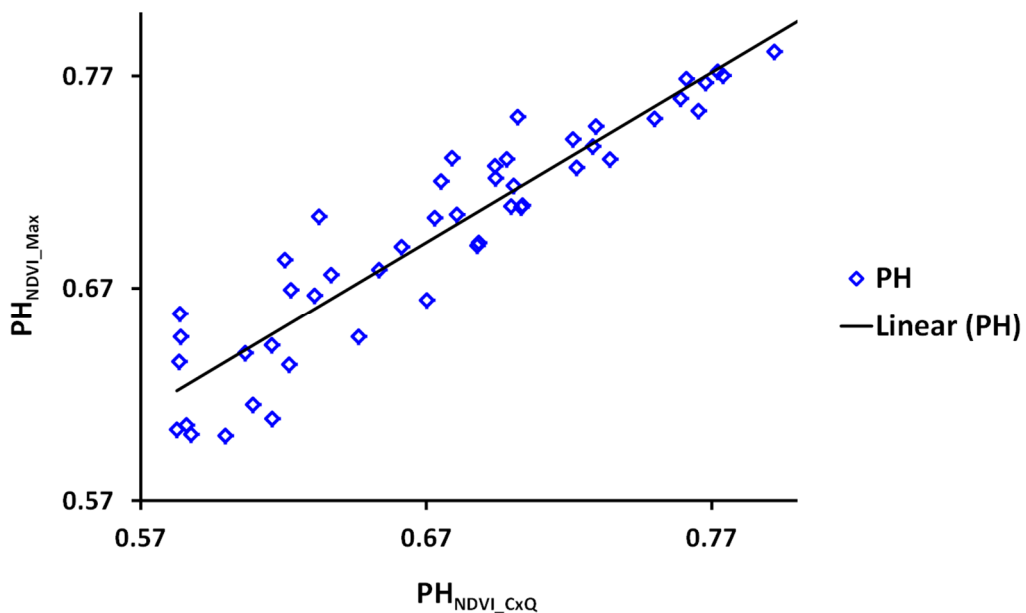


**Figure 4-12.** Scatter plot and linear fit of the CxQ model derived and maximum-value determined NDVI PH from the same MODIS dataset for 2003-2010. The linear fit for PH phenometrics from the two approaches of the same dataset was high with  $r^2$  0.88.

#### 4.4.2 Heatwave Responses of VODs and NDVI

We have noted the 2010 heatwave affecting Russia and Kazakhstan (Dole et al., 2011; Trenberth & Fasullo, 2012) and the 2007 heatwave affecting Ukraine (Founda & Giannakopoulos, 2009) in our previous work (Alemu & Henebry, 2013, 2016). Here, we have presented these heatwave effects on croplands as revealed by the time series of VODs and NDVIs, the relative comparison of the two LSP measures, and also CxQ model derived NDVI PH and NDVI at half-TTP metrics. During the heatwave years the VODs and NDVIs were well below the average VOD and NDVI for non-heatwave years, as croplands were negatively impacted by the heatwave (figure 4-13). Heatwave years are more evident in the VODs compared to their counterpart NDVI, as VOD strongly responds to vegetation water content. The CxQ model derived NDVI at half-TTP as a function of PH NDVI for sites affected by the 2010 heatwave was lower relative to the

other non-heatwave years (figure 4-14). The marker in the upper-right corner marker is the mixed forest site in Mari El, Russia, showing little effect of the heatwave on that site.

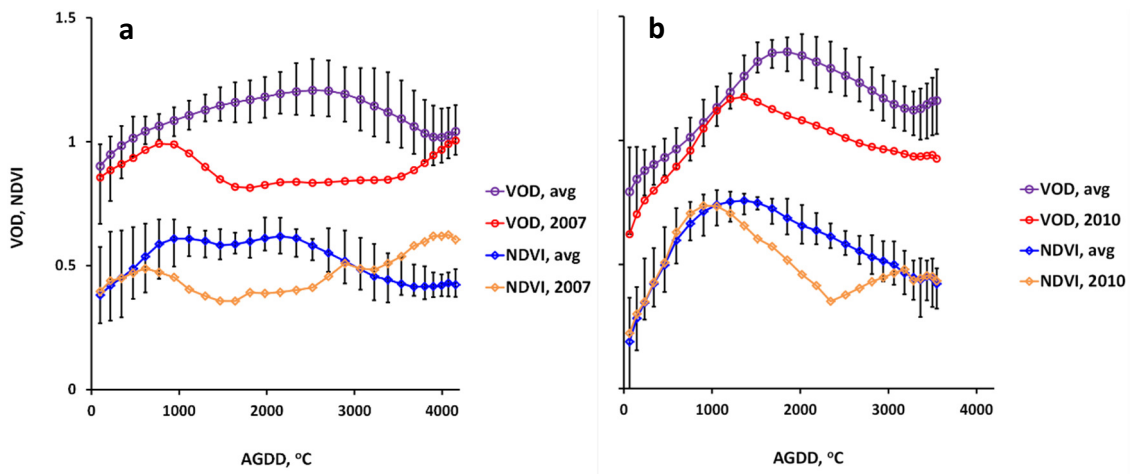


**Figure 4-13.** VOD and NDVI plots for sample sites (a) Mykolayiv, UA, and (b) Voronezh, RU, affected by the 2007 and 2010 Ukrainian and Russian heatwaves, respectively. In both plots, purple circle represents  $VOD_{10.7\text{GHz}}$  and blue diamond represent NDVI plots average (2003 – 2010) excluding the respective heatwave years with relative maximum and minimum error bars. The red circle and orange diamond plots represent heatwave year VODs and NDVIs respectively for both sites. Note the PH in both the average and heatwave affected years. Note also the shapes and magnitudes of the time series in the heatwave years relative to the average of the other years.

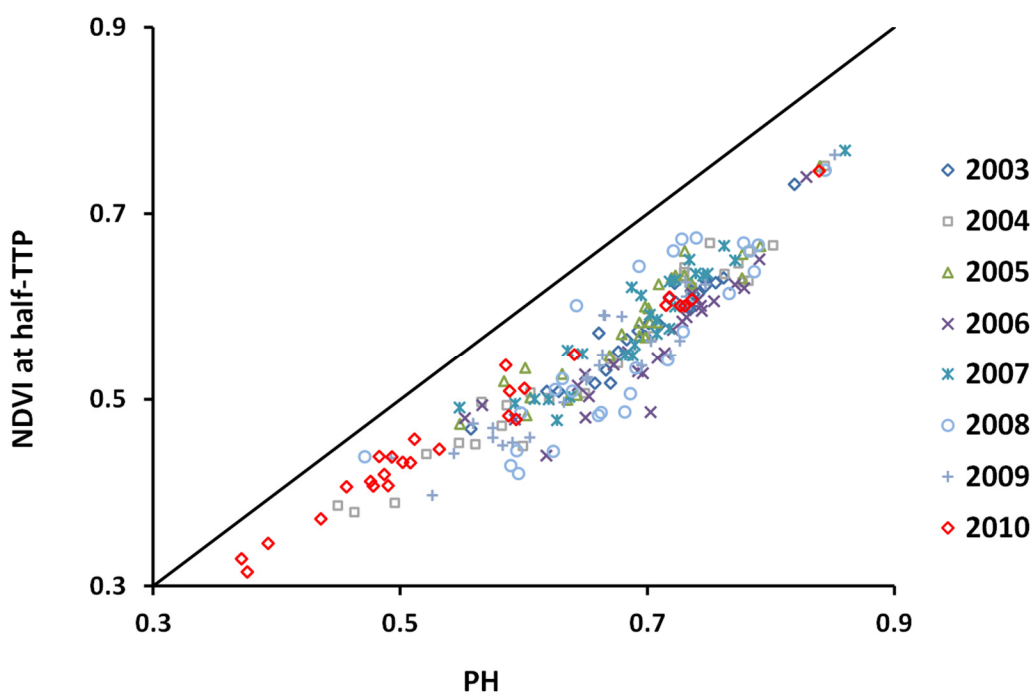


**Figure 4-14.** Scatterplot of NDVI at half-TTP as a function of NDVI PH derived from a CxQ model for the 2010 heatwave affecting Russia and Kazakhstan. Note the position of the 2010 phenometrics presented by red diamonds relative to the other years in their respective sites. Note also the 2010 marker for the upper-right corner which is for the MFO site in Russia (Mari El).

#### 4.5 Conclusions and Recommendations

In this paper we have compared and contrast the peak timing of cropland vegetation maturity using two complementary remote sensing datasets. Time series of LSP of VOD (in three microwave frequencies – 6.9, 10.7, and 18.7 GHz) from the passive microwave Advanced Microwave Scanning Radiometer on EOS (AMSR-E) was able to capture the seasonality of croplands (both bimodal and unimodal seasonal patterns) similar to that of the MODIS NDVI. The higher microwave frequency generates

higher VOD due to the fact that smaller wavelengths are more quickly attenuated by vegetation.

The timing and magnitude of the growing season peak (TTP, PH) are more consistent quantitative cropland phenometrics, in large part because they are minimally affected by snow or frost, unlike the common phenometrics of Start of Season and End of Season. The vegetation optical depth (VOD) retrieved from passive microwave data is more robust to atmospheric effects and biomass saturation than phenometrics based on NDVI.

We have also demonstrated the application of the convex quadratic (CxQ) function to model cropland dynamics using MODIS NDVI yielding strong fits ( $0.78 < r^2 < 0.99$ ). The passive microwave AMSR-E VOD PH determined using the maximum value of the growing season approach favorably corresponded with that of the VNIR MODIS peak greenness (NDVI PH) derived using the CxQ model over the study domain. The 10.7 GHz VOD PH achieved the best linear regression fit ( $R^2=0.84$ ) and with lowest standard error (SEE=0.128) with the NDVI peak greenness and, therefore, recommend for further exploration of VOD-based land surface phenology studies. However, based on an ANCOVA model, the slopes from the linear regression fit are not significantly different by microwave frequency, and thus it is possible to make analysis using anyone of the three microwave frequency VOD. The intercepts from the ANCOVA analysis were significantly different, given the different magnitudes of the VODs in the three

frequencies resulting from the difference in microwave emission attenuation by crop vegetation.

Despite the strong correspondence between peak LSPs of the two datasets, there was a general lag of AMSR-E PH VOD by two – three weeks compared to that of MODIS peak greenness. Based on peak greenness analysis of same dataset using the two procedures, we found a one-week bias of the two methods. We concluded that maximum value based PH VOD can yield phenometrics complementary to those from the CxQ model based on NDVI, especially in cloud and aerosol obscured parts of the world.

We included one representative mixed forest (MFO) site in our analysis to compare it with croplands LSP and LSS. The peak height croplands were found to have more interannual dynamics compared to that of the MFO, due to the more resilience of the MFO for climatic variability and interannual crop and land rotations of croplands.

Even though AMSR-E ceased to function in October 2011 due to antenna failure, its legacy has been continued by AMSR2, which is the improved version of AMSR-E but with similar functionality since May 2012 (Du et al., 2014). In this dataset, the data time gap between the two sensors was filled by the Microwave Radiation Imager (MWRI) sensor data on-board the Chinese FengYun 3B (FY3B) satellite (Du et al., 2015; Du et al., 2014).

#### **4.6 Acknowledgements**

This research was supported in part through the NASA Earth and Space Sciences Fellowship program (NNX13AN58H), and NASA LCLUC (NNX11AB77G) and NASA

Science of Terra and Aqua (NNX14AJ32G) programs. The AMSR-E data were accessed from Numerical Terradynamic Simulation Group (NTSG) website ([www.ntsg.umd.edu/project/amsrelp](http://www.ntsg.umd.edu/project/amsrelp)). The MODIS data were obtained from the NASA/USGS Land Processes Distributed Active Archive Center (LP DAAC) ([https://lpdaac.usgs.gov/products/modis\\_products\\_table](https://lpdaac.usgs.gov/products/modis_products_table)).

#### **4.7 Author Contributions**

W.G.A. and G.M.H conceived and designed the experiments; W.G.A. performed the experiments; W.G.A. and G.M.H. analyzed the data; and W.G.A. and G.M.H. wrote the paper.

#### **4.8 Conflicts of Interest**

The authors declare no conflicts of interest.

#### **4.9 References**

- Alemu, W. G., & Henebry, G. M. (2013). Land surface phenologies and seasonalities using cool earthlight in mid-latitude croplands. *Environmental Research Letters*, 8, 045002. <http://dx.doi.org/10.1088/1748-9326/8/4/045002>.
- Alemu, W. G., & Henebry, G. M. (2016). Characterizing Cropland Phenology in Major Grain Production Areas of Russia, Ukraine, and Kazakhstan by the Synergistic Use of Passive Microwave and Visible to Near Infrared Data. *Remote Sensing*, 8(12). <http://dx.doi.org/10.3390/rs8121016>.

- Brown, M. E., de Beurs, K. M., & Marshall, M. (2012). Global phenological response to climate change in crop areas using satellite remote sensing of vegetation, humidity and temperature over 26 years. *Remote Sensing of Environment*, *126*, 174-183. <http://dx.doi.org/10.1016/j.rse.2012.08.009>.
- DAAC-LP. (2014). MODIS Products Table. Retrived 24 December, 2013, from [https://lpdaac.usgs.gov/dataset\\_discovery/modis/modis\\_products\\_table](https://lpdaac.usgs.gov/dataset_discovery/modis/modis_products_table).
- de Beurs, K. M., & Henebry, G. M. (2004). Land surface phenology, climatic variation, and institutional change: Analyzing agricultural land cover change in Kazakhstan. *Remote Sensing of Environment*, *89*, 497-509. <http://dx.doi.org/10.1016/j.rse.2003.11.006>.
- de Beurs, K. M., & Henebry, G. M. (2008). Northern annular mode effects on the land surface phenologies of northern Eurasia. *Journal of Climate*, *21*, 4257-4279. <http://dx.doi.org/10.1175/2008jcli2074.1>.
- de Beurs, K. M., & Henebry, G. M. (2010). Spatio-temporal statistical methods for modelling land surface phenology. In I. L. Hudson, & M. R. Keatley (Eds.), *Phenological research: Methods for environmental and climate change analysis* (pp. 177-208): Springer Netherlands. [http://dx.doi.org/10.1007/978-90-481-3335-2\\_9](http://dx.doi.org/10.1007/978-90-481-3335-2_9).
- De Bono, A., Peduzzi, P., Kluser, S., & Giuliani, G. (2004). Impacts of summer 2003 heat wave in Europe. *Environment Alert Bulletin no. 2*, UNEP. <http://archive-ouverte.unige.ch/unige:32255>.
- Dole, R., Hoerling, M., Perlwitz, J., Eischeid, J., Pegion, P., Zhang, T., Quan, X.-W., Xu, T., & Murray, D. (2011). Was there a basis for anticipating the 2010 Russian heat

- wave? *Geophysical Research Letters*, 38, L06702.  
<http://dx.doi.org/10.1029/2010GL046582>.
- Du, J., Kimball, J. S., & Jones, L. A. (2015). Satellite microwave retrieval of total precipitable water vapor and surface air temperature over land from AMSR2. *IEEE Transactions on Geoscience and Remote Sensing*, 53, 2520-2531.  
<http://dx.doi.org/10.1109/TGRS.2014.2361344>.
- Du, J., Kimball, J. S., Shi, J., Jones, L. A., Wu, S., Sun, R., & Yang, H. (2014). Inter-calibration of satellite passive microwave land observations from AMSR-E and AMSR2 using overlapping FY3B-MWRI sensor measurements. *Remote Sensing*, 6, 8594-8616. <http://dx.doi.org/10.3390/rs6098594>.
- Founda, D., & Giannakopoulos, C. (2009). The exceptionally hot summer of 2007 in Athens, Greece — a typical summer in the future climate? *Global and Planetary Change*, 67, 227-236. <http://dx.doi.org/10.1016/j.gloplacha.2009.03.013>.
- Friedl, M. A., Sulla-Menashe, D., Tan, B., Schneider, A., Ramankutty, N., Sibley, A., & Huang, X. M. (2010). MODIS collection 5 global land cover: Algorithm refinements and characterization of new datasets. *Remote Sensing of Environment*, 114, 168-182. <http://dx.doi.org/10.1016/j.rse.2009.08.016>.
- Frolking, S., Fahnestock, M., Milliman, T., McDonald, K., & Kimball, J. (2005). Interannual variability in North American grassland biomass/productivity detected by SeaWinds scatterometer backscatter. *Geophysical Research Letters*, 32, L2140.  
<http://dx.doi.org/10.1029/2005GL024230>.



- Frolking, S., Milliman, T., McDonald, K., Kimball, J., Zhao, M., & Fahnestock, M. (2006). Evaluation of the SeaWinds scatterometer for regional monitoring of vegetation phenology. *Journal of Geophysical Research: Atmospheres (1984–2012)*, *111*, D17302. <http://dx.doi.org/10.1029/2005JD006588>.
- Frolking, S., Milliman, T., Palace, M., Wisser, D., Lammers, R., & Fahnestock, M. (2011). Tropical forest backscatter anomaly evident in seawinds scatterometer morning overpass data during 2005 drought in Amazonia. *Remote Sensing of Environment*, *115*, 897-907. <http://dx.doi.org/10.1016/j.rse.2010.11.017>.
- Henebry, G., & de Beurs, K. (2013). Remote sensing of land surface phenology: A prospectus. In M. D. Schwartz (Ed.), *Phenology: An integrative environmental science* (pp. 385-411): Springer, Netherlands. [http://dx.doi.org/10.1007/978-94-007-6925-0\\_21](http://dx.doi.org/10.1007/978-94-007-6925-0_21).
- Henebry, G. M. (2013). Phenologies of North American grasslands and grasses. In M. D. Schwartz (Ed.), *Phenology: An integrative environmental science* (pp. 197-210): Springer Netherlands. [http://dx.doi.org/10.1007/978-94-007-6925-0\\_11](http://dx.doi.org/10.1007/978-94-007-6925-0_11).
- Henebry, G. M., de Beurs, K. M., Wright, C. K., Ranjeet, J., & Lioubimtseva, E. (2013). Dryland East Asia in hemispheric context. In J. Chen, S. Wan, G. Henebry, J. Qi, G. Gutman, G. Sun, & M. Kappas (Eds.), *Dryland East Asia: Land dynamics amid social and climate change* (pp. 23-43): Higher Education Press and Walter de Gruyter GmbH, Berlin/Boston. <http://dx.doi.org/10.1515/9783110287912.23>.

- Jolly, W. M., Nemani, R., & Running, S. W. (2005). A generalized, bioclimatic index to predict foliar phenology in response to climate. *Global Change Biology*, *11*, 619-632. <http://dx.doi.org/10.1111/j.1365-2486.2005.00930.x>.
- Jones, L. A., & Kimball, J. S. (2011). Daily global land surface parameters derived from AMSR-E. Boulder colorado USA: National Snow and Ice Data Center. *Digital media* (<http://nsidc.org/data/nsidc-0451.html>).
- Jones, M. O., Jones, L. A., Kimball, J. S., & McDonald, K. C. (2011). Satellite passive microwave remote sensing for monitoring global land surface phenology. *Remote Sensing of Environment*, *115*, 1102-1114. <http://dx.doi.org/10.1016/j.rse.2010.12.015>.
- Jones, M. O., Kimball, J. S., Jones, L. A., & McDonald, K. C. (2012). Satellite passive microwave detection of North America start of season. *Remote Sensing of Environment*, *123*, 324-333. <http://dx.doi.org/10.1016/j.rse.2010.12.015>.
- Kim, Y., Kimball, J. S., McDonald, K. C., & Glassy, J. (2011). Developing a global data record of daily landscape freeze/thaw status using satellite passive microwave remote sensing. *Geoscience and Remote Sensing, IEEE Transactions on*, *49*, 949-960. <http://dx.doi.org/10.1109/TGRS.2010.2070515>.
- Kimball, J. S., McDonald, K. C., Running, S. W., & Froking, S. E. (2004). Satellite radar remote sensing of seasonal growing seasons for Boreal and Subalpine evergreen forests. *Remote Sensing of Environment*, *90*, 243-258. <http://dx.doi.org/10.1016/j.rse.2004.01.002>.
- Kimball, J. S., McDonald, K. C., & Zhao, M. (2006). Spring thaw and its effect on terrestrial vegetation productivity in the Western Arctic observed from satellite

- microwave and optical remote sensing. *Earth Interactions*, 10, 1-22.  
<http://dx.doi.org/10.1016/j.rse.2004.01.002>.
- Li, L., Njoku, E. G., Im, E., Chang, P. S., & Germain, K. S. (2004). A preliminary survey of radio-frequency interference over the US in Aqua AMSR-E data. *IEEE Transactions on Geoscience and Remote Sensing*, 42, 380-390.  
<http://dx.doi.org/10.1109/TGRS.2003.817195>.
- Liu, Y. Y., de Jeu, R. A. M., McCabe, M. F., Evans, J. P., & van Dijk, A. I. J. M. (2011). Global long-term passive microwave satellite-based retrievals of vegetation optical depth. *Geophysical Research Letters*, 38, L18402.  
<http://dx.doi.org/10.1029/2011GL048684>.
- Liu, Y. Y., Dijk, A. I. J. M., McCabe, M. F., Evans, J. P., & Jeu, R. A. M. (2013). Global vegetation biomass change (1988–2008) and attribution to environmental and human drivers. *Global Ecology and Biogeography*, 22, 692-705.  
<http://dx.doi.org/10.1111/geb.12024>.
- McMaster, G. S. (2005). Phytomers, phyllochrons, phenology and temperate cereal development. *Journal of Agricultural Science*, 143, 137-150.  
<http://dx.doi.org/10.1017/S0021859605005083>.
- McMaster, G. S., & Wilhelm, W. W. (1997). Growing degree-days: One equation, two interpretations. *Agricultural and Forest Meteorology*, 87, 291-300.  
[http://dx.doi.org/10.1016/S0168-1923\(97\)00027-0](http://dx.doi.org/10.1016/S0168-1923(97)00027-0).
- McNairn, H., Duguay, C., Boisvert, J., Huffman, E., & Brisco, B. (2001). Defining the sensitivity of multi-frequency and multi-polarized radar backscatter to post-harvest

- crop residue. *Canadian Journal of Remote Sensing*, 27, 247-263.  
<http://dx.doi.org/10.1080/07038992.2001.10854941>.
- McNairn, H., Duguay, C., Brisco, B., & Pultz, T. J. (2002). The effect of soil and crop residue characteristics on polarimetric radar response. *Remote Sensing of Environment*, 80, 308-320. [http://dx.doi.org/10.1016/S0034-4257\(01\)00312-1](http://dx.doi.org/10.1016/S0034-4257(01)00312-1).
- Min, Q., & Lin, B. (2006). Determination of spring onset and growing season leaf development using satellite measurements. *Remote Sensing of Environment*, 104, 96-102. <http://dx.doi.org/10.1016/j.rse.2006.05.006>.
- Njoku, E. G., Ashcroft, P., Chan, T. K., & Li, L. (2005). Global survey and statistics of radio-frequency interference in AMSR-E land observations. *IEEE Transactions on Geoscience and Remote Sensing*, 43(5), 938-947. doi:  
<http://dx.doi.org/10.1109/TGRS.2004.837507>.
- Owe, M., de Jeu, R., & Walker, J. (2001). A methodology for surface soil moisture and vegetation optical depth retrieval using the microwave polarization difference index. *IEEE Transactions on Geoscience and Remote Sensing*, 39, 1643-1654.  
<http://dx.doi.org/10.1109/36.942542>.
- Owen, S. V., & Froman, R. D. (1998). Focus on qualitative methods uses and abuses of the analysis of covariance. *Research in Nursing and Health*, 21, 557-562.
- Sarma, A., Kumar, T. V. L., & Koteswararao, K. (2008). Development of an agroclimatic model for the estimation of rice yield. *Journal of Indian Geophysical Union* 12, 89-96.

- Schaaf, C. B., Gao, F., Strahler, A. H., Lucht, W., Li, X. W., Tsang, T., Strugnell, N. C., Zhang, X. Y., Jin, Y. F., Muller, J. P., Lewis, P., Barnsley, M., Hobson, P., Disney, M., Roberts, G., Dunderdale, M., Doll, C., d'Entremont, R. P., Hu, B. X., Liang, S. L., Privette, J. L., & Roy, D. (2002). First operational BRDF, albedo Nadir reflectance products from MODIS. *Remote Sensing of Environment*, 83, 135-148. Pii S0034-4257(02)00091-3. [http://dx.doi.org/10.1016/S0034-4257\(02\)00091-3](http://dx.doi.org/10.1016/S0034-4257(02)00091-3).
- Schwartz, M. D., & Hanes, J. M. (2010). Intercomparing multiple measures of the onset of spring in eastern North America. *International Journal of Climatology*, 30, 1614-1626. <http://dx.doi.org/10.1002/joc.2008>.
- Shi, J., Jackson, T., Tao, J., Du, J., Bindlish, R., Lu, L., & Chen, K. S. (2008). Microwave vegetation indices for short vegetation covers from satellite passive microwave sensor AMSR-E. *Remote Sensing of Environment*, 112, 4285-4300. <http://dx.doi.org/10.1016/j.rse.2008.07.015>.
- Trenberth, K. E., & Fasullo, J. T. (2012). Climate extremes and climate change: The Russian heat wave and other climate extremes of 2010. *Journal of Geophysical Research-Atmospheres*, 117, D17103. <http://dx.doi.org/10.1029/2012jd018020>.
- Tucker, C. J. (1979). Red and photographic Infrared linear combinations for monitoring vegetation. *Remote Sensing of Environment*, 8, 127-150. [http://dx.doi.org/10.1016/0034-4257\(79\)90013-0](http://dx.doi.org/10.1016/0034-4257(79)90013-0).
- USDA-FAS. (2011a). Kazakhstan - Crop Production Maps. Retrieved 15 February, 2014, from [http://www.pecad.fas.usda.gov/rssiws/al/kz\\_cropprod.htm](http://www.pecad.fas.usda.gov/rssiws/al/kz_cropprod.htm).

- USDA-FAS. (2011b). Russia - Crop Production Maps. Retrieved 15 February 2014, from [http://www.pecad.fas.usda.gov/rssiws/al/rs\\_cropprod.htm](http://www.pecad.fas.usda.gov/rssiws/al/rs_cropprod.htm).
- USDA-FAS. (2011c). Ukraine - Crop Production Maps. Retrieved 15 February, 2014, from [http://www.pecad.fas.usda.gov/rssiws/al/up\\_cropprod.htm](http://www.pecad.fas.usda.gov/rssiws/al/up_cropprod.htm).
- Viña, A., Henebry, G. M., & Gitelson, A. A. (2004). Satellite monitoring of vegetation dynamics: Sensitivity enhancement by the wide dynamic range vegetation index. *Geophysical Research Letters*, *31*, L04503. <http://dx.doi.org/10.1029/2003GL019034>.
- Wang, J., Price, K. P., & Rich, P. M. (2001). Spatial patterns of NDVI in response to precipitation and temperature in the central great plains. *International Journal of Remote Sensing*, *22*, 3827-3844. <http://dx.doi.org/10.1080/01431160010007033>.
- Wang, Q., Tenhunen, J., Dinh, N. Q., Reichstein, M., Otieno, D., Granier, A., & Pilegarrd, K. (2005). Evaluation of seasonal variation of MODIS derived Leaf Area Index at two European deciduous broadleaf forest sites. *Remote Sensing of Environment*, *96*, 475-484. <http://dx.doi.org/10.1016/j.rse.2005.04.003>.
- Yang, W., Yang, L., & Merchant, J. W. (1997). An assessment of AVHRR/NDVI-ecoclimatological relations in Nebraska, U.S.A. *International Journal of Remote Sensing*, *18*, 2161-2180. <http://dx.doi.org/10.1080/014311697217819>.

## 4.10 Appendix A

**Appendix 4-1.** Study sites average GDD, and PH VOD lags (in weeks) relative to their counterpart PH NDVI

Site No.	Name	Latitude	Longitude	Lag, 6.9	Lag, 10.7	Lag, 18.7	Site No.	Name	Latitude	Longitude	Lag, 6.9	Lag, 10.7	Lag, 18.7
1	Cherkessk, RU	44.4	43.5	2.7	2.4	4.4	26	Kursk, RU	52.1	37.5	5.1	3.8	7.0
2	Stavropol, RU	45.0	42.4	2.6	3.3	3.1	27	Orenburg, RU	52.4	55.2	1.4	1.2	1.1
3	Krasnodar, RU	45.6	39.6	4.8	6.7	7.2	28	Kokshetau 1, KZ	52.7	69.2	2.7	2.5	2.6
4	Simferopol', UA	45.6	34.1	1.7	1.8	1.3	29	Barnaul 2, RU	52.7	83.0	1.0	1.7	1.9
5	Tulcea, UA	45.8	29.2	2.5	3.5	4.6	30	Kuybyshev 2, RU	52.7	50.2	1.1	2.3	4.0
6	Rostov-on-Don 2, RU	46.7	39.8	1.5	2.5	2.3	31	Orel, RU	52.7	35.7	2.7	2.9	3.5
7	Odesa, UA	47.3	30.7	3.1	3.7	4.4	32	Kokshetau 2, KZ	53.0	67.4	1.7	1.7	1.6
8	Rostov-on-Do 1, RU	47.5	40.9	4.7	3.5	4.5	33	Lipetsk, RU	53.0	39.1	1.6	2.0	2.3
9	Donets'k, UA	47.5	37.7	3.6	3.9	5.0	34	Kokshetau 3, KZ	53.7	68.2	0.9	0.8	1.2
10	Mykolayiv, UA	47.5	32.3	4.4	4.9	5.4	35	Kostanay 1, KZ	53.7	63.3	1.0	0.9	0.7
11	Zaporihzhya 1, UA	47.8	35.7	-0.3	0.3	1.1	36	Kostanay 2, KZ	53.7	62.2	0.9	0.5	0.5
12	Zaporihzhya 2, UA	48.1	34.1	1.4	2.4	2.4	37	Kurgan, KZ	53.7	65.6	1.5	1.0	1.0
13	Luhans'k, RU	48.7	40.4	0.7	1.0	0.6	38	Barnaul_1, RU	53.7	79.4	1.5	1.6	1.9
14	Volgograd, RU	48.7	44.8	-0.1	-0.1	-0.9	39	Kokshetau 4, KZ	54.0	69.0	1.1	1.8	1.9
15	Kirovohrad, UA	48.7	31.8	1.8	1.0	2.2	40	Kostanay 3, KZ	54.0	64.0	1.3	0.9	0.7
16	Kharkiv 2, UA	49.0	36.2	1.8	2.2	2.6	41	Petropavlovsk 2, KZ	54.4	70.8	1.5	2.3	2.4
17	Khmel'nyts'kyz, UA	49.0	26.8	3.9	4.3	4.4	42	Petropavlovsk 3, KZ	54.4	67.4	1.1	1.4	1.6
18	Vinnytsya, UA	49.0	28.9	2.3	3.1	5.8	43	Kuybyshev 1, RU	54.4	50.8	2.8	3.0	2.8
19	Poltava, UA	49.6	35.1	1.3	2.7	3.0	44	Ryazan, RU	54.4	39.3	2.5	2.8	3.0
20	Kharkiv 1, UA	49.9	37.0	0.0	0.8	1.1	45	Petropavlovsk 1, KZ	54.7	69.5	1.5	1.7	1.8
21	Saratov 1, RU	50.8	46.9	0.1	-0.3	-0.7	46	Omsk 1, RU	54.7	72.9	1.3	1.9	2.2
22	Sumy, UA	50.8	34.1	-0.8	0.6	1.2	47	Omsk 2, RU	55.0	74.5	0.3	1.8	2.0
23	Semipalatinsk, RU	51.4	81.7	0.6	0.8	1.4	48	Cheboksary, RU	55.7	47.1	3.0	3.0	5.1
24	Voronezh, RU	51.4	39.8	2.9	3.2	3.7	49	Kazan', RU	56.1	49.5	2.3	2.8	2.4
25	Saratov 4, RU	51.8	45.3	1.7	2.2	2.0	50	Mari El*	56.4	48.4	-0.7	4.7	6.9
	<b>Max*</b>										<b>5.1</b>	<b>6.7</b>	<b>7.2</b>
	<b>Min*</b>										<b>-0.8</b>	<b>-0.1</b>	<b>-0.9</b>
	<b>Average*</b>										<b>2.7</b>	<b>2.9</b>	<b>3.1</b>

\*excludes Saratov 1 and Mari El

## **CHAPTER 5 : Land Surface Phenology and Seasonality Using Cool Earthlight in Croplands of Eastern Africa**

### Paper #4

Alemu, W.G.; Henebry, G.M.; Senay G.B. Land Surface Phenology and Seasonality Using Cool Earthlight in Croplands of Eastern Africa. To be submitted in February, 2017

**Research Question:** Is it possible to characterize cropland dynamics in tropical eastern Africa using the blended AMSR-E/AMSR2 passive microwave dataset?

**Research Answer:** Yes,

- Croplands in eastern Africa displayed distinct spatio-temporal dynamics tracked in moisture time (CVD) rather than in thermal time (AGDD).
- The passive microwave blended AMSR dataset was revealed effects of the El Niño/Southern Oscillation (ENSO) and Indian Ocean Dipole (IOD) climate modes on croplands in eastern Africa
- Linkages to crop production statistics were uncertain, due to significant discrepancies between data officially reported to FAO and the interannual variability of growing season conditions.
- More reliable crop production and yield data, perhaps available at lower administrative levels or independent sources are needed to verify these linkages.



## 5.0 Abstract

Across eastern Africa, croplands cover 45 million ha. The traditional rain-fed agriculture in the region is moisture limited, which is vulnerable to extreme weather events that leads to food insecurity. Weather station data are scarce and access is limited, while optical satellite data are obscured by heavy clouds limiting their value to study cropland dynamics. Here, we characterized cropland dynamics in eastern Africa for 2003-2015 using precipitation data from Tropical Rainfall Measuring Mission (TRMM) and a passive microwave dataset of land surface variables that blends data from the Advanced Microwave Scanning Radiometer (AMSR) on the Earth Observing System (AMSR-E) from 2002-2011 with data from AMSR2 from 2012-2015 with a Chinese microwave radiometer to fill the gap. These time series were analyzed in terms of either cumulative precipitable water vapor-days (CVD) rather than as day of year. Time series of the land surface variables displayed unimodal seasonality at study sites in Ethiopia and South Sudan, in contrast to bimodality at sites in Tanzania. Interannual moisture variability was at its highest at the beginning of the growing season affecting planting times of crops, while it was lowest at time of peak moisture. Actual evapotranspiration (ETa) from the simple surface energy balance (SSEB) model was sensitive to track both unimodal and bimodal rainfall patterns. ETa as a function of cumulative ETa days (CETaD) was fitted by a convex quadratic model ( $r^2 > 0.8$ ) better than precipitable water vapor ( $r^2 > 0.6$ ). Moisture time to peak (MTP) for the land surface variables showed strong and logical correspondence among variables (all  $r^2 > 0.73$ ). Land surface parameters responded to El Niño-Southern Oscillation and the Indian Ocean Dipole forcings. Area

under curve of the diel difference in vegetation optical depth) showed strong correspondence to crop production and yield data at the woreda (or district) level.

## 5.1 Introduction

Across eastern Africa, croplands cover 45 million ha. Ethiopia (ET) and Tanzania (TZ) are the two major crop producing countries in the region, accounting for 14 million ha and 13 million ha of croplands, respectively. The African economy is heavily dependent on smallholder traditional rain-fed peasant agriculture (up to 90% in East Africa), which is vulnerable to extreme weather events such as drought and floods (Adhikari et al., 2015; Becker-Reshef et al., 2010; Brown et al., 2010). Food crops mainly produced in the region include maize, sorghum, wheat, barley, millet, rice, teff (produced only in Ethiopia), beans and peas (Dixon et al., 2001). Farming systems in Ethiopia are mainly highland temperate mixed and maize mixed, while in Tanzania it is mainly maize mixed, and in South Sudan cereal-root crop mixed (Dixon et al., 2001). The highland temperate mixed farming system produces small grains, such as wheat, barley, teff, and livestock. The maize mixed farming system mainly produces maize and livestock. In the cereal-root crop mixed farming system, production is based on cereals (e.g., maize, sorghum, millet), vegetables, and animal products. Moreover, sluggish economic development in the region has been unable to feed the fast growing population, leading to chronic risk of regional food insecurity (Funk et al., 2008; Korotayev & Zinkina, 2015).

In Ethiopia, there is a minor rainy season in March called *belg*, while the main rainy season falls between June and September, known as *kiremt*). Tanzania experiences a short rainy season between October and December and longer rains between March and May; while in South Sudan, the rainy season spans May to October. Regional rainfall trends have been decreasing but they are highly variable in space and time (Lyon & DeWitt, 2012). Thus, the region has been one of the most food insecure parts of the world. A study in western Africa found that the timing and length of the sowing period depend on the arrival of rains and soil moisture (Brown & de Beurs, 2008). During the past century, shortage of rainfall in Ethiopia led to recurrent drought, which has resulted in substantial shortfalls in agricultural production and recurrent famine (Rientjes et al., 2013). However, highland regions get excess rainfall concentrated into the few months of their rainy season, which leads to flooding and soil erosion that, in turn, deplete soil nutrients and reduce crop productivity.

To address issues of food insecurity, we need a comprehensive understanding of cropland dynamics for major commodity crops. Land surface dynamics in tropical eastern Africa are less well characterized than those in the major crop growing regions of developed nations. We used our previous experience using passive microwave data to track temperate cropland dynamics in the spring wheat belts of the Northern Hemisphere (Alemu & Henebry, 2013, 2016, 2017) as reference areas to contrast with the cropland dynamics of tropical East Africa.

Many studies have used vegetation indices (VIs) derived from visible and near infrared (VNIR) sensors to study land surface phenology (LSP) in terms of day of year (Ganguly et al., 2010; Sakamoto et al., 2006; Zhang et al., 2004), but far fewer using thermal time (Alemu & Henebry, 2013, 2016, 2017; de Beurs & Henebry, 2004; Henebry, 2013; Henebry & de Beurs, 2013). However, tropical croplands generally do not have temperature constraints; rather, they are strongly dependent on rainfall and moisture for crop growth and development. In addition, the skies over eastern Africa are obscured by heavy seasonal clouds and dust contamination, limiting intensive observation of the vegetated land surface by VNIR sensors as well as reducing insolation and surface air temperature. To characterize cropland dynamics in eastern Africa, specifically in Ethiopia, Tanzania, and the new nation of South Sudan, we used rainfall data from TRMM (Tropical Rainfall Measuring Mission) and a blended dataset (Du et al., 2014) of enhanced land surface variables from the passive microwave radiometers AMSR-E (Advanced Microwave Scanning Radiometer on EOS) and AMSR2 (hereafter simply AMSR). These variables were characterized in terms of cumulative precipitable water vapor days, which is a continuous field in space and time, in contrast to rainfall. These products are critical in regions where meteorological stations are sparse and high quality rainfall measurements are missing or unavailable (Bolten & Crow, 2012; Bolten et al., 2010), such as eastern Africa. The finer temporal resolution of passive microwave datasets is also another significant advantage to monitor cropland dynamics, given the rapid pace of plant growth and development. The major drawback of passive microwave

datasets is their coarse spatial resolution (25 km) relative to the region's small field sizes and fragmented croplands.

## **5.2 Study Region, Data, and Methodology**

### **5.2.1 Study Region**

Across eastern Africa, croplands cover 45 million ha. Our study focuses on croplands in the two major crop producing countries in the region, Ethiopia (ET) and Tanzania (TZ), and in the new nation of South Sudan (SS). Ethiopia and Tanzania contain 14 million ha and 13 million ha of croplands, respectively. South Sudan, however, remains a bit of a mystery; it is still too new and torn by civil war to appear in the FAO agricultural databases.

Specific AMSR pixels were selected in these countries in a two-step process. We first developed cropland cover stability map in eastern Africa for cropland class (12) from the International Geosphere Biosphere Program (IGBP) land cover scheme using the MODIS fractional land cover layer in MCD12C1 for 2003-2012. We calculated the maximum, minimum, and mean land cover percentage over the study period and then displayed the maximum, mean, and range in the red, green, and blue color planes, respectively (Henebry et al., 2013). Thus, yellow shows temporally stable core areas of the cropland class; white shows temporally unstable core areas; magenta displays unstable peripheral areas; and black shows where the croplands class did not occur 2003-2012 (figure 5-1, table 5-1). The MODIS land cover product could not resolve finely fragmented croplands in the study region and, therefore, while we used the MODIS data as general guidance, we used the finer resolution imagery available in Google Earth

Image to select and check visually our study sites. We have identified 100 study AMSR cropland pixels, 14 in Tanzania, 6 in South Sudan and 80 in Ethiopia (figure 5-1).

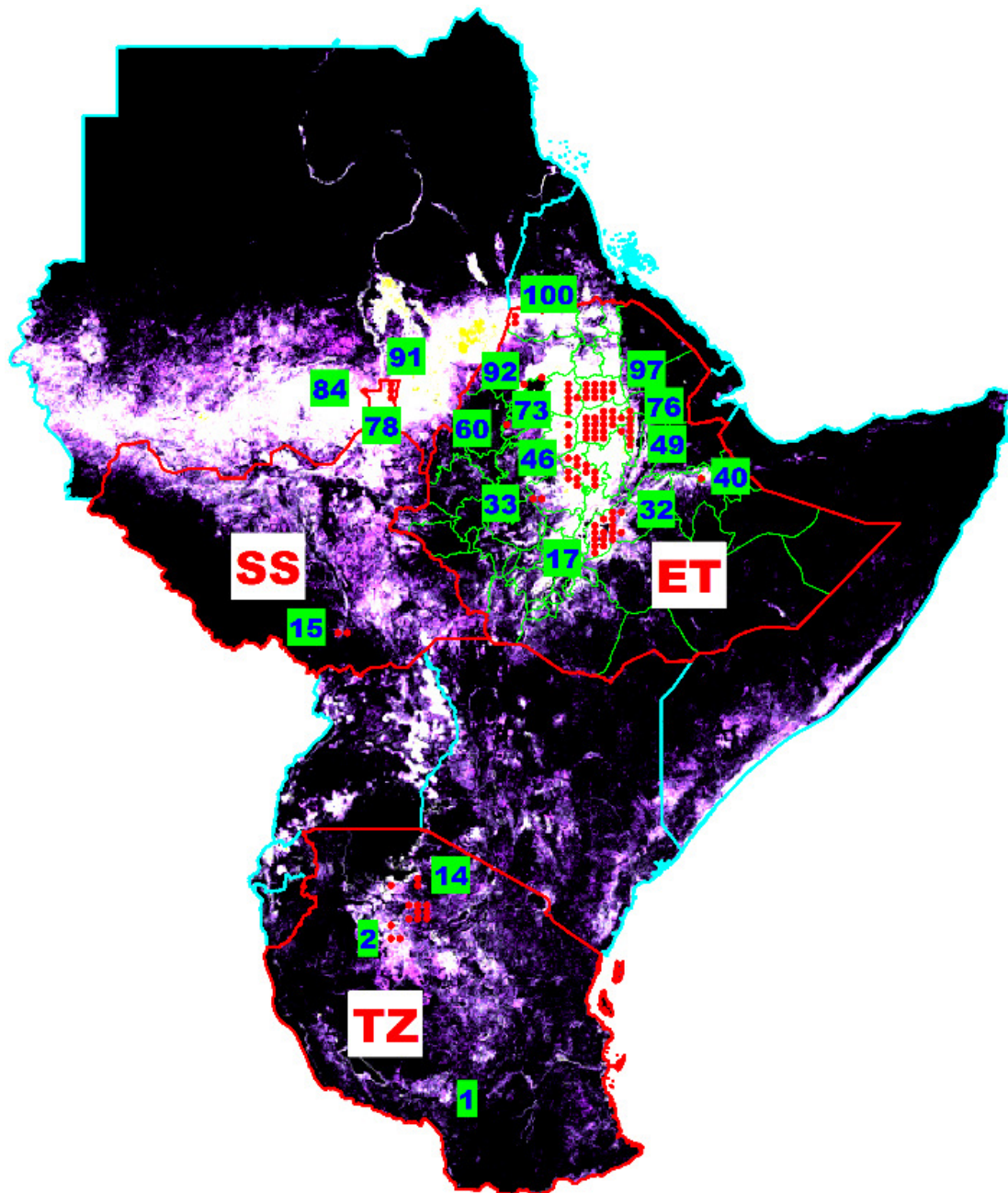


**Figure 5-1.** Cropland class stability map in East Africa for 2003–2012. Yellow shows stable core cropland areas; white displays unstable core areas; magenta displays unstable

peripheral areas; and black shows where croplands do not occur in the study period. Superimposed are 100 AMSR pixels (red dots) selected on dominant cropland areas. Pixels are numbered from S to N and then from W to E (all numbers are not labeled due to space limitations).

**Table 5-1.** Interpretive legend for Figures 5-1 that display IGBP MODIS 0.05° land cover variation from 2003-2012 in the study region. Modified from (Henebry et al., 2013)

Color in LC Map	Red = Max% LC	Green = Mean% LC	Blue = Range% LC	Interpretation
Black	None	None	None	Land cover (LC) class absent
Blues	Low	Low	High	Temporally unstable but ephemeral periphery; rare and erratic
Magentas	High	Low	High	Temporally unstable but persistent periphery; sometimes high, but usually low
Whites	High	High	High	Temporally unstable core; sometimes low, but usually high
Yellows	High	High	Low	Temporally stable core of LC; always high, so range is low

We subset the Landsat 7 ETM+ 30m resolution Global Land Cover data layer (tree cover, bare ground, and waterbodies; USGS, 2016) by each study AMSR pixels and calculate the proportions of these land cover within each AMSR pixel. The tree cover and bare ground were raster layers with proportion of these covers per pixel (1-100%) in 2010, while the water layer was a thematic layer where the ground was persistently water from 2000-2012. The tree cover and bare ground that were within the AMSR study pixels were averaged separately. Proportion of waterbodies within the AMSR pixel were also calculated. Thus, a given AMSR pixel can have proportional tree cover, bare ground,

water, and other residual land covers. Any residual percentage land cover could be croplands, shrubs, and other land covers. In our case, since we purposely selected cropland dominated AMSR pixels for this study, residual land covers should be mainly croplands, but at some of these locations there could be a mixture of grasslands and shrublands. Among our study pixels, there are two sites (92 and 98) that have a considerable proportion of waterbody, 25% and 30%, respectively (figure 5-2). These sites are located near Lake Tana, the biggest lake in Ethiopia. There are some other sites with up to 30% of tree cover and bare ground combined.



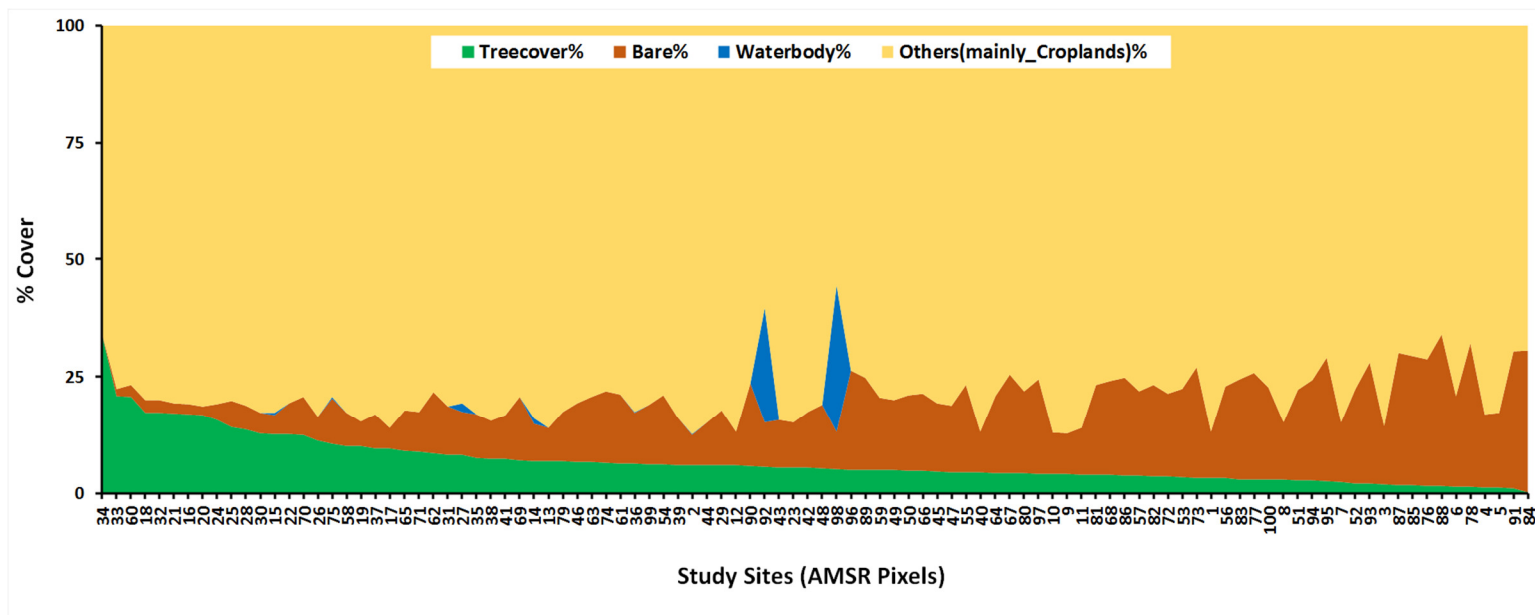


**Figure 5-2.** Percent tree cover, bare ground, and waterbody from the Landsat ETM+ 30m resolution Global Land Cover product. Data from (USGS, 2016).

### 5.2.2 Remote Sensing Data

Here, we have primarily used variables retrieved from the passive microwave data of AMSR-E and AMSR2. The AMSR-E was launched onboard the NASA-EOS Aqua satellite in May 2002 and operated successfully for more than 9 years before it stopped properly functioning in October 2011, due to failure of the rotational antenna spin mechanism. Its measurement legacy has been effectively continued since May 2012 by AMSR2, which is the improved version of AMSR-E, but with similar functionality. AMSR2 is onboard the Japan Aerospace Exploration Agency (JAXA) Global Change Observation Mission 1st-Water (GCOM-W1) “SHIZUKU” satellite. We used the blended AMSR-E/AMSR2 dataset developed by the Numerical Terradynamic Simulation Group (NTSG) at the University of Montana (Du et al., 2014). The NTSG filled the gap between the AMSR-E and AMSR2 sensors using brightness temperature observations from the Microwave Radiation Imager (MWRI) onboard the Chinese FengYun 3B (FY3B) satellite that was launched in November 2010 (Du et al., 2014). The AMSRs record observations twice daily (daytime ~1330 and nighttime ~0130). The gridded data products have a spatial resolution of 25 km. The NTSG blended AMSR dataset includes up to twice daily observations from June 2002 to December 2015 of surface air temperatures ( $t_a$ ; ~2 m height), fractional open water inundation ( $fw$ ), vegetation canopy transmittance ( $tc$ ) at 10.65 GHz, volumetric soil moisture ( $vsm$ ;  $\leq 2$  cm soil depth), and atmosphere precipitable water vapor ( $V$ ) for the total column (Du et al., 2014; Jones & Kimball, 2011). The data set will continue to be extended as long as the AMSR2 continues to produce data (J.S. Kimball, personal communication).

The second dataset used in this study is rainfall data from TRMM, which combines active and passive microwave sensors. A joint US-Japan space mission, TRMM was launched in November 1997 to monitor and study tropical rainfall (50° N – 50° S latitude), and officially concluded on April 15, 2015. Its measurement legacy is continued by the Global Precipitation Measurement (GPM) mission that was launched on February 2014. The TRMM Multi-satellite Precipitation Analysis (TMPA) version 7 (TRMM 3B42 (V7)) is a 3-hourly temporal resolution and a 0.25-degree by 0.25-degree spatial resolution rainfall dataset developed by NASA. It provides TRMM-adjusted gridded rainfall rate (mm/hr) data from multiple satellite independent precipitation estimates (TRMM, 2011b). Here, we have used the daily accumulated rainfall product that is derived from the 3-hourly product (TRMM 3B42 (V7)-daily; TRMM, 2011a).

We also used actual evapotranspiration (ET<sub>a</sub>) data estimated from the simple surface energy balance model (SSEB, Senay et al., 2007; Senay et al., 2013). These data have 1 km spatial resolution and 10 day (dekadal) temporal resolution. The datasets used as input for the SSEB model include (1) MODIS Land Surface Temperature (MOD11A2), (2) MODIS 16-day NDVI product at 250-m resolution (MOD13Q1), and (3) global 1-degree reference evapotranspiration (ET<sub>o</sub>) based on NOAA's 6-hourly Global Data Assimilation Systems (GDAS) model output.

We chose AMSR pixels dominated by croplands. We used the 30 m Global Land Cover data developed by USGS and the University of Maryland, Department of Geographical Sciences (USGS, 2016). It includes land cover

classes derived from Landsat 7 ETM+ data: tree cover (ca. 2010), open water (as persistent surface water layer 2000-2012) and bare ground (ca. 2010) (USGS, 2016). We used these data to calculate the proportions of these classes within our study sites.

For specific cropland study area identification, we mainly used two datasets: the International Geosphere Biosphere Programme (IGBP) global land cover classification scheme in the MODIS land cover product at spatial resolution of  $0.05^\circ$  (MCD12C1; DAAC-LP, 2014), and the USDA Foreign agriculture service (FAS) crop layers ([USDA-FAS, 2015a](#)). Since the croplands are fragmented across the study region, we also used finer spatial resolution imagery available through Google Earth for a close visual check to select the specific cropland sites.

### **5.2.3 Methods**

We analyzed 14 full years (2003–2015) of twice-daily AMSR data. We applied an 8-day retrospective moving average filter to daytime and nighttime AMSR data separately to minimize data gaps due to orbit and swath width. We then averaged the daytime and nighttime values for all variables except surface air temperature ( $t_a$ ) to get one value per 24 hours. The  $t_a$  time series were processed into growing degree-days (GDD), the daily thermal-time increment above a certain threshold (base temperature) for plant growth (de Beurs & Henebry, 2004; McMaster & Wilhelm, 1997; Sarma et al., 2008). GDD were calculated from the AMSR air temperature ( $t_a$ ) data with a base temperature of  $0^\circ\text{C}$  ( $=273.15\text{ K}$ ) as follows:

$$\text{GDD} = \max\left[\frac{t_{ASC} + t_{DES}}{2} - 273.15, 0\right] \quad [1]$$

where  $t_{ASC}$  and  $t_{DES}$  are ascending and descending pass temperatures, which roughly corresponds to the maximum and minimum daily temperatures.

We previously modeled the seasonal course of NDVI in temperate croplands as a convex quadratic function of accumulated growing degree-days (Alemu & Henebry, 2013, 2016, 2017). However, for the moisture limited croplands of tropical eastern Africa, this approach is not appropriate: temperature is not the key limiting factor in the timing and progress of crop growth.

To illustrate the differential seasonality of croplands, Figure 5-3 displays growing degree-days (GDD) and precipitable water vapor (V) at two cropland sites, one in Zegie, Ethiopia and the other in Saratov, Russia, showing the quasi-periodic behavior of GDD versus V in both croplands. At the tropical site, a larger dynamic range of V and smaller dynamic range of GDD within the year is evident compared to the temperate site (figure 5-3). This pattern reflects that moisture is the key limiting factor in the tropical croplands, and temperature is limiting in the temperate croplands. Brown & de Beurs (2008) successfully applied a convex quadratic model in western Africa croplands to characterize cropland NDVI as a function of accumulated relative humidity.

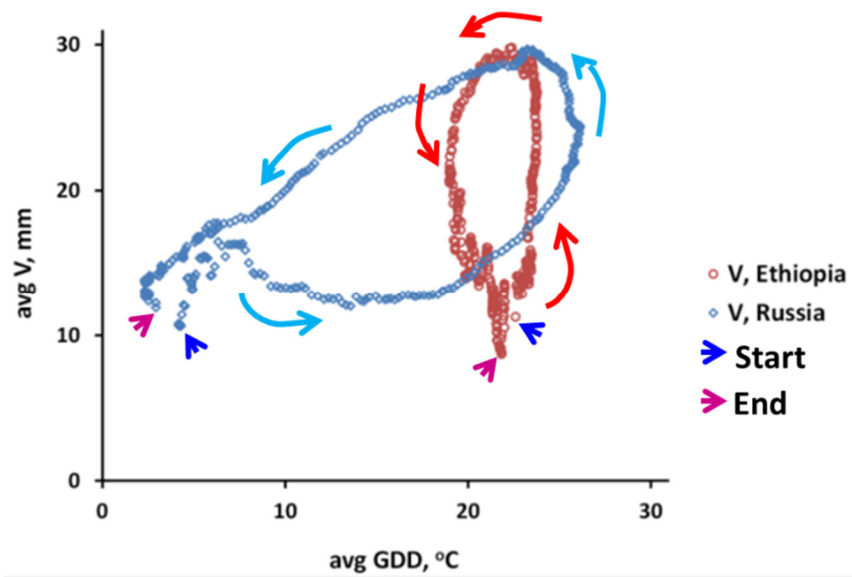


**Figure 5-3.** Scatterplot of 30-day retrospective moving average of mean AMSR-E atmospheric water vapor (V) as a function of average growing degree-days (GDD) for Zegie, Ethiopia (maroon circles), and Saratov, Russia (blue diamonds) for 2003 to 2010. Blue arrows indicate initial points in January, while magenta arrows indicate end points of the annual cycle in December. Red arrows show intra-annual cycles of V for Zegie, ET and cyan arrows for Saratov, RU. Note the relative dynamical range of the variables.

Rainfall in eastern Africa is erratic and sporadic. In contrast, precipitable water vapor (V), is a continuous spatiotemporal field. Thus, we analyzed the time series of biophysical and climatic variables as a function of precipitable water vapor. Cumulative water vapor days (CVD) are the simple summation of AMSR V throughout the whole year. That is, the passage of days is weighted by the quantity of V occurring that day:

$$CVD_t = CVD_{t-1} + V_t \quad [2]$$

where  $V_t$  is daily precipitable water vapor at time  $t$ .

Vegetation Optical Depth (VOD) was calculated as a negative logarithm of vegetation transmittance [ $VOD = -\log_e(tc) = -\ln(tc)$ ]. From a daily TRMM rainfall data, we calculated 8-day retrospective cumulative rainfall for our study.

The actual evapotranspiration (ETa) estimates were a retrospective summation for every 10 days (dekad). To match the time scale, we produced comparable AMSR and TRMM dekadal datasets by summing the daily data. We compare the ETa data with the AMSR and TRMM datasets. We have cumulative annual ETa and V data (designated as CETaDd [Cumulative ETa Dekad] and CVDDd [Cumulative V Dekad]) to characterize all our study variables as a function of CETaDd and CVDDd:

$$CETaDd_t = CETaDd_{t-1} + ETa_t \quad [3]$$

$$CVDDd_t = CVDDd_{t-1} + V_t \quad [4]$$

where ETa is dekadal actual evapotranspiration, and  $V_t$  is dekadal atmospheric precipitable water vapor at time t.

To characterize the seasonal progression of moisture, we fitted the ETa from SSEB model product and V from AMSR as a convex quadratic (CxQ) functions of CETaDd and CVDDd, respectively:

$$ETa_t = \alpha + \beta CETaDd_t - \gamma CETaDd_t^2 \quad [5]$$

$$V_t = \alpha + \beta CVDDd_t - \gamma CVDDd_t^2 \quad [6]$$

where the intercept  $\alpha$  is the start of observation period ETa/V value, the linear parameter  $\beta$  affects the slope, and the quadratic parameter  $\gamma$  controls the

curvature. Since our model is convex quadratic in shape, the sign of  $\beta$  is positive while the sign of  $\gamma$  is negative.

At sites with two rainfall seasons, the ETa and V time series display bimodal patterns. At these sites, we fitted two separate CxQ models, one for each rainfall season. From the observed data, the breakpoints for these two rainfall seasons were more or less similar in time and space, but different between the northern and southern hemispheres. Therefore, for the CxQ model fit, we divided the observations into two growing season phases. The first phase for Ethiopia and South Sudan ran from DOY 001 – 201 (January 1<sup>st</sup> - July 20<sup>th</sup>) and the second phase ran from DOY 202-365 (July 21<sup>st</sup> - December 31<sup>st</sup>). In Tanzania, the phases ran from DOY 182-052 (July 1<sup>st</sup> – February 21<sup>st</sup>) and DOY 053-181 (February 22<sup>nd</sup> – June 30<sup>th</sup>).

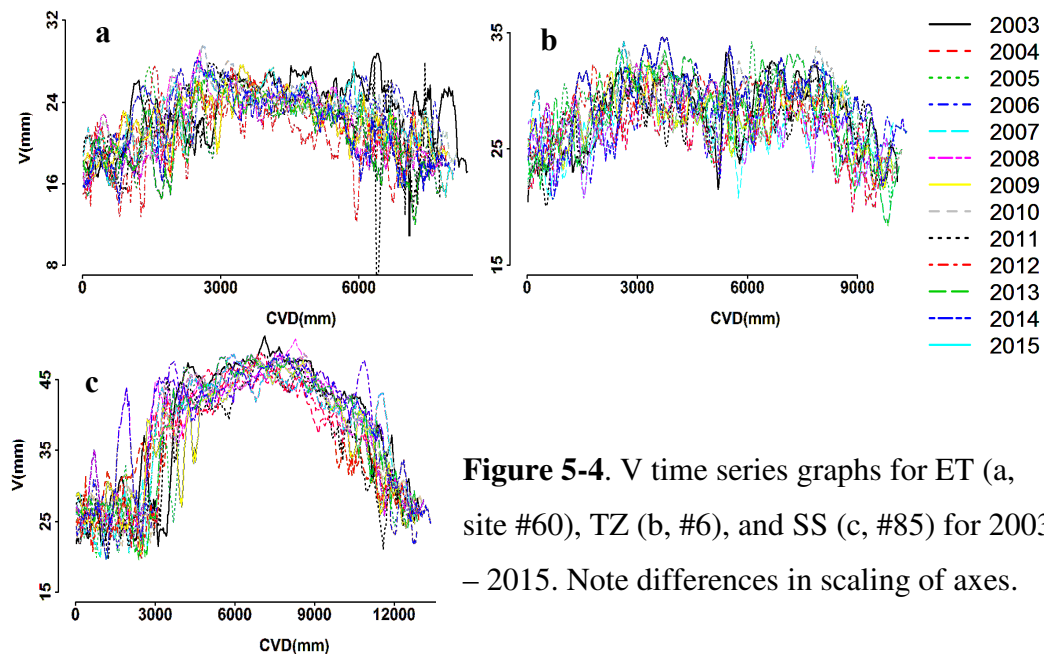
We modeled characteristics of each biophysical and climatic variable in terms of cumulative moisture time. We determined Peak Height (PH) of each variable using the seasonal maxima, and the corresponding moisture time to peak (MTP) measured in CVDs. We also calculated the PH lag time between biophysical and climatic variables.



## 5.3 Results

### 5.3.1 Land Surface Seasonalities of Precipitable Water Vapor

Precipitable water vapor ( $V$ ) in the northwestern and central parts of the croplands in the Ethiopian highlands displayed weak unimodal seasonality and stronger intra-seasonal variation (figure 5-4). Croplands in the drier lowlands of northern South Sudan experienced strong unimodal  $V$  seasonality and minimal intra-seasonal variation. Croplands in Tanzania showed clear bimodal  $V$  seasonality as well as strong intra-seasonal variation.



### 5.3.2 Land Surface Seasonality and Phenology of AMSR Land Parameters & TRMM Rainfall

AMSR land surface parameters and TRMM rainfall time series displayed a unimodal seasonality in Ethiopia and South Sudan, while there is clear bimodality for sites in Tanzania. In Ethiopia, there is a minor rainy season in

March called *belg*, while the main rainy season, locally known as *kiremt*, falls between June and September. Study sites in Tanzania experience a short rainy season between October and December and longer rains between March and May.

In the drier lowlands of South Sudan, there was high intra-annual dynamic range of V and soil moisture (vsm) and higher magnitude of V and GDD (figure 5-5b, #78) compared to the highlands of Ethiopia (figure 5-5a, #73) or Tanzania (figure 5-5c, #14). Rainfall and VOD had higher magnitude in the humid highlands of Ethiopia followed by Tanzania. In Ethiopia vsm rose as the rainy season starts, and sharply dropped as VOD increased due to soil moisture drawdown by growing vegetation, and finally bounced back as the canopy senesced.

GDD dropped during the rainfall and active vegetation growing season, despite the overhead sun during this time of the year. First, the rainfall season in this part of the world is characterized by a heavy cloud deck that reflects back much of the insolation, thereby reducing the amount of light available at the surface for plant growth (Dagg et al., 1970; Woodhead, 1966, 1967). Second, evapotranspiration from actively growing crops cools down the surrounding air (evaporative cooling) (lower Bowen Ratio; Alemu & Henebry, 2016).

The behavior of VOD as a function of CVD exhibited distinctive land surface phenology trajectories. During the growing season, VODs rapidly ascended to a unimodal peak value and declined gradually. The pace of fractional green vegetation cover development was quicker than during its disappearance (figure 5-6). The diel difference in the VOD ( $VOD_{dd} = VOD_{DSC} - VOD_{ASC}$ ) was highest during the rainy season due to high evapotranspiration in daytime by actively growing crop vegetation.

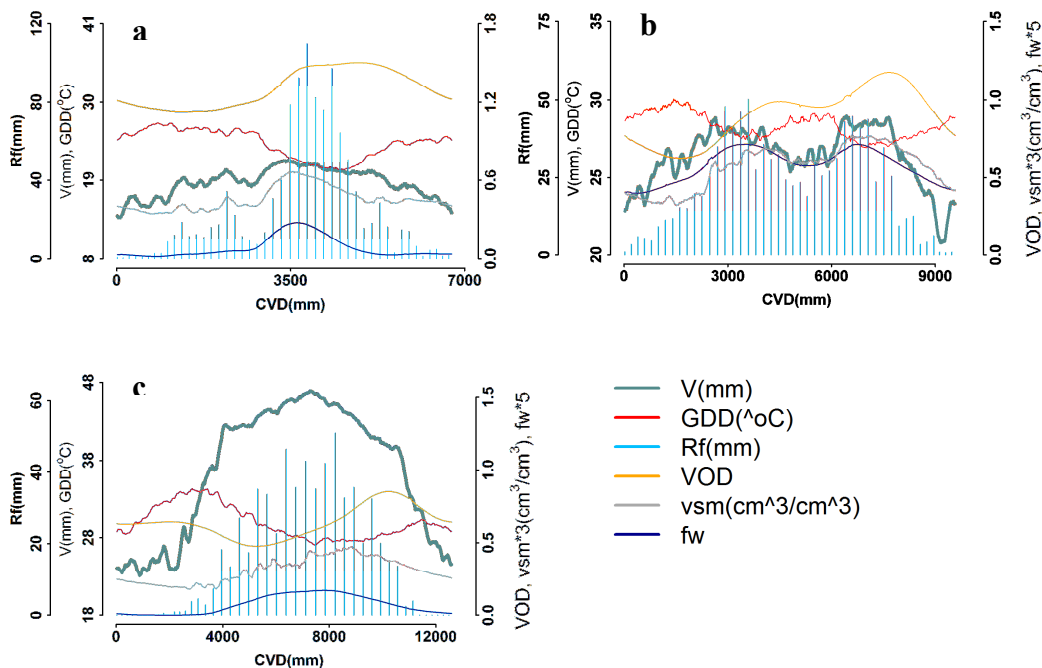


**Figure 5-5.** Line graphs and bars of multiyear average (2003-2015) of AMSR V, GDD, vsm, fw and VOD (10.65GHz) with TRMM rainfall (Rf) as a function of cumulative vapor days (CVD) for an AMSR pixel at sites in Ethiopia (a, #73), South Sudan (b, #78) and Tanzania (c, #14). Note axes scaling differs.

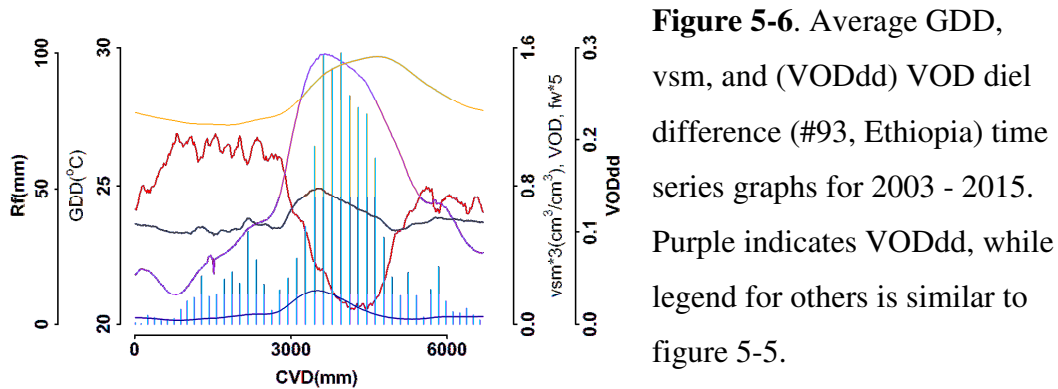


**Figure 5-6.** Average GDD, vsm, and (VODdd) VOD diel difference (#93, Ethiopia) time series graphs for 2003 - 2015. Purple indicates VODdd, while legend for others is similar to figure 5-5.

### 5.3.3 Land Surface Seasonality of Soil Moisture

Interannual moisture variability was at its highest at the beginning of the growing season affecting planting times of crops, while it was at its lowest at the time of peak moisture. Variability was higher for South Sudan sites (figure 5-7c, #91) followed by Tanzania (figure 5-7b, #5), while it was lower for Ethiopia (figure 5-7a, #35).

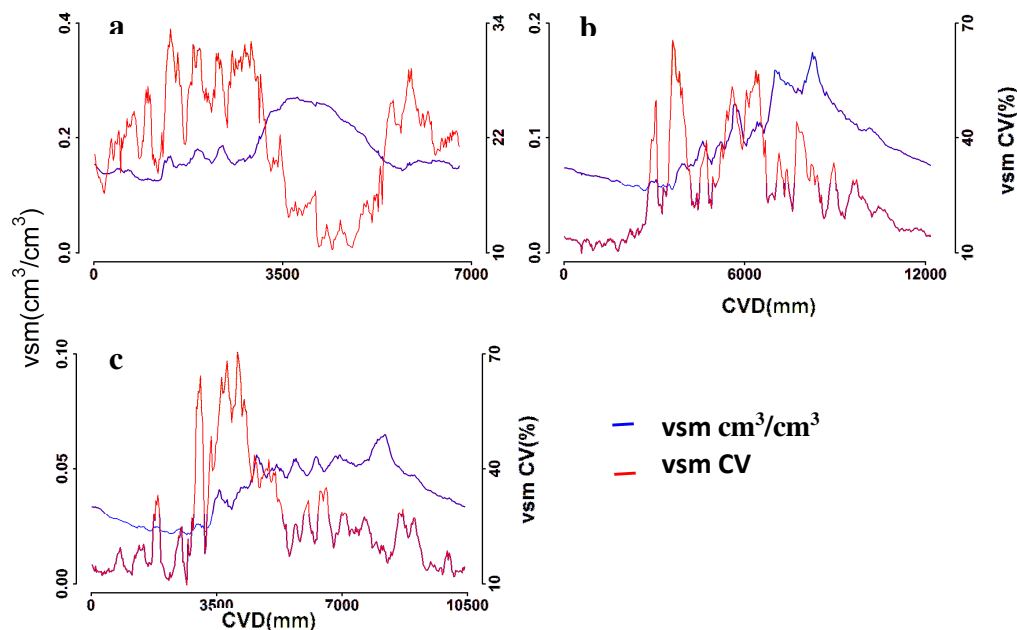


**Figure 5-7.** Average (2003 – 2015) vsm superimposed with its interannual CV (%) and standard error bars for site #35 (a, Ethiopia), #5 (b, South Sudan), & #91 (c, Tanzania). Note axes scaling differs.

### 5.3.4 Land Surface Seasonality of Actual Evapotranspiration

Actual evapotranspiration (ETa) from the simple surface energy balance model closely tracked the rainfall pattern in time and space. ETa was very sensitive to track both the unimodal and bimodal rainfall patterns (figure 5-8). ETa increased while there was sufficient soil moisture for evapotranspiration demand and reached its peak slightly later than the peak rainfall period (~ two weeks; table 5-2). The ETa from the active growing vegetation and the wet ground in the rainfall season cooled down the surrounding surface air (evaporative cooling) resulting in lower GDD. The relationship among these land surface and atmospheric variables held true for both the unimodal and bimodal growing season dynamics. ETa was higher at lowland cropland sites that received enough moisture for evapotranspiration demand.

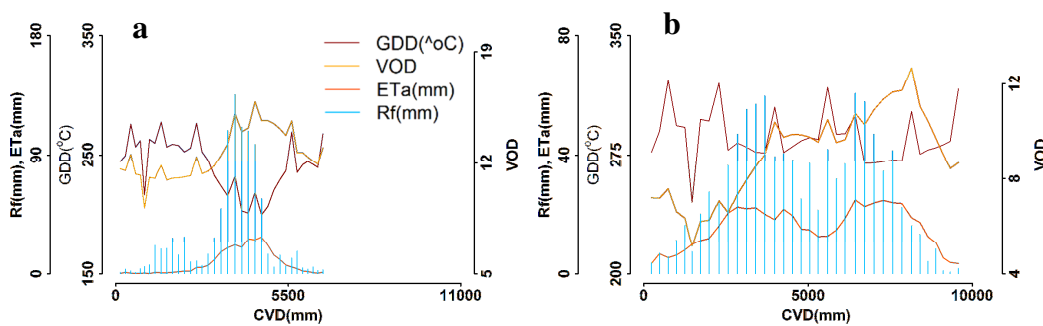


**Figure 5-8.** Time series of MODIS rainfall, SSEB ETa, and AMSR GDD and VOD for (a) #87, Ethiopia and (b) #14, Tanzania for 2003–2015. Note relationships among variables.

The CxQ model fits for ETa and V for sites with unimodal growing season were strong (figure 5-9a&b). The CxQ fits of ETa and V at sites with bimodal growing seasons were fitted with two separate models, one for each growing

season (figure 5-9c&d). These fits were generally strong, but the fits of the second (main) growing season were better ( $r^2>0.8$ ) than the first growing season ( $r^2>0.6$ ). ETa fits were better than the V fits. ETa displayed sharp seasonal dynamics, being more responsive to rainfall and soil and vegetation moisture compared to V.

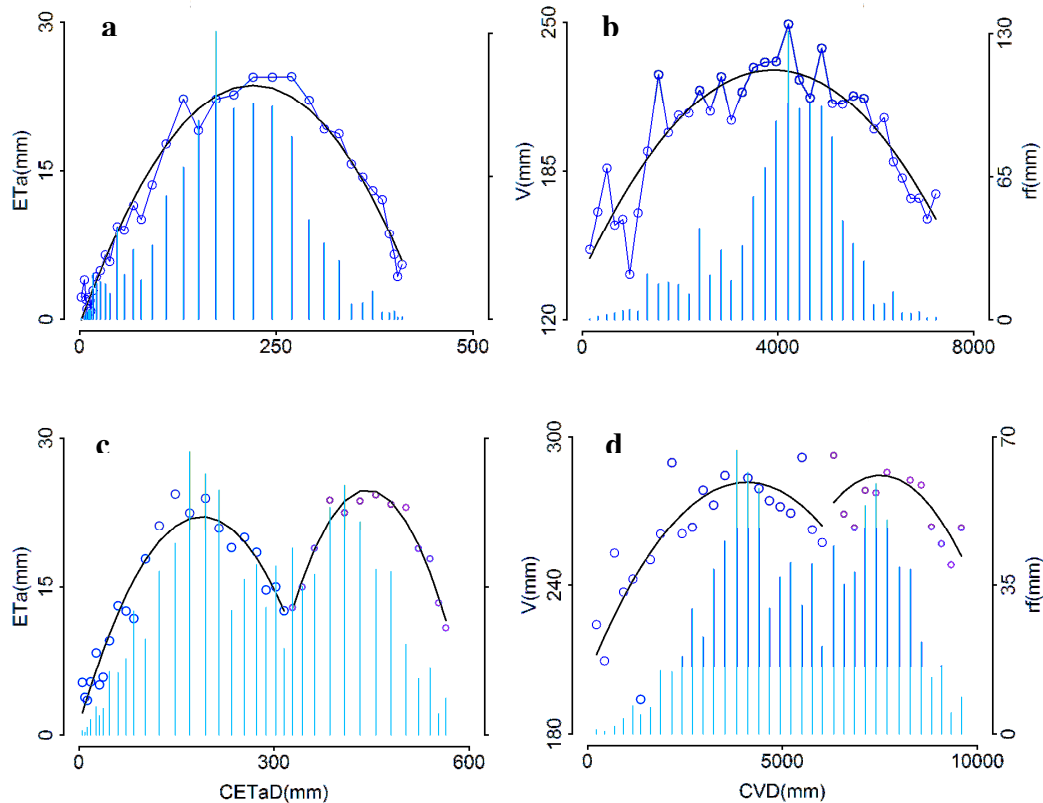


**Figure 5-9.** Convex quadratic model fit of average ETa (unimodal [a,  $r^2=0.97$ ] and bimodal [c,  $r^2=0.93\&0.96$ ]) and V (unimodal [b,  $r^2=0.79$ ] and bimodal [d,  $r^2=0.63\&0.38$ ]) growing season for 2003-2015. Blue bars are rainfall (rf) graphs for the same period. (a&b) are for site #48, Ethiopia, while (c&d) are for site #14, Tanzania. Note the relative dynamics of ETa and V in relation to rf; and also axis value differences for the given variables by site.

### 5.3.5 Seasonal Peak and Moisture Time to Peak (MTP) for Land Surface

#### Phenologies and Seasonalities

Moisture time to peak (MTP) for LSPs and LSSs showed strong correspondence between and among land surface parameters derived from AMSR, rainfall from TRMM, and ETa from SSEB with  $r^2 > 0.73$  for most variables in the Ethiopian study sites (figure 5-10). Furthermore, lags between variables were logical. For example, MTP rainfall lagged MTP precipitable water vapor by about five weeks, since the precipitable water vapor has to pass through the process of condensation (figure 5-10; table 5-2). MTP volumetric soil moisture leads MTP rainfall due to earlier achievement of wetting and saturation period of the soil ahead of peak rainfall period. In addition, soil moisture was drawn down by actively growing crop vegetation, decreasing the soil moisture. The soil moisture saturation period depends, in part, on soil texture and type, land cover type, and land use. MTP VOD lags the MTP rainfall and volumetric soil moisture by about seven and eleven weeks, respectively. In Ethiopia VOD attained its peak in mid-October, while rainfall peaks in mid-August. The MTP for some variables occurred about the same time, e.g., MTP VOD diel difference & MTT GDD (Moisture Time to Trough, which is the CVD to the seasonal lowest GDD). GDD dropped to its lowest point due to evaporative cooling from the growing crop. There was no relationships of MTP among variables in the South Sudan sites due to few data points and different land covers of cropland and crop-natural vegetation mosaic sites. The same holds true for the Tanzanian sites where some sites support a double growing season while others support single growing season.

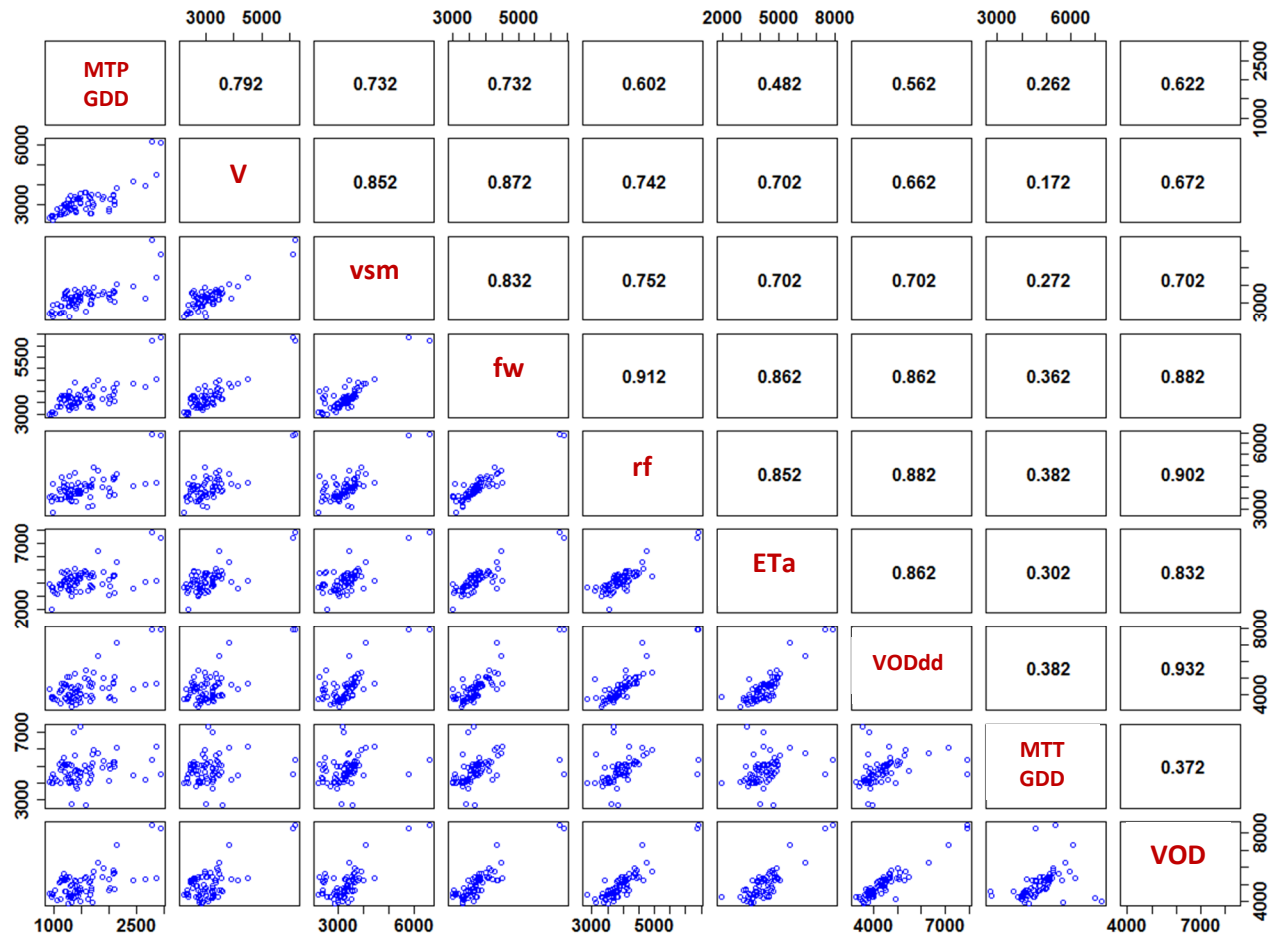


**Figure 5-10.** Moisture Time to Peak (MTP) or Moisture Time to Trough (MTT) for cropland land surface variables in Ethiopia for 2003 to 2015 ( $r^2 > 0.8$ ). The variables listed in the diagonal of the figure from top-left to bottom-right include moisture time to peak or trough for MTP for growing degree-days (MTP GDD), precipitable water vapor (V), volumetric soil moisture (vsm), fractional open water (fw), rainfall (rf), actual evapotranspiration (ETa), vegetation optical depth diel difference (VODdd), MTT for growing degree-day (MTT GDD), and vegetation optical depth (VOD). Note that peak rf lags peak V, peak soil moisture, and peak VOD; but VODdd lags peak rf. Upper panel shows the Pearson correlation coefficients. All correlations were significant with  $p < 0.01$ . To identify variables combination for any given plot or r-value, make horizontal and vertical lines towards the diagonal line of the square matrix containing the variables.



**Table 5-2.** MTP lag in weeks between each variable averaged in space and time (2003-2015) for Ethiopian sites. Note that these lags can vary in space and time for particular sites.

	MTPGDD	MTPV	MTPvsm	MTPfw	MTPRf	MTPETa	MTPVODdd	MTTGDD	MTPVOD
MTPGDD		11	12	15	16	18	20	20	24
MTPV			1	4	5	7	9	9	12
MTPvsm				3	4	6	7	8	11
MTPfw					1	3	4	5	8
MTPRf						2	3	4	7
MTPETa							2	2	5
MTPVODdd								0	4
MTTGDD									3
MTPVOD									

## 5.4 Discussion

### 5.4.1 Climate Modes

Primary climate variables, such as pressure, temperature, and precipitation, are forced in part by intrinsic dynamical modes of the climate system. These modes include the Arctic Oscillation (AO) and its Southern Hemisphere counterpart the Antarctic Oscillation (AAO), also known as the Northern and Southern Annular Mode (NAM and SAM, respectively), the El Niño-Southern Oscillation (ENSO), the Pacific Decadal Oscillation (PDO), and the Indian Ocean Dipole (IOD), among others (Behera et al., 2005; Wang & Schimel, 2003).

Due to these dynamic modes, climatic variability in one part of the planet can be teleconnected to a geographically distant part of the planet. Many observed climatic changes can be related to one of more of the leading modes (Wang & Schimel, 2003). Crop production in eastern Africa is traditional and rainfed, which therefore is susceptible to climatic mode anomalies, particularly to extremes of the ENSO and IOD modes.

#### ***5.4.1.1 El Niño/Southern Oscillation and the Indian Ocean Dipole***

Rainfall over eastern Africa responds to global scale circulation patterns linked to conditions in both the Pacific and Indian oceans, such as the ENSO and the IOD (Behera et al., 2005; Black, 2005; Nicholson, 2015; Owiti et al., 2008; Williams & Hanan, 2011). Rainfall in the region is influenced more by IOD than ENSO (Behera et al., 2005; Hoell & Funk, 2014; Hoell et al., 2016; Marchant et al., 2007; Williams & Hanan, 2011). Niño3, one of many complementary ENSO indices, is the sea surface temperature (SST) anomaly averaged over the region spanning 150°–90°W, 5°S–5°N (Meyers et al., 2007). El Niño events have usually produced anomalously drier conditions in eastern Africa, while La Niña events are associated with wetter conditions (Nicholson & Kim, 1997; Schreck & Semazzi, 2004; Souverijns et al., 2016). IOD is represented by an anomalous SST gradient between the western equatorial Indian Ocean (50E-70E and 10S-10N) and the southeastern equatorial Indian Ocean (90E-110E and 10S-0N; Saji et al., 1999; Webster et al., 1999). This gradient is named as Dipole Mode Index (DMI). When the DMI is positive, the phenomenon is referred to as a positive IOD, and vice versa. Positive IOD is associated with wetter periods in eastern Africa; whereas, negative IOD means drier periods (Black, 2005; Nicholson & Kim, 1997; Pervez & Henebry, 2015; Schreck & Semazzi, 2004; Williams & Hanan, 2011).

Here we used the monthly time series of the Optimum Interpolation Sea Surface Temperature (OISST.v2) Niño3 index from NOAA National Weather Service Climate Prediction Center (NOAA, 2015b) to identify El Niño and La Niña events during our study period. To identify positive and negative Indian Ocean Dipole (IOD) phenomena, we used the Dipole Mode Index (DMI) time series from Japan Agency for Marine-Earth

Science and Technology (JAMSTEC), which is based on the Hadley Centre Sea Ice and Sea Surface Temperature (HadISST) dataset (JAMSTEC, 2016).

For the ENSO analysis, we standardized the Niño3 index data using a 30-year (1986 – 2015) climatology to obtain the average and standard deviation (Meyers et al., 2007; NOAA, 2015a). We then filtered the standardized data using a 5-month retrospective moving average (Meyers et al., 2007; figure 5-11). If the index value exceeded  $\pm 1$  for at least two consecutive months in the rainy season, that year was labeled as El Niño for positive deviations or La Niña for negative deviations (Meyers et al., 2007). A similar approach was applied to the DMI time series with the positive (or negative) IOD mode indicated by the DMI remaining above 1 (or below -1) for at least two consecutive months in the rainy season (Meyers et al., 2007). Any given year may experience a positive (El Niño) or negative (La Niña) or neutral ENSO mode and a positive or negative or neutral IOD mode. Therefore, there were nine possible combinations of these events in a given year. Five of the nine possible ENSO/IOD events combinations were observed during the study period, and no instance of a negative IOD was observed (table 5-2).

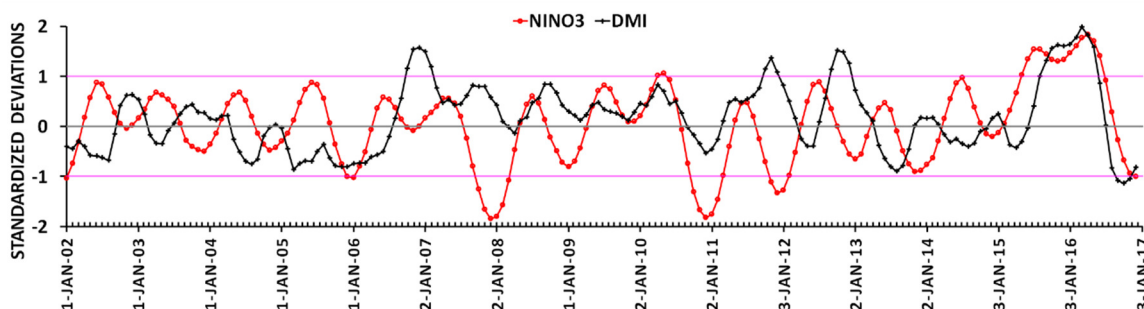


**Figure 5-11.** Thirty years (1986-2015) standardized anomaly five months retrospective smoothed time series plots of NIÑO3 (blue) and DMI (black) for 2002–2016. Pink horizontal lines represent  $\pm$  standard deviation.

**Table 5-3.** Classification of years when El Niño or La Niña and/or positive or negative Indian Ocean dipole occurred.

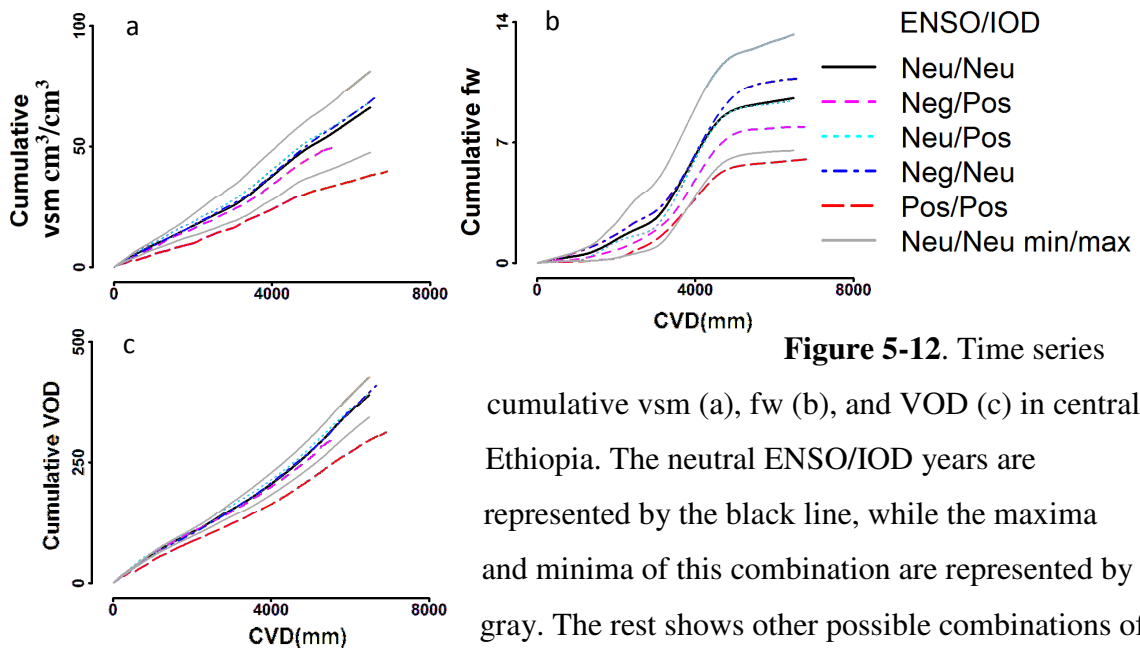
IOD/ENSO	-ve IOD	Neutral	+ve IOD
El Niño	--	--	2015
Neutral	--	2003-2005, 2008-2009, 2013-2014	2006, 2012
La Niña	--	2007, 2010	2011

In 2006, a positive IOD year, brought heavy rainfall to the region (figure 5-12, table 5-2), resulting in major nationwide flooding in Ethiopia (DPPA, 2006; Gashaw & Legesse, 2011; IFRC, 2006; Jury, 2011; UN-OCHA, 2006). Moreover, the rainfall was concentrated in few months of the rainy season causing unprecedented flooding. The flood affected eight out of the country's eleven administrative regions and led to acute food insecurity for at least for 10 million people (IFRC, 2006; UN-OCHA, 2006). This extreme event caused internal mass displacement and considerable damage to property and infrastructure. In addition, the floods contributed to an increased incidence of water-borne diseases, including acute watery diarrhea (UN-OCHA, 2006).

In 2010, a La Niña year, there was heavy rainfall and flooding in Ethiopia (IFRC, 2010). The flooding affected nearly 1 million people across several administrative regions (UNCIEF, 2011). Rainfall in 2010 was above normal but distributed throughout the rainy season. Thus, the flooding and associated damage in Ethiopia were not as severe as in 2006 (IFRC, 2006, 2010). Soil moisture and fractional water were high in these positive IOD and La Niña years compared to the neutral years, while the VOD looked similar to the neutral years (figure 5-12).

The worst drought in over 30 years occurred in 2015. It claimed human and animal life and devastated crop production, especially in eastern Ethiopia (FEWS-NET,

2016; GEOGLAM, 2016; IFPRI, 2015; UN-OCHA, 2016; UN-WFP, 2016). More than 10 million people (~10 % of Ethiopia's population) were in need of food assistance (UN-OCHA, 2016; UN-WFP, 2016). This year was both an El Niño and a positive IOD year (figure 5-11; table 5-2). Even though the effect of El Niño and positive IOD may have been expected to cancel out each other (Pervez & Henebry, 2015; Williams & Hanan, 2011), the severe drought of 2015 might be due to the three months of the El Niño event occurring before the positive IOD mode (in 2015 NINO3>1 occurred three months earlier than DMI>1; figure 5-12). In figure 5-12, soil moisture (a) and fractional water (b) in 2015 (both represented by red dashed color) were well below the minimum boundary envelope of the neutral years (gray color). Since the severe drought devastated crop production, VOD in 2015 (figure 5-12c; red color) was well below to that of the minimum boundary of the neutral years. In 2016, a La Niña year, most parts of eastern Africa received heavy rainfall (FEWS-NET, 2016).



ENSO/IOD.

**Figure 5-12.** Time series cumulative vsm (a), fw (b), and VOD (c) in central Ethiopia. The neutral ENSO/IOD years are represented by the black line, while the maxima and minima of this combination are represented by gray. The rest shows other possible combinations of

#### 5.4.2 Crop Production Responses to Biophysical Factors

We gathered agricultural sample survey reports for Ethiopia for 2003 to 2014 at zone level (CSA, 2015a, 2015b; HarvestChoice, 2015) organized by Ethiopian Central Statistical Agency (CSA). The reports are for “private peasant holdings” by season of production organized at three levels (national, regional and zonal levels) and each level includes crop area, crop production and yield by crop type. More than 85% of Ethiopian population is a rural resident dependent mainly on small holding subsistence agriculture. Commercial farms in Ethiopia are few and are limited to the remote peripheral lowlands of the country. We also obtained woreda (district) level crop production and yield data for 2014 from the Amhara National Regional State Bureau of Agriculture (ANSR BoA) organized by the Zonal agricultural offices.

We used the assumption that crop biomass and crop evapotranspiration are linked to crop production to link cropland LSP to crop production and yield statistical data in the region. We calculated the area under the curve (AUC) for the growing season VOD as a proxy for crop biomass and the AUC for the growing season VOD diel difference ( $VOD_{dd}$ ) as a proxy for crop evapotranspiration. We calculated separate AUCs for the VODs derived from the ascending and descending orbits in addition to the average VOD. We assessed the relationship between the growing season maximum VOD and the crop production data, since growing season maximum NDVI has corresponded with crop production data in past research (Bolton & Friedl, 2013b). Actual evapotranspiration data from the simplified surface energy balance (SSEB) model was used to link it with crop production and yield data. One way to determine the AUC cut points (points to start and end the integration) was by using volumetric soil moisture (vsm) dynamics. The vsm

started to rise continuously as the main rainfall season began, and then started to drop as moisture was drawn down by growing crops. The moisture started to rise again as the crop dried out (figure 5-13). The AUC was integrated between the cut points, and the crop production and yield data were linked to AUCs using simple linear regression.

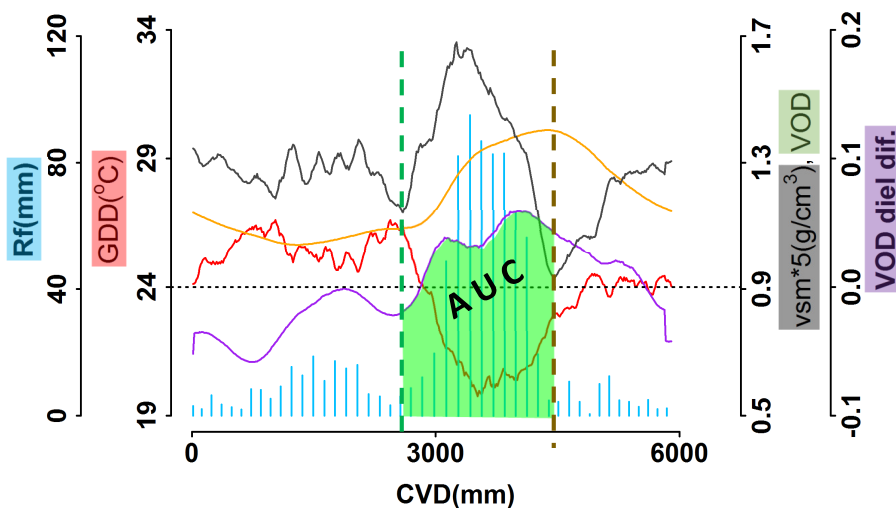


**Figure 5-13.** AUC of VODdd (green area under purple curve) at AMSR pixel cropland site in Ethiopia (Site 82). The cut points were determined based on the seasonality of volumetric soil moisture.

Even though crop production statistical data lower level of aggregation and AMSR data spatial resolution were comparable in size, they may not necessarily overlap each other. Therefore, before trying to link crop production and the derived LSP and LSS metrics (AUC, maximum VOD, and rainfall), we normalized these variables as follows.

$$\text{Crop production: } CA_s/TAA*CP_s \quad [7]$$

where  $CA_s$  is cultivated area in a given administrative division at season  $s$ ,  $TA$  is administrative division total area, and  $CP_s$  is crop production at season  $s$ . This formulation presumes that the crop production is evenly distributed across the

administrative division, but while we know that agriculture is not evenly distributed, it is a reasonable first-order assumption given the scale differences of these data.

$$\text{LSP or LSS metric: } OA/TPA * PSM \quad [8]$$

where OA is overlap area of AMSR pixel and administrative division, TPA is total sampled AMSR pixel(s) area, and PSM is the LSP or LSS metric.

We examined crop production and yield data for the Amhara Region of Ethiopia at two administrative levels: woreda (smaller) and zone (larger). Some zone were also included from Oromia Region, Ethiopia. The woreda level data were collected by Amhara National Regional State Bureau of Agriculture (ANRS BoA) for 2014. These data were better fit ( $r^2=0.60$ ) by a logarithmic curve (figure 5-14a) than a line ( $r^2=0.57$ ; data not shown). This fit may be attributable to VOD saturation, exaggerated crop production reports, and/or spatial extent disagreement between the satellite product and the crop production areal unit unresolved by the normalization. Jones et al. (2011) found that there is little evidence of VOD signal saturation at higher biomass levels. VODdd AUC showed a weak but significant correspondence to crop yield data with  $r^2$  of 0.25 (figure 5-14b). The woredas for which crop production and yield data were analyzed included Dejen, Enemay and Enbise Sar Midir in West Gojjam Zone, Simada and Lay Gaint in South Gondar Zone, Jama, Legehida, Legambo and Delanta in South Wollo Zone, and Wadla and Gidan in North Wollo Zone.



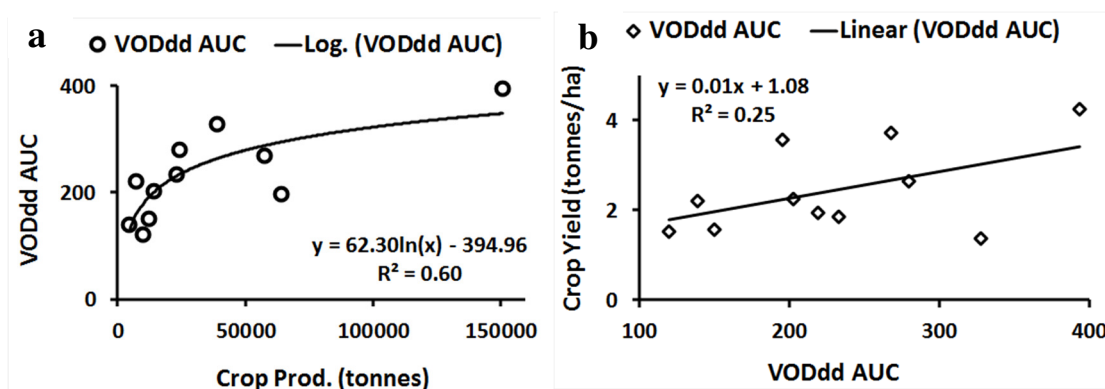


**Figure 5-14.** Relationships between area under VOD<sub>dd</sub> curve and crop production (a) and yield (b) statistical data at the woreda level in the Amhara Region in northwestern Ethiopia for 2014. Both fits are significant at  $p < 0.01$ .

The Zone level CSA data in the highland agricultural areas of Amhara and Oromia Regions for 2003 to 2008 and 2010 (2009 data were not available) displayed that crop production was substantially increased (figure 5-15). There is weaker evidence of cultivated area increase during the same period in these zones. VODdd AUC also showed that there is very little change during this period, except in 2010. Even though 2010 was flood year in some parts of Ethiopia, rainfall was distributed throughout the rainy season, which in turn supported good crop growth and production. North Wollo zone showed consistently lower crop production, cultivated area, and VODdd AUC time series: it is the drier and more degraded part of the study sites. North Wollo is one of the more food insecure zones in Ethiopia. The zones in figure 5-15c were clustered into two general groups. The lower VODdd AUC value clusters were North Wollo, South Wollo, and East Gojjam, while the remaining four zones make up the higher VODdd AUC value clusters. The lower VODdd AUC values for North and South Wollo make sense, as these zones are known to be among the lowest crop producing zones among the study sites. The

VODdd AUC displayed weak but significant correspondence with crop production data at zone level in five of seven zones. Significant relationships were found in West Shewa, North Shewa, East Gojjam, South Wollo and North Wollo Zones with coefficients of determination ranging from 0.25 to 0.72. No significant relationship was found in either Arsi or South Gondar Zones (data not shown). The VODdd AUC also showed significant correspondence with rainfall data in the same five zones ( $0.29 < r^2 < 0.73$ ) but not in South Gondar or Arsi. Maximum VOD showed a significant correspondence with crop production data in four of seven zones (West Shewa, East Gojjam, South Wollo, and North Wollo). In general, rainfall, VODdd AUC, of VOD AUC, and VODmax did not show noticeable increases during the study period (2003 – 2015). However, smallholder agricultural crop production data from the Ethiopian CSA in these zones has reportedly more than doubled in just eight years. Based on this governmental report, crop production has grown at an annual rate of 6.5%, while the population growth was 2.6% for the same period. Yet, a paradox arises in that millions have been food insecure every year during the study period, including more than 10 million in the 2015 drought year (IFPRI, 2015; UN-WFP, 2016).

Uncertainties in the National statistical data are not well characterized. In Ethiopia, administrative offices below the federal level lack organized historical datasets, and access to data at these offices is difficult. However, we also acknowledge that uncertainties also arise in the remote sensing data due to the mixture of other land covers with croplands within the 625 km<sup>2</sup> of each AMSR-E pixel, and potential biases arising from differences in the areal distribution of croplands within woredas that were not attenuated by the normalization procedures. FAO crop production data (FAO, 2013,

2014) for Ethiopia show a strong upward exponential trend since 2008; whereas, comparable data from Tanzania show only weak linear growth with high interannual variation (figure 5-16).

VODmax showed strong correspondence with NDVI max ( $r^2 > 0.8$ ) in sites in northern Eurasia (Alemu & Henebry, 2017). A long-term (1988-2008) global vegetation biomass change study on major world biomes found correspondence between VOD and production of major crops (Liu et al., 2013). Passive microwave data were found to be relevant to study tropical cropland dynamics, but additional study is needed for these data to be used effectively.

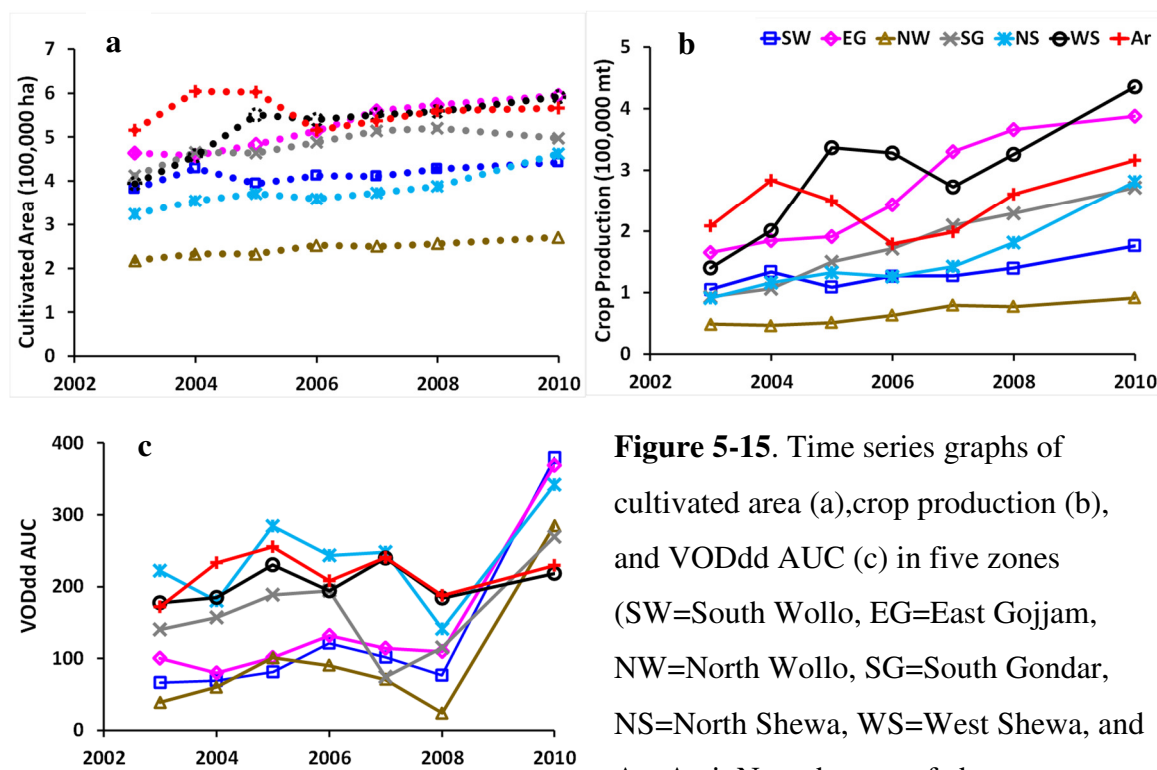


**Figure 5-15.** Time series graphs of cultivated area (a), crop production (b), and VODdd AUC (c) in five zones (SW=South Wollo, EG=East Gojjam, NW=North Wollo, SG=South Gondar, NS=North Shewa, WS=West Shewa, and Ar=Arsi). Note the rate of change

difference of the crop production data particularly relative to the VODdd AUC satellite derived data.

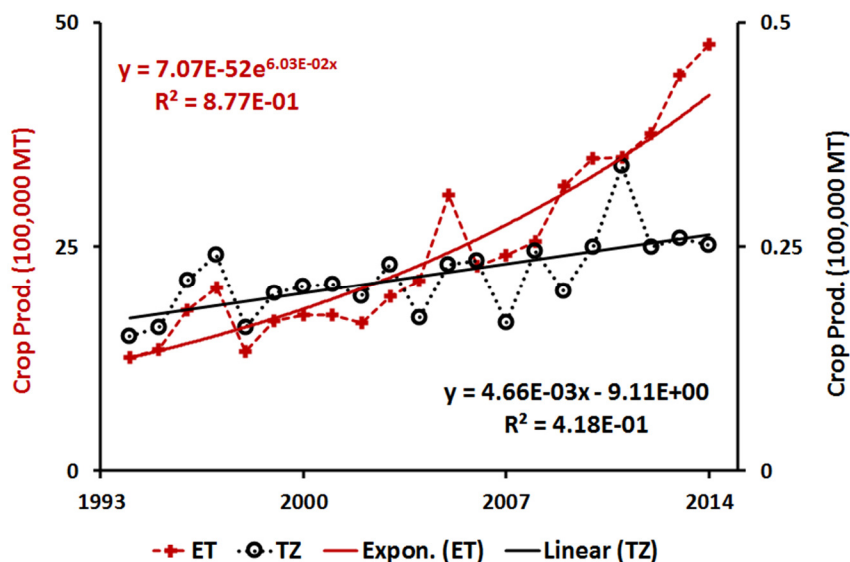


**Figure 5-16.** Time series graphs of national annual crop production data in Ethiopia and Tanzania for 1993-2015. Source: (FAO, 2013). Note the exponential growth rate of crop production data in Ethiopian relative to the lower linear growth rate in Tanzania.

## 5.5 Conclusion and Recommendations

The economies of east Africa are heavily dependent on traditional rain-fed agriculture that is vulnerable to extreme weather events, such as drought and floods. Even in the absence of conflict, this region has been one of the most food insecure parts of the world over the past three decades or more. Weather station data are scarce and difficult to obtain, while optical satellite data are limited by obscuring clouds. Satellite passive microwave data are less sensitive to clouds and atmospheric effects. Therefore, we explored using passive microwave data to study cropland dynamics in Ethiopia, Tanzania, and South Sudan. Since crop production in the region is moisture limited, seasonal dynamics of the microwave datasets were characterized as a function of cumulated precipitable water vapor, in contrast to the commonly used day-of-year or accumulated growing degree-days in temperate areas.

The microwave data were able to track cropland dynamics in time and space. Soil moisture was sensitive to rainfall and crop cover. It started to rise when rainfall commenced, and attain its peak during the peak rainfall season, then sharply dropped during the active vegetation growth period due to soil moisture drawdown by growing vegetation, and finally started to rise once the vegetation senesced. Soil moisture interannual variability was higher during the beginning of the growing season affecting planting times of croplands. Precipitable water vapor was able to capture seasonal and intra-seasonal atmospheric water vapor across cropland sites. It was also able to differentiate unimodal and bimodal growing seasons in the study region.

Actual evapotranspiration (ETa) derived from simple surface energy balance model was sensitive to rainfall dynamics. ETa tracked well both the unimodal and bimodal rainfall dynamics in space and time compared to precipitable water vapor. Both the unimodal and bimodal ETa time series were fitted by the convex quadratic model better than that of precipitable water vapor. Moisture times to peak (MTP) showed strong correspondence between and among land surface variables. The lags and co-occurrences between and among these land surface variables occurred in logical sequences.

Global circulation patterns and climate modes linked to the Pacific and Indian oceans, such as El Niño Southern Oscillation (ENSO) and the Indian Ocean Dipole (IOD) modes affect rainfall in eastern Africa. The biophysical and geophysical variables derived from passive microwave data responded to ENSO and IOD events occurring during the study period, including major floods (2006, 2010) and an extreme drought (2015).

The correspondence between passive microwave land surface parameters and crop production and crop yield was more complicated. The spatial resolution of satellite passive microwave data and crop production statistical data in Ethiopia is roughly similar. We addressed the spatial overlay mismatch between the AMSR pixel and crop production area through data normalization. However, a major problem with the crop production data is data uncertainty and the lack of high quality, long-term data at woreda level. Data access is highly centralized at federal level. Crop production data from the Ethiopian Statistical Agency (CSA) is not well characterized, and access to data below the Zone level is restricted. The correspondence between the passive microwave data metrics and crop production data at the woreda level was encouraging, but these data were made available from a regional agricultural office through personal communication. In contrast, the correspondence between passive microwave data metrics with crop production data at zone level (using data from CSA) was very weak with no correspondence at some sites. Note that the woreda level analysis is correspondence across space in one year (2014), while the zone level analysis is correspondence in time (2003-2008 & 2010). According to the CSA, smallholder peasant agricultural crop production data in the study Zones in northwestern Ethiopia has reportedly more than doubled in just eight years. This figure strains credulity given the interannual variation in precipitation. However, we acknowledge that the mixture of other land covers with croplands within the 25 km AMSR-E pixel may contribute to the discrepancies of the LSP product with crop production data. While the passive microwave products are found to be relevant for the study of cropland dynamics, additional study is needed to understand how they can best be used. Access to crop production and yield statistical data

at village level and the synergistic use of VNIR vegetation index data might complement such research efforts.

## 5.6 Acknowledgments

This research was supported in part by NASA grants NNX13AN58H & NNX14AJ32G. The AMSR-E data were accessed from Numerical Terradynamic Simulation Group (NTSG) ([www.ntsg.umd.edu/project/amsreelp](http://www.ntsg.umd.edu/project/amsreelp)), TRMM data from [ftp://disc2.nascom.nasa.gov/ftp/data/s4pa/TRMM\\_L3/TRMM\\_3B42\\_daily/](ftp://disc2.nascom.nasa.gov/ftp/data/s4pa/TRMM_L3/TRMM_3B42_daily/) and crop production data at zone level from Ethiopian Central Statistical Agency (CSA), and at woreda level from Amhara National Regional State Bureau of Agriculture (personal communication), Ethiopia.

## 5.7 References

- Adhikari, U., Nejadhashemi, A. P., & Woznicki, S. A. (2015). Climate change and eastern Africa: a review of impact on major crops. *Food and Energy Security*, 4(2), 110-132. doi: 10.1002/fes3.61.
- Alemu, W. G., & Henebry, G. M. (2013). Land surface phenologies and seasonalities using cool earthlight in mid-latitude croplands. *Environmental Research Letters*, 8(4). doi: <http://dx.doi.org/10.1088/1748-9326/8/4/045002>
- Alemu, W. G., & Henebry, G. M. (2016). Characterizing Cropland Phenology in Major Grain Production Areas of Russia, Ukraine, and Kazakhstan by the Synergistic Use of Passive Microwave and Visible to Near Infrared Data. *Remote Sensing*, 8(12). <http://dx.doi.org/10.3390/rs8121016>.

- Alemu, W. G., & Henebry, G. M. (2017a). Comparing Passive Microwave with Visible-to-Near-Infrared Phenometrics in Croplands of Northern Eurasia. In review at Remote Sensing journal.
- Becker-Reshef, I., Justice, C., Sullivan, M., Vermote, E., Tucker, C., Anyamba, A., Small, J., Pak, E., Masuoka, E., Schmaltz, J., Hansen, M., Pittman, K., Birkett, C., Williams, D., Reynolds, C., & Doorn, B. (2010). Monitoring Global Croplands with Coarse Resolution Earth Observations: The Global Agriculture Monitoring (GLAM) Project. *Remote Sensing*, 2(6), 1589. doi: <http://www.mdpi.com/2072-4292/2/6/1589>
- Behera, S. K., Luo, J.-J., Masson, S., Delecluse, P., Gualdi, S., Navarra, A., & Yamagata, T. (2005). Paramount Impact of the Indian Ocean Dipole on the East African Short Rains: A CGCM Study. *Journal of Climate*, 18(21), 4514-4530. doi: <http://dx.doi.org/10.1175/JCLI3541.1>
- Black, E. (2005). The relationship between Indian Ocean sea–surface temperature and East African rainfall. *Philosophical Transactions of the Royal Society A: Mathematical, Physical and Engineering Sciences*, 363(1826), 43. doi: <http://rsta.royalsocietypublishing.org/content/363/1826/43.abstract>
- Bolten, J. D., & Crow, W. T. (2012). Improved prediction of quasi-global vegetation conditions using remotely-sensed surface soil moisture. *Geophysical Research Letters*, 39(19), L19406. doi: 10.1029/2012GL053470
- Bolten, J. D., Crow, W. T., Xiwu, Z., Jackson, T. J., & Reynolds, C. A. (2010). Evaluating the Utility of Remotely Sensed Soil Moisture Retrievals for Operational Agricultural Drought Monitoring. *IEEE Journal of Selected Topics in*



*Applied Earth Observations and Remote Sensing*, 3(1), 57-66. doi:  
10.1109/JSTARS.2009.2037163

- Bolton, D. K., & Friedl, M. A. (2013). Forecasting crop yield using remotely sensed vegetation indices and crop phenology metrics. *Agricultural and Forest Meteorology*, 173, 74-84. doi: <http://dx.doi.org/10.1016/j.agrformet.2013.01.007>
- Brown, M. E., de Beurs, K., & Vrieling, A. (2010). The response of African land surface phenology to large scale climate oscillations. *Remote Sensing of Environment*, 114(10), 2286-2296. doi: <http://dx.doi.org/10.1016/j.rse.2010.05.005>
- Brown, M. E., & de Beurs, K. M. (2008). Evaluation of multi-sensor semi-arid crop season parameters based on NDVI and rainfall. *Remote Sensing of Environment*, 112(5), 2261-2271. doi: <http://dx.doi.org/10.1016/j.rse.2007.10.008>
- CSA. (2015a). Agricultural Sample Survey, Time Series Data For National & Regional Level. Retrieved September 24, 2015, from [http://www.csa.gov.et/images/general/news/agss\\_time\\_series%20report](http://www.csa.gov.et/images/general/news/agss_time_series%20report)
- CSA. (2015b, September 15). Ethiopian National Data Archive ( ENADA). Retrieved September 24, 2015, from <http://213.55.92.105/enada/index.php/catalog/>
- DAAC-LP. (2014). MODIS Products Table. Retrieved 16, April 2014, from Land Processes Distributed Active Archive Center [https://lpdaac.usgs.gov/dataset\\_discovery/modis/modis\\_products\\_table](https://lpdaac.usgs.gov/dataset_discovery/modis/modis_products_table)
- Dagg, M., Woodhead, T., & Rijks, D. A. (1970). EVAPORATION IN EAST AFRICA. *International Association of Scientific Hydrology. Bulletin*, 15(1), 61-67. doi: 10.1080/02626667009493932

- de Beurs, K. M., & Henebry, G. M. (2004). Land surface phenology, climatic variation, and institutional change: Analyzing agricultural land cover change in Kazakhstan. *Remote Sensing of Environment*, 89(4), 497-509. doi:  
<http://dx.doi.org/10.1016/j.rse.2003.11.006>
- de Beurs, K. M., & Henebry, G. M. (2010). Spatio-Temporal Statistical Methods for Modelling Land Surface Phenology. In I. L. Hudson & M. R. Keatley (Eds.), *Phenological Research: Methods for Environmental and Climate Change Analysis* (2nd edition ed., [http://dx.doi.org/10.1007/978-90-481-3335-2\\_9](http://dx.doi.org/10.1007/978-90-481-3335-2_9)pp. 177-208): Springer Netherlands.
- Dixon, J., Gulliver, A., & Gibbon, D. (2001). *Farming Systems and Poverty: Improving Farmers' Livelihoods in a Changing World* (M. Hall Ed. doi:  
[http://iridl.ldeo.columbia.edu/maproom/Agriculture/Farming\\_Systems/Africa/](http://iridl.ldeo.columbia.edu/maproom/Agriculture/Farming_Systems/Africa/)).  
Rome and Washington D.C.: FAO and World Bank.
- DPPA. (2006). Joint Government and Humanitarian Partners Flash Appeal for the 2006 Flood Disaster in Ethiopia (doi:  
<http://www.dppc.gov.et/downloadable/reports/appeal/2006/Flood%20Appeal%20II%20MASTER%20Final.pdf>pp. 25).
- Du, J., Kimball, J. S., & Jones, L. A. (2015). Satellite Microwave Retrieval of Total Precipitable Water Vapor and Surface Air Temperature Over Land From AMSR2. *IEEE Transactions on Geoscience and Remote Sensing*, 53(5), 2520-2531. doi:  
<http://dx.doi.org/10.1109/TGRS.2014.2361344>
- Du, J., Kimball, J. S., Shi, J., Jones, L. A., Wu, S., Sun, R., & Yang, H. (2014). Inter-Calibration of Satellite Passive Microwave Land Observations from AMSR-E and

- AMSR2 Using Overlapping FY3B-MWRI Sensor Measurements. *Remote Sensing*, 6(9), 8594-8616. doi: <http://dx.doi.org/10.3390/rs6098594>
- FAO. (2014). *FAO STATISTICAL YEARBOOK for Africa* Regional Office for Africa, Accra: FAO
- FAO. (2013). FAOSTAT. Retrieved August 24, 2012, from <http://faostat.fao.org/site/567/default.aspx#ancor>
- FEWS-NET. (2016). FEWS NET El Niño Monitoring Resources. Retrieved 21 November, 2016, from <http://www.fews.net/fews-net-el-ni%C3%B1o-monitoring-resources>
- Ganguly, S., Friedl, M. A., Tan, B., Zhang, X., & Verma, M. (2010). Land surface phenology from MODIS: Characterization of the Collection 5 global land cover dynamics product. *Remote Sensing of Environment*, 114(8), 1805-1816. doi: <http://dx.doi.org/10.1016/j.rse.2010.04.005>
- Gashaw, W., & Legesse, D. (2011). Flood Hazard and Risk Assessment Using GIS and Remote Sensing in Fogera Woreda, Northwest Ethiopia. In A. M. Melesse (Ed.), *Nile River Basin: Hydrology, Climate and Water Use* (10.1007/978-94-007-0689-7\_9pp. 179-206). Dordrecht: Springer Netherlands.
- GEOGLAM. (2016). Early Warning Crop Monitor Report Retrieved 21 November, 2016, from <http://www.cropmonitor.org/pages/archive.php>
- HarvestChoice. (2015). [Ethiopia] Agricultural Sample Survey. Retrieved September 24, 2015, from <https://harvestchoice.org/topics/surveycensus-archive>
- Henebry, G. M. (2013). Phenologies of North American Grasslands and Grasses. In M. D. Schwartz (Ed.), *Phenology: An Integrative Environmental Science*

([http://dx.doi.org/10.1007/978-94-007-6925-0\\_11](http://dx.doi.org/10.1007/978-94-007-6925-0_11)pp. 197-210). Netherlands:  
Springer.

Henebry, G. M., & de Beurs, K. M. (2013). Remote Sensing of Land Surface Phenology: A Prospectus. In M. D. Schwartz (Ed.), *Phenology: An Integrative Environmental Science* ([http://dx.doi.org/10.1007/978-94-007-6925-0\\_21](http://dx.doi.org/10.1007/978-94-007-6925-0_21)pp. 385-411): Springer Netherlands.

Henebry, G. M., de Beurs, K. M., Wright, C. K., Ranjeet, J., & Lioubimtseva, E. (2013). Dryland East Asia in Hemispheric Context. In J. Chen, et al. (Eds.), *Dryland East Asia: Land Dynamics amid Social and Climate Change* (<http://dx.doi.org/10.1515/9783110287912.23>pp. 23-43). Berlin/Boston: Higher Education Press and Walter de Gruyter GmbH.

Hoell, A., & Funk, C. (2014). Indo-Pacific sea surface temperature influences on failed consecutive rainy seasons over eastern Africa. *Climate Dynamics*, 43(5), 1645-1660. doi: 10.1007/s00382-013-1991-6

Hoell, A., Funk, C., Zinke, J., & Harrison, L. (2016). Modulation of the Southern Africa precipitation response to the El Niño Southern Oscillation by the subtropical Indian Ocean Dipole. *Climate Dynamics*, 10.1007/s00382-016-3220-6, 1-12. doi: 10.1007/s00382-016-3220-6

IFPRI. (2015). Ethiopia's 2015 drought: No reason for a famine. Retrieved 21 November, 2016, from <http://www.ifpri.org/blog/ethiopias-2015-drought-no-reason-famine>

IFRC. (2006). Ethiopia: Floods; Emergency Appeal (doi: <http://www.ifrc.org/docs/appeals/06/MDRET003rev.pdf>).

- IFRC. (2010). Ethiopia: Response to seasonal floods (doi: <http://www.ifrc.org/docs/appeals/10/MDRET009.pdf>).
- JAMSTEC. (2016). Indian Ocean Dipole. Retrieved 2016, from JAMSTEC <http://www.jamstec.go.jp/frcgc/research/d1/iod/DATA/dmi.monthly.txt>
- Jones, L. A., & Kimball, J. S. (2011). Daily Global Land Surface Parameters Derived from AMSR-E. Boulder Colorado USA: National Snow and Ice Data Center. *Digital media* (<http://nsidc.org/data/nsidc-0451.html>).
- Jones, M. O., Jones, L. A., Kimball, J. S., & McDonald, K. C. (2011). Satellite passive microwave remote sensing for monitoring global land surface phenology. *Remote Sensing of Environment*, 115(4), 1102-1114. doi: <http://dx.doi.org/10.1016/j.rse.2010.12.015>
- Jury, M. R. (2011). Meteorological scenario of Ethiopian floods in 2006–2007. *Theoretical and Applied Climatology*, 104(1), 209-219. doi: 10.1007/s00704-010-0337-0
- Korotayev, A., & Zinkina, J. (2015). East Africa in the Malthusian Trap? *Journal of Developing Societies*, 31(3), 385-420. doi: 10.1177/0169796X15590322
- Liu, Y. Y., van Dijk, A. I. J. M., McCabe, M. F., Evans, J. P., & de Jeu, R. A. M. (2013). Global vegetation biomass change (1988-2008) and attribution to environmental and human drivers. *Global Ecology and Biogeography*, 22(6), 692-705. doi: 10.1111/geb.12024
- Lyon, B., & DeWitt, D. G. (2012). A recent and abrupt decline in the East African long rains. *Geophysical Research Letters*, 39(2), L02702. doi: 10.1029/2011GL050337

- McMaster, G. S., & Wilhelm, W. W. (1997). Growing degree-days: one equation, two interpretations. *Agricultural and Forest Meteorology*, 87(4), 291-300. doi: [http://dx.doi.org/10.1016/S0168-1923\(97\)00027-0](http://dx.doi.org/10.1016/S0168-1923(97)00027-0)
- Meyers, G., McIntosh, P., Pigot, L., & Pook, M. (2007). The years of El Niño, La Niña, and interactions with the tropical Indian Ocean. *Journal of Climate*, 20(13), 2872-2880.
- Nicholson, S. E. (2015). Long-term variability of the East African ‘short rains’ and its links to large-scale factors. *International Journal of Climatology*, 35(13), 3979-3990. doi: 10.1002/joc.4259
- Nicholson, S. E., & Kim, J. (1997). The Relationship of the El Niño–Southern Oscillation to African rainfall. *International Journal of Climatology*, 17(2), 117-135. doi: 10.1002/(SICI)1097-0088(199702)17:2<117::AID-JOC84>3.0.CO;2-O
- NOAA. (2015a). Description of Changes to Oceanic Niño Index (ONI). Retrieved 22 June, 2016, from [http://www.cpc.ncep.noaa.gov/products/analysis\\_monitoring/ensostuff/ONI\\_change.shtml](http://www.cpc.ncep.noaa.gov/products/analysis_monitoring/ensostuff/ONI_change.shtml)
- NOAA. (2015b). Monthly Atmospheric and Sea Surface Temperature Indices. Retrieved 22 June, 2016, from National Weather Service Climatic Prediction Center <http://www.cpc.ncep.noaa.gov/data/indices/sstoi.indices>
- Pervez, M. S., & Henebry, G. M. (2015). Spatial and seasonal responses of precipitation in the Ganges and Brahmaputra river basins to ENSO and Indian Ocean dipole modes: implications for flooding and drought. *Nat. Hazards Earth Syst. Sci.*, 15(1), 147-162. doi: 10.5194/nhess-15-147-2015

- Rientjes, T., Haile, A. T., & Fenta, A. A. (2013). Diurnal rainfall variability over the Upper Blue Nile Basin: A remote sensing based approach. *International Journal of Applied Earth Observation and Geoinformation*, *21*, 311-325. doi: <http://dx.doi.org/10.1016/j.jag.2012.07.009>
- Saji, N. H., Goswami, B. N., Vinayachandran, P. N., & Yamagata, T. (1999). A dipole mode in the tropical Indian Ocean. *Nature*, *401*(6751), 360-363.
- Sakamoto, T., Van Nguyen, N., Ohno, H., Ishitsuka, N., & Yokozawa, M. (2006). Spatio-temporal distribution of rice phenology and cropping systems in the Mekong Delta with special reference to the seasonal water flow of the Mekong and Bassac rivers. *Remote Sensing of Environment*, *100*(1), 1-16. doi: <http://dx.doi.org/10.1016/j.rse.2005.09.007>
- Sarma, A., Kumar, T. V. L., & Koteswararao, K. (2008). Development of an agroclimatic model for the estimation of rice yield. *Journal of Indian Geophysical Union*, *12*(2), 89-96. doi: <http://igu.in/12-2/4sarma.pdf>
- Schreck, C. J., & Semazzi, F. H. M. (2004). Variability of the recent climate of eastern Africa. *International Journal of Climatology*, *24*(6), 681-701. doi: 10.1002/joc.1019
- Senay, B. G., Budde, M., Verdin, P. J., & Melesse, M. A. (2007). A Coupled Remote Sensing and Simplified Surface Energy Balance Approach to Estimate Actual Evapotranspiration from Irrigated Fields. *Sensors*, *7*(6). doi: 10.3390/s7060979
- Senay, G. B., Bohms, S., Singh, R. K., Gowda, P. H., Velpuri, N. M., Alemu, H., & Verdin, J. P. (2013). Operational Evapotranspiration Mapping Using Remote Sensing and Weather Datasets: A New Parameterization for the SSEB Approach.

*JAWRA Journal of the American Water Resources Association*, 49(3), 577-591.

doi: 10.1111/jawr.12057

Souvereinjs, N., Thiery, W., Demuzere, M., & Lipzig, N. P. M. V. (2016). Drivers of future changes in East African precipitation. *Environmental Research Letters*, 11(11), 114011. doi: <http://stacks.iop.org/1748-9326/11/i=11/a=114011>

TRMM. (2011a). TRMM/TMPA 3B42 TRMM and Others Rainfall Estimate Data V7.

Retrieved 15, August 2011, from Goddard Space Flight Center Distributed Active Archive Center (GSFC DAAC) [https://mirador.gsfc.nasa.gov/cgi-](https://mirador.gsfc.nasa.gov/cgi-bin/mirador/granlist.pl?page=1&dataSet=TRMM_3B42_Daily&version=7&allversion=7&keyword=TRMM_3B42_daily&pointLocation=(-90,-180),(90,180)&location=(-90,-180),(90,180)&searchType=Location&event=&startTime=2002-01-01&endTime=2015-12-31%2023:59:59&search=&CGISESSID=a7437ab781d5a93281ff3163b0044d1b&nr=5114&temporalres=1%20day&prodpg=https://mirador.gsfc.nasa.gov/collections/TRMM_3B42_Daily__7.shtml&longname=TRMM%20(TMPA)%20Precipitation%20L3%201%20day%200.25%20degree%20x%200.25%20degree%20V7&granulePresentation=ungrouped)

[bin/mirador/granlist.pl?page=1&dataSet=TRMM\\_3B42\\_Daily&version=7&allversion=7&keyword=TRMM\\_3B42\\_daily&pointLocation=\(-90,-](https://mirador.gsfc.nasa.gov/cgi-bin/mirador/granlist.pl?page=1&dataSet=TRMM_3B42_Daily&version=7&allversion=7&keyword=TRMM_3B42_daily&pointLocation=(-90,-180),(90,180)&location=(-90,-180),(90,180)&searchType=Location&event=&startTime=2002-01-01&endTime=2015-12-31%2023:59:59&search=&CGISESSID=a7437ab781d5a93281ff3163b0044d1b&nr=5114&temporalres=1%20day&prodpg=https://mirador.gsfc.nasa.gov/collections/TRMM_3B42_Daily__7.shtml&longname=TRMM%20(TMPA)%20Precipitation%20L3%201%20day%200.25%20degree%20x%200.25%20degree%20V7&granulePresentation=ungrouped)

[180\),\(90,180\)&location=\(-90,-](https://mirador.gsfc.nasa.gov/cgi-bin/mirador/granlist.pl?page=1&dataSet=TRMM_3B42_Daily&version=7&allversion=7&keyword=TRMM_3B42_daily&pointLocation=(-90,-180),(90,180)&location=(-90,-180),(90,180)&searchType=Location&event=&startTime=2002-01-01&endTime=2015-12-31%2023:59:59&search=&CGISESSID=a7437ab781d5a93281ff3163b0044d1b&nr=5114&temporalres=1%20day&prodpg=https://mirador.gsfc.nasa.gov/collections/TRMM_3B42_Daily__7.shtml&longname=TRMM%20(TMPA)%20Precipitation%20L3%201%20day%200.25%20degree%20x%200.25%20degree%20V7&granulePresentation=ungrouped)

[180\),\(90,180\)&searchType=Location&event=&startTime=2002-01-](https://mirador.gsfc.nasa.gov/cgi-bin/mirador/granlist.pl?page=1&dataSet=TRMM_3B42_Daily&version=7&allversion=7&keyword=TRMM_3B42_daily&pointLocation=(-90,-180),(90,180)&location=(-90,-180),(90,180)&searchType=Location&event=&startTime=2002-01-01&endTime=2015-12-31%2023:59:59&search=&CGISESSID=a7437ab781d5a93281ff3163b0044d1b&nr=5114&temporalres=1%20day&prodpg=https://mirador.gsfc.nasa.gov/collections/TRMM_3B42_Daily__7.shtml&longname=TRMM%20(TMPA)%20Precipitation%20L3%201%20day%200.25%20degree%20x%200.25%20degree%20V7&granulePresentation=ungrouped)

[01&endTime=2015-12-](https://mirador.gsfc.nasa.gov/cgi-bin/mirador/granlist.pl?page=1&dataSet=TRMM_3B42_Daily&version=7&allversion=7&keyword=TRMM_3B42_daily&pointLocation=(-90,-180),(90,180)&location=(-90,-180),(90,180)&searchType=Location&event=&startTime=2002-01-01&endTime=2015-12-31%2023:59:59&search=&CGISESSID=a7437ab781d5a93281ff3163b0044d1b&nr=5114&temporalres=1%20day&prodpg=https://mirador.gsfc.nasa.gov/collections/TRMM_3B42_Daily__7.shtml&longname=TRMM%20(TMPA)%20Precipitation%20L3%201%20day%200.25%20degree%20x%200.25%20degree%20V7&granulePresentation=ungrouped)

[31%2023:59:59&search=&CGISESSID=a7437ab781d5a93281ff3163b0044d1b&](https://mirador.gsfc.nasa.gov/cgi-bin/mirador/granlist.pl?page=1&dataSet=TRMM_3B42_Daily&version=7&allversion=7&keyword=TRMM_3B42_daily&pointLocation=(-90,-180),(90,180)&location=(-90,-180),(90,180)&searchType=Location&event=&startTime=2002-01-01&endTime=2015-12-31%2023:59:59&search=&CGISESSID=a7437ab781d5a93281ff3163b0044d1b&nr=5114&temporalres=1%20day&prodpg=https://mirador.gsfc.nasa.gov/collections/TRMM_3B42_Daily__7.shtml&longname=TRMM%20(TMPA)%20Precipitation%20L3%201%20day%200.25%20degree%20x%200.25%20degree%20V7&granulePresentation=ungrouped)

[nr=5114&temporalres=1%20day&prodpg=https://mirador.gsfc.nasa.gov/collections/TRMM\\_3B42\\_Daily\\_\\_7.shtml&longname=TRMM%20\(TMPA\)%20Precipitation%20L3%201%20day%200.25%20degree%20x%200.25%20degree%20V7&gr](https://mirador.gsfc.nasa.gov/cgi-bin/mirador/granlist.pl?page=1&dataSet=TRMM_3B42_Daily&version=7&allversion=7&keyword=TRMM_3B42_daily&pointLocation=(-90,-180),(90,180)&location=(-90,-180),(90,180)&searchType=Location&event=&startTime=2002-01-01&endTime=2015-12-31%2023:59:59&search=&CGISESSID=a7437ab781d5a93281ff3163b0044d1b&nr=5114&temporalres=1%20day&prodpg=https://mirador.gsfc.nasa.gov/collections/TRMM_3B42_Daily__7.shtml&longname=TRMM%20(TMPA)%20Precipitation%20L3%201%20day%200.25%20degree%20x%200.25%20degree%20V7&granulePresentation=ungrouped)

[anulePresentation=ungrouped](https://mirador.gsfc.nasa.gov/cgi-bin/mirador/granlist.pl?page=1&dataSet=TRMM_3B42_Daily&version=7&allversion=7&keyword=TRMM_3B42_daily&pointLocation=(-90,-180),(90,180)&location=(-90,-180),(90,180)&searchType=Location&event=&startTime=2002-01-01&endTime=2015-12-31%2023:59:59&search=&CGISESSID=a7437ab781d5a93281ff3163b0044d1b&nr=5114&temporalres=1%20day&prodpg=https://mirador.gsfc.nasa.gov/collections/TRMM_3B42_Daily__7.shtml&longname=TRMM%20(TMPA)%20Precipitation%20L3%201%20day%200.25%20degree%20x%200.25%20degree%20V7&granulePresentation=ungrouped)

TRMM. (2011b). TRMM/TMPA 3B42 TRMM and Others Rainfall Estimate Data V7

Product Summary. Retrieved 15 August, 2015, from

[https://mirador.gsfc.nasa.gov/collections/TRMM\\_3B42\\_\\_007.shtml](https://mirador.gsfc.nasa.gov/collections/TRMM_3B42__007.shtml)



- UN-OCHA. (2006). OCHA Annual Report 2006: Activities and use of extrabudgetary funds. Part III, Coordination Activities in the Field, Ethiopia (doi: [http://www.unocha.org/annualreport/2006/html/part3\\_ethiopia.html](http://www.unocha.org/annualreport/2006/html/part3_ethiopia.html)).
- UN-OCHA. (2016). El Niño in East Africa. Retrieved 21 November, 2016, from <http://www.unocha.org/el-nino-east-africa>
- UN-WFP. (2016). Drought In Ethiopia: 10 Million People In Need. Retrieved 21 Novemebr, 2016, from <https://www.wfp.org/stories/drought-ethiopia-10-million-people-need>
- UNCIEF. (2011). Eastern and Southern Africa: Ethiopia (doi: [https://www.unicef.org/hac2011/files/HAC2011\\_4pager\\_Ethiopia.pdf](https://www.unicef.org/hac2011/files/HAC2011_4pager_Ethiopia.pdf)).
- USDA-FAS. (2015). Global Food Supply Monitoring; Crop Production Maps. Retrieved 15, January 2015, 2015, from [http://www.pecad.fas.usda.gov/rssiws/al/estafrica\\_crop\\_prod.htm](http://www.pecad.fas.usda.gov/rssiws/al/estafrica_crop_prod.htm).
- USGS. (2016). 30 Meter Global Land Cover. Retrieved 24 May, 2016, from USGS file:///D:/30m\_Global\_LandCover/30%20Meter%20Global%20Land%20Cover.html.
- Wang, G., & Schimel, D. (2003). Climate change, climate modes, and climate impacts. *Annual Review of Environment and Resources*, 28(1), 1-28.
- Webster, P. J., Moore, A. M., Loschnigg, J. P., & Leben, R. R. (1999). Coupled ocean–atmosphere dynamics in the Indian Ocean during 1997–98. *Nature*, 401(6751), 356-360.

- Williams, C. A., & Hanan, N. P. (2011). ENSO and IOD teleconnections for African ecosystems: evidence of destructive interference between climate oscillations. *Biogeosciences*, 8(1), 27.
- Woodhead, T. (1966). Empirical Relations Between Cloud Amount, Insolation and Sunshine Duration in East Africa: I. *East African Agricultural and Forestry Journal*, 32(2), 211-213. doi: 10.1080/00128325.1966.11662119
- Woodhead, T. (1967). Empirical Relations Between Cloud Amount, Insolation and Sunshine Duration in East Africa: II. *East African Agricultural and Forestry Journal*, 32(4), 474-477. doi: 10.1080/00128325.1967.11662165
- Zhang, X. Y., Friedl, M. A., Schaaf, C. B., & Strahler, A. H. (2004). Climate controls on vegetation phenological patterns in northern mid- and high latitudes inferred from MODIS data. *Global Change Biology*, 10(7), 1133-1145. doi: <http://dx.doi.org/10.1111/j.1529-8817.2003.00784.x>

## **CHAPTER 6 : Research Summary and Recommendations**

## 6.1 Summary of the Research Results

In this study, I have characterized land surface phenologies (LSPs) and land surface seasonalities (LSSs) in the temperate spring wheat growing regions of North Dakota, USA and the Canadian Prairies and the major grain production areas of Eurasia (Ukraine [UA], southwestern Russian [RU] and northern Kazakhstan [KZ]) and the grain producing areas of eastern Africa (Ethiopia, Tanzania, and South Sudan). The temperate study regions are important cropland sites to insure global food security, while eastern Africa is one of the most food insecure regions of the world. Moreover, cropland dynamics in eastern Africa are less well characterized. Thus I was aiming to transfer the knowledge and experience gained from our Eurasian studies to the croplands of eastern Africa.

Many studies have used vegetation indices (VIs) and land surface temperature data derived from visible to near infrared (VNIR) and thermal infrared (TIR) sensors, respectively, to study LSP and LSS, despite the confounding effects of cloudiness, aerosols, and smoke, and, especially at high latitudes, solar illumination constraints. Passive microwave data are less sensitive to these effects resulting in finer temporal resolution data including nighttime acquisitions, albeit at coarse spatial resolution (25 km). In contrast, VNIR data have finer spatial resolution at coarser temporal resolution (8 to 16 day) due to compositing to minimize cloud effects. I selected cropland study sites using the MODIS land cover percentage data, the USDA Foreign Agricultural Service (FAS) crop maps, and Google Earth Images. From the MODIS land cover data, I developed cropland stability maps in the study period to select sites that were persistently croplands. This selection was supported by USDA FAS crop maps and visual assessment

of imagery in Google Earth. Cropland “sites” are in this case Advanced Microwave Scanning Radiometer on EOS (AMSR-E) pixels with 25 km spatial resolutions (625 km<sup>2</sup>). In this study I have addressed four research questions that translated into four manuscripts of which two are now published, one is in review, and another will soon be in review. The key findings of the research are summarized below.

**Research Question 1.**

*Can we use convex quadratic (CxQ) models of land surface phenology, which have been successfully used with VNIR and TIR data on herbaceous vegetation in the temperate and boreal regions, with AMSR-E passive microwave data products—air temperature and VOD—to study land surface phenology & seasonality in temperate croplands?*

The answer to this research question was partially yes. The passive microwave air temperature retrieved AMSR-E GDD as a function of AGDD was well fitted with a CxQ model in time and space with  $r^2 > 0.90$ . LSP of the VODs were able to differentiate cropland seasonalities between the spring wheat producing sites in North America and the winter and spring grain producing sites in the Volga river basin of Russia. The shape of the VODs was not suitable to fit a CxQ model. However, the core-growing season of VODs were well fitted with CxQ model with  $r^2 > 0.90$ .

**Research Question 2.**

*Can the synergistic use of the VNIR MODIS NDVI and the passive microwave AMSR-E-retrieved air temperature data enable characterization of cropland dynamics in the mid-latitudes?*

GDD from AMSR-E air temperature able to track cropland seasonal dynamics, including finer weekly and monthly GDD oscillations. AMSR-E air temperature and MODIS LST GDD as a function of their respective AGDDs were perfectly fitted with a CxQ model ( $0.88 \leq r^2 \leq 0.98$ ), and were able to track similar cropland dynamics. The CxQ model fit for the AMSR-E GDD was superior for most sites, compared to that of the MODIS LST derived GDD. GDD residuals resulting from the comparison of observed and modeled GDD were able to manifest the evaporative cooling effect from a growing crop vegetation during the vegetation peak greenness period.

MODIS VIs (NDVI and EVI) as a function of AMSR-E AGDD were able to differentiate winter and/or spring grain producing areas latitudinal gradient in the study region. Middle latitude and northern study sites ( $>48^\circ$  N) supported spring grains while southern sites ( $\leq 48^\circ$  N) supported winter and/or spring grains. The former sites exhibit shorter unimodal growing season, while the latter exhibit unimodal or bimodal growing season. This synergistic use of the VNIR MODIS NDVI and the passive microwave AMSR-E AGDD was able to capture cropland sites interannual shifts between unimodal and bimodal growing season patterns. This synergistic analysis was also able to manifest the effect of regional heat waves that devastated grain production in 2007 in Ukraine and in 2010 in Russia and Kazakhstan. The answer for the research question is “yes” given the findings.

### **Research Question 3.**

*Can AMSR-E passive microwave derived VOD peak height (PH) phenometrics track cropland seasonal dynamics complementary to that of the VNIR MODIS NDVI peak vegetation greenness?*

Time series of LSP of VODs at three microwave frequencies (6.925 GHz, 10.65 GHz, and 18.7 GHz) from the passive microwave AMSR-E were able to track unimodal and bimodal seasonal patterns of croplands similar to the VNIR MODIS NDVI. NDVI was favorably fitted with CxQ model with  $0.88 < r^2 < 0.99$ . Peak NDVI phenometrics ranged between  $0.88 < r^2 < 0.99$ , while it was 0.58 – 0.84 for the VOD.

Spatial patterns of PH VOD phenometrics favorably corresponded with that of the NDVI peak greenness phenometrics over the study domain with  $r^2 > 0.77$ , but with a general temporal lag of the former by one to two weeks than the latter. A plausible explanation for this lag effect is that canopy water content bound in the aboveground biomass, which VOD senses, peaks later than canopy greenness that the NDVI senses. Therefore, the answer to the research question 3 is “yes”. The peak height of VOD can be a complementary phenological metric for peak NDVI greenness, especially in parts of the world often obscured by clouds and aerosols. However, more research is needed on how best to use that complementarity.

#### **Research Question 4.**

*Is it possible to characterize cropland dynamics in tropical eastern Africa using the blended AMSR-E/AMSR2 passive microwave dataset?*

The AMSR passive microwave blended dataset captured the distinct spatio-temporal dynamics of eastern African croplands when tracked in moisture time (CVD) rather than in thermal time (AGDD) as was useful in temperate croplands. The AMSR land surface variables tracked cropland seasonalities similar to the independent datasets of TRMM rainfall and SSEB ETa, including the unimodal growing season patterns in

South Sudan and Ethiopia that have one strong rainfall season, as well as the bimodal growing seasons in Tanzania that have a distinct short and long rainy seasons.

AMSR volumetric soil moisture was sensitive to other data variables (TRMM rainfall and AMSR VOD) that in the humid highland croplands of Ethiopia, it rises as the rainfall season starts, sharply drops (before the peak rainfall season) due to drawdown of soil moisture by growing vegetation as revealed by the VOD, and then bounces back (despite the rainfall season ends) due to crop vegetation senescence. Interannual soil moisture variability is at its highest at the start of the growing season affecting when crops are planted. The moisture times to peak (MTP) showed strong correspondences ( $r^2 > 0.80$ ) among the biophysical variables and showed logical lag sequences. The answer for the fourth research question is “yes” given the findings.

AMSR datasets were able to show the effects of the ENSO and IOD global circulation modes on eastern African croplands. The 2006 and 2010 major flood years in Ethiopia were associated with positive IOD and La Niña events, respectively. The 2015 severe drought year in Ethiopia was associated with a long duration El Niño, which is linked to dry periods. Even though this was a positive IOD occurrence year too, the El Niño event occurred far ahead of the positive IOD event and, therefore, the latter state was unable to lessen the effect of the former event resulting in the most severe drought in the region in the last three decades. The drought left more than 10 million people (~10% of the country's total population) in acute need of food aid.

Land surface phenology and land surface seasonality linkages to crop production statistics were uncertain, due to significant discrepancies between the data officially reported to FAO and data reported at the local level. Thus, crop production and yield data



from local offices or other independent sources are needed to verify the linkages identified in my research.

## **6.2 Recommendations and Future Directions**

The creation of long-term passive microwave dataset by combining AMSR-E (June 2002 - October 2011) and AMSR2 (May 2012 - present), is a great resource for studies on land surface phenology and seasonality. I observed that in Ethiopia, there are some gaps on the AMSR data on important cropland sites that are located on a relatively level terrain that might be due to contamination from neighboring water bodies at certain times of year. More refinement of the AMSR data in this regard will enhance the suitability of this dataset for agricultural cropland studies, at least in the regions that I have studied.

Passive microwave data, in general, need increased spatial resolution to be effectively used for cropland monitoring. Fields are very much smaller in area compared to the 625 km<sup>2</sup> of the microwave pixels. This scaling mismatch is more prevalent in the tropics where croplands are very small in size, fragmented, and the surrounding terrain is rugged. The effort made on the NASA's Soil Moisture Active Passive (SMAP) mission is a great example in this regard. The data produced from the L-band combined passive microwave radiometer (36km) and the active microwave radar (3 km) was to yield products with a spatial resolution of 9 km. Unfortunately, the radar on SMAP failed in the summer of 2015, but the L-band passive radiometer is still functional. The soil moisture data from the SMAP radiometer should work well for cropland monitoring.

Although there has traditionally been little overlap between the microwave and VNIR communities, the time has come to explore the synergistic use of reflected sunlight

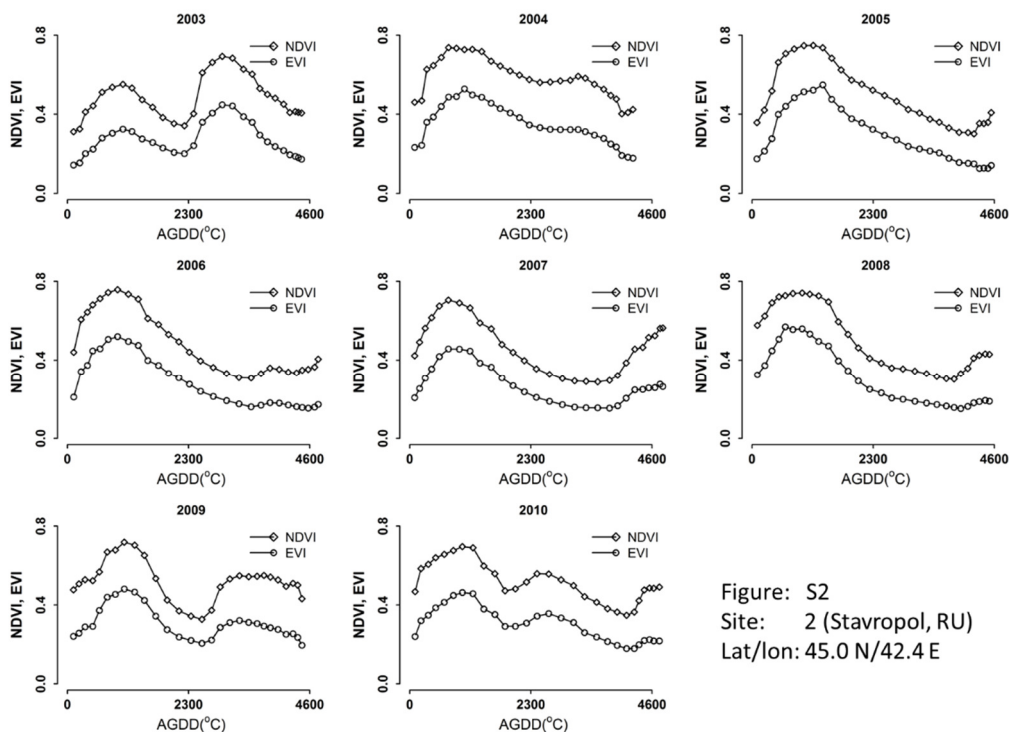
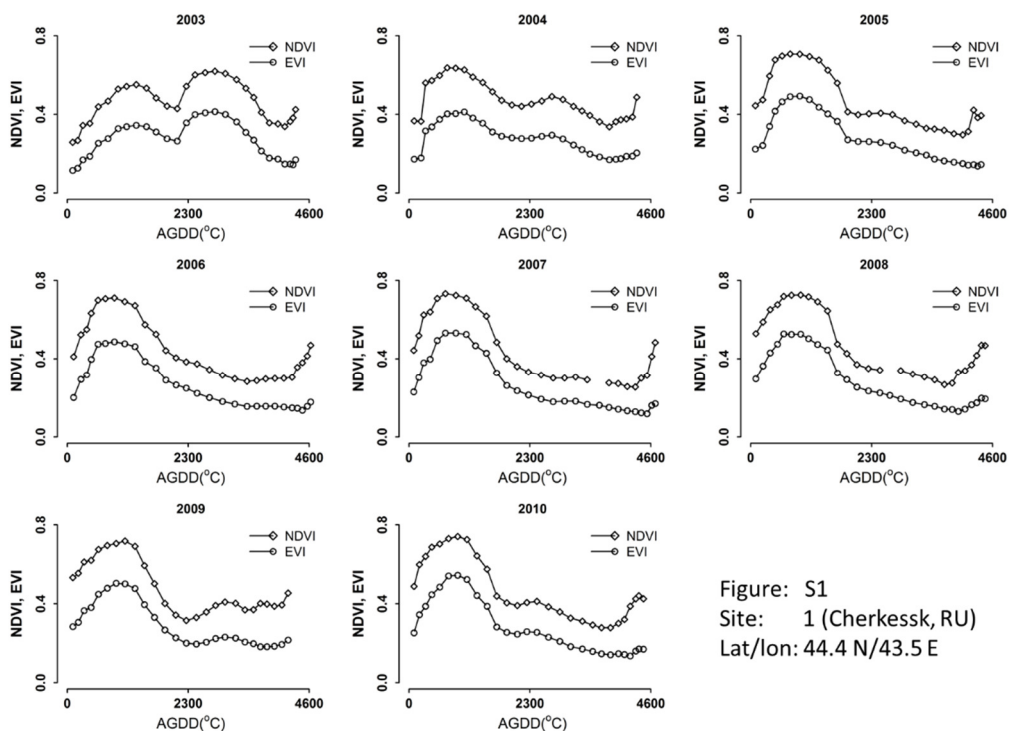
and emitted earthlight for potential applications in agricultural monitoring, natural resource management, ecosystems ecology, and Earth system science. My dissertation research offers a small but definite step in that direction.

### 6.3 References

- Alemu, W. G., & Henebry, G. M. (2017b). *Cropland land surface phenology and seasonality in East Africa: Ethiopia, Tanzania, and South Sudan. To be submitted to Remote Sensing journal in February, 2017.*
- Du, J., Kimball, J. S., & Jones, L. A. (2015). Satellite Microwave Retrieval of Total Precipitable Water Vapor and Surface Air Temperature Over Land From AMSR2. *IEEE Transactions on Geoscience and Remote Sensing*, 53(5), 2520-2531. doi: <http://dx.doi.org/10.1109/TGRS.2014.2361344>
- Du, J., Kimball, J. S., Shi, J., Jones, L. A., Wu, S., Sun, R., & Yang, H. (2014). Inter-Calibration of Satellite Passive Microwave Land Observations from AMSR-E and AMSR2 Using Overlapping FY3B-MWRI Sensor Measurements. *Remote Sensing*, 6(9), 8594-8616. doi: <http://dx.doi.org/10.3390/rs6098594>

## Supplementary Figures

**Figures S1–S49.** NDVI and EVI interannual variability for all the 49 study sites described in chapter 3 for 2003–2010. Whether due to changes in cultivation practice or to crop failures, the VI curves showed no, one, or two changes during the study period.



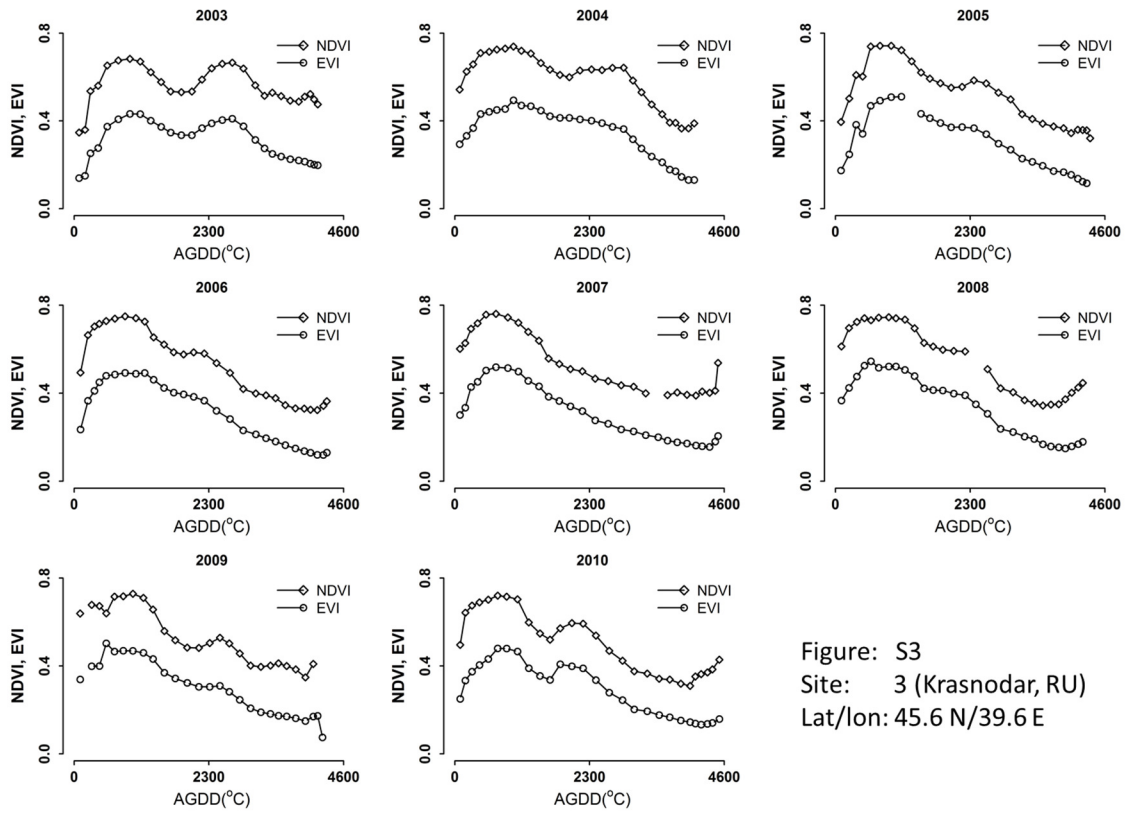


Figure: S3  
 Site: 3 (Krasnodar, RU)  
 Lat/Ion: 45.6 N/39.6 E

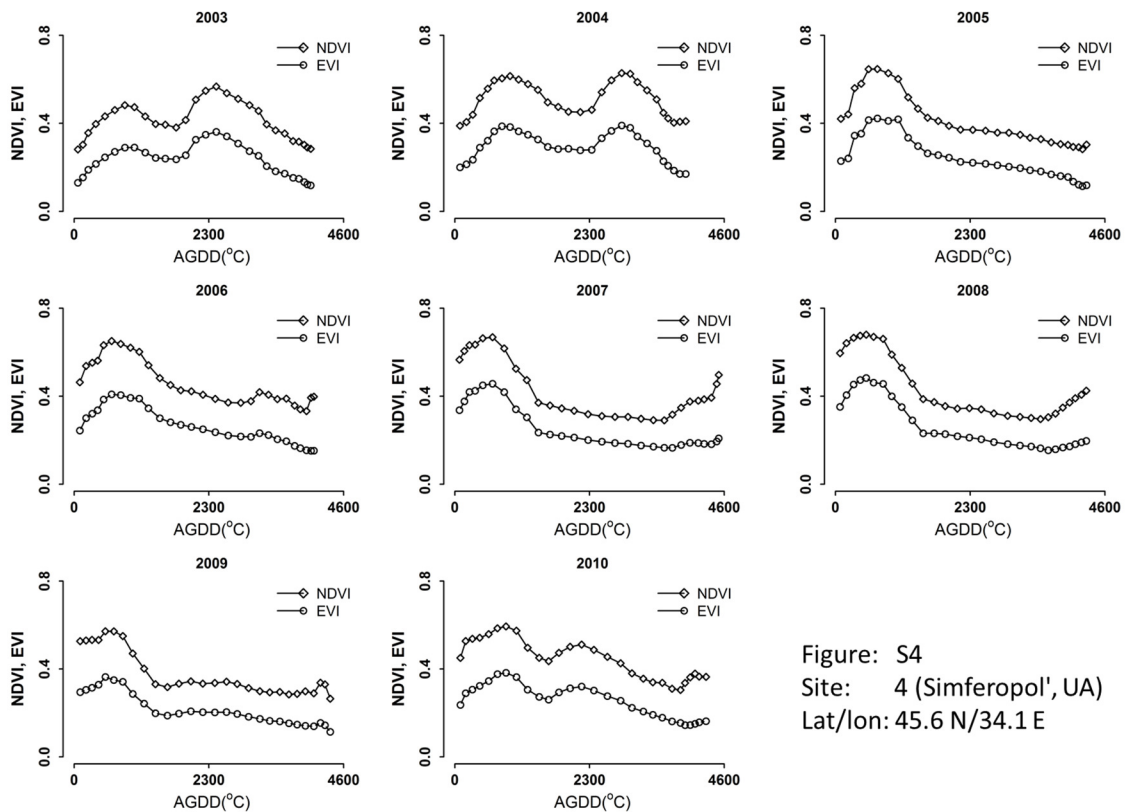


Figure: S4  
 Site: 4 (Simferopol', UA)  
 Lat/Ion: 45.6 N/34.1 E

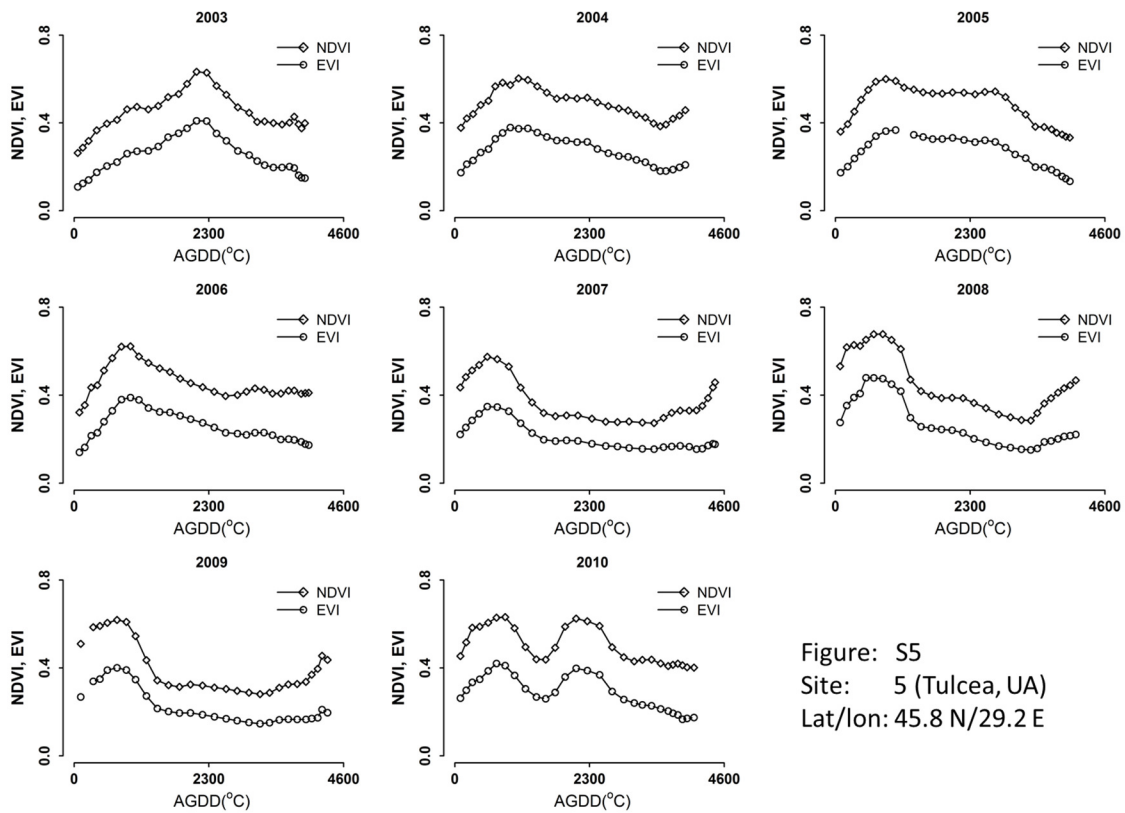


Figure: S5  
 Site: 5 (Tulcea, UA)  
 Lat/Ion: 45.8 N/29.2 E

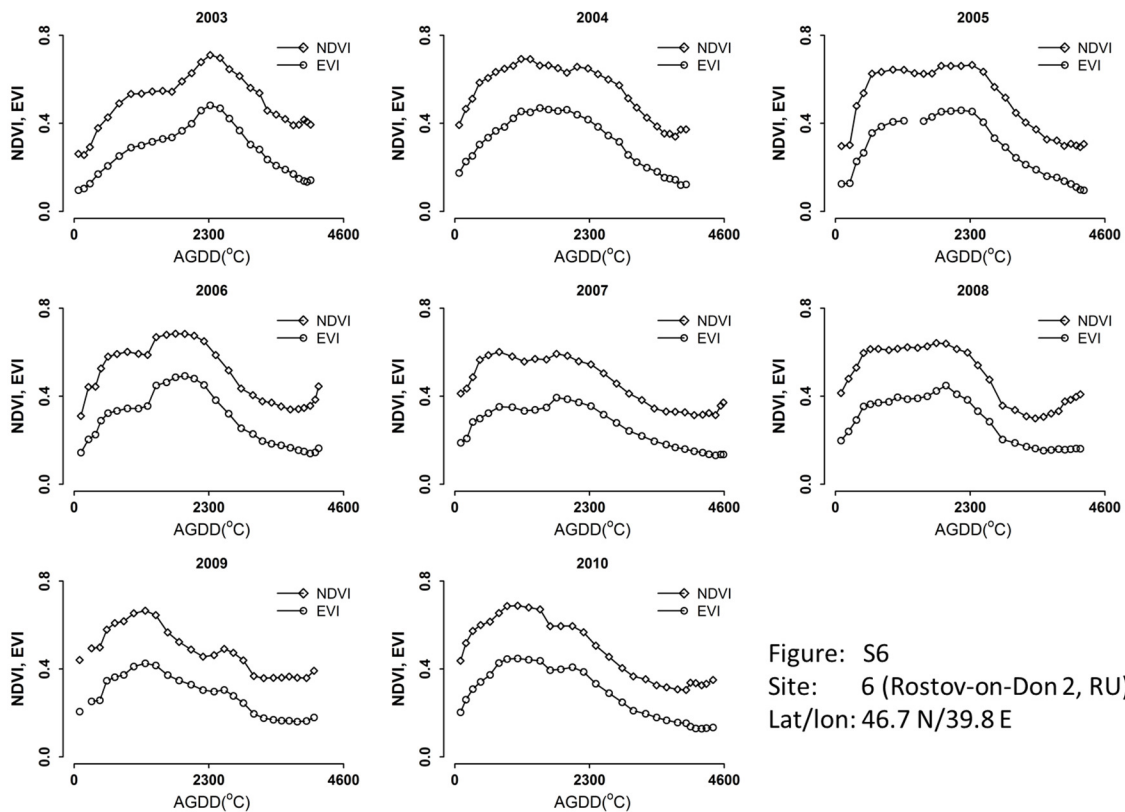


Figure: S6  
 Site: 6 (Rostov-on-Don 2, RU)  
 Lat/Ion: 46.7 N/39.8 E

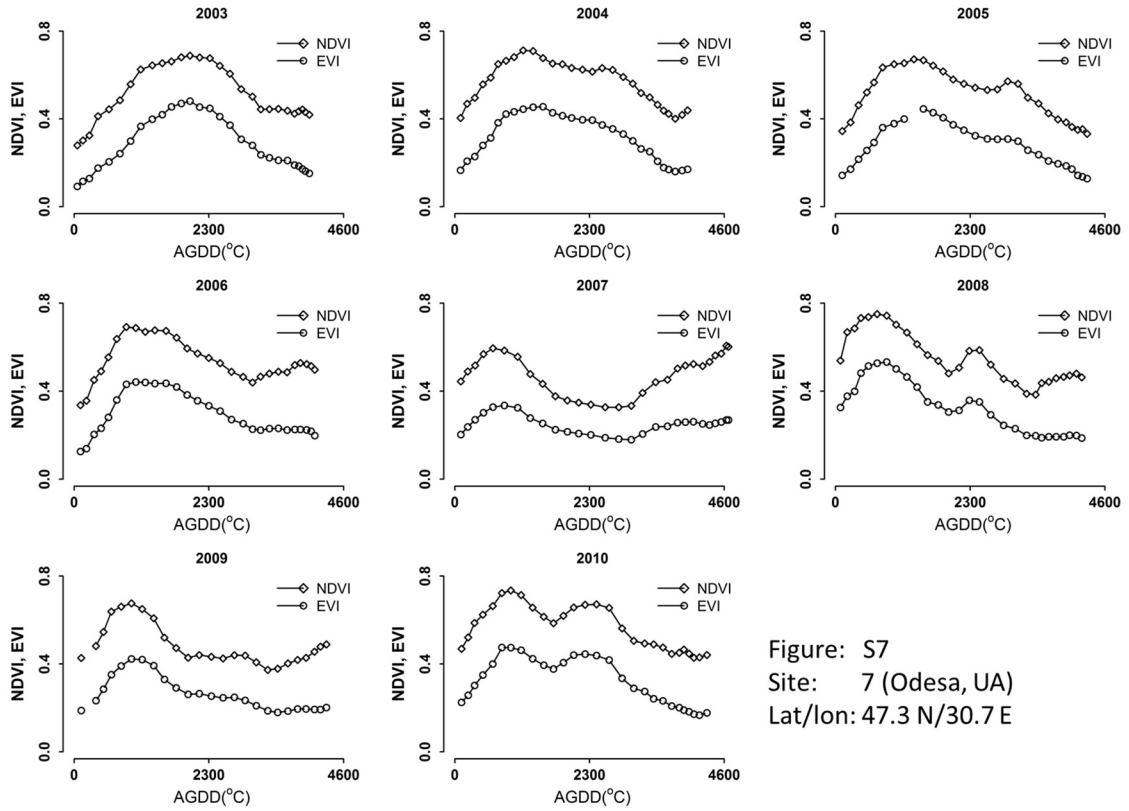


Figure: S7  
 Site: 7 (Odesa, UA)  
 Lat/lon: 47.3 N/30.7 E

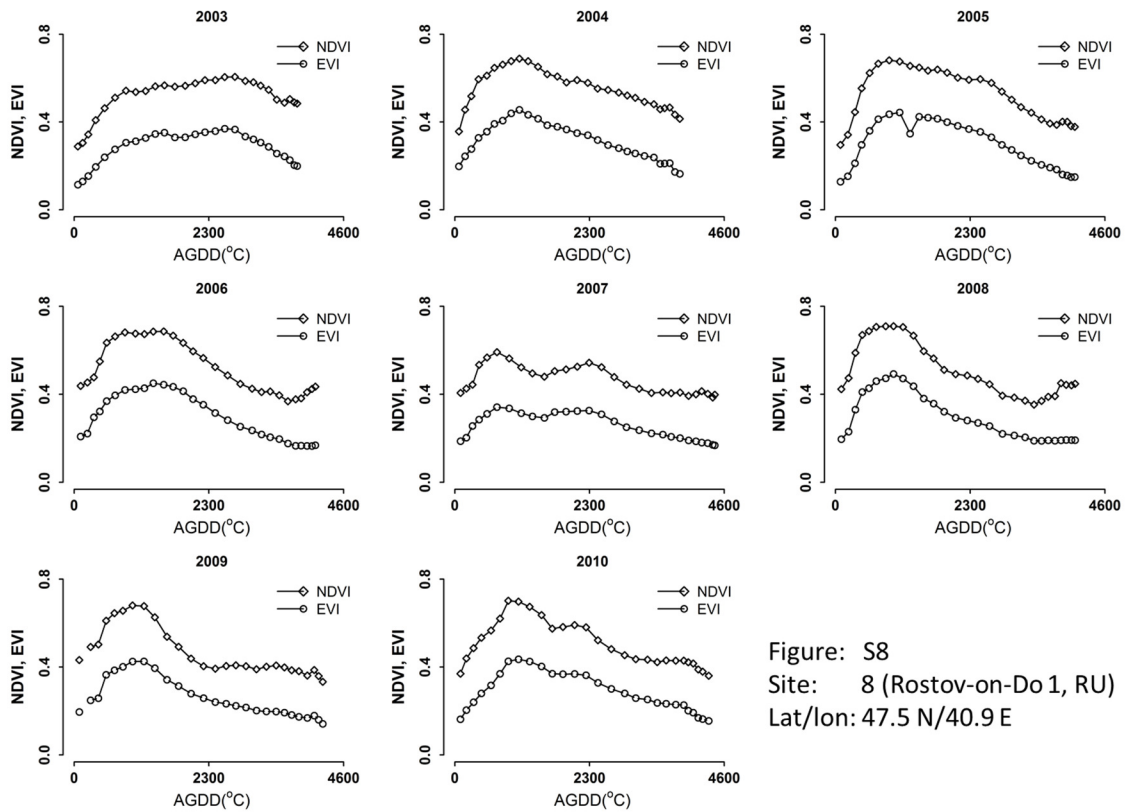


Figure: S8  
 Site: 8 (Rostov-on-Do 1, RU)  
 Lat/lon: 47.5 N/40.9 E

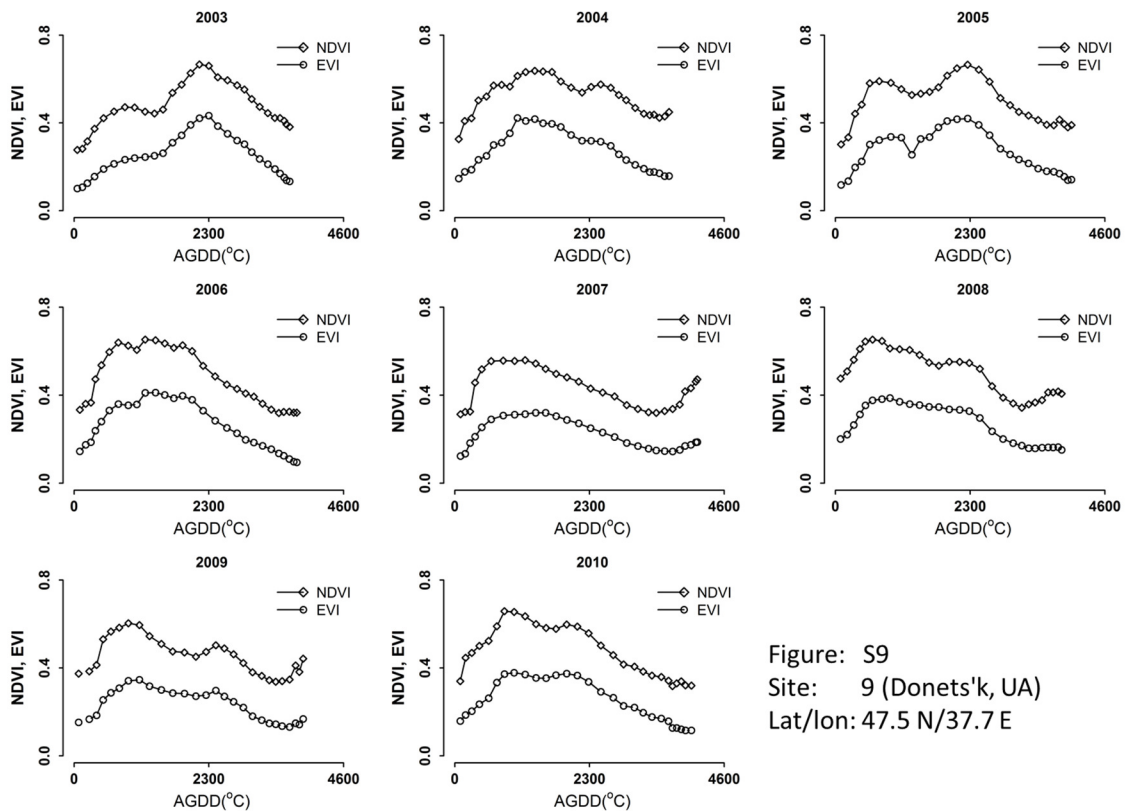


Figure: S9  
 Site: 9 (Donets'k, UA)  
 Lat/lon: 47.5 N/37.7 E

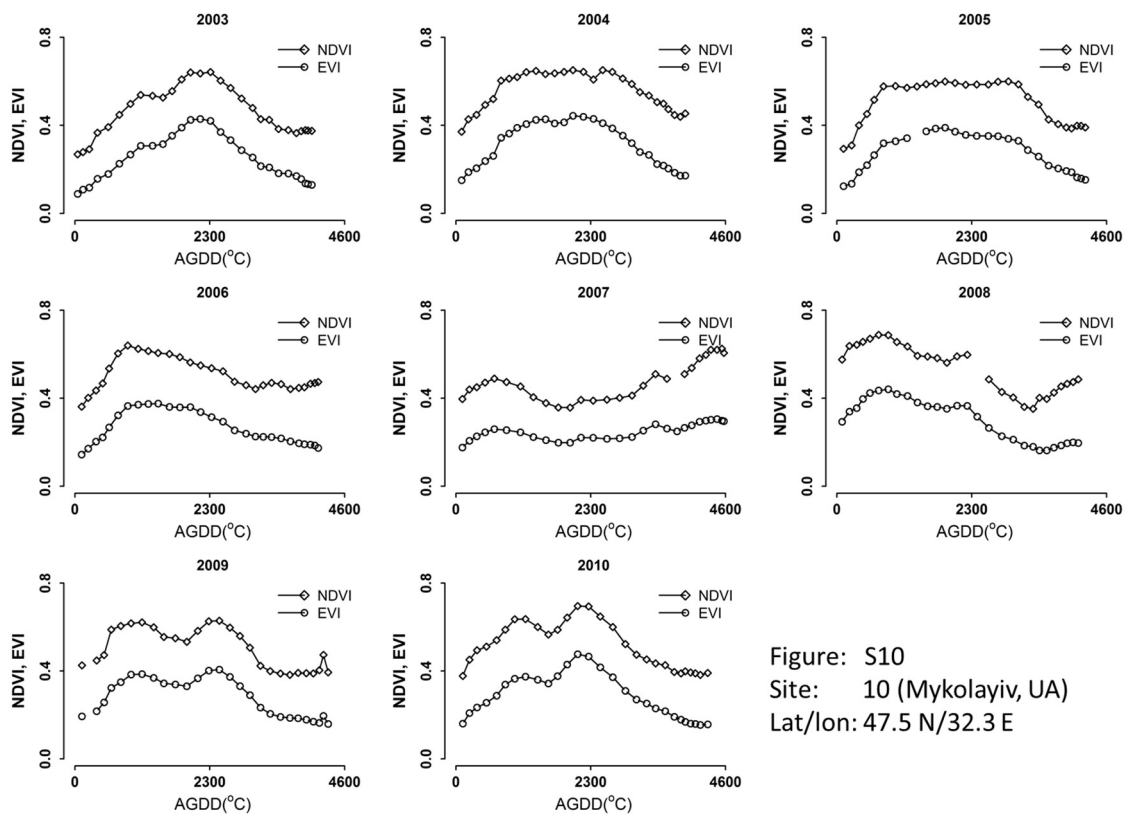


Figure: S10  
 Site: 10 (Mykolayiv, UA)  
 Lat/lon: 47.5 N/32.3 E

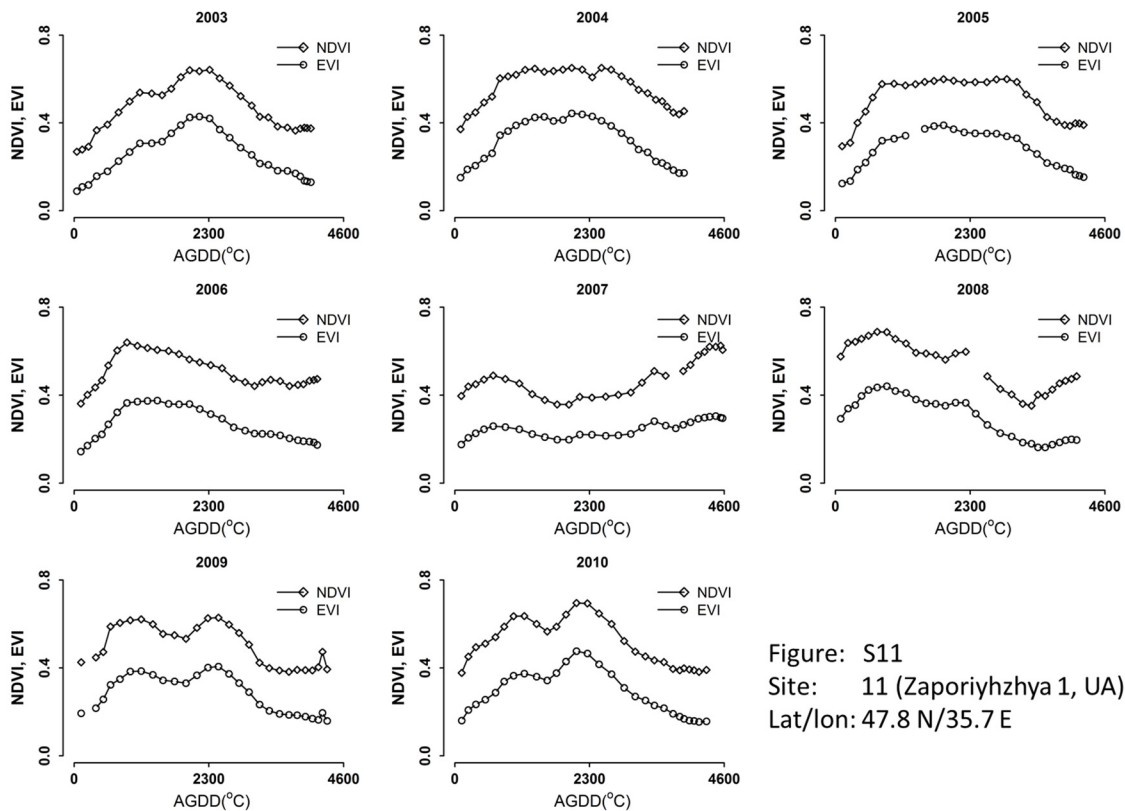


Figure: S11  
 Site: 11 (Zaporiyhzhya 1, UA)  
 Lat/Ion: 47.8 N/35.7 E

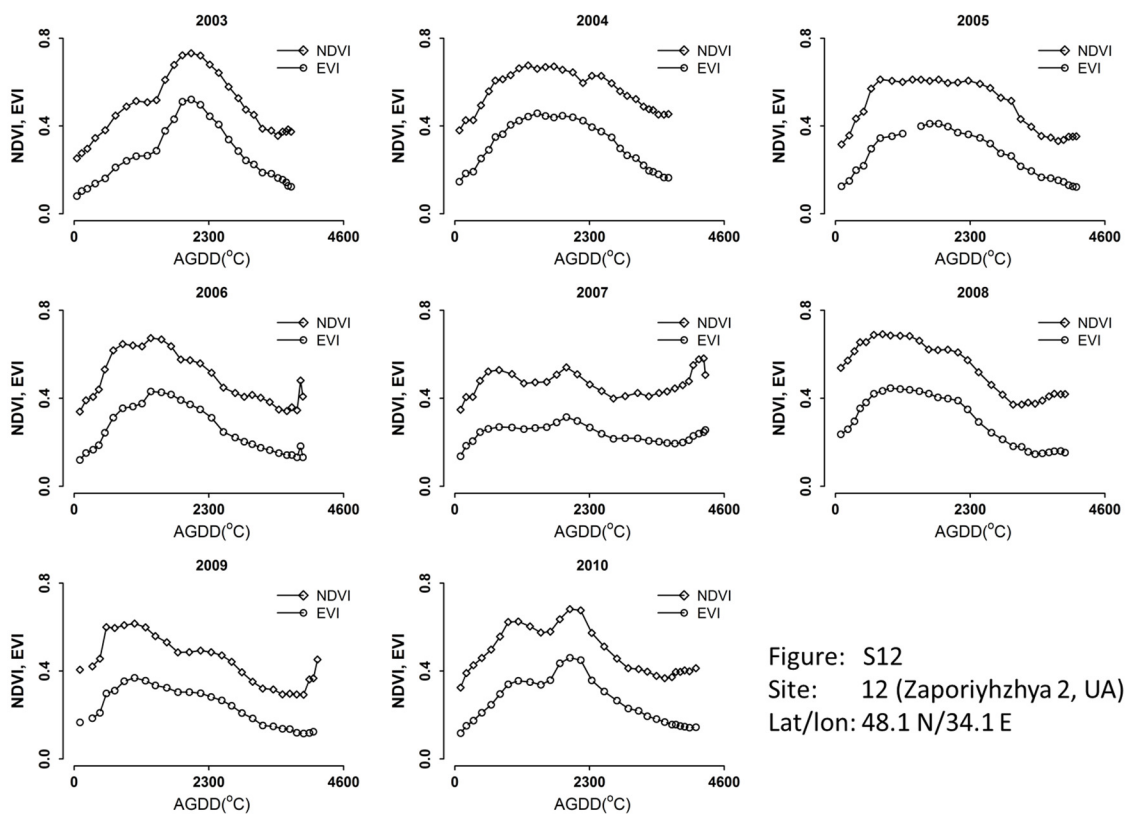


Figure: S12  
 Site: 12 (Zaporiyhzhya 2, UA)  
 Lat/Ion: 48.1 N/34.1 E



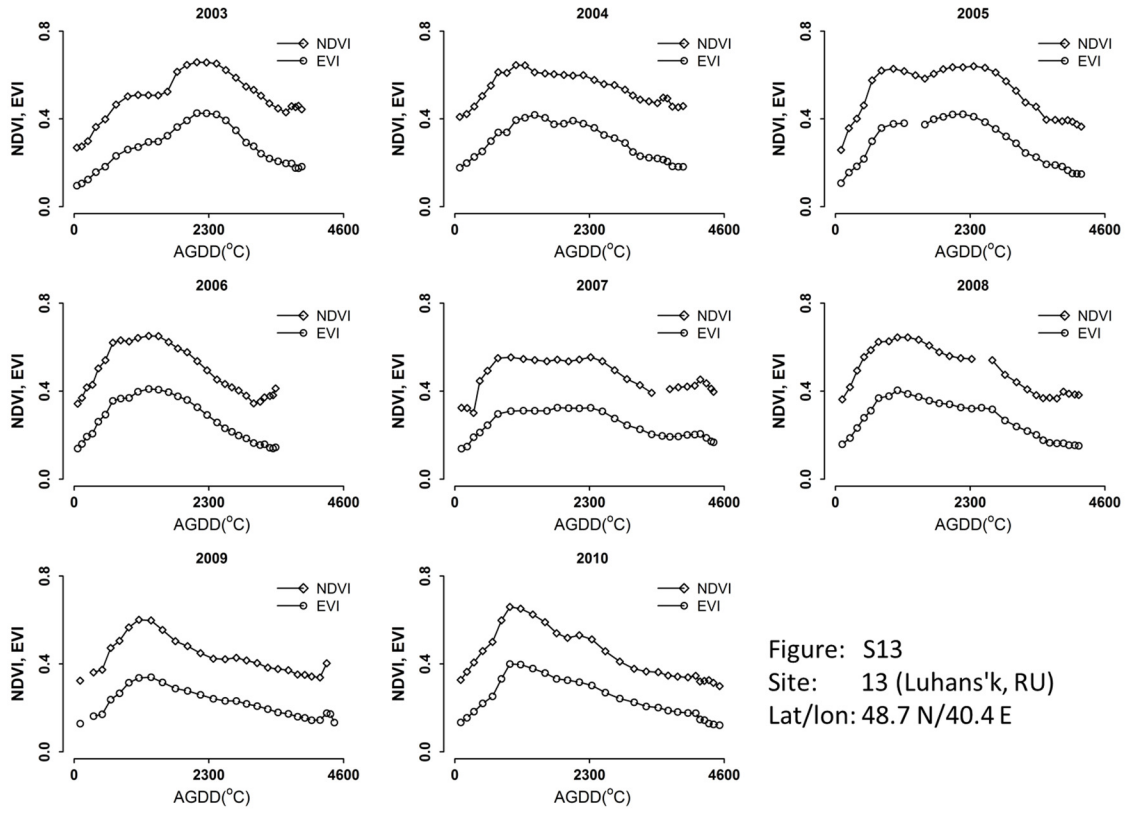


Figure: S13  
 Site: 13 (Luhans'k, RU)  
 Lat/lon: 48.7 N/40.4 E

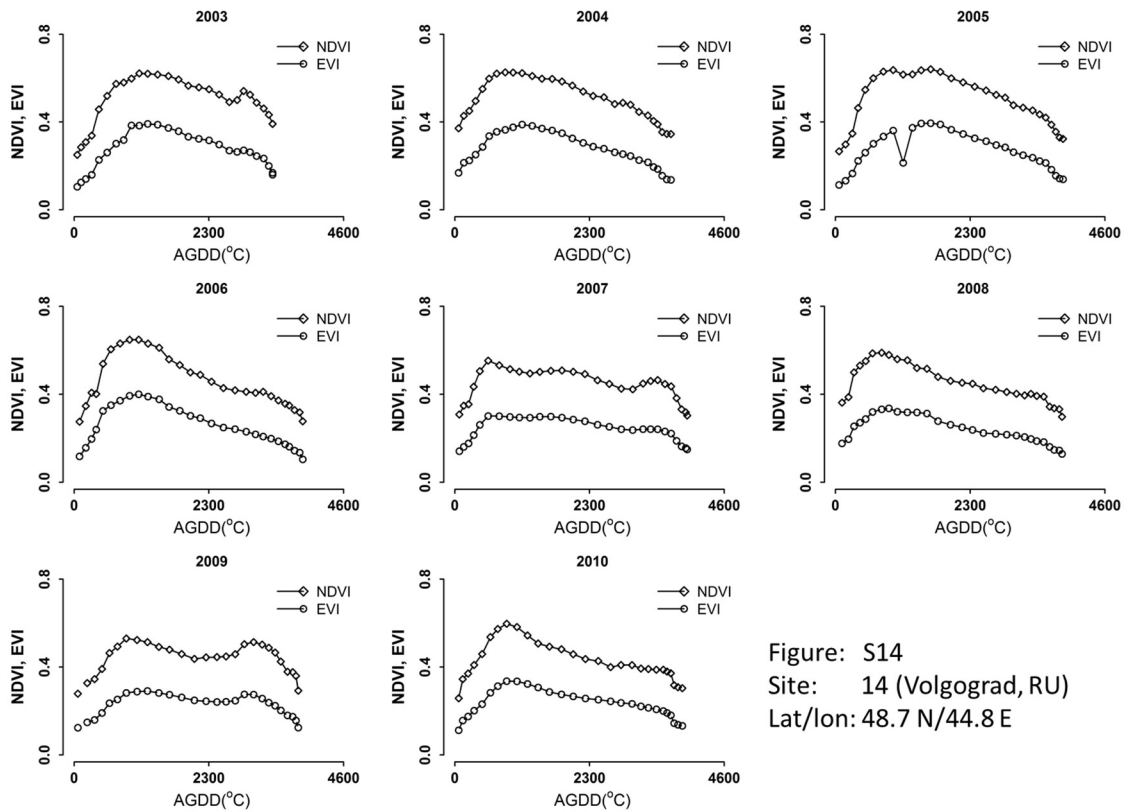


Figure: S14  
 Site: 14 (Volgograd, RU)  
 Lat/lon: 48.7 N/44.8 E

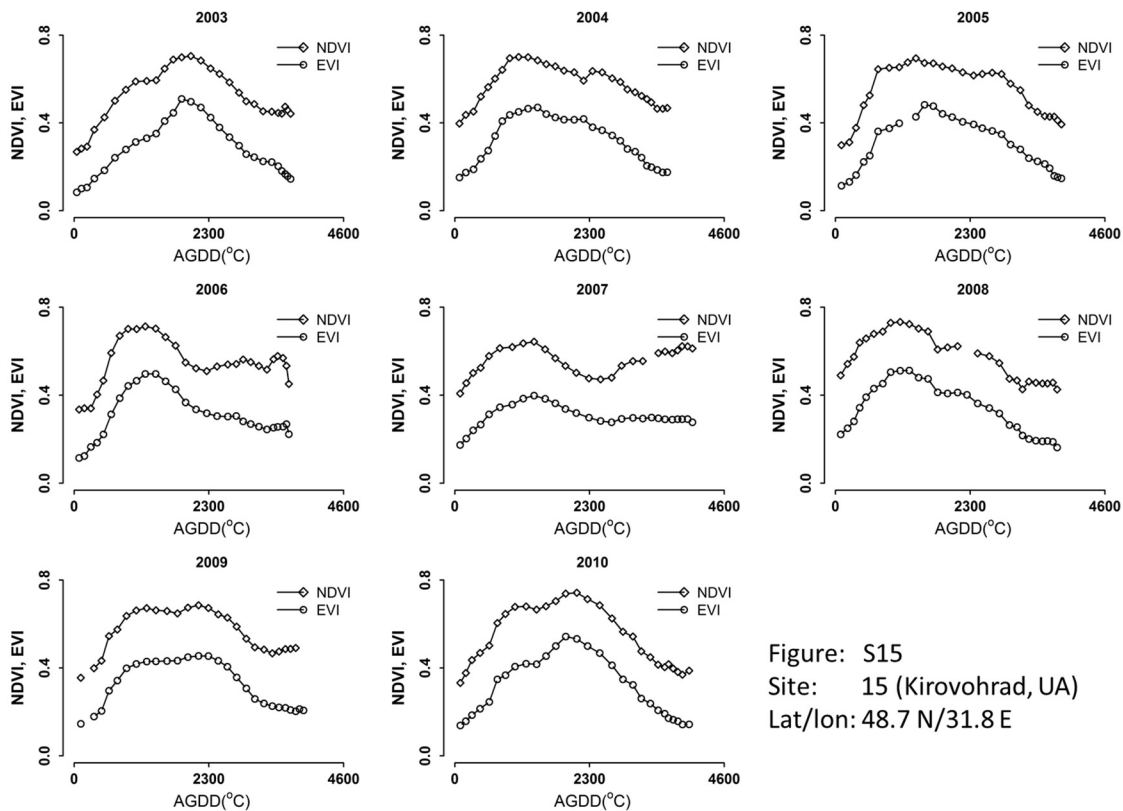


Figure: S15  
Site: 15 (Kirovohrad, UA)  
Lat/lon: 48.7 N/31.8 E

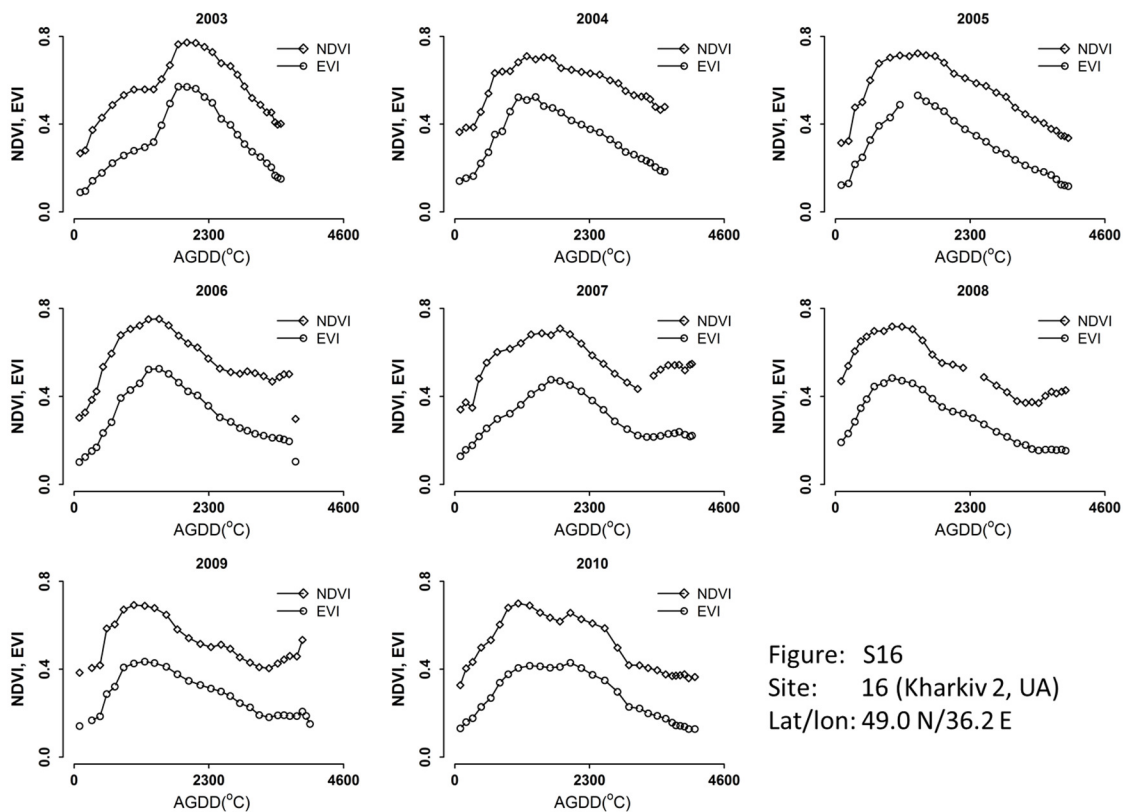


Figure: S16  
Site: 16 (Kharkiv 2, UA)  
Lat/lon: 49.0 N/36.2 E

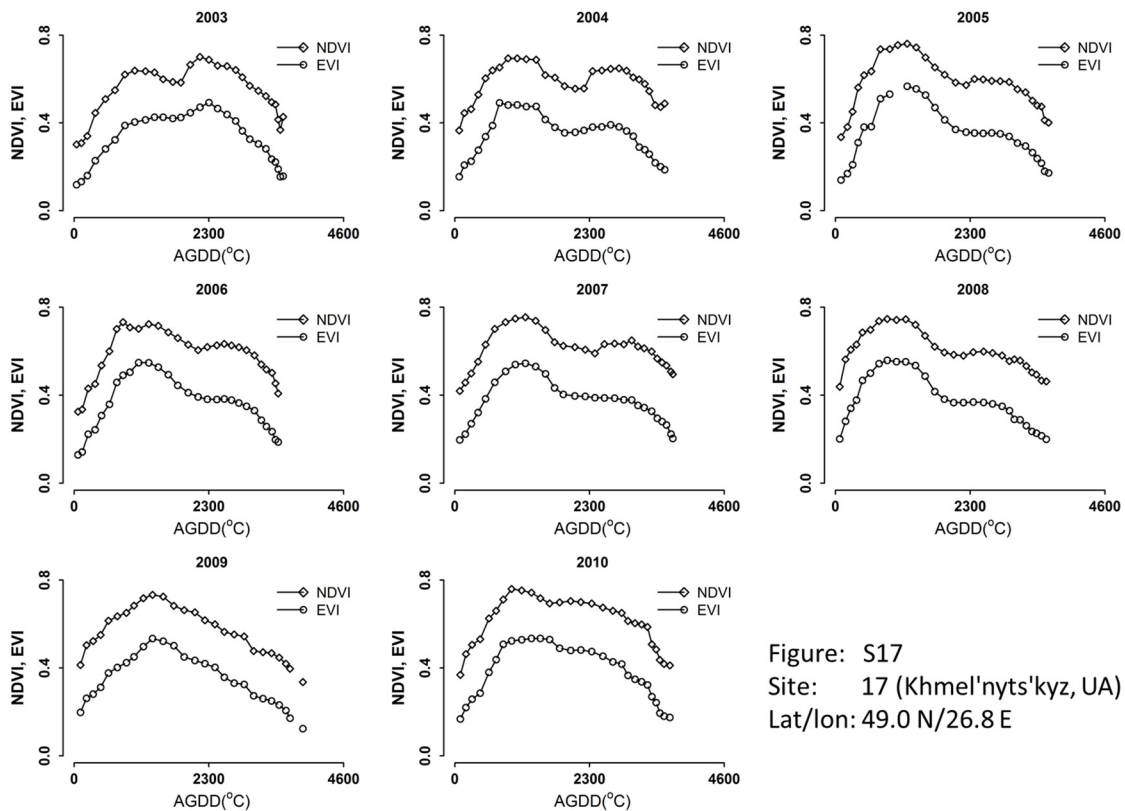


Figure: S17  
 Site: 17 (Khmel'nyts'kyz, UA)  
 Lat/lon: 49.0 N/26.8 E

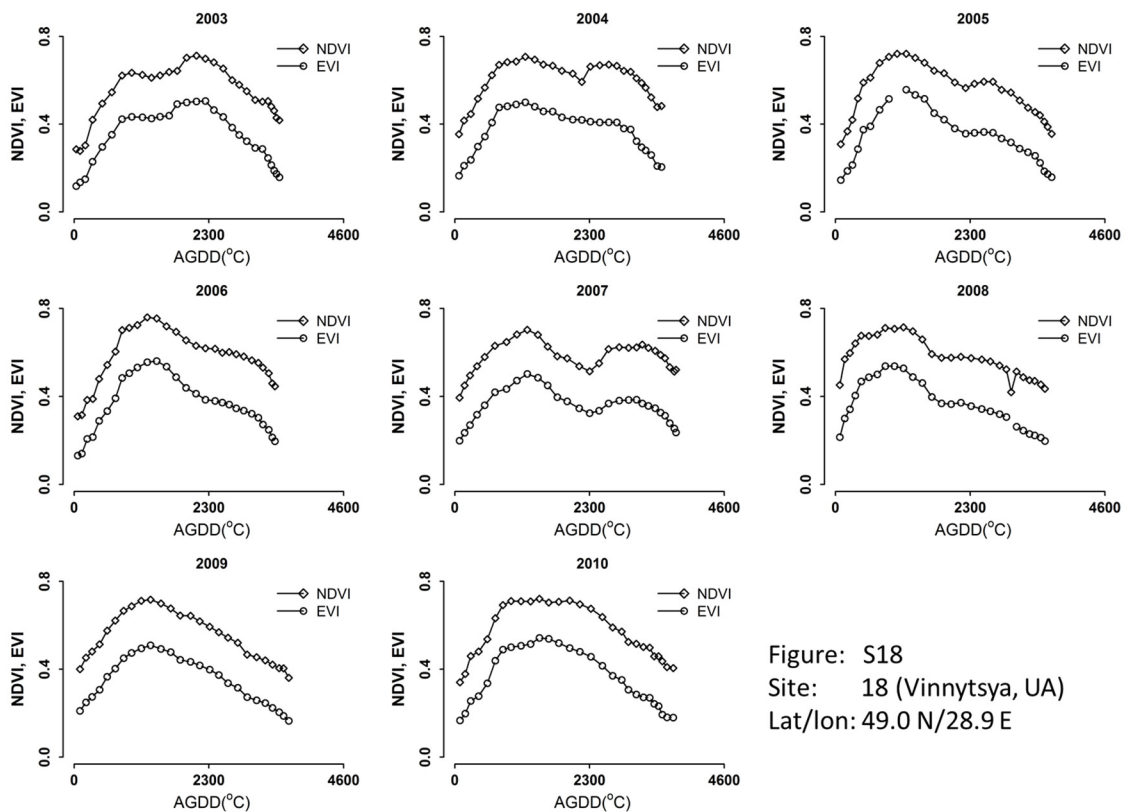


Figure: S18  
 Site: 18 (Vinnytsya, UA)  
 Lat/lon: 49.0 N/28.9 E

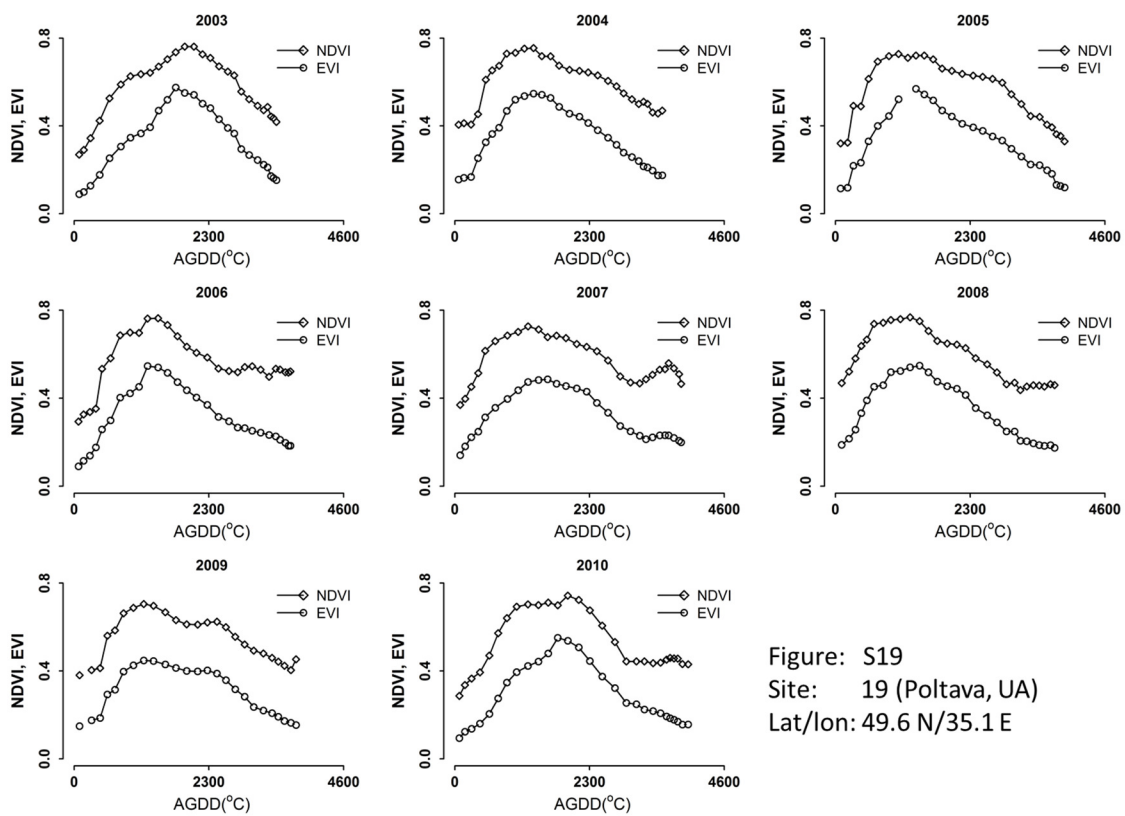


Figure: S19  
 Site: 19 (Poltava, UA)  
 Lat/lon: 49.6 N/35.1 E

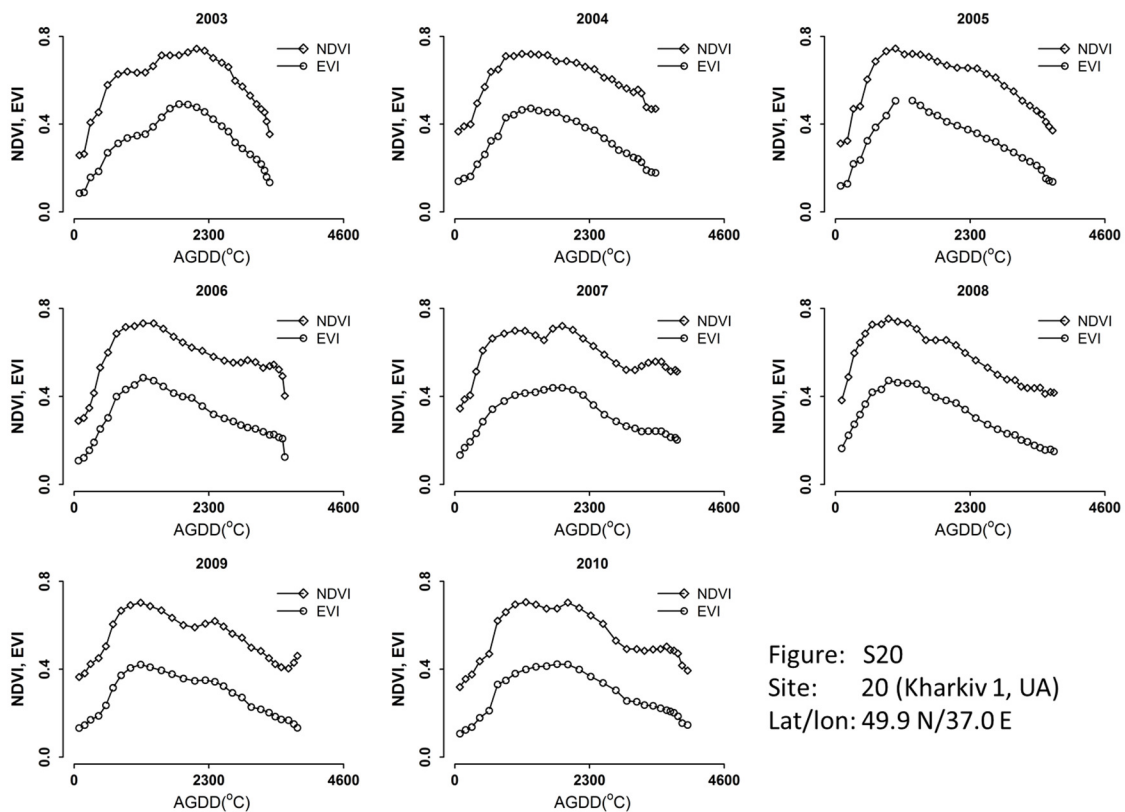


Figure: S20  
 Site: 20 (Kharkiv 1, UA)  
 Lat/lon: 49.9 N/37.0 E

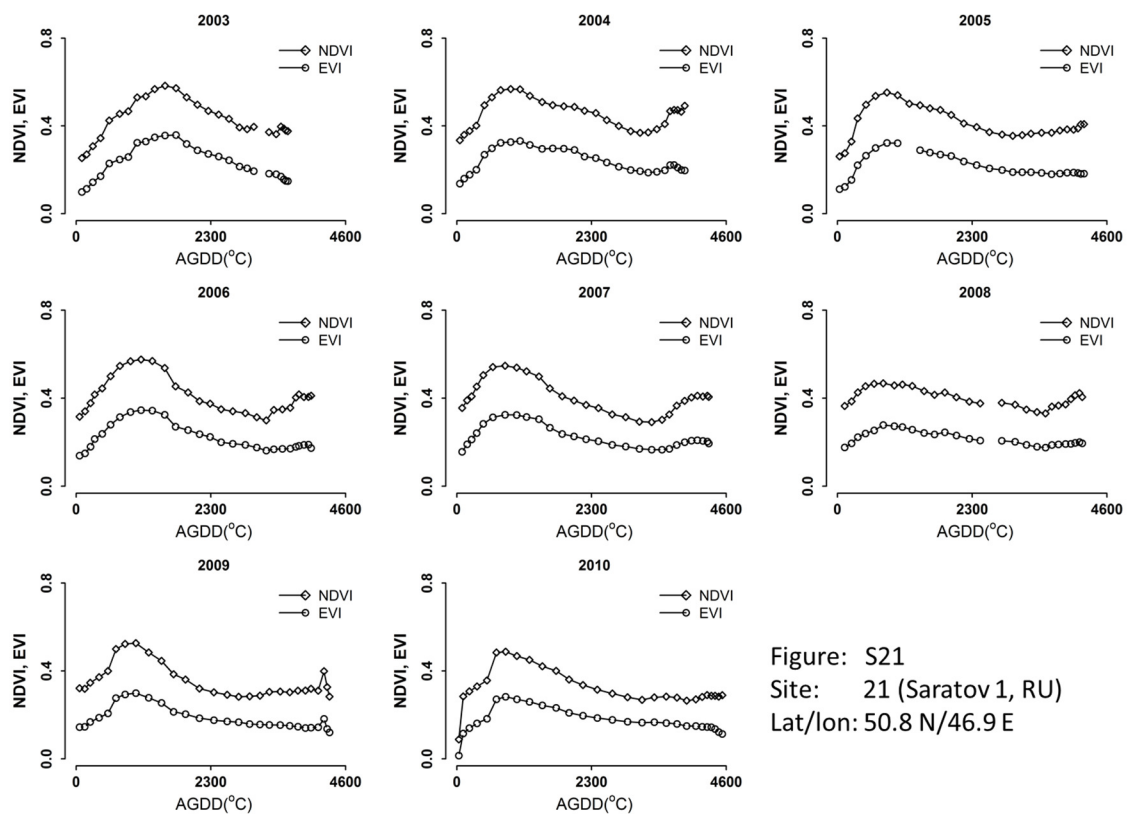


Figure: S21  
 Site: 21 (Saratov 1, RU)  
 Lat/lon: 50.8 N/46.9 E

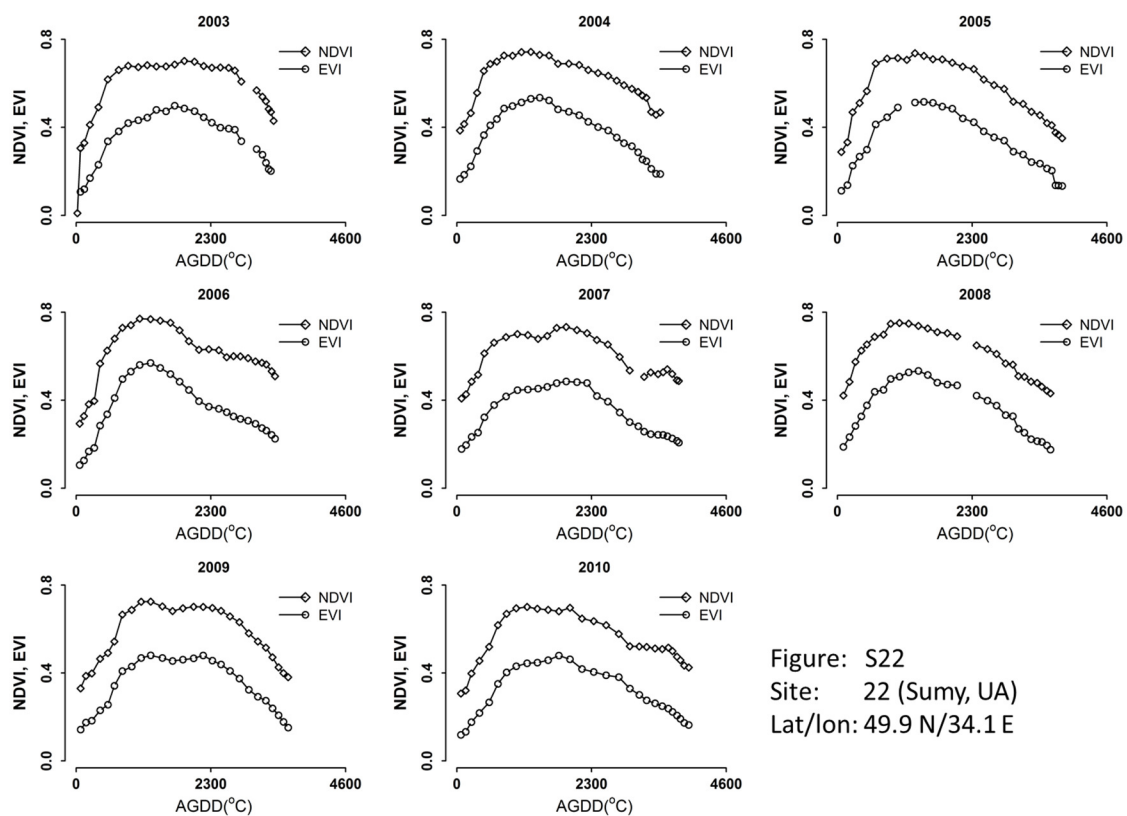


Figure: S22  
 Site: 22 (Sumy, UA)  
 Lat/lon: 49.9 N/34.1 E

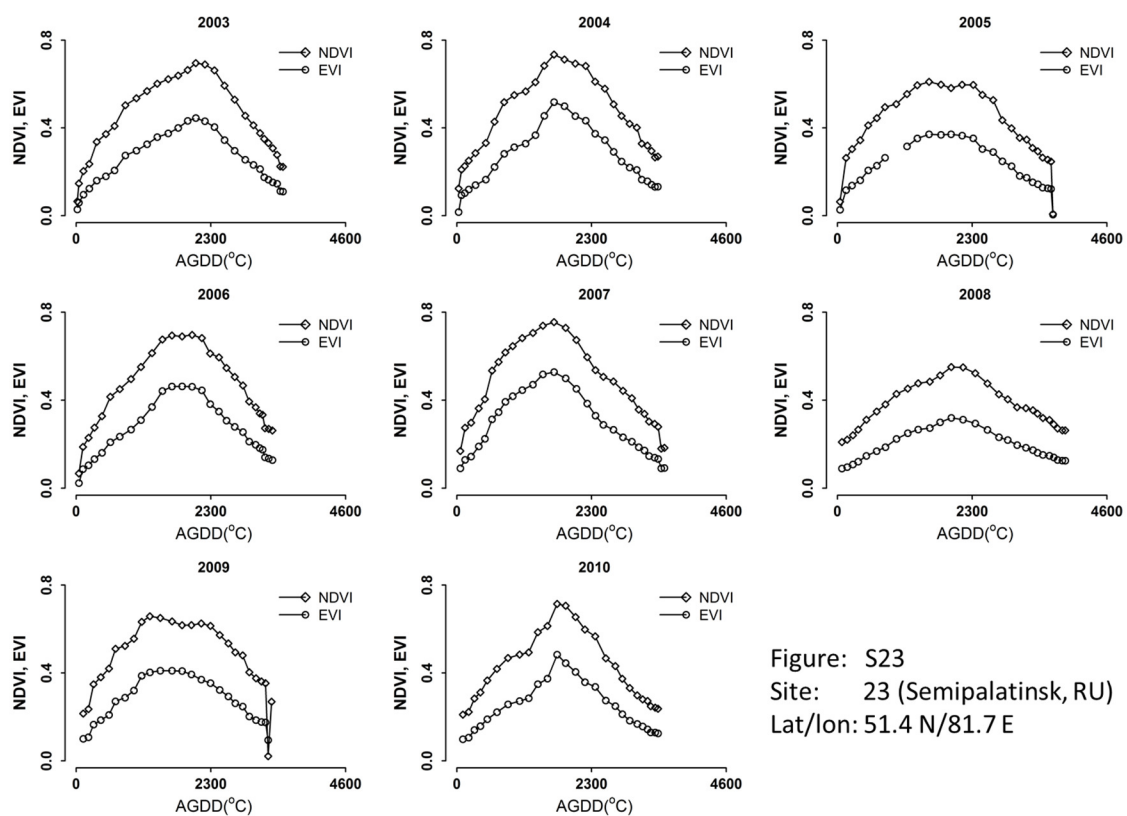


Figure: S23  
 Site: 23 (Semipalatinsk, RU)  
 Lat/Ion: 51.4 N/81.7 E

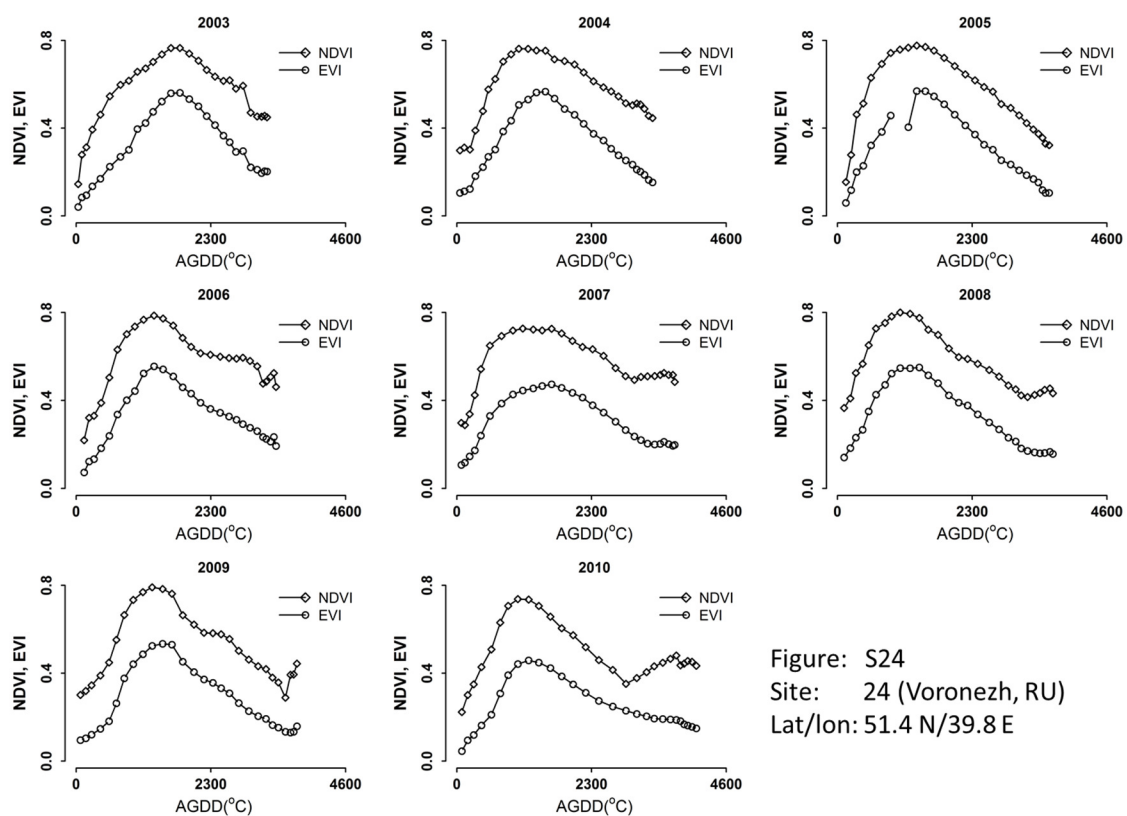


Figure: S24  
 Site: 24 (Voronezh, RU)  
 Lat/Ion: 51.4 N/39.8 E

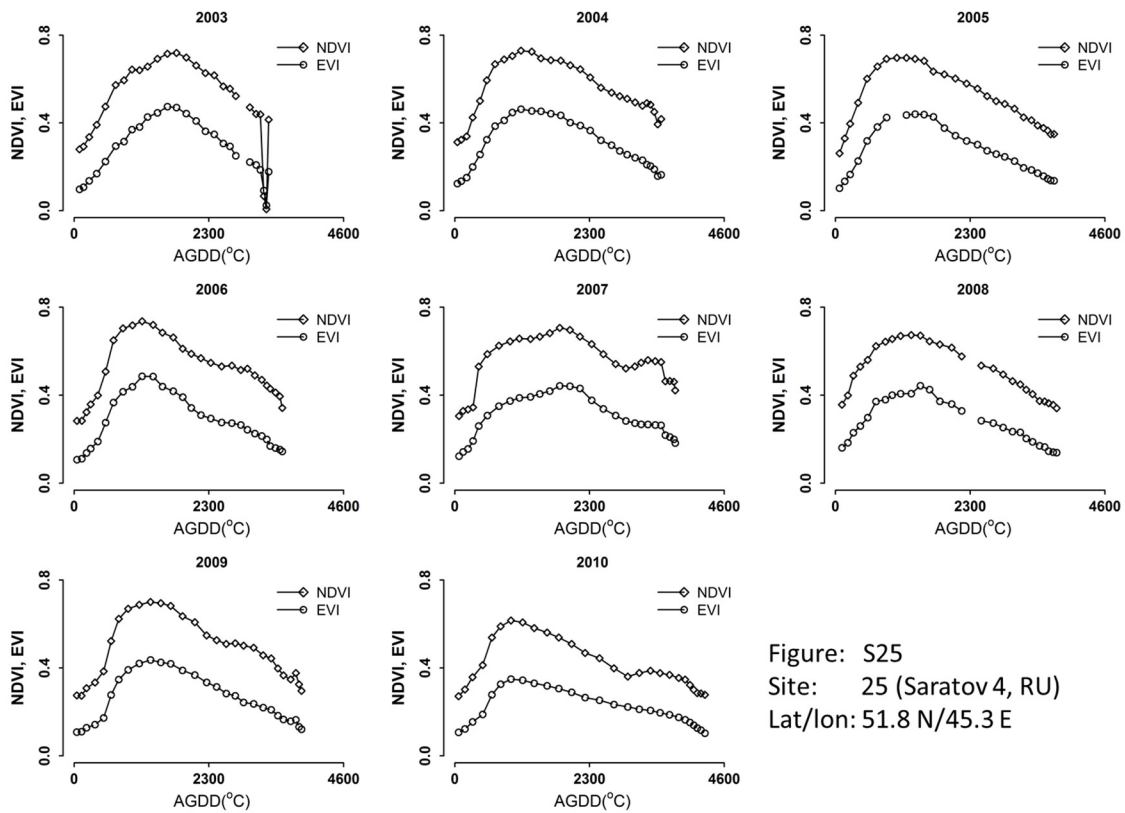


Figure: S25  
 Site: 25 (Saratov 4, RU)  
 Lat/lon: 51.8 N/45.3 E

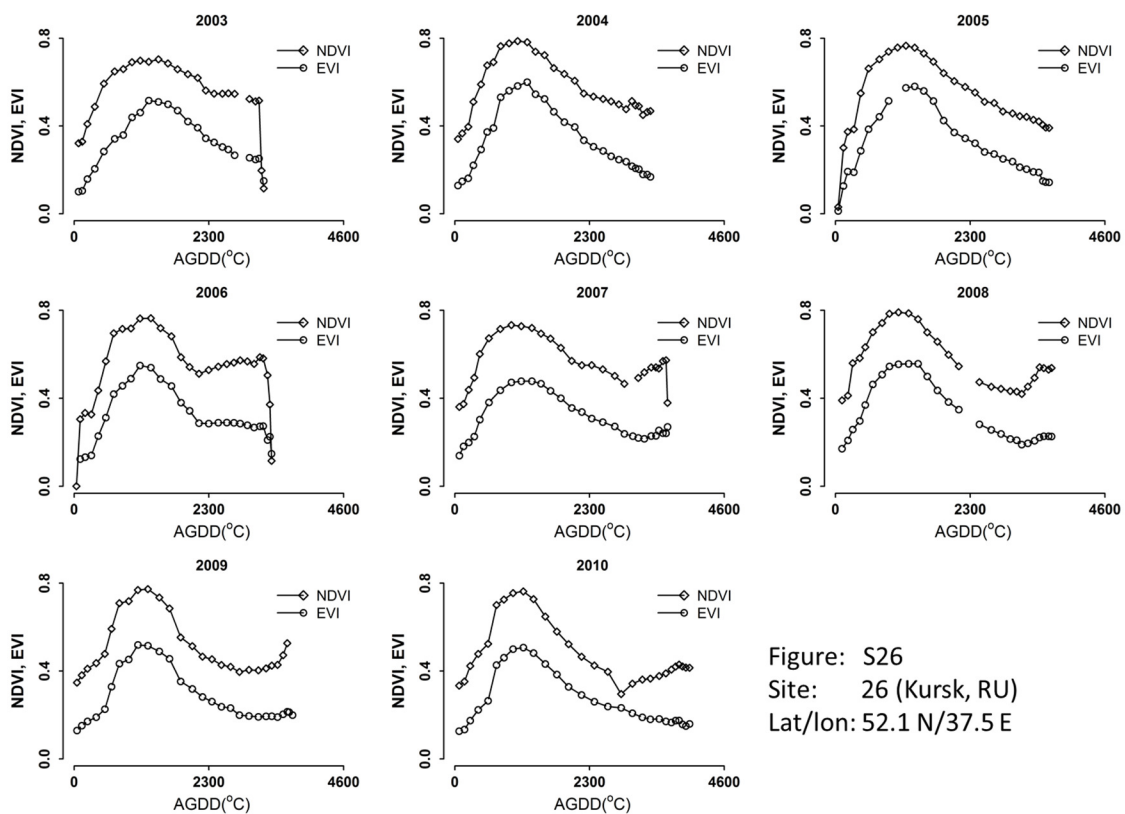


Figure: S26  
 Site: 26 (Kursk, RU)  
 Lat/lon: 52.1 N/37.5 E

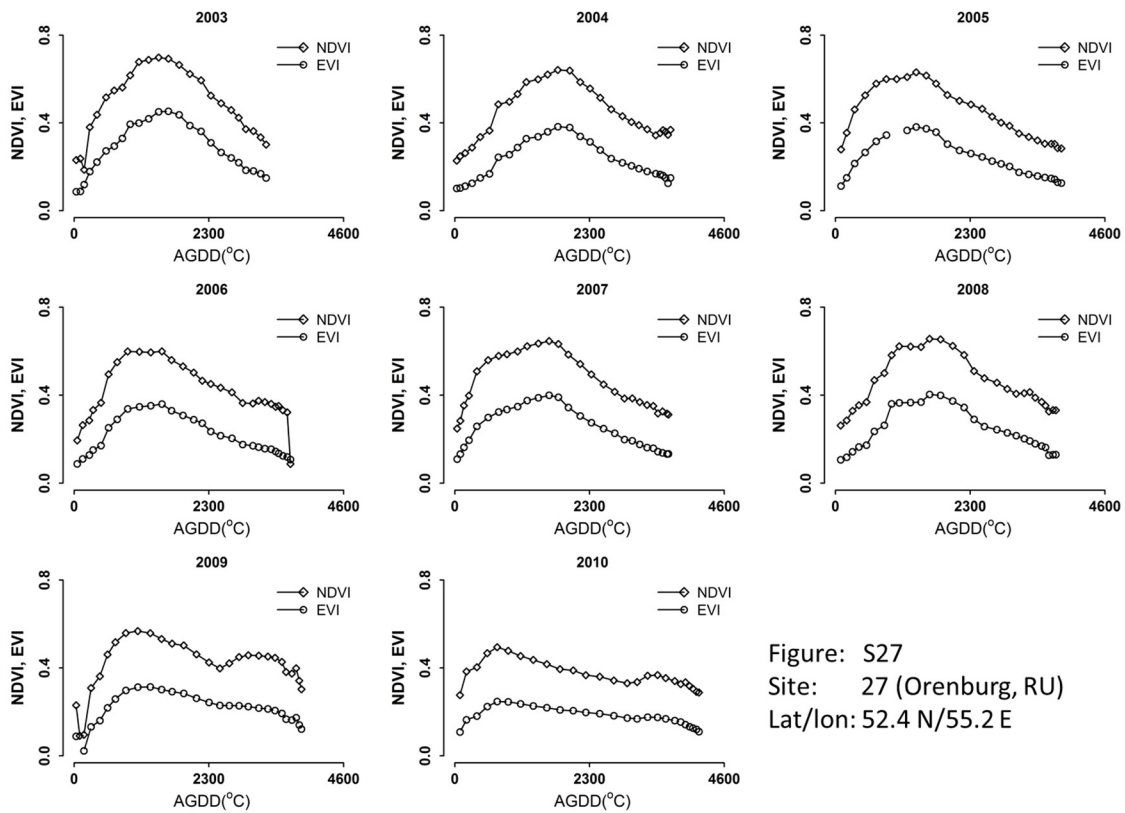


Figure: S27  
 Site: 27 (Orenburg, RU)  
 Lat/Ion: 52.4 N/55.2 E

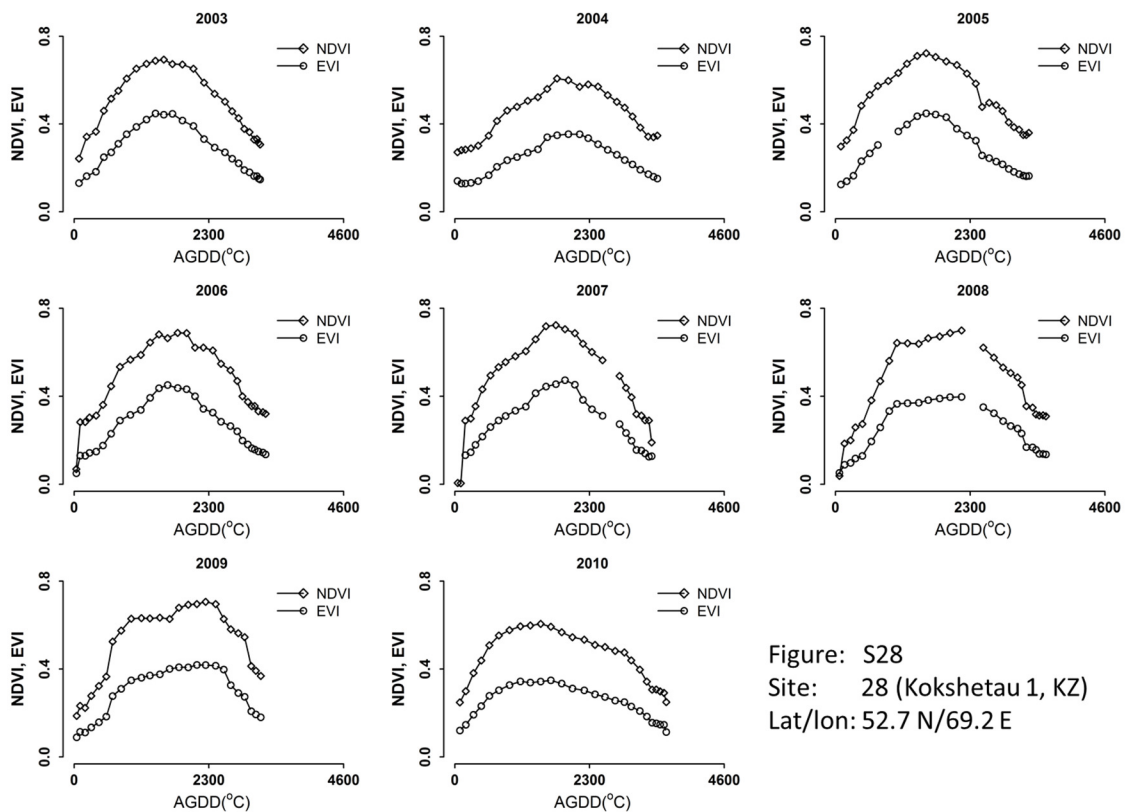


Figure: S28  
 Site: 28 (Kokshetau 1, KZ)  
 Lat/Ion: 52.7 N/69.2 E



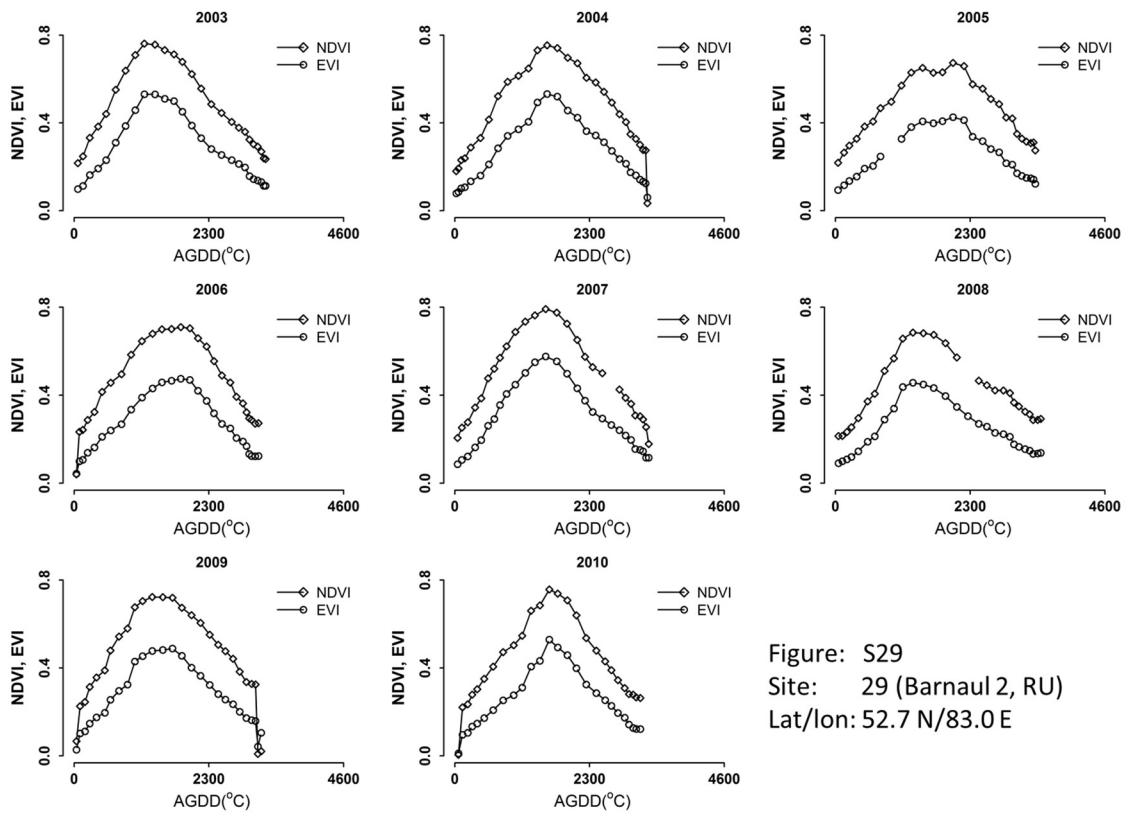


Figure: S29  
 Site: 29 (Barnaul 2, RU)  
 Lat/lon: 52.7 N/83.0 E

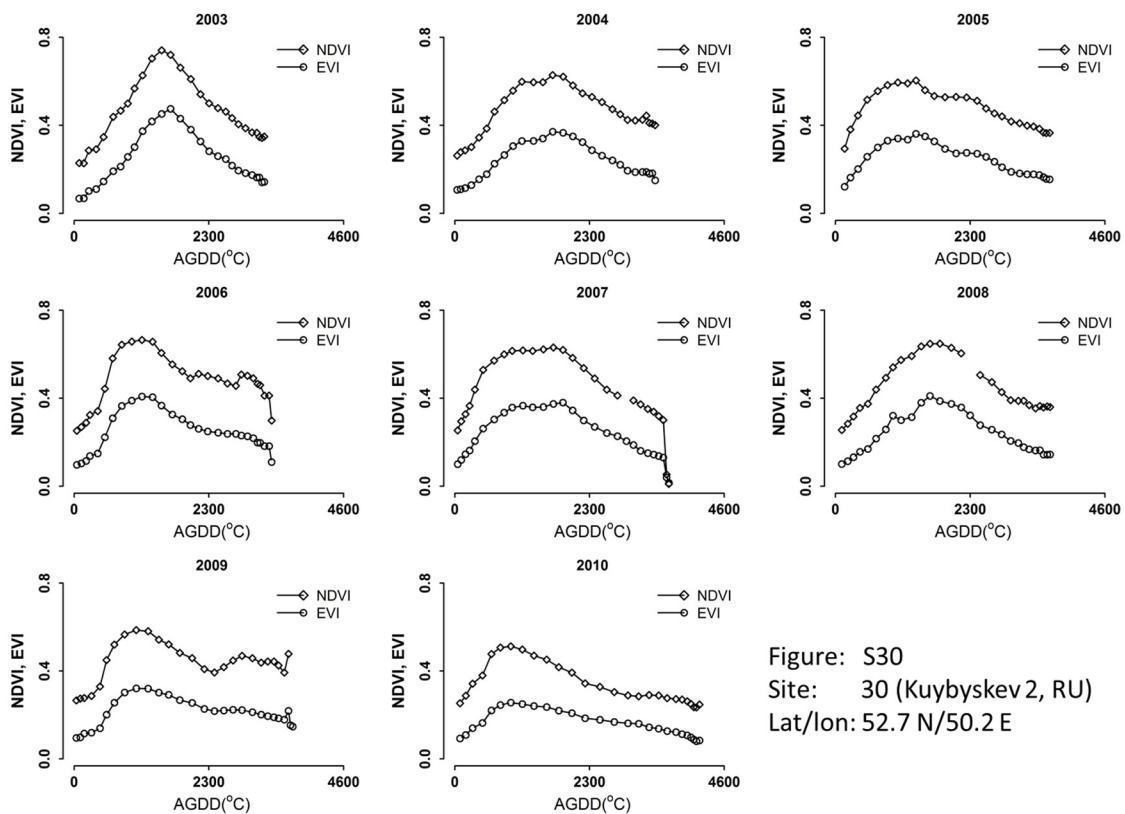


Figure: S30  
 Site: 30 (Kuybyshev 2, RU)  
 Lat/lon: 52.7 N/50.2 E

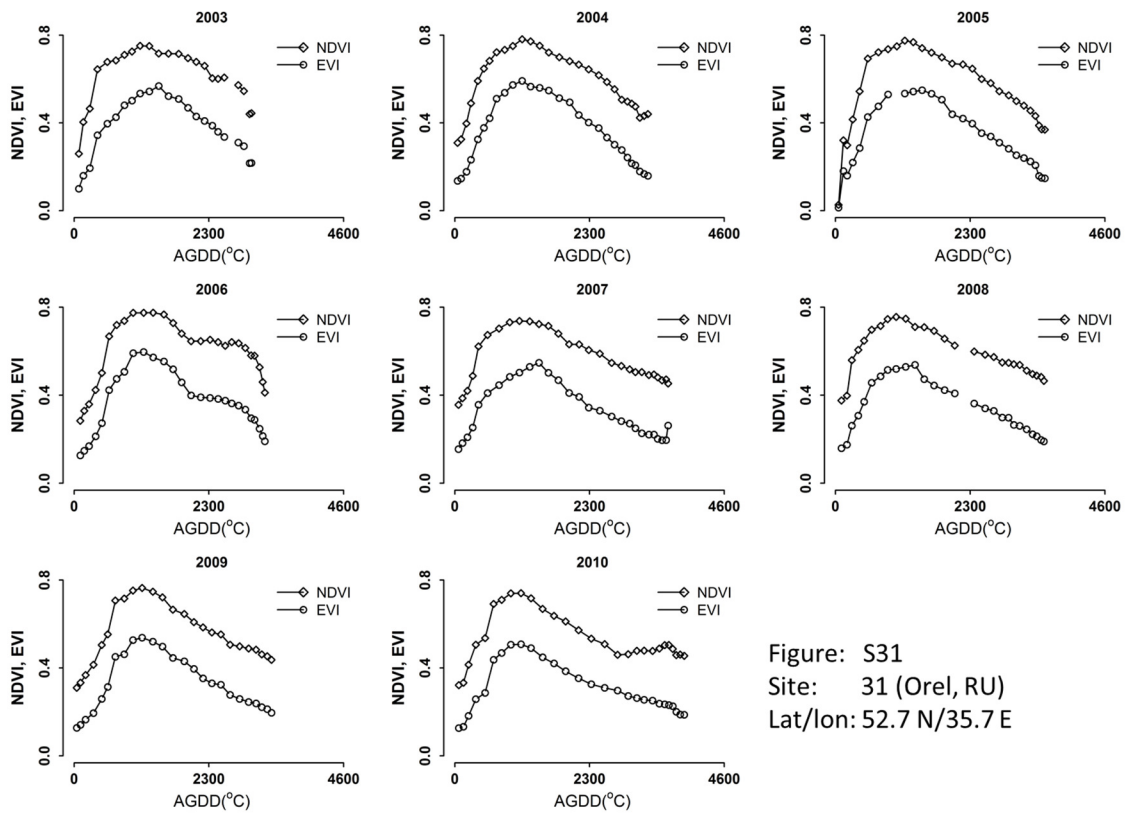


Figure: S31  
 Site: 31 (Orel, RU)  
 Lat/Ion: 52.7 N/35.7 E

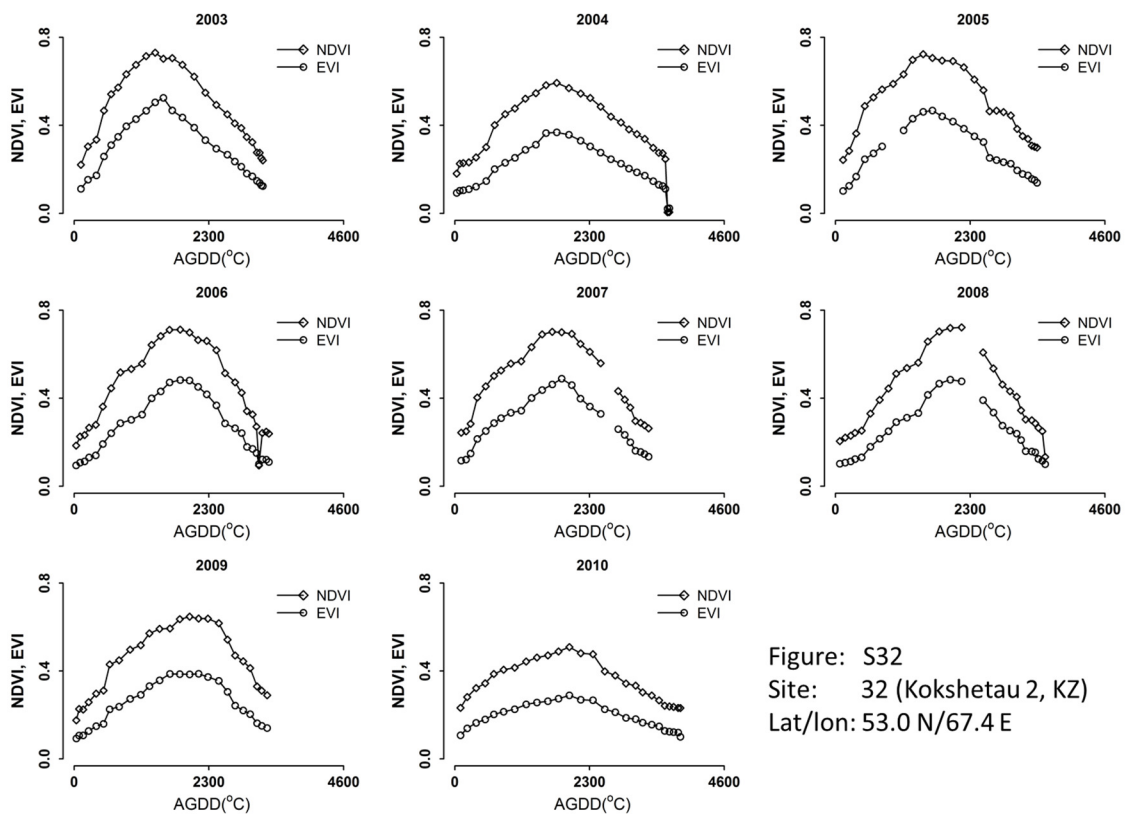


Figure: S32  
 Site: 32 (Kokshetau 2, KZ)  
 Lat/Ion: 53.0 N/67.4 E

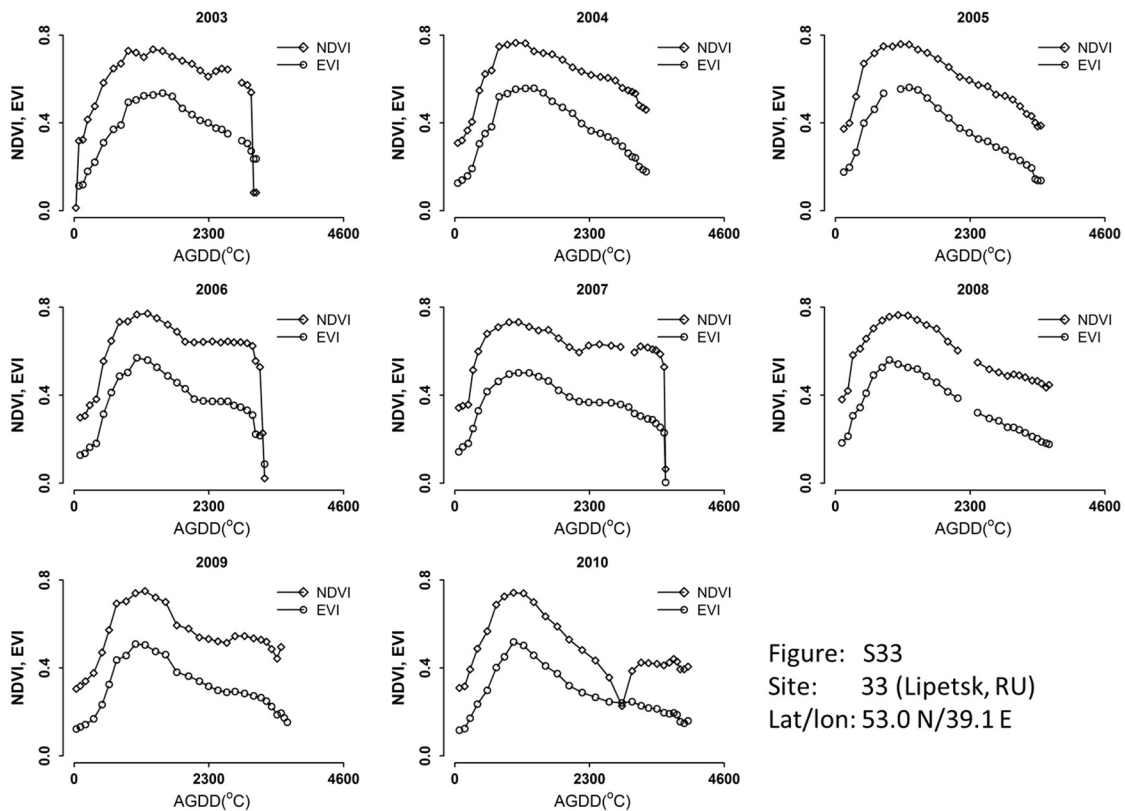


Figure: S33  
 Site: 33 (Lipetsk, RU)  
 Lat/Ion: 53.0 N/39.1 E

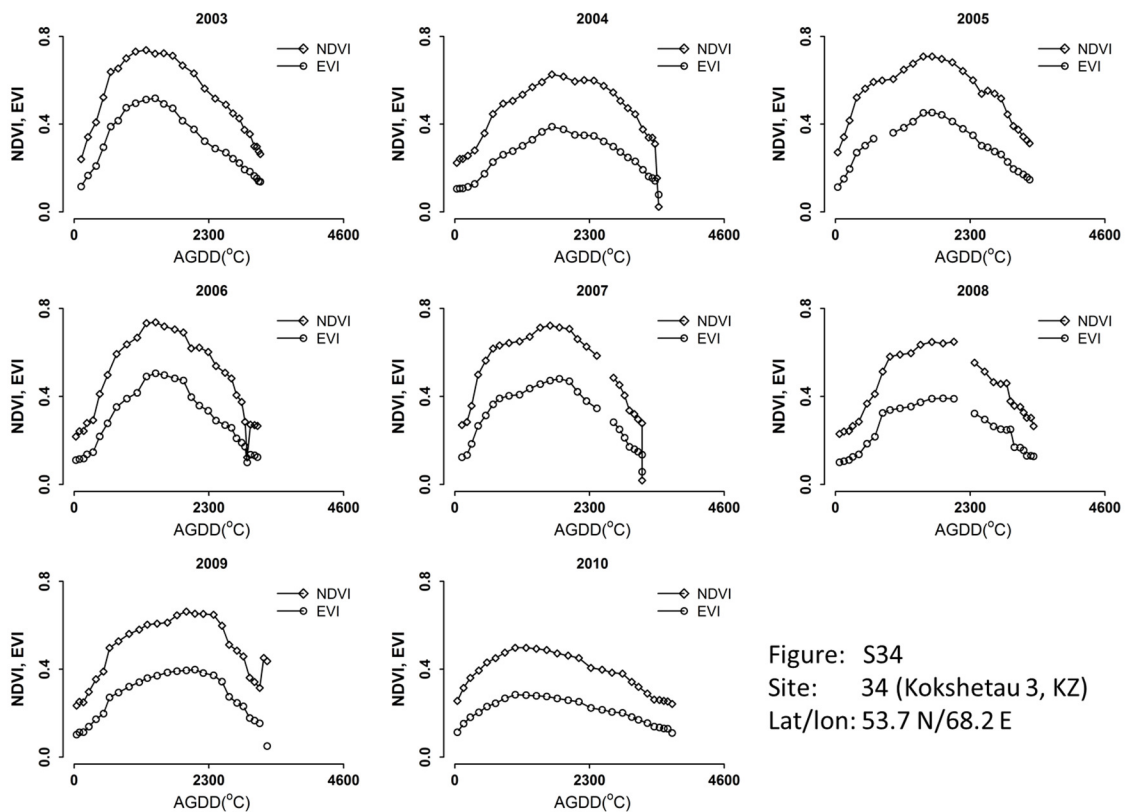
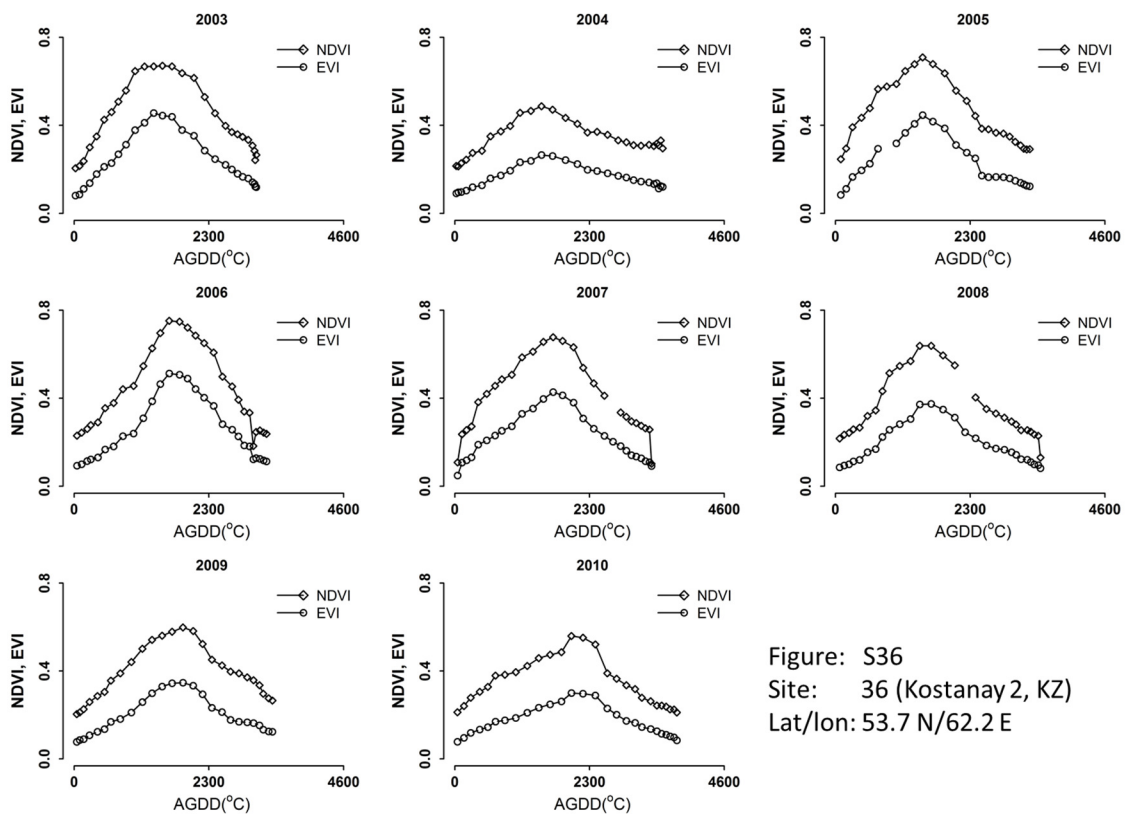
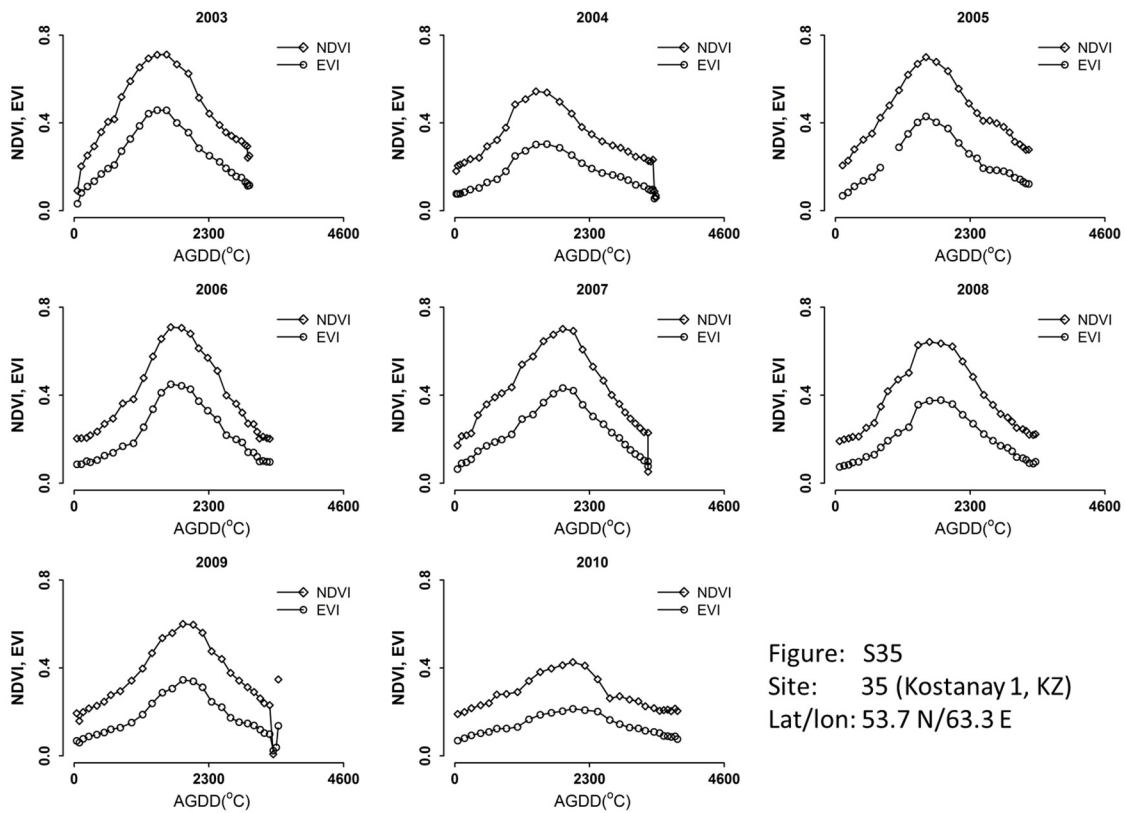


Figure: S34  
 Site: 34 (Kokshetau 3, KZ)  
 Lat/Ion: 53.7 N/68.2 E



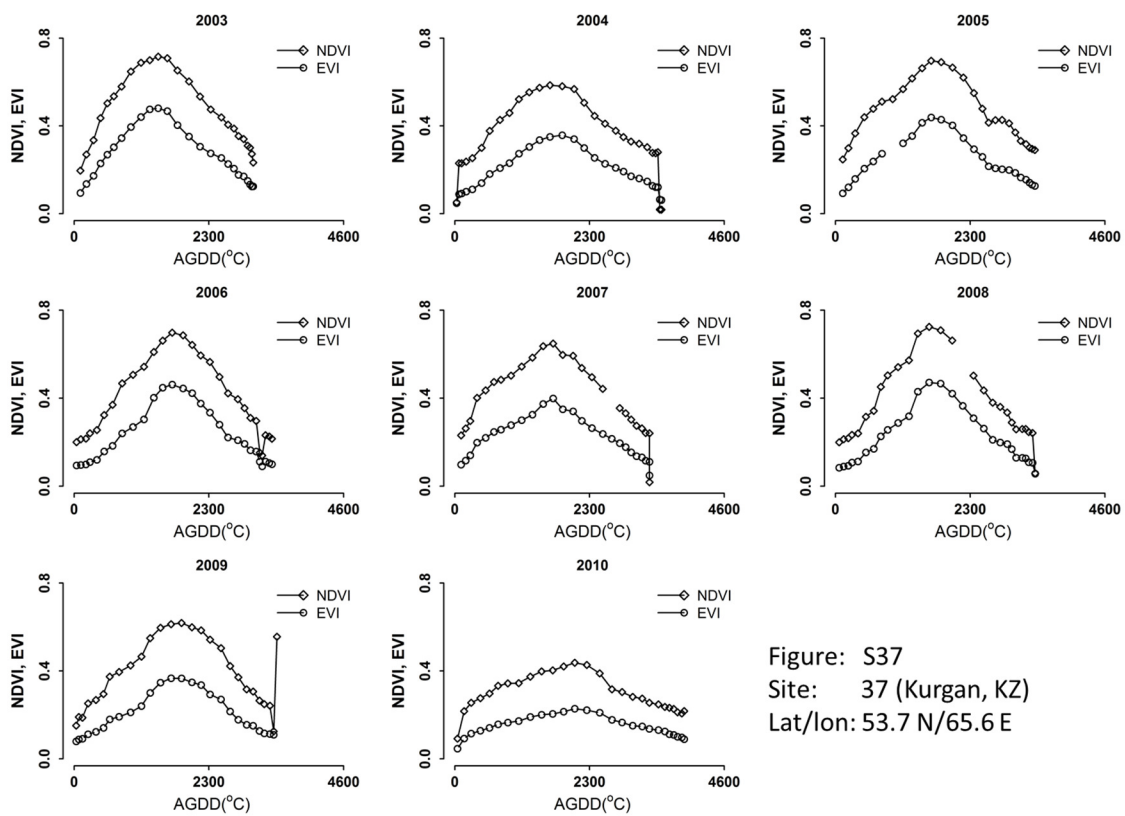


Figure: S37  
 Site: 37 (Kurgan, KZ)  
 Lat/Ion: 53.7 N/65.6 E

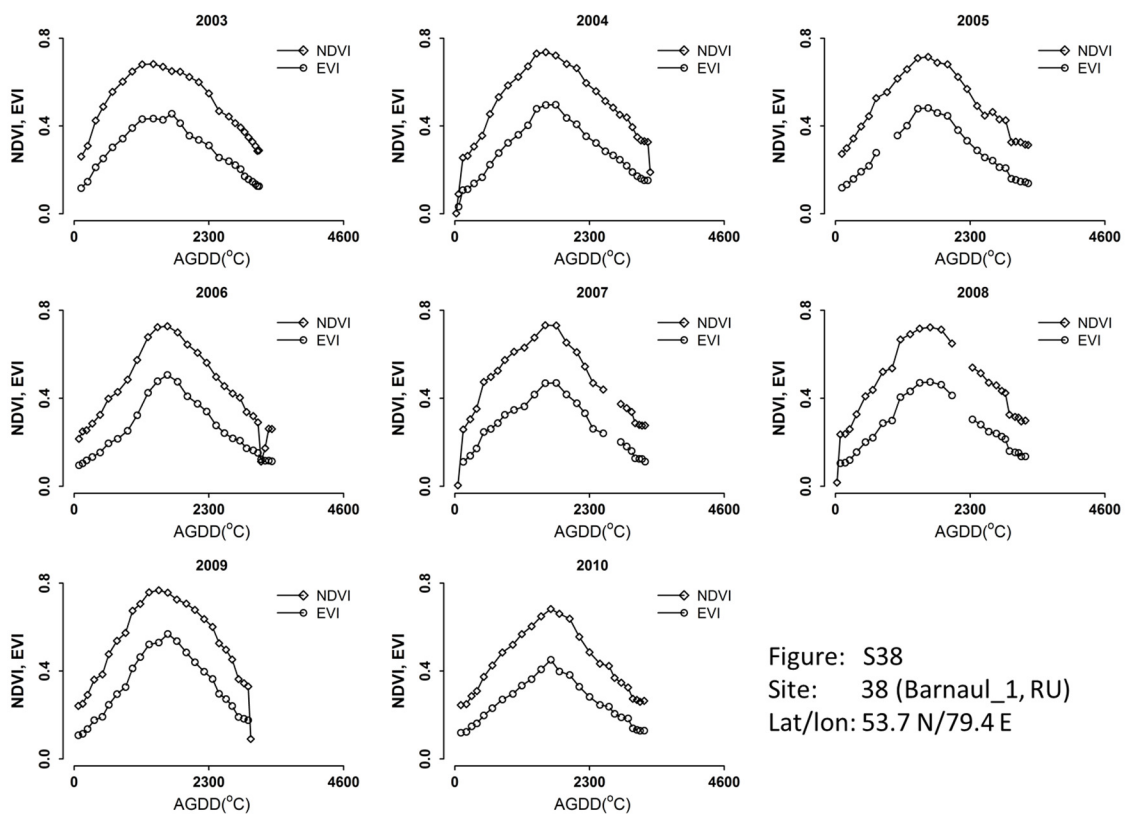
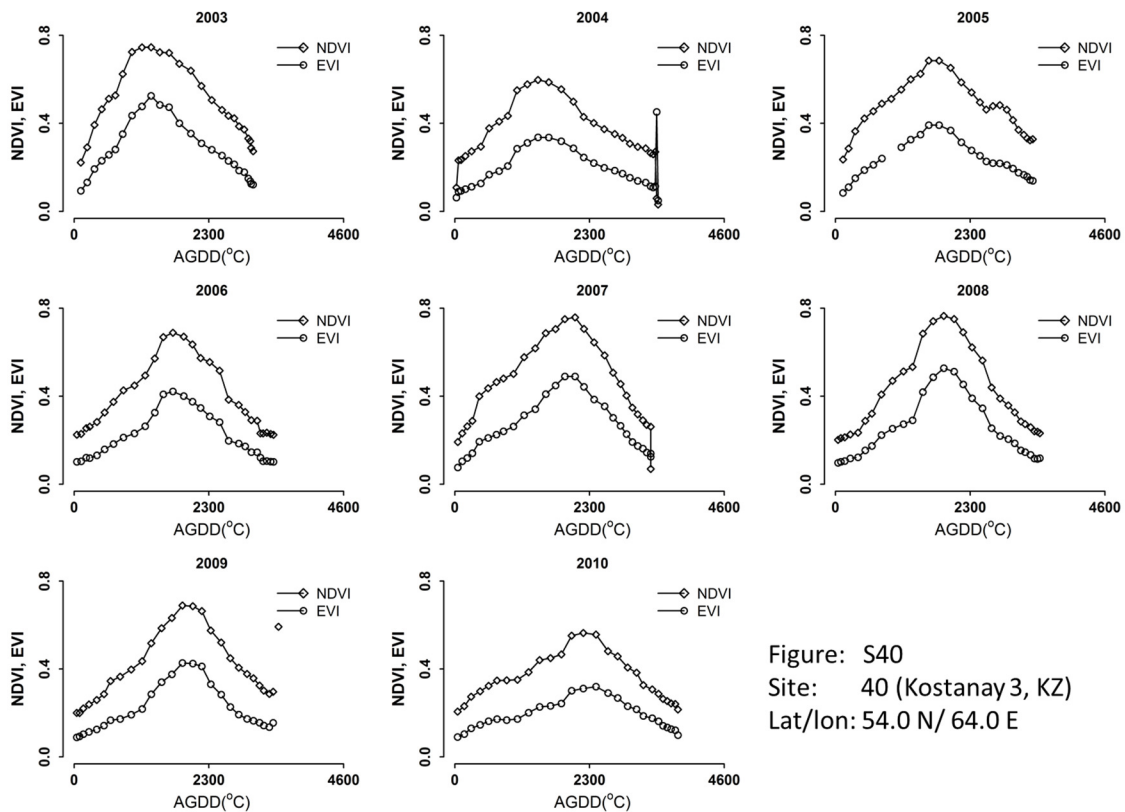
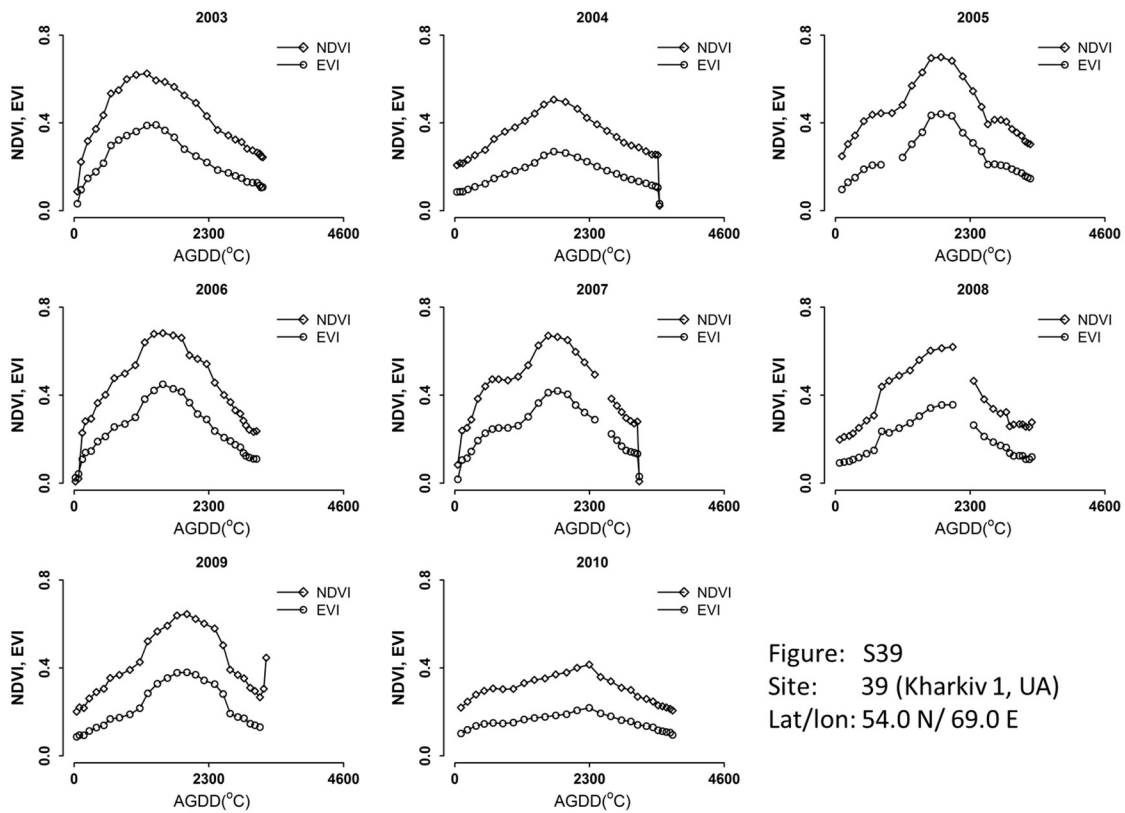


Figure: S38  
 Site: 38 (Barnaul\_1, RU)  
 Lat/Ion: 53.7 N/79.4 E



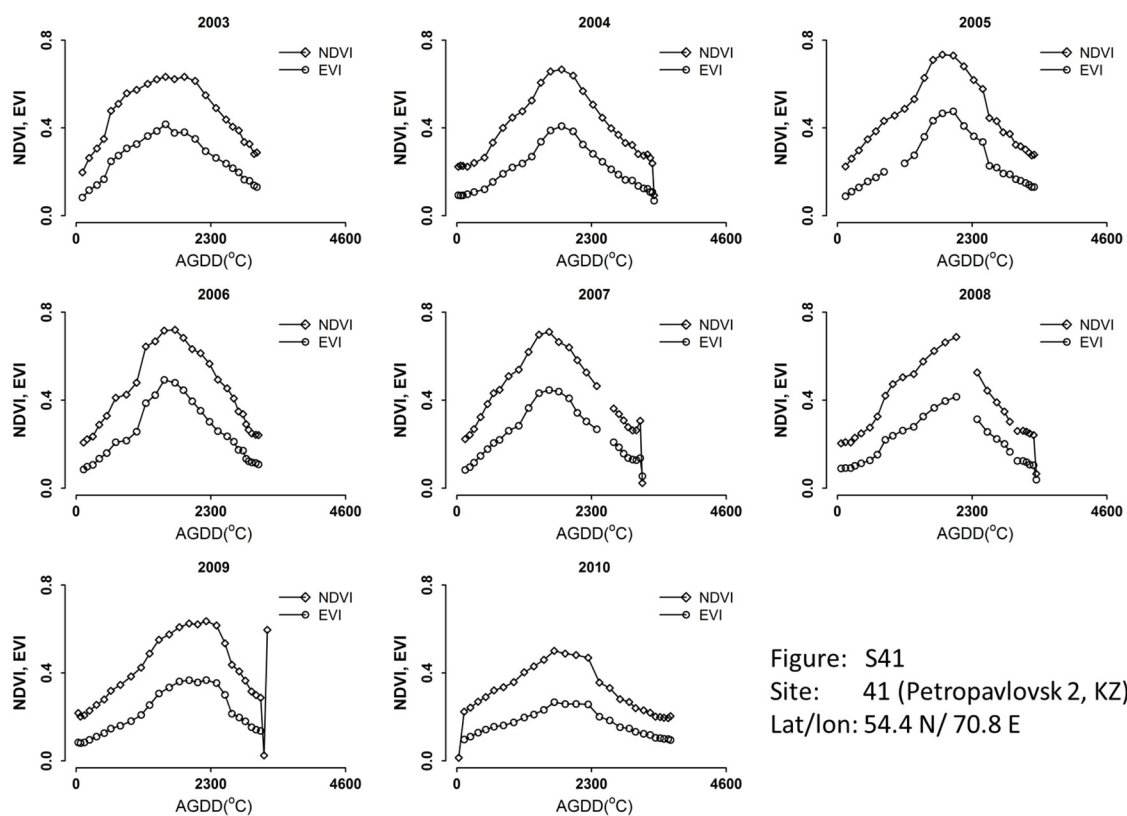


Figure: S41  
 Site: 41 (Petropavlovsk 2, KZ)  
 Lat/Ion: 54.4 N/ 70.8 E

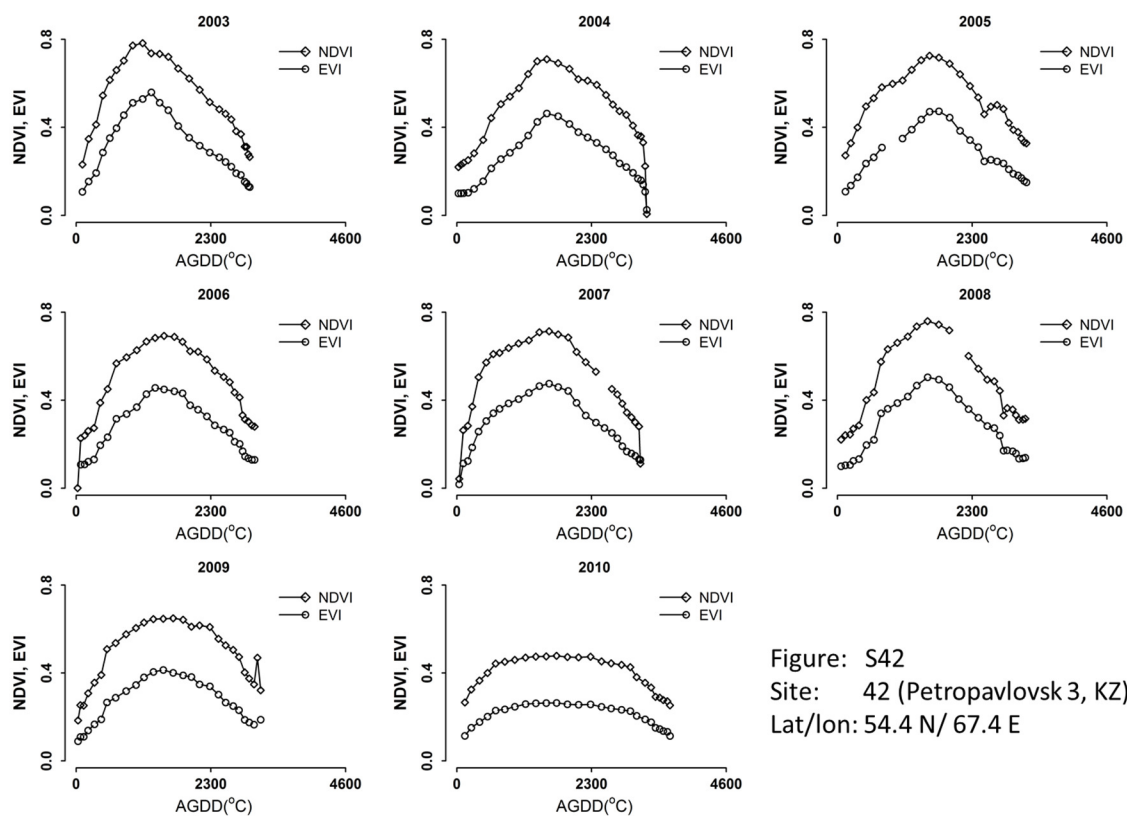


Figure: S42  
 Site: 42 (Petropavlovsk 3, KZ)  
 Lat/Ion: 54.4 N/ 67.4 E

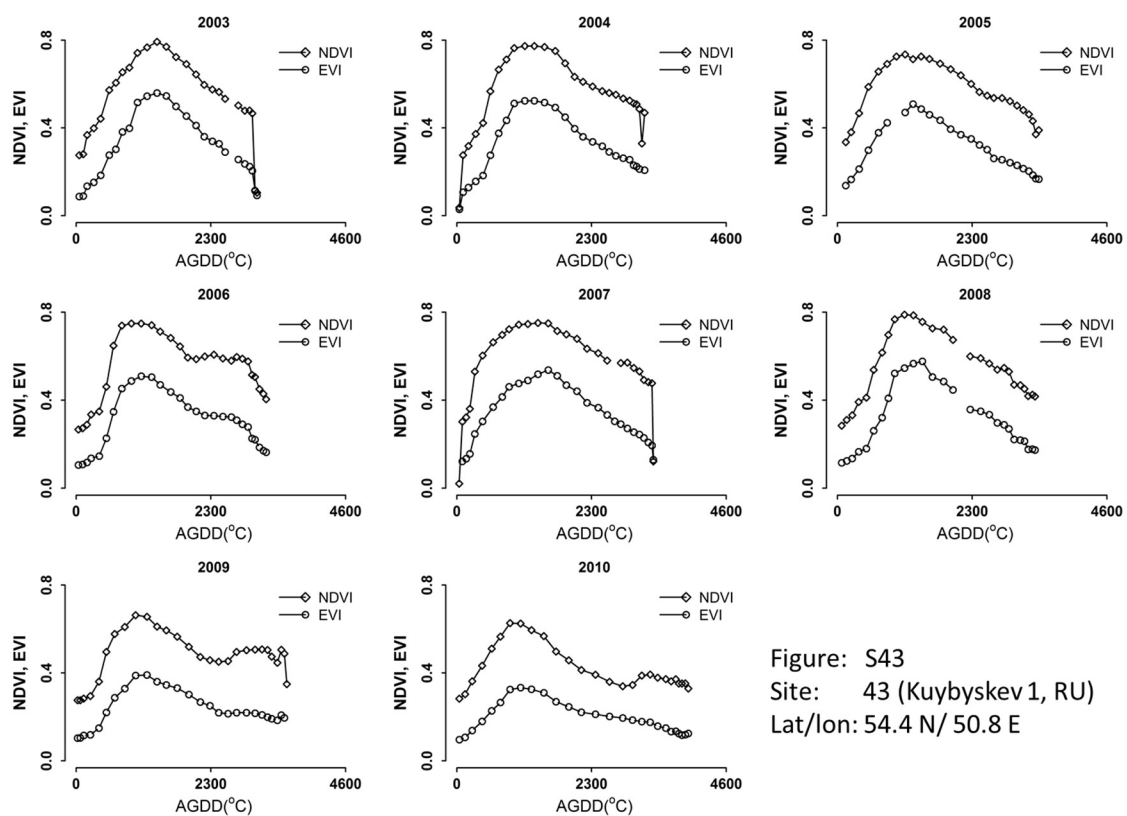


Figure: S43  
 Site: 43 (Kuybyshev 1, RU)  
 Lat/Ion: 54.4 N/ 50.8 E

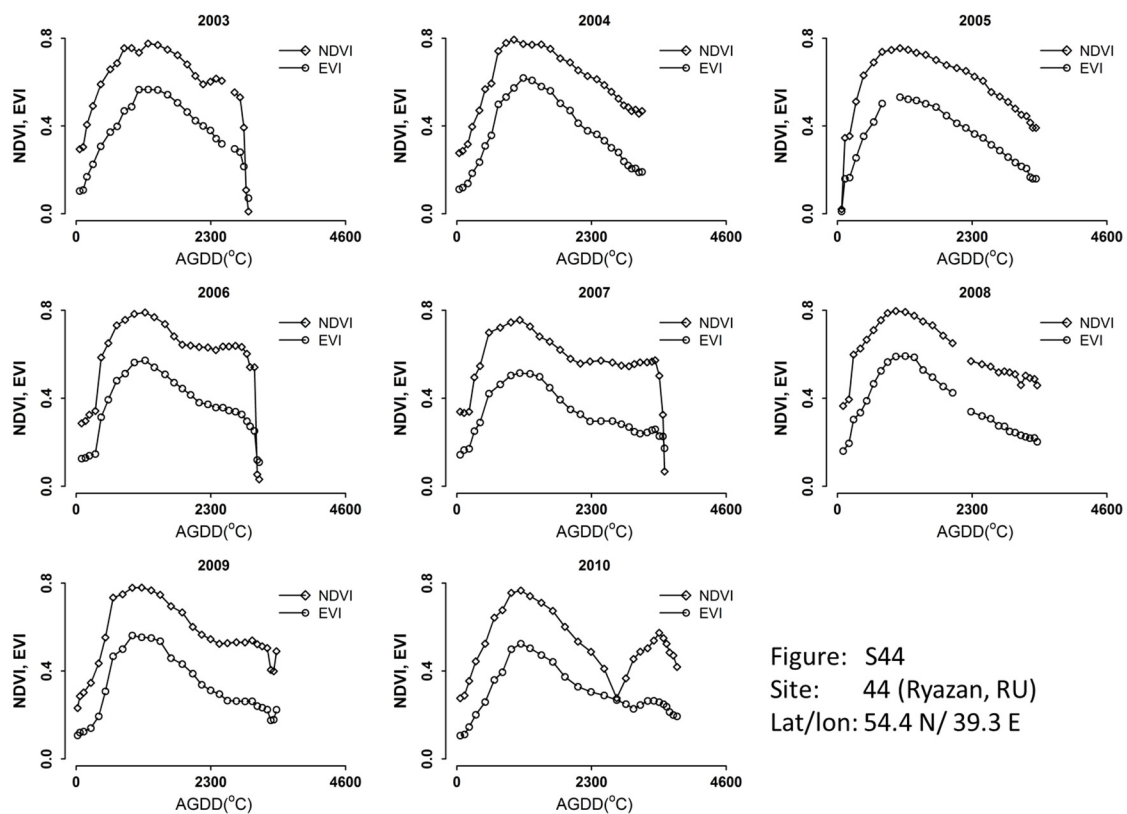


Figure: S44  
 Site: 44 (Ryazan, RU)  
 Lat/Ion: 54.4 N/ 39.3 E



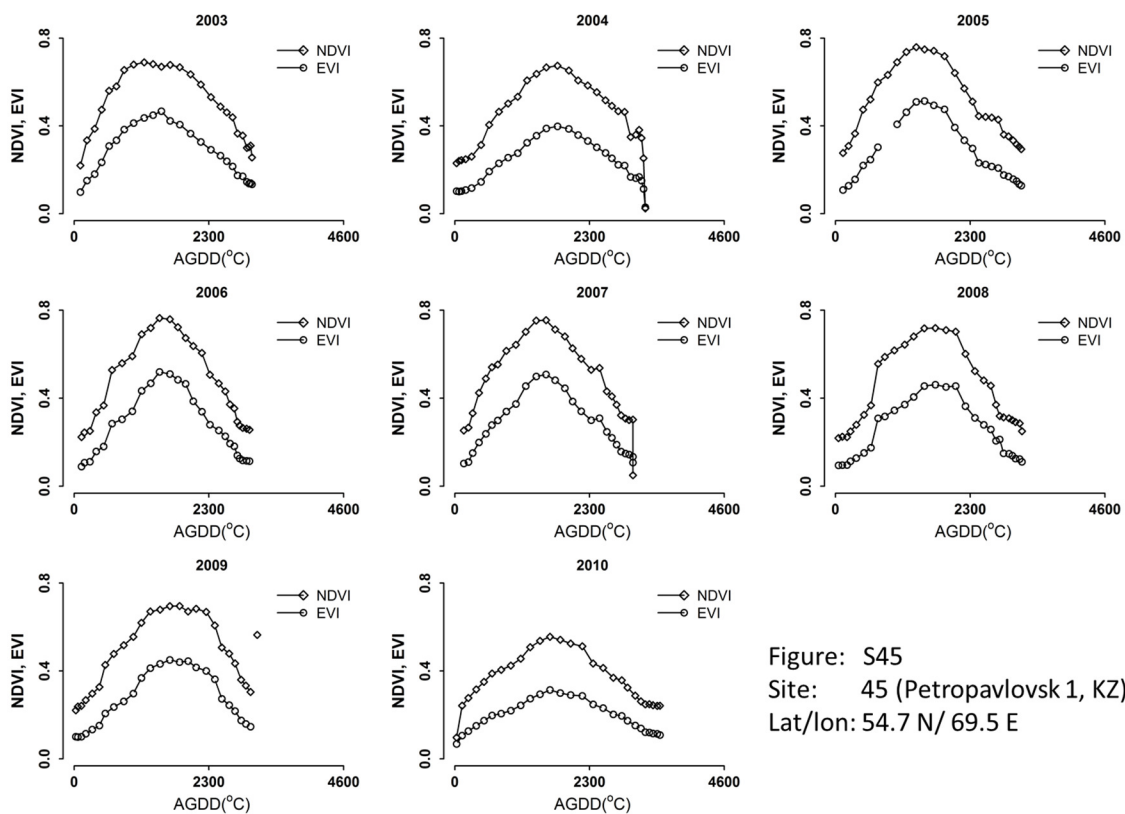


Figure: S45  
 Site: 45 (Petropavlovsk 1, KZ)  
 Lat/Ion: 54.7 N/ 69.5 E

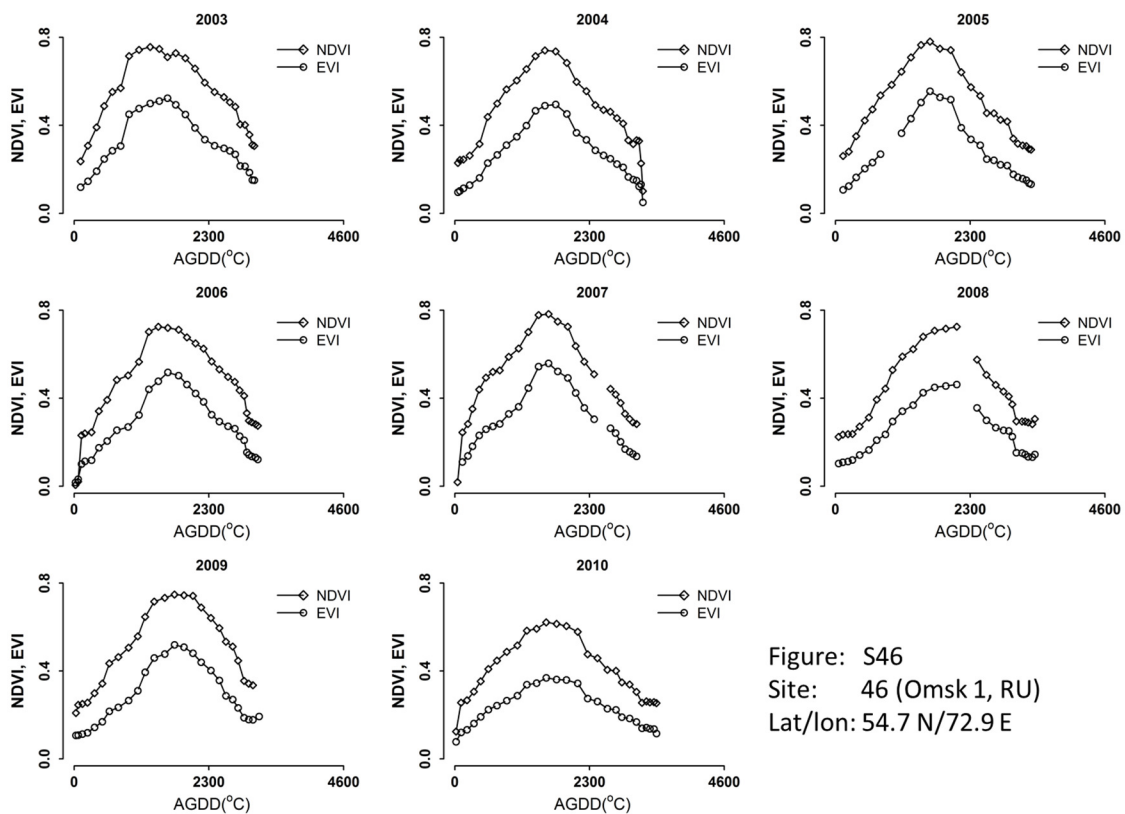


Figure: S46  
 Site: 46 (Omsk 1, RU)  
 Lat/Ion: 54.7 N/72.9 E

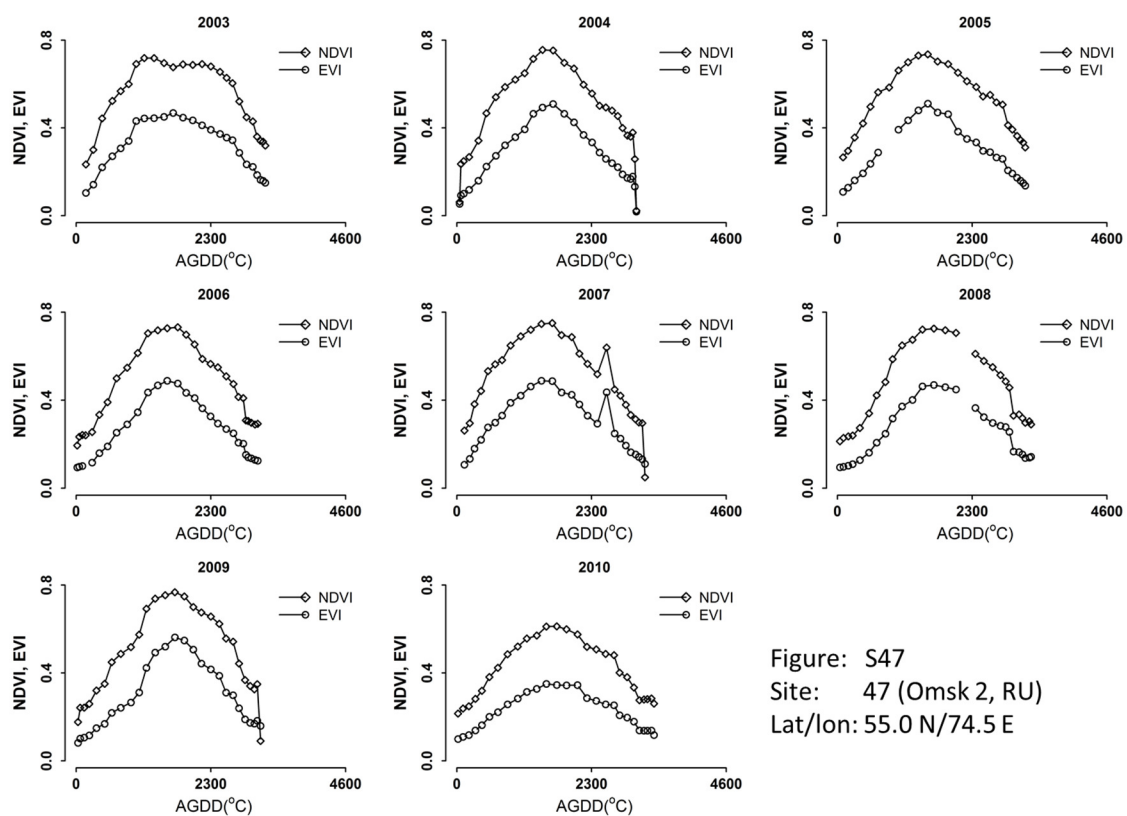


Figure: S47  
 Site: 47 (Omsk 2, RU)  
 Lat/lon: 55.0 N/74.5 E

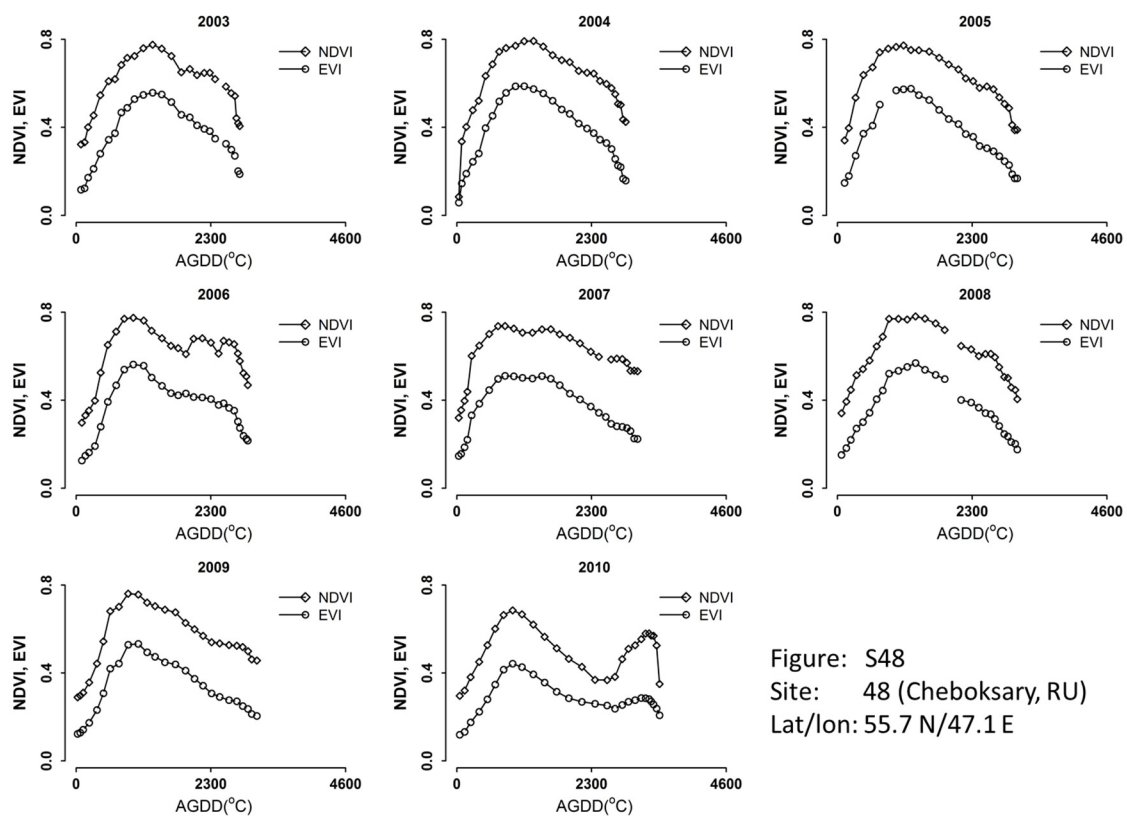


Figure: S48  
 Site: 48 (Cheboksary, RU)  
 Lat/lon: 55.7 N/47.1 E

